



**Department of Mechanical and Industrial Engineering**

**XXI Ph.D. Fellowship  
(2006-2008)**

**Multi-Step Approaches  
for Comprehensive Modeling of Diesel Engine  
Fuel Injection Processes**

Fulvio Palmieri

Advisor Professor:

chiar.mo prof. ing. Giancarlo Chiatti

Coordinator:

chiar.mo prof. ing. Edoardo Bemporad

# Contents

## Section I – Map of the work

<b>1.</b>	<b>Abstract</b>	<b>6</b>
<b>2.</b>	<b>Introduction</b>	<b>7</b>
2.1	Overview	7
2.2	Specific overview, state of the art	9
2.2.1	Injection rate	
2.2.2	Atomization and air-fuel mixture formation	
2.3	Motivation and Methodologies	13
2.3.1	Numerical modeling of injection processes	
2.3.2	Multi-step modeling (0D-3D CFD) for injection processes simulation	
2.3.3	Double step modeling (3D-0D) of fuel metering component operation for inline pump injection systems	
2.3.4	Comprehensive multi-step lumped modeling of injection system operation, spray formation and fuel vaporization	
2.4	Applications	19
2.4.1	Development of a three-step cascade modeling procedure for sequential simulation of inline-pump injection system operation, nozzle flow features and in-cylinder spray formation	
2.4.2	Application of the cascade modeling procedure evaluating fuel influence on common rail system performances	
2.4.3	Comprehensive modeling of injection: the introduction of the fuel in the combustion chamber as the result of the correct integration of component roles	
2.4.4	Evaluation of injector dynamic and nozzle flow features in multiple injection strategies. Modeling capabilities of the multi step unitary approach	
2.4.5	Contribution of sequential modeling approach investigating dynamic features of injectors	
2.4.6	Two step 3D-0D modeling of inline pump systems. The CFD contribution for detailed parameter lumping	
2.4.7	Multi step lumped modeling of injection process. Development of a comprehensive injection process model for low computational effort investigations	

## Section II Case studies

Each chapter of this section is conceived as a single unit, which consists of a complete investigation on specific facets related to the injection process and its modeling. In order to ease the consultation of the work, all the chapters are provided with independent nomenclature and list of references.

<b>3.</b>	<b>Coupling Codes For a Multi-step Modeling Approach of Diesel Injection System</b>	<b>23</b>
3.1	Introduction	23
3.2	Injection system.	24
3.3	Nozzle flow modelling	24
3.4	Spray and chamber flow simulation	27
3.5	Results	30
	3.5.1 Injection characteristics	
	3.5.2 Injector flow	
	3.5.3 Chamber flow/spray	
3.6	Concluding remarks	41
3.7	Nomenclature	42
3.8	References	43
<b>4.</b>	<b>Multi-step Modeling of Fuel Influence on Common Rail Injection System Performance</b>	<b>45</b>
4.1	Injection system	45
4.2	Spray and chamber flow simulation	47
4.3	Results	50
4.4	Injection characteristics	50
4.5	Injector flows	52
4.6	Spray features	55
4.7	Concluding remarks	58
4.8	Nomenclature	59
4.9	References	60
<b>5.</b>	<b>Injector Dynamic and Nozzle Flow Features in Multiple Injection Modeling</b>	<b>62</b>
5.1	Injection system	62
5.2	Injector features and nozzle type	64
5.3	Results	66
	5.3.1 Injection System	
	5.3.2 Nozzle flow	
5.4	Concluding remarks	76
5.5	Nomenclature	76
5.6	Appendix	77
5.7	References	78
<b>6.</b>	<b>Diesel VCO Injector: Geometric Layout and Operating Condition influence. Nozzle Flow Modeling and 3D in-Cylinder Simulation</b>	<b>80</b>
6.1	Injection system	80
6.2	Injector geometry and configuration	81
6.3	Spray and chamber flow simulation	84

6.4	<b>Results</b>	<b>87</b>
6.4.1	Injection System	
6.4.2.	Nozzle Flow	
6.4.3	Chamber Flow/Spray	
6.5	<b>Concluding remarks</b>	<b>98</b>
6.6	<b>Nomenclature</b>	<b>98</b>
6.7	<b>References</b>	<b>100</b>
<b>7.</b>	<b>Mini-sac Injector: Modeling Needle Motion Influence on Nozzle Flow in High Pressure Injection System</b>	<b>102</b>
7.1	Introduction	102
7.2	Injector model	104
7.3	Injector flow modeling	104
7.4	Results	108
7.5	Concluding remarks	115
7.6	Nomenclature	116
7.7	References	117
<b>8.</b>	<b>Flow Features in Reduced Dwell Time Diesel Injector</b>	<b>119</b>
8.1	Introduction	119
8.2	0/1-D injection system model	120
8.3	Injector features and lift modeling	122
8.4	Results	124
8.5	Concluding remarks	134
8.6	Nomenclature	134
8.7	References	135
<b>9.</b>	<b>Inline Pump Internal Flow Characterization for Optimized Diesel Injection – 3D-CFD Evaluation of Pump Passages Discharge Coefficients</b>	<b>136</b>
9.1	Introduction	136
9.2	Fuel injection system	137
9.3	Lumped/1D approach	137
9.3.1	Flow through orifices modeling	
9.3.2	3D flow analysis	
9.3.3	Discharge coefficient evaluation	
9.4	Simulated system performance	143
9.5	Concluding remarks	147
9.6	Appendix A - Multiphase flow modeling	147
9.7	Appendix B – $C_d$ setting influence	148
9.8	Nomenclature	149
9.9	References	150
<b>10.</b>	<b>Multi-Step Lumped Parameter Fuel Injection and Vaporization Modeling for Diesel Engine Performance Analysis</b>	<b>151</b>
10.1	Introduction	151
10.2	Fuel injection system	151
10.3	Injection system modeling - I Simulation Module	152
10.4	Fuel spray dynamics - II Simulation Module	153
10.5	Droplet evaporation - III Simulation Module	154
10.6	Comparison among models and validation	156



10.7	Results	157
10.8	Fuel spray model	160
10.9	Vaporization model	162
10.10	Fuel influence on engine performance	165
10.11	Concluding remarks	165
10.12	Nomenclature	166
10.13	Appendix A	167
10.14	References	172
11.	References of Published Works	176
12.	Concluding Remarks	177
13.	Next Outlooks	179

# **1. Abstract**

The overall optimization of diesel fuel injection equipment and combustion process is mandatory to fulfill the future emission regulations. Among the involved phenomena, a preliminary role is played by the strong link between the combustion behavior and the adopted strategies to promote the mixing of reactants. The aim of the present work is to develop a comprehensive modeling approach, having the capability to take the deep connection between fuel injection phenomena into account. For this scope, different computational tools, characterized by different roles, have been used and coupled, accounting for the interdependencies of the relevant sub-processes. Three main multi-step modeling approaches are outlined and then used in the analysis of practical cases; these can be summarized as follows: 1) multi-step modeling (0D-3D CFD) for injection process and spray simulation with a unitary approach; 2) double step modeling (3D-0D) of fuel metering component operation; 3) comprehensive multi-step lumped modeling of injection system operation, spray formation and fuel vaporization. The mechanical-hydraulic modeling of the injection systems is based on the 0-1D code AMESim. To model the in-cylinder flows and the 3D transient nozzle flow, the commercial FIRE code is used, whereas the lumped modeling of evaporation processes in cylinder ambient is self FORTRAN implemented. Several cases have been considered and the contribution of the modeling approach is presented evaluated. Two different injection system types (inline pump and common rail systems) are considered in the applications. Investigations are devoted to evaluate the influence on injection process of fuel characteristics and composition, injection strategies, injector layout, geometrical features and needle operating conditions.

## **2. Introduction**

### **2.1 Overview**

The market share of diesel equipped passenger car has become wider and wider during the last years. Among the various factors, low fuel consumption, high power density and torque behavior are the main reasons of such a relatively recent diffusion.

As regards the new production cars, since 1998 the European Automobile Manufacturers' Association (ACEA) is playing an active part in the reduction of the mean fuel consumption. To achieve such a goal, it is widely acknowledged that diesel engine represents a valid answer to the problem; the manufacturers plans (until 2012) count to increase the diesel market at 50% (in respect to gasoline) and to maintain it. Indeed, due to the relatively high efficiency, direct injected diesel engines retain an advantage in fuel economy (compared to the spark ignited engine performances). The biggest challenge in diesel applications is the future emission legislation in mostly all markets over the world.

Currently more and more countries around the globe are legislating controls aimed at achieving safe concentrations of these pollutants by regulating their level of emissions from combustion sources, notably those discharged from the exhausts of automobiles. The maximum allowable levels of emissions from automobiles are already regulated by many governments using measures in grams per kilometer or grams per mile. Emission control standards were initially established in the major

centers of Japan, the United States, and the European Union. These regions have similar approaches to emission reduction, although each set of regulations is tailored to specific requirements. The US system, based on groups of regulations called Tiers, has decreasing emissions limits and increasing durability requirements. The European regulations also define increasing restrictions. Currently Euro V sets limits to 2014 when Euro VI will take effect. The most stringent emissions standards in the world are to be found in California which has become the benchmark for worldwide environmental legislation. The legislation refers to LEV (Low Emission Vehicle), ULEV (Ultra LEV), SULEV (Super Ultra LEV), and ZEV (Zero Emission Vehicle).

In such a scenario, the goal of research and development activities is the definition of strategies able to satisfy the emissions regulations; diesel finds itself more and more faced with continuously burdening challenges which have to be overcome within the technical progress. While the gasoline engine settles the benchmark for noise vibration harshness (NVH), the complexity of the overall diesel system becomes tends to increase in spite of the tremendous desire to lower the overall system costs. To overcome this challenge an overall system optimization of the fuel injection equipment, the engine and combustion process and the exhaust gas treatment are mandatory.

In the frame of direct injected diesel engines, a preliminary role is played by the strong link that exists between the combustion behavior and the strategies that are adopted to promote the mixing among reactants in combustion chamber. From an operational point of view, fuel is introduced in combustion chamber as a fine spray and it evolves into heat release and pollutant emission. The recent trends in combustion control research are gaining significance, much more evidently than in the past. Heat release (and pollutant formation) is supposed to be controlled by a refined shaping of fuel injection rate. Therefore, it seems that research approaches take advantage of consideration that fuel spray formation is an aspect of several interrelated phenomena. According to this viewpoint, a chain process (that lasts until the exhaust phase) starts when fuel is injected into the combustion chamber. So the engine can be viewed as a combustion system in which injection system, cylinder volume and gas flows have strongly interrelated tasks.

## **2.2 Specific Overview and State of the art**

### **2.2.1 Injection rate**

Diesel engine optimization is a challenging task due to the interrelation among the several phenomena that take place in the cylinder. Injection systems features (e.g. maximum injection pressure - tied to fuel atomization and droplet velocity), and flexibility (e.g. fuel rate shape capability and multiple injection) define the limits in determining the optimum system configuration for the above mentioned diesel engine goals. An important contribution comes from the introduction of common rail systems. During the recent years, multiple injection strategies have been implemented for simultaneously reducing diesel engine NO<sub>x</sub> and particulate emissions. Moreover, the up to date engine tests show that improvement of multiple injection still has the potential of achieving a reduction in the peak heat release and the NO<sub>x</sub> and particle emissions. To stay on very small injection quantities and fully flexible multiple injection events, the optimization of injection dynamics with at higher pressure level is desired.

The need for short dwell time and the small amount of fuel to deliver has driven the research to the development of piezo actuated injectors. Previous injector designs used electro-magnetic solenoids to pilot the movement of needle and feed fuel to the combustion chamber. In piezo injectors, a stack of piezo crystals expand when an electric current is applied. The first generation of piezo injectors used an indirect servo-hydraulic actuation mechanism; the development is going ahead and, in the latest implementations, the piezo ceramic actuator directly actuates the needle, so it responds to commands even more quickly, allowing the timing of the fuel pulses to

be smaller, and more accurately timed. In practice, beside the classical requirements of injection systems, like:

- flexible injection pressure
- level of maximum injection pressure,
- flexible timing of multiple injections
- small and stable injection quantities to realize pilot and post injections

it is possible to outline the specific features that realize a desired injection rate (all the features show themselves during the injection time transient)

- fast needle opening
- low injection rate during ignition delay, but
- strong increase of the injection rate after start of combustion
- high maximum injection rate
- fast rate decrease at the end of injection and also high needle closing velocity.

The stable and repeatable achievement of such a kind of requirements (on wide engine operating conditions) leads to a full flexible rate shape in the whole engine map, that means low emissions, high engine performance, low noise level and low fuel consumption. The automotive industry, has based the injection process improvement (and diesel engine future, as well) on the common rail systems development. With its improved performance and higher torque, common rail gave to diesel engine a new image. In conjunction with turbo charging, the injection system has helped the diesel engine achieve a breakthrough.

As a consequence the successful application of lowest emission, diesel combustion strategies must always be seen in close connection with the required engine control strategy. It is realistic, in the next future, the deep integration among the several electronically controlled systems of the engine, as VG-turbocharger, injection system and valve camshafts timing; closed loop combustion control is being developed since the recognition that, with today's flexibility on diesel engines, the start of combustion is not only controlled by the fuel injection timing. Charge condition parameters have significant effects on the combustion and thus on engine out emissions. Applying some kind of closed loop combustion control reduces the dispersion when shooting for lowest emissions and also enables future combustion strategies.

### **2.2.2 Atomization and air-fuel mixture formation**

Injection pressure of up to 200 MPa is becoming a mandatory feature for the latest injection strategies. The liquid enters the combustion chamber with velocities that can overcome the value of 500 m/s, and the jet evolves according to the mechanisms proper of the dominating atomization regime. Two main atomization mechanisms can be identified; immediately after leaving the nozzle hole, the jet starts

to break up into a conical spray. Such a first break-up of the liquid is called primary break-up and results in large ligaments and droplets that form the dense spray in the proximity of the nozzle exit hole. In case of high-pressure injection, cavitation and turbulence, which are generated inside the injection holes, are the main break-up mechanisms. Concerning the case of turbulence induced disintegration, if the radial turbulent velocity fluctuations inside the jet, which are generated inside the nozzle, are strong enough, turbulent eddies can overcome the surface tension and leave the jet to form primary drops. Turbulence-induced primary break-up is regarded as one of the most important break-up mechanisms of high-pressure sprays. In the cavitation-induced disintegration, cavitation structures develop inside the nozzle holes because of the decrease of static pressure due to the strong acceleration of the liquid (axial pressure gradient) combined with the strong curvature of the streamlines (additional radial pressure gradient) at the inlet edge. Hence, a two-phase flow exists inside the nozzle holes. The intensity and spatial structure of the cavitation zones depends on nozzle geometry and pressure boundary conditions. The cavitation bubbles implode when leaving the nozzle because of the high ambient pressure inside the cylinder. Different opinions exist regarding whether the energy that is released during these bubble collapses contributes to the primary break-up either by increasing the turbulent kinetic energy of the jet or by causing a direct local jet break-up. However, experimental investigations have shown that the transition from a pure turbulent to a cavitating nozzle hole flow results in an increase of spray cone angle and in a decrease of penetration length. The two main break-up mechanisms in the case of high-pressure full-cone occur usually simultaneously. Injector design tries to take into account the role of the phenomena that happen inside the hole, in order to achieve a trade off among many factors such as atomization performances, material stress, nozzle lifetime, production costs and so on.

The subsequent break-up processes of already existing droplets into smaller ones are called secondary break-up and are due to aerodynamic forces caused by the relative velocity between droplets and surrounding gas. The aerodynamic forces decelerate the droplets. The drops at the spray tip experience the strongest drag force and are much more decelerated than droplets that follow in their wake. For this reason the droplets at the spray tip are continuously replaced by new ones, and the spray penetration increases. The droplets with low kinetic energy are pushed aside and form the outer spray region. Altogether, a conical full-cone spray (spray cone angle) is formed that is more and more diluted downstream the nozzle by the entrainment of air. Most of the liquid mass is concentrated near the spray axis, while the outer spray regions contain less liquid mass and more fuel vapor. Droplet velocities are maximal at the spray axis and decrease in the radial direction due to interaction with the entrained gas. In the dense spray, the probability of droplet collisions is high. These collisions can result in a change of droplet velocity and size. Droplets can break up into smaller ones, but they can also combine to form larger drops, in case of droplet coalescence. In the dilute spray further downstream the main factors of influence on further spray disintegration and evaporation are the boundary conditions imposed by

the combustion chamber such as gas temperature and density as well as gas flow (tumble, swirl). The penetration length is limited by the distance between the nozzle and the piston bowl. In detail, It has to be highlighted that gas flows inside cylinder volume play a preeminent role when a relatively few nozzle holes are present (e.g. small DI diesel engines equipped with inline pump systems). In the case of high injection pressure and long injection duration (full load) or low gas densities (early injection) the spray may impinge on the wall, and the formation of a liquid wall film is possible. Liquid wall films usually have a negative influence on emissions, because the wall film evaporates slower and may only be partially burnt.

It has to be highlighted that the pollutant formation mechanisms are governed by intrinsically local sub-processes. Drawbacks can be induced by the improvement of some processes like fuel atomization, too; a very fine spray can induce the formation of lean combustion zones that burn at a relatively low temperature. In such conditions, the carbon monoxide formation could affect diesel processes as well. During transient operation of the engine (e.g. acceleration phase) the fuel-air ratio increases, caused by the delayed response of the turbocharger and the increased amount of injected fuel. Obviously, in order to fulfill future emission limitations, the use of exhaust gas after-treatment systems represents an effective methodology, especially for heavy vehicles. However, the reduction of engine raw emissions, by means of a proper control of the combustion process, still remains an attractive challenge.



## **2.3 Motivation and Methodologies**

### **2.3.1 Numerical modeling of injection processes**

On the basis of joined numerical models and experimental activities it is possible to achieve relevant improvements in the process of internal combustion engine optimization. Besides the uncertainties typical of the simulations, the advantages resulting from the modeling of the processes that take place within the engine are becoming crucial during the research and development phases. Simulation models, which have been carefully adjusted to a specific range of boundary conditions, can be used to perform extensive parametric studies, which are usually faster and cheaper than experiments. Despite the higher uncertainty compared to experiments, numerical simulation can give much more extensive information about the complex in-cylinder processes than experiments could ever provide. Using numerical simulations, it is possible to calculate the temporal behavior of every variable of interest at any place inside the computational domain. This allows getting a detailed knowledge of the relevant processes, and is a prerequisite in order to improve them. Furthermore, the numerical simulation can be used to investigate processes that take place at time and length scales or at places that are not accessible and thus cannot be investigated experimentally.

In the case of high-pressure diesel injection for example, the spray break-up near the nozzle is mainly influenced by the flow conditions inside the injection holes. However, because of the small hole diameters (less than 200  $\mu\text{m}$  for passenger cars) and the high flow velocities (about 600 m/s and more), the three-dimensional turbulent and cavitating two-phase flow is not accessible by measurement techniques. One very

costly and time-consuming possibility of getting some insight into these processes is to manufacture a glass nozzle in real-size geometry and to use laser-optical measurement techniques. Outside the nozzle in the very dense spray measurements of the three-dimensional spray structure (droplet sizes, velocities etc.) become even more complicated, because the dense spray does not allow any sufficient optical access of the inner spray core. In these and other similar cases numerical simulations can give valuable information and can help to improve and optimize the processes of interest.

As it will be exposed in the next paragraphs, a crucial advantage of the process modeling is the possibility to describe the interactions and the interdependencies among the relevant processes.

The aim of the present work is to develop a comprehensive modeling approach having the capability of take the deep connection between fuel injection phenomena (e.g. injection strategy, fuel flows, jet atomization, evaporation and mixture formation) into account. For this scope, different computational tools, characterized by different roles, have been used and coupled, in order to take into account the interdependencies that characterize the relevant sub-processes. The following paragraphs illustrate the three main modeling approaches that have been outlined and then used in the analysis of several practical cases. In section II, several application cases have been considered and the contribution of the modeling approach has been presented evaluated.

### **2.3.2 Multi-step modeling (0D-3D CFD) for injection process and spray simulation with a unitary approach**

In fuel injection investigations, simulation tools are significantly supported by research and development activities. At present, injection system simulation tools and spray modeling singly achieve good results, as they have been successfully improved (Fig.2.1). On the other hand, by considering the whole injection process and its effects on engine performance, a unitary modeling approach is desirable. As pointed out in the precedent paragraphs, the flow condition inside the orifice is one of the factors that promote the spray to break up into droplets, as well the interaction between the spray and the ambient. Moreover, the flow characteristics are influenced by the injection pressure, and consequently its time variations. The injector geometry also plays a role. Interesting experimental and computational works have investigated the influence of injection strategies over engine performance, emissions and over the spray behavior. The modeling goal is to develop an integrated tool able to take the deep connection between fuel injection phenomena (injection strategy, jet atomization, evaporation and mixture formation) into account. For this scope, two computational codes, characterized by different roles, have been used.

A multi step simulation procedure has been outlined and used. In the former step, a phenomenological model is built to simulate the operation of the complete injection system; the attention spots on the system analysis and on the investigation of the effect of specific components and parameter settings on the system performance. In the second step, the latter computational tool, based on a 3D CFD environment, has been initialized by means of the results obtained from the injection system simulation and has been used to perform the 3D investigation of the internal nozzle flow. Such a simulation is aimed at evaluating the effect of physical fuel features on local flow characteristics and their influence on the system performances.

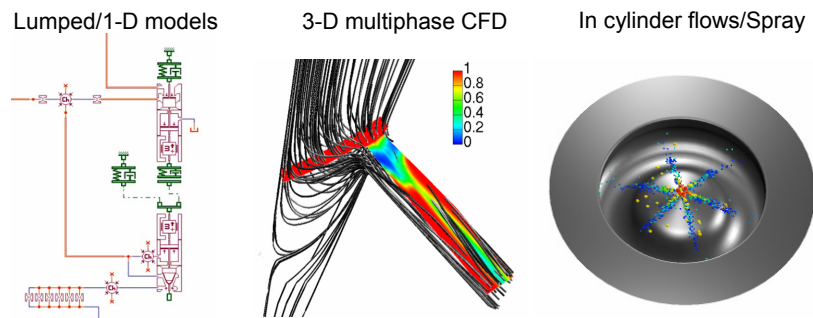


**Figure 2.1:** Use of simulation tools in diesel injection modeling

Since experiments can be difficult to manage for injection conditions (small-scaled, high-speed flow) a numerical simulation seems to be an appropriate tool to get an interesting model of the flow features inside and at the exit of the injector nozzle. In the third simulation step, the model and of the spray formation within the combustion chamber is performed.

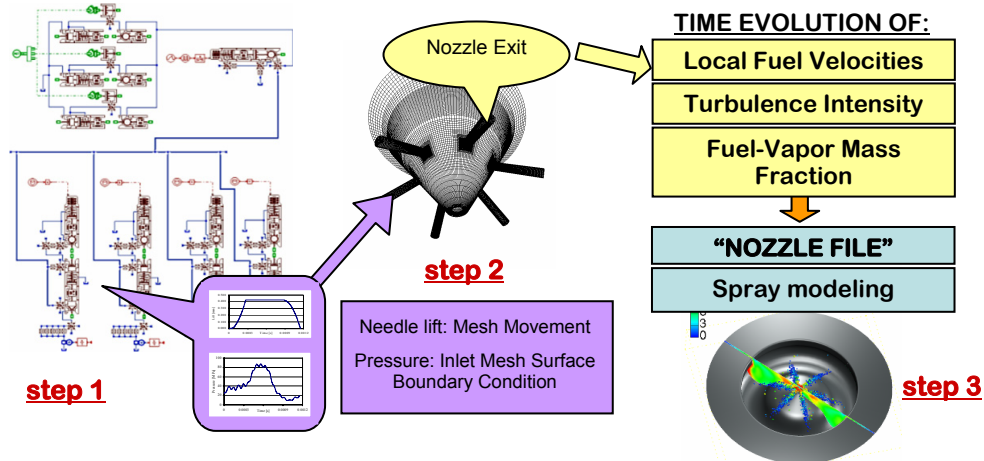


**Figure 2.2:** Schematic of the multistep modeling approach

Aimed at achieving a realistic link between the nozzle flow results and the spray model, the data of the two phase flow calculation inside the nozzle are used as initial condition for an Euler/Lagrange spray calculation. Although there is no direct

coupling between the internal nozzle flow simulation and the spray calculation, nozzle data are used as boundary conditions for spray calculation. At the interface, the values of liquid velocities, densities and turbulence quantities are stored into a data file. For a transient calculation, an arbitrary number of data sets can be saved at different time steps. During the Lagrangian spray simulation, the initial values are linearly interpolated from the available data sets. This approach helps to obtain reliable initial conditions for injection velocity and initial spray angle and it offers the possibility of applying more detailed primary break-up models, since detailed information about turbulence quantities and cavitation bubbles at the nozzle exit are available (Fig.2.2).

### **2.3.3 Double step modeling (3D-0D) of fuel metering component operation for inline pump injection systems**

Small diesel engines are largely used in industry and agriculture. Reliability and cost effectiveness are often key features of such a kind of engines. In several applications, sophisticated electronic or electric devices (common in automotive field) cannot be used; furthermore, especially for the smaller units, battery lack is often necessary or recommended (e.g. manual start). If reliability is preferred to absolute performance, these engines are equipped with relatively simple auxiliary components. Nonetheless, the pollutant emission standards define limits that must be strictly satisfied. Therefore, simple engine layouts do not mean obsolete technology; on the contrary, accurate research and development activities are required to match reliability, cost effectiveness and emission standard accordance. As exhaust-gas after-treatment systems cannot be easily used (for the already described reason), the in-chamber pollutant formation control is pre-eminent. In such a frame of reference, fuel-air mixing process plays a major role and it is deeply influenced by the injection strategy. More in detail, the engine performance is widely influenced by the ensemble inline pump-delivery valve; as known, injected fuel amounts, fuel pressure level and process length are reciprocally related. Engine operation is controlled by the positioning of the helicoidal groove, whose rotation angle defines engine load, injection phase and pressure evolution.

The proposed investigation approach is based on a lumped/1D model of the injection system that is set in a double step simulating procedure. The main mechanical-hydraulic model uses the indications obtained by a 3D CFD characterization of the most influencing components. Indeed, the discharge coefficients needed by the lumped approach are evaluated by means of 3D numerical experiments, allowing for a detailed component characterization. The detailed evaluation of the flow through the fuel metering components makes also possible the evaluation of the fuel characteristics influence on the system operation (in terms of fuel rate time evolution and injected amount). Due to the interesting capability to draw useful indications about the injection system, the used modeling approach is very

helpful in advanced system design and development (Fig.2.3). The fine modeling of fuel delivery process is directly tied to the description accuracy of combustion processes; therefore, it represents a key factor during the engine optimization in the matter of performance and emission reduction. The present approach is implemented in the modeling procedure that is described in the next paragraph, as well.

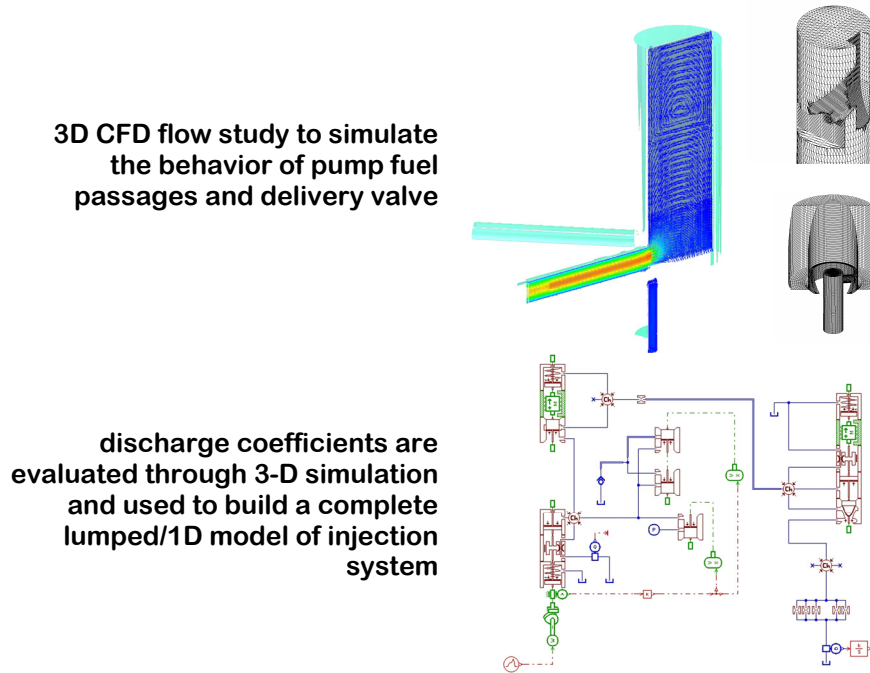


**Figure 2.3:** Schematic of the double step modeling approach

### **2.3.4 Comprehensive multi-step lumped modeling of injection system operation, spray formation and fuel vaporization**

Accurate research and development activities are required to match reliability, cost effectiveness and emission standard accordance, which defines limits for the considered engine category. Due to the interesting capability to draw useful indications about the injection system operation, an appropriate modeling approach is helpful in advanced system design and development. The fine modeling of fuel delivery process and the consequent evolution in terms of spray formation is directly tied to the description accuracy of engine performances; therefore, it represents a key factor during the engine optimization in the matter of performance and emission reduction. With a comprehensive simulation strategy, an injection system numerical model is set-up. The modeling approach is based on the mechanical-hydraulic representation of the system; such a main model is worked up in order to build in two additional modules. The modules permit the evaluation of the fuel jet characteristics and the subsequent evaporation process. Therefore, the complete model is totally

composed of three sequential main modules. Each module is based on a zero/one-dimensional approach, which is computationally not expensive. Indeed, it allows to easily execute time-efficient calculations or pre-calculations, parametric studies and system operation preliminary adjustment. Concerning the first computation module, a fully mechanical injection system is considered. The lumped model is used with a predictive approach to compute needle lift and fuel flow rate time traces.

The second simulation module is devoted to the fuel spray characteristics evaluation, in terms of jet penetration, spray cone angle and droplet atomization. Such a computation step is based on the use of empirical correlations and it is coupled to the first simulation module, in order to evaluate the time evolution of jet penetration, Sauter mean diameter and cone angle during the injection shot.

In a further step, the third one, the vaporization process is simulated. The model takes into account the effect of the droplet heating before the evaporation and it is implemented according to two different approaches, in order to evaluate the role of the droplet thermal conductivity on the vaporization rate. In principle, the coupling between such a computation step and the previous one is based on the values of the Sauter mean diameter, which is considered to be representative of the simulated atomization behavior.

The three modules of the model allow for the integrated simulation of the multiple and complementary aspects of the injection process, so that it is possible to infer an effective picture of the injection system behavior, taking into account the role of each sub-phase and the links among them. In addition, the use of such a model is extended to the influence evaluation of different types of fuel on the injection process.

Finally, moving from the single component fuel, the third simulation module is adjusted in order to model the evaporation behavior of mixtures, in which usually high boiling point components are blended with low boiling point species. Binary mixtures are modeled; the time evolution of the specie concentration (both for vapor and liquid states) is computed and the differences in vaporization rate are highlighted. Finally, the integration of the injection-vaporization model with a single-zone combustion model is tested, allowing for the evaluation of fuel influence on engine performance.

## 2.4 Applications

**Overview.** On the basis of the modeling approaches that are described in section 2.3, the roles of several factors influencing the injection process are investigated. The next paragraphs give a description of the application cases.

Two different injection system types are considered in the applications; they are inline pump and common rail systems. Indeed, the adopted simulating approaches can be adopted in each case, independently from the particular system, device or fuel type. The contribution of each simulation step is investigated and highlighted, pointing out the modeling approach capability in the evaluation of the relevant phenomena. A preliminary investigation phase has been devoted to the choice of the simulation tools and environments to be used for the model building. To model the in-cylinder flows and the 3D transient nozzle flow, the commercial FIRE code has been selected and used. The mechanical-hydraulic modeling of the various injection systems has been based on the 0-1D code AMESim. Moreover, the lumped modeling of evaporation processes in cylinder ambient is self FORTRAN implemented in order to achieve an effective computational module that can be easily integrated in a comprehensive simulating environment.

### **2.4.1 Development of a three-step cascade modeling procedure for sequential simulation of inline-pump injection system operation, nozzle flow features and in-cylinder spray formation**

The application deals with a numerical investigation of a single cylinder diesel engine equipped with mechanical fuel direct injection system and focuses on the fuel injection system modeling with the aim of predicting the performance of the entire injection system, the spray characteristics, the interaction among spray-cones, combustion chamber flows and geometry. In the simulations, two different codes have been used. With the former one, AMESim code, the complete injection system has been analyzed and the single components have been selected and modeled. The

results obtained from the injection system simulation, in terms of injection needle lift, injection flow rate, pressure time evolution, have been used to initialize the latter computation tool, FIRE code, in which 3D flow numerical investigation of the internal injector flow has been performed. Since such a flow is directly linked to the spray modeling, the primary break-up effects have been taken into account. The details of the adopted modeling strategy have been shown and the results of each simulation step have been presented. In order to highlight the relationship among the nozzle flow condition and the spray formation-vaporization characteristics, a comparison between two different calculation setups has been shown.

#### **2.4.2 Application of the cascade modeling procedure evaluating fuel influence on common rail system performances**

A model for the analysis of diesel engine common rail injection system has been developed and the influence that different fuels have on the injection performances has been investigated. Diesel fuel, biodiesel and kerosene have been used and the differences of injection flow rate, injection pressure time trace, nozzle flow features and break up mechanism have been highlighted. The coupling of two different codes has been used in the simulations: the former one, AMESim code, has been adopted to model the common rail system and to investigate the fuel flow rate and the injection pressure dependence on the fuel type. The latter computational tool, FIRE code, has been initialized by means of the results obtained from the injection system simulation and has been used to perform the 3D investigation of the internal nozzle flow and of the spray formation phenomena, aimed at evaluating the effect of physical fuel features on local flow characteristics and their influence on the system performances. Details of the adopted modeling strategy are described and results of each simulation step are presented.

#### **2.4.3 Comprehensive modeling of injection: the introduction of the fuel in the combustion chamber as result of the correct integration of component roles**

A multi-step modeling procedure is presented with the aim of analyzing the complete fuel injection system, the spray characteristics, the combustion chamber flows. Such a modeling procedure is based on an integrated use of two different computation codes (0D-1D and 3D), each one developed and well suited for a specific task: the investigation of overall injection system performance, phenomena connected to the internal injector flow, spray formation and in-cylinder flows. By means of a 0D-1D code, the complete injection system is realized, providing the relevant indications about the injection process. The investigation deepens into the nozzle flow condition in



the second step of the procedure, where the results coming from the injection system model (flow rate, pressure and needle lift time traces) are used to initialize a 3D calculation, with the objective of evaluating the influence of the injector features (e.g. hole geometry, asymmetries and needle eccentricity) on the development of two phase cavitating flows. In the last computation step, the 3D CFD modeling of the phenomena that take place in the combustion chamber (spray formation) is performed. Results and details of each computation steps are presented in order to illustrate the modeling approach and its capabilities.

#### **2.4.4 Evaluation of injector dynamic and nozzle flow features in multiple injection strategies. Modeling capabilities of the multi step unitary approach**

This application deals with the integrated modeling of a multiple injection common rail system. The aim of the numerical investigation is to capture the behavior of the multiple injections, in terms of electro-injector dynamic and nozzle flow development. In detail, the multiple injection investigation focuses on the transient phenomena of the injector, in order to evaluate their role on the definition of two aspects of the injection strategy, the fuel rate time evolution and their influence on the nozzle flow features. In the simulations, a 0/1-D code has been used to analyze the complete injection system. The results obtained from the injection system simulation, in terms of injection needle lift, injection flow rate, pressure time evolution, have been used as boundary conditions for the 3-D CFD computation tool, in which the numerical investigation of the internal injector flow has been performed.

#### **2.4.5 Contribution of sequential modeling approach investigating dynamic features of injectors**

The research and development activities on diesel injection systems have focused some key-factors that improve the solenoid actuated injector performance, especially in the frame of the multi-event injection strategies. This application deals with a sequential 0D-3D numerical investigation in order to highlight the nozzle flow features of different injector layouts. A comparison between a last generation standard injector and an optimized unit characterized by an improved dynamics, different number of holes and reduced maximum lift is performed. By means of transient numerical simulations, the behavior of the fuel flows, the tendency to cavitation development and the response to the deviation from the standard operating conditions (highlighted by introducing a radial perturbation on the lift motion) are investigated.

#### **2.4.6 Two step 3D-0D modeling of inline pump systems. The CFD contribution for detailed parameter lumping**

The attention is focused on relatively small diesel units, equipped with fully mechanical injection systems; in detail, the considered system layout is based on the use of spring injectors; the amount of delivered fuel is controlled by the positioning of the pump plunger groove. The application highlights the role of the inline pump and the influence of fuel characteristics on the system operation. A two step modeling approach is outlined: by means of a three-dimensional numerical flow study, the behavior of pump fuel passages and delivery valve is simulated. Then, on the basis of the system features, a complete lumped/one-dimensional numerical model is realized, in which the discharge coefficients evaluated through the three-dimensional simulation are employed. Fuel injection rate and local pressure time histories are investigated, paying specific attention to the occurrence of the relevant phenomena in the system components.

#### **2.4.7 Multi step lumped modeling of injection process. Development of a comprehensive injection process model for low computational effort investigations**

The work aims at developing and setting up a model able to predict the diesel spray evolution to be integrated into a complete thermodynamic engine model. Previous application has been devoted to realize a numerical model for the injection system, in which a lumped parameter + one-dimensional approach is employed. Such a model has then enhanced by introducing a quasi-dimensional model for fuel break up, diffusion and penetration processes. Moreover a self-developed heating sub-model is included in the model, which enables the evaluation of the influence of the fuel properties on the evaporation process. As a result, the injection system simulation model gives indications on the spray formation process and it is used into a lumped parameter model of the combustion process. Results concerning the influence of fuel properties on the evaporation process are presented and discussed, pointing out its effect on engine performance.

### **3. Coupling Codes For a Multi-step Modeling Approach of Diesel Injection System**

**3.1 Introduction.** Although simulation tools can be viewed as standard things today, the predictive quality of the sub-models is constantly supported and enhanced by research and development activities [1,2]. At present, injection system simulation and spray modelling singly achieve good results, due to the more and more accurate and modeling of the relevant processes [3]. On the other hand, by considering the whole injection process and its effects on engine performance, a unitary approach is desirable [4]. It is well known that the flow condition inside the orifice is one of the factors that promote the spray to break up into droplets, as well the interaction between the spray and its ambient. Moreover, the flow characteristics are influenced by the injection pressure, and consequently its time variations. The injector geometry also plays a role [5]. Interesting experimental and computational works have investigated the influence of injection strategies over engine performance, emissions and over the spray behaviour [6-8]. The aim of this section is to show the development of an integrated tool able to take into account the deep connection between fuel injection phenomena (injection strategy, jet atomisation, evaporation and mixture formation). For this scope, two computational codes, characterized by different roles, have been used. AMESim software [9], as a phenomenological environment, is based on zero/one-dimensional code; in the modelling of the complete injection system, the attention spots on the system analysis and on the investigation of the effect of specific components and parameter settings on the system performance. Since experiments can be difficult to manage for injection conditions (small-scaled, high-speed flow) [10], a numerical simulation seems to be an appropriate tool to get an interesting model of the flow features inside and at the exit of the injector nozzle. The knowledge of the injector mass flow rate and the flow conditions at the nozzle exit is considered to be a key issue for a successful simulation of all the subsequent processes of mixture formation, and eventually combustion and pollutant formation. In order to take the impact of geometrical details on the highly transient nature of the cavitating injector flow into account, a comprehensive multidimensional two-phase flow model, available in the FIRE environment [11], has been used. Aimed at achieving a realistic link between the nozzle flow results and the spray model, the so-called 'nozzle interface' has been adopted [12]. The idea behind the 'nozzle interface' is to use the data of a two phase flow calculation inside the nozzle as an initial condition for an Euler/Lagrange spray calculation. Although there is no direct coupling between the internal nozzle flow simulation and the spray calculation, nozzle data have been used as boundary conditions for FIRE spray calculation. At the interface, the values of liquid velocities, densities and turbulence quantities are stored into a data file. For a

transient calculation, an arbitrary number of data sets can be saved at different time steps. During the Lagrangian spray simulation, the initial values are linearly interpolated from the available data sets. This method retains two advantages:

- it delivers reliable initial conditions for injection velocity and initial spray angle;
- it offers the possibility of applying more detailed primary break-up models, since detailed information about turbulence quantities and cavitation bubbles at the nozzle exit are available.

Results of each modelling step are presented in terms of injection laws, nozzle flow results and spray droplet visualisation, in order to describe and clarify the adopted procedure; results based on a different break-up setting are presented, in order to explore its influence on the solution.

**3.2 Injection system.** The injection system modelling has been performed in AMESim environment. It is made of a cam-driven reciprocating pump, a delivery valve, an high-pressure duct, a fully mechanical injector (Fig.3.1).

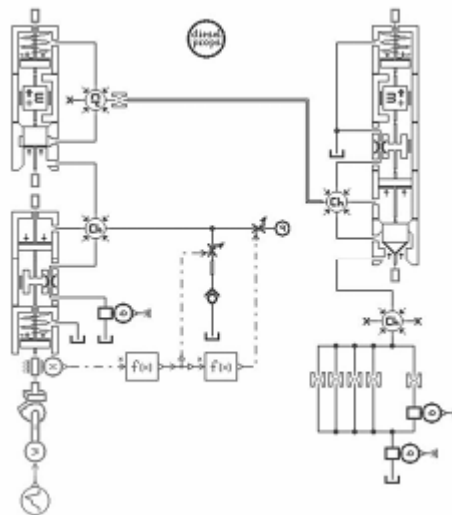


**Figure 3.1:** Injection system

The fuel is delivered to the injector as soon as the fuel pressure reaches a predefined value. The delivery valve closes as the pressure decreases. This represents an already well-studied system and it doesn't need a detailed description, but it must be noted that the same modelling strategy can be adopted if an high pressure common rail system is considered. In the present case, a simple system has been chosen, since this work focuses on the modelling approach.

**3.3 Nozzle flow modelling.** In order to evaluate the role of the cavitation, FIRE Multiphase Flow Module [12] has been used. The adopted multiphase simulation is based on the Euler-Euler Approach, that is the most general approach to simulate multiphase flows. The Multifluid Model (it is one of the default models available in Fire environment) has been adopted. In such a model, all conservation equations are

solved for each phase; in particular, in the modelling of closure terms in the turbulence kinetic energy equation, the following assumptions are made [13]:

- the interfacial interaction between the two phases is neglected;
- the turbulence level of the dispersed phase is assumed to be equal to the continuous phase turbulence level.

The modelling of the mass transfer between the fluid phases is based on the Linear Cavitation Model, available in the Fire library. The relation for the mass exchange is:

$$\Gamma_c = \rho N''' 4R^2 \dot{R} = -\Gamma_d \quad (1)$$

where  $N'''$  is bubble number density and  $R$  is bubble radius. The time derivative of the bubble radius is estimated from the Rayleigh equation:

$$R \ddot{R} + \frac{3}{2} \dot{R}^2 = \frac{\Delta p}{\rho_c} \quad (2)$$

By linearizing the above equation neglecting the inertial term, the mass exchange can be derived to be equal to:

$$\Gamma_c = \frac{1}{C_{CR}} \text{sign}(\Delta p) 3.85 \frac{\rho_d}{\sqrt{\rho_c}} N'''^{\frac{1}{3}} \alpha_d^{\frac{2}{3}} |\Delta p|^{\frac{1}{2}} = -\Gamma_d \quad (3)$$

where the effective pressure difference equals:

$$\Delta p = p_{\text{sat}} - \left( p - C_E \frac{2}{3} \rho_c k_c \right) \quad (4)$$

The effective pressure difference,  $\Delta p$ , includes the effects of pressure fluctuations. The closure coefficient–Egler coefficient,  $C_E$ , depends on local turbulence level [14].  $C_{CR}$  is the condensation reduction factor; in the present case, the following values have been adopted:  $C_{CR}=1$ ;  $C_E=1.2$ . Bubble number density,  $N'''$ , is calculated according to the assumed diminishing linear ramp:

$$N''' = \begin{cases} N'''_0 & \alpha_d \leq 0.5 \\ 2(N'''_0 - 1)(1 - \alpha_d) + 1 & \alpha_d > 0.5 \end{cases} \quad (5)$$

The (5) is a heuristic formula, used to model coalescence effects. The initial bubble number density,  $N'''_0$ , depends on the characteristics of the liquid phase [15]: in the present case, the value  $N'''_0 = 1012$  is used. The number density should not be smaller than the one constrained by the maximum bubble diameter:

$$N''' = \max \left( N'''_0, \frac{6\alpha_d}{\pi D_{b,\text{max}}^3} \right) \quad (6)$$

The maximum bubble diameter,  $D_{b,\text{max}}$ , is a function of the geometry. This value is chosen so that it practically does not affect the calculation of the number density,  $N'''$ . The used value for the maximum bubble diameter is equal to 0.01 m. The bubble diameter is uniquely defined if volume fraction,  $\alpha_d$ , and the number density,  $N'''$ , are known:

$$D_b = \left( \frac{6\alpha_d}{\pi N'''} \right)^{\frac{1}{3}} \quad (7)$$

The implemented interfacial momentum source includes drag and turbulent dispersion forces:

$$M_c = C_D \frac{1}{8} \rho_c A_i'' |\mathbf{v}_r| \mathbf{v}_r + C_{TD} \rho_c k_c \nabla \alpha_d = -M_d \quad (8)$$

where the relative velocity is defined as:

$$\mathbf{v}_r = \mathbf{v}_d - \mathbf{v}_c \quad (9)$$

The interfacial area density for bubbly flow equals:

$$A_i'' = \pi D_b^2 N''' = (36\pi)^{\frac{1}{3}} \alpha_d^{\frac{2}{3}} \quad (10)$$

Number density,  $N'''$ , is obtained from the cavitation mass exchange model. Drag coefficient,  $C_D$ , is a function of the bubble Reynolds number,  $Re_b$ , defined as:

$$Re_b = \frac{v_r D_b}{\nu_c} \quad (11)$$

The correlation for drag coefficient for bubbles is used [16]:

$$C_D = \begin{cases} \frac{192}{Re_b} (1 + 0.10 Re_b^{0.75}) & Re_b \leq 1000 \\ 0.438 & Re_b > 1000 \end{cases} \quad (12)$$

Turbulent dispersion force accounts for the vapour diffusion due to turbulent mixing processes. The margins for bubbly flows are:  $C_{TD} = 0.05 \div 0.5$ . In this case  $C_{TD} = 0.1$ .

The nozzle flow simulation is based on the injector calculation grid. Figure 3.2 shows the injector mesh. It's made of 92630 cells.

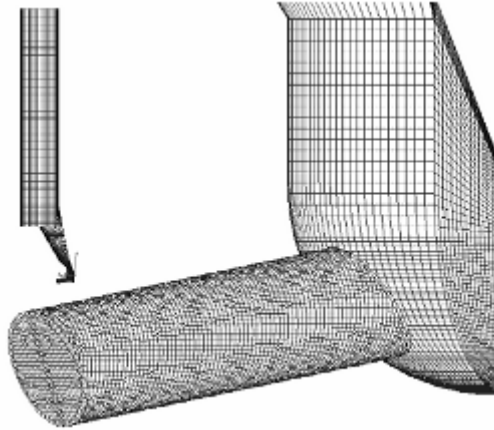


**Figure 3.2:** Injector mesh

The sac and the body parts are based on a structured grid. The nozzle surface has been separately meshed and then connected to the sac volume. The whole injector mesh represents an angular portion of the complete volume. A polar flow symmetry has been supposed. The fuel considered in the work is a typical European diesel fuel with 86% of carbon content and 13% of hydrogen content. In order to simulate the

needle lift, a mesh set generation is required. The needle displacement is imposed to the meshes by an external law (Fig.3.5), that has been obtained as a data file coming from the injection system simulation. In order to investigate the nozzle flow, an injection pressure law must be imposed to the inlet surface of the injector mesh. Such a law (Fig.3.6), as the needle lift one, comes from the injection system simulation. In this way, the coupling between AMESim code and FIRE code is realized.

**3.4 Spray and chamber flow simulation.** Spray simulation involves two-phase flow phenomena, then it requires the numerical solution of conservation equations for the gas and the liquid phase simultaneously. With respect to the liquid phase, the spray calculation is based on a statistical method referred to the Discrete Droplet Method (DDM). All the adopted following models are default models in FIRE [13]. The k- $\epsilon$  closure for a RANS solution has been adopted.

*Breakup model.* Wave model has been used to simulate the droplet break-up process. According to such a model [17-19], the growth of an initial perturbation on a liquid surface is linked to its wavelength and to other physical and dynamic parameters of the injected fuel and the fluid domain.

*Turbulent dispersion model.* O'Rourke [20] model has been adopted. As particles pass through the flow, it is assumed that they interact with the individual turbulent eddies. Each interaction deflects the particle as dictated by the instantaneous velocity of the turbulent eddy and the particle inertia. The particle trajectory is determined similar to a random walk computation until the particle passes out of the region under consideration. The instantaneous gas velocity within a turbulent eddy is obtained from the mean domain fluid velocity and the turbulence kinetic energy. Both are known from the solution of the gas phase equations. The interaction time of a particle with the individual eddies is estimated from two criteria, the turbulent eddy life time and the time required for a particle to cross the eddy.

*Particle interaction model.* With the viewpoint of the statistical particle method [21] which builds the basis of the current spray simulation module, the particle collisions are modelled by a statistical rather than a deterministic approach [22]. The probability distribution governing the number and nature of the collisions between particles is sampled statistically. The collision calculation is performed for pairs of particles only if they are in the same computational cell. It is assumed that the particles associated with each parcel are uniformly distributed within the sampling volume (computational cell) in which they are located. The particles, on the basis of their behaviour, can be divided in collectors and droplets. The collision frequency between a particle of parcel 1 and all particles associated with another parcel, within the computational volume, is used to calculate the probability that a particle of parcel 1 will collide with a particle of the other parcel (pairs).

*Wall interaction model.* Wall interaction of liquid droplets can play a major role for diesel and gasoline engines. Especially for small bore diesel engines, the distance between the injector and the bowl can be very small, so that large parts of the fuel are not yet evaporated or atomized when they hit the wall. Walljet2 is the adopted model,

and it is based on the spray/wall impingement model of Naber and Reitz [23]. Depending on the engine run condition, a vapour cushion is formed under the droplets and they rebound or slide along the walls. In the currently implemented model, it is assumed that a droplet which hits the wall suffers one of the two consequences, namely rebound or reflection in the manner of a liquid jet, depending on the Weber number. The transition criterion between these two regimes is described by a critical Weber number ( $We_c=80$ ):

- low Weber number regime ( $We < We_c$ ) (rebound);
- high Weber number regime ( $We > We_c$ ) (jet regime).

The droplet diameter after the impingement  $d_1$  depends on  $d_0$  and on the following Weber number criteria (Fig.3.3):

$We \leq 50$	$d_1=d_0$
$50 < We \leq 300$	$d_1=d_0 [1-(We_{lin}-50)/500]$
$We > 300$	$d_1=0.5d_0$

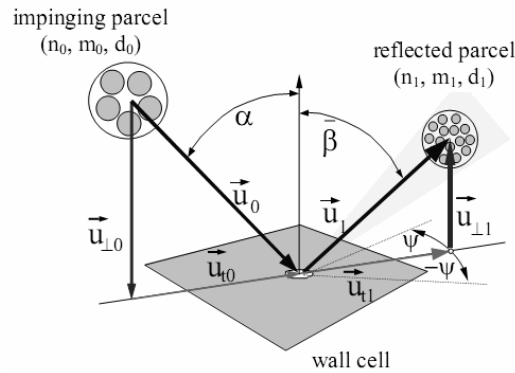


**Figure 3.3:** Impinging parcel

*Evaporation model.* The heat and mass transfer processes are described by the model originally derived by Dukowicz [24] and based on the following assumptions:

- spherical symmetry;
- quasi steady gas-film around the droplet;
- uniform droplet temperature along the drop diameter;
- uniform physical properties of the surrounding fluid;
- liquid–vapour thermal equilibrium on the droplet surface.

In such evaporation model, it is considered that the droplet is evaporating in an incondensable gas.

*Primary break-up:* Diesel Blob Injection Primary Break-up Model plus Nozzle Flow Results. To set up the primary fuel jet disintegration within the framework of the DDM, the following method has been used: introduction of a series of large blobs of approximately nozzle diameter, which close to the nozzle represent the coherent liquid jet. Their diameter is subsequently reduced according to the mass detachment rate



calculated from the primary break-up model. The primary atomisation model is based on the simulation of the competing effects of turbulence, cavitation and aerodynamic induced break-up processes. The WAVE model is used to determine the aerodynamic break-up rate. Model constants  $C_1$  and  $C_2$  are used to adjust break-up time and characteristic droplet radius. In the model, the spray angle is calculated immediately from atomization physics. The turbulence induced break-up is accounted for by solving an additional equation for the turbulence kinetic energy and its dissipation rate within the liquid fuel core. The impact of the collapsing cavitation bubbles on the primary break-up is modelled via additional source terms in the turbulence model. The turbulence and cavitation induced break-up competes with the aerodynamic one until, at a certain distance downstream of the nozzle exit, the aerodynamic break-up processes become dominant. The boundary conditions required for the primary break-up spray simulation are obtained from the results of the two-phase nozzle flow calculation. For the individual injector configurations and operating conditions, the nozzle flow results provide the relevant information on the local fuel velocity, turbulence intensity and fuel vapour mass fraction at the nozzle exit. The aim is to capture the highly transient nature of the cavitating nozzle flow characteristics. To cover the locally resolved flow data in the nozzle orifice, the ligament release positions are randomly chosen within the orifice cross section at each time step. The numerical implementation of the primary break-up model adopts an Eulerian-Lagrangian two-phase flow method which is based on the basic concept of transporting particle pdf's representing the statistics of the ligaments formed in the primary break-up region. Close to the nozzle exit, the ligament properties and interaction processes are modelled in order to account for dense spray effects and according to the above primary break-up model, in the far field of the nozzle the two-phase flow method reduces to the well known discrete droplet approach (DDM). Transition from ligaments to droplets occurs according to Weber number and diameter criteria.

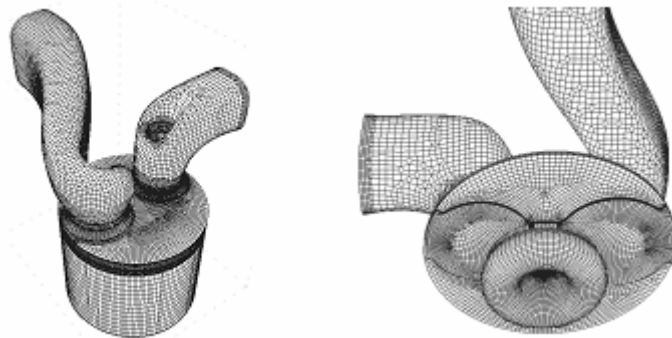


**Figure 3.4:** Engine mesh

The simulation has been performed on a relatively complex computational grid, representing a diesel engine combustion chamber. It allows to simulate the complete engine cycle, taking into account the intake/exhaust manifold effects on the chamber flows. The flow calculation begins at 135 CABTDC and ends at 117

CAATDC, in order to consider the whole flow field evolution during the compression-expansion phase. In this way it is possible to evaluate the role of the piston bowl and its interaction with the spray cloud.

**3.5 Results.** The simulation has been performed on a single cylinder diesel engine whose main features are listed in Tab.3.1:

displacement [m <sup>3</sup> ]	401.3*10 <sup>-6</sup>
bore x stroke [m]	0.082 x 0.076
compression ratio	20.3:1
fuel injection system	direct injection
injector nozzle diameter [m]	0.159*10 <sup>-3</sup>
injector nozzle length [m]	0.72*10 <sup>-3</sup>
sac diameter	0.495*10 <sup>-3</sup>
sac volume [m <sup>3</sup> ]	1.589*10 <sup>-10</sup>
number of holes	5

**Table 3.1:** Main characteristics of the diesel engine

The simulations refer to the following conditions:

engine speed [Hz]	50
Start of injection CABTDC	6
injected mass [MPa]	1.78*10 <sup>-5</sup>

**Table 3.2:** Simulation conditions

**3.5.1 Injection characteristics.** The following figures show the needle lift trace (Fig.3.5, maximum value 0.425 mm), the injection pressure trend (Fig.3.6) and the injection flow rate curve (Fig.3.7) respectively. The total injected mass has been computed and has been used to verify the nozzle flow results, in terms of fuel flow rate time integral at the nozzle exit.

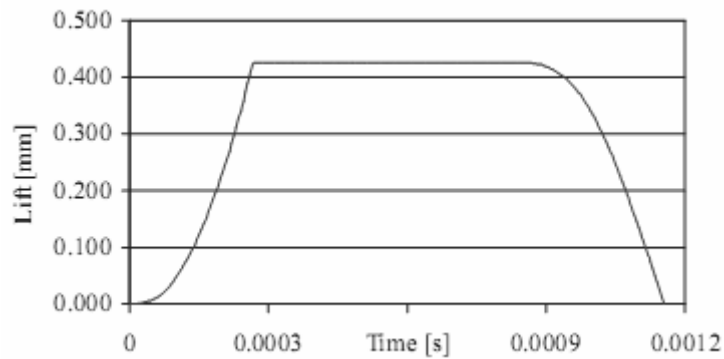


**Figure 3.5:** Poppet lift

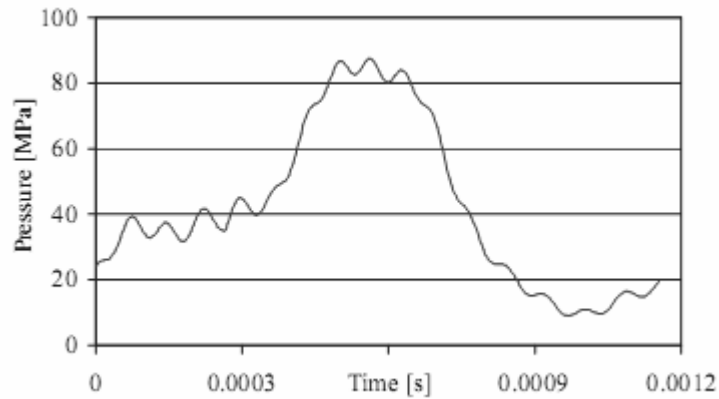


**Figure 3.6:** Injection pressure

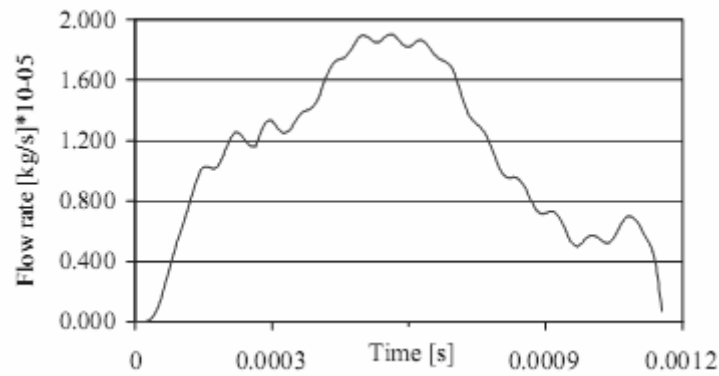


**Figure 3.7:** Flow rate

**3.5.2 Injector flow.** The flow visualization is displayed by means of a cut surface containing the nozzle axis. The earlier state of the injection condition is shown in the following figure. The needle lift and the injection pressure values are 0.05 mm and 33.9 MPa respectively. At 0.1 ms after SOI a vapour region grows from the inlet corner of the hole and extends downstream without involving significantly the nozzle exit (Fig.3.8, Left); the vapour/liquid volume fraction does not exceed the limit of 0.6 in the core, as the isocontour lines highlight.

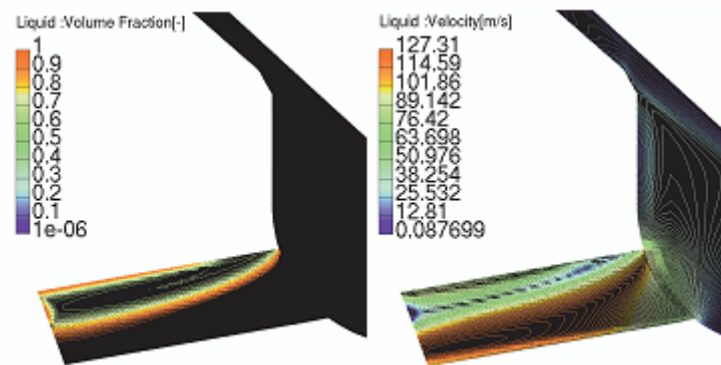


**Figure 3.8:** Left, Vapour/liquid volume fraction – 0.1 ms ASOI  
Right, Injector flow velocity isolines - 0.1 ms ASOI

The flow velocity values in the region of liquid are in the range of 80÷120 m/s. The vapour region causes a restriction of the normal duct section whose entity increases from the inlet section to the exit. The injector flow 3D streamlines (Fig.3.9) reveal the presence of an helicoidal flow motion in the vapour zone; moreover a large eddy zone is generated in the injector sac.

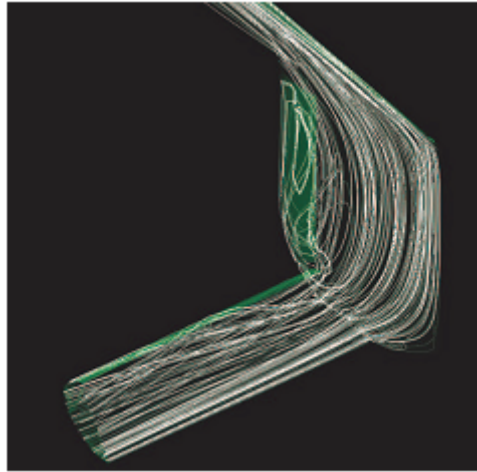


**Figure 3.9:** 3D injector flow streamlines - 0.1 ms ASOI

Figure 3.10 refers to 0.375 ms ASOI. The needle is at the maximum of the lift and the pressure level is equal to 41.7 MPa. The vapour/liquid fraction is significantly decreased (equal to the minimum in the core cavitating region) and the cavitating zone is characterized by an evident contour (Fig.3.10, Left). The vapour region increases to reach the nozzle exit. The flow velocity is increased and the values are in the range of 300 m/s. The flow in the sac presents an increment, too: the velocity is in the range of 70÷100 m/s (Fig.3.10, Right). In the 3D visualisation of the streamlines (Fig.3.11), the helicoidal structures are emphasized and characterize the flow in the vapour region; on the other hand, in the sac volume, the streamlines are back straight.

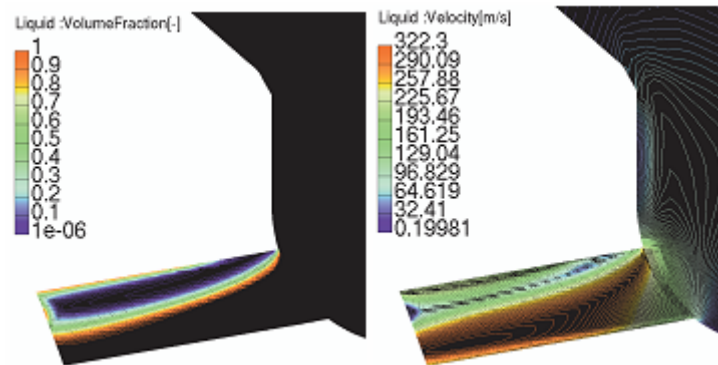


**Figure 3.10:** Left, Vapour/liquid volume fraction – 0.315 ms ASOI  
Right, Injector flow velocity isolines - 0.315 ms ASOI



**Figure 3.11:** 3D injector flow streamlines - 0.315 ms ASOI

At 0.575 ms ASOI, the vapour region is still relevant (Fig.3.12, Left), but at the exit section of the nozzle, the vapour/liquid volume fraction reaches lower values compared to the previous visualisation; in particular, a decrement of about 40% is obtained. The isolines map (Fig.3.12, Right) shows a decrement of values (approximately 15% of reduction).

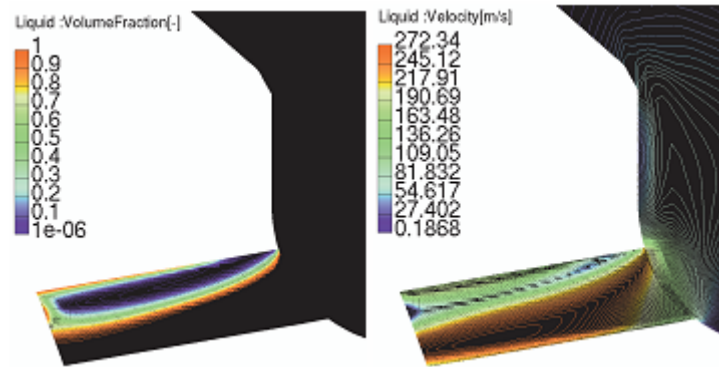


**Figure 3.12:** Left, Vapour/liquid volume fraction – 0.575 ms ASOI  
Right, Injector flow velocity isolines - 0.575 ms ASOI

Different flow conditions characterize the subsequent injection phase: the visualization in correspondence to 0.865 ms ASOI (Fig.3.13, Left – needle lift 0.425 mm, injection pressure 19.4 MPa) shows that the vapour region completely collapses before the nozzle exit. The gradient of vapour/liquid fraction towards the nozzle wall is decreased respect to the previous case, as the result points out. The velocity in the liquid flow region (Fig.3.13, Right) is in the range of 180÷220 m/s.

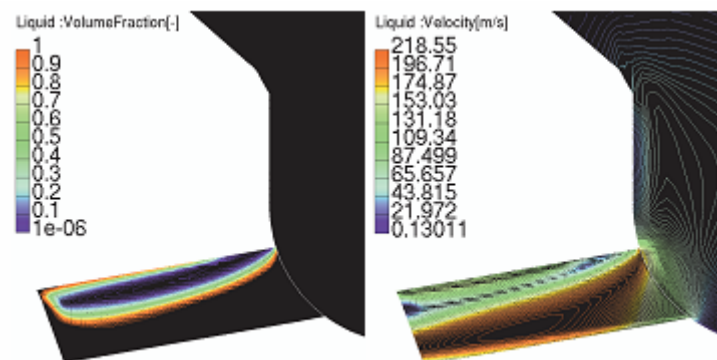


**Figure 3.13:** Left, Vapour/liquid volume fraction – 0.865 ms ASOI  
Right, Injector flow velocity isolines – 0.865 ms ASOI

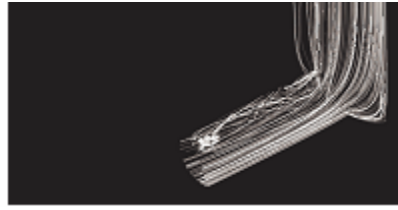


**Figure 3.14:** 3D injector flow streamlines – 0.865 ms ASOI

The streamlines still show the highlighted helicoidal shape, but they converge in a restricted region in correspondence to the zone in which the vapour bubbles collapse takes place (Fig.3.14). The end of the injection is characterized by the detachment of the cavitating region from the corner of the hole. A vapour bubble is conveyed downstream and another one is involved in a sac eddy (Fig.3.15).

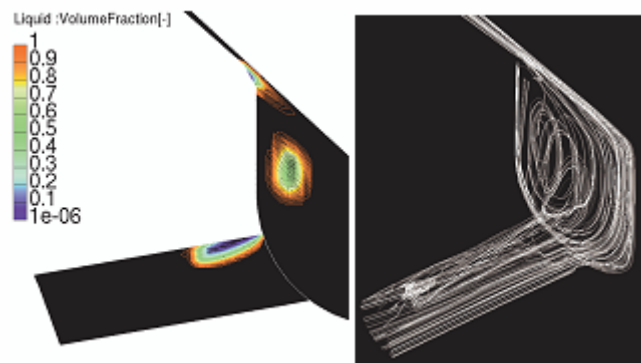


**Figure 3.15:** Left, Vapour/liquid volume fraction – EOI  
Right, 3D injector flow streamlines – EOI

The flow features highlighted in this section are in agreement with the experimental investigations concerning cavitation inception and its development [25]:

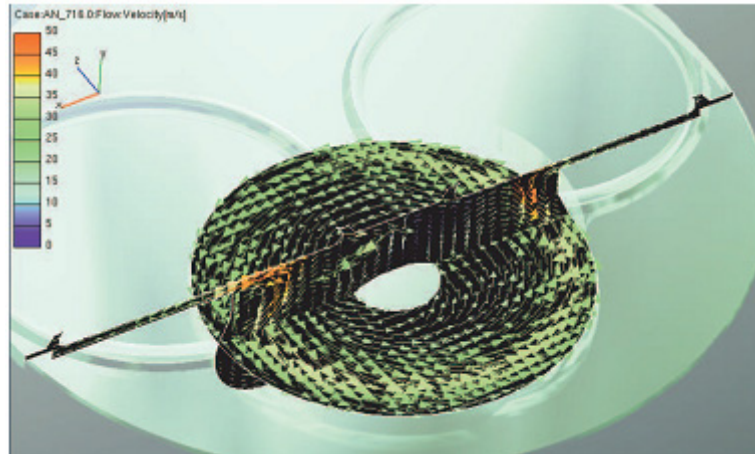
- the hole inlet flow around the side corners of an injection hole is a possible mechanism of cavitation;
- the cavitation flow patterns exhibit a more stable structure with increasing needle lift;
- in the lower nozzle tip volume, no appreciable liquid movement is identified;

Figure 3.16 refers to a developed flow through a mini sac type nozzle showing cavitation [25].



**Figure 3.16:** Developed flow through a mini sac type nozzle showing cavitation (high speed imaging) [25]

**3.5.3 Chamber flow/spray.** The flow visualisation is displayed by means of two cut surfaces, in order to evaluate the swirl and the squish effects. A well structured swirl motion structure is present in the bowl, generated by the intake manifold. A squish effect is visible: there is no symmetry because of the bowl offset respect to the cylinder axis. At 4 CABTDC (fig.3.17), the swirl motion and a squish eddy are evident in the bowl. The presence of the injection jet is shown by the velocity field.



**Figure 3.17:** Bowl velocity field – 4 CABTDC

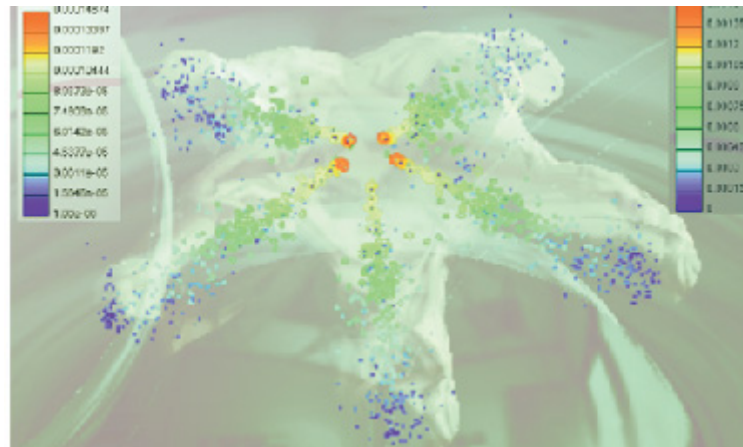


**Figure 3.18:** Spray droplet diameter- Diesel mass fraction isosurface (0.001) – 4 CABTDC

Figure 3.18 gives an idea of the vaporisation process; the spray cones are visualized at the beginning of injection. An isosurface representing the fuel/air ratio of 0.001 is depicted and it is located around the spray jet. At TDC (Fig.3.19, Left) the jet is represented after 0.33 ms after SOI. The spray droplets interact with the bowl flow field. The droplet having little diameter are conveyed by the swirl stream and there is no wall impingement.



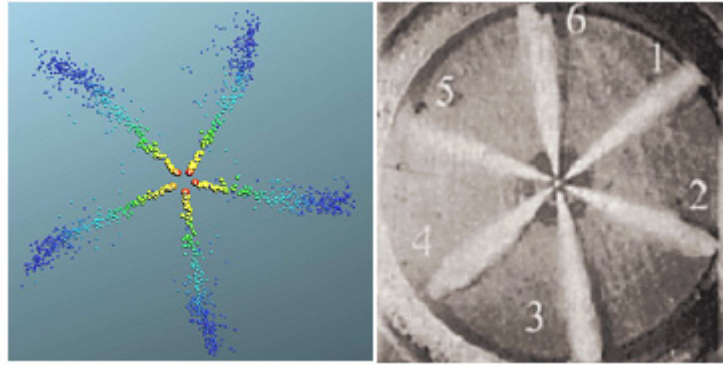


**Figure 3.19:** Left, Spray result at TDC  
Right, Minisac six-hole developed spray [26]

The spray cone angle is approximately in the range of  $20\div 25$  degree. This characteristic can be qualitatively compared to an experimental spray cones visualization of minisac multi-hole nozzles (Fig.3.19, Right) [26] and a good degree of agreement can be observed. The result refers to a minisac six-hole nozzle,  $0.124\cdot 10^{-03}$  m hole diameter,  $80\cdot 10+06$  Pa injection pressure,  $2.7\cdot 10+06$  Pa ambient pressure. At 6 CAATDC, the effect of the spray cones on the swirl stream is increased. Five sub-streams indicate the droplets-chamber flow interaction: the mixing process involves the whole chamber (Fig.3.20).

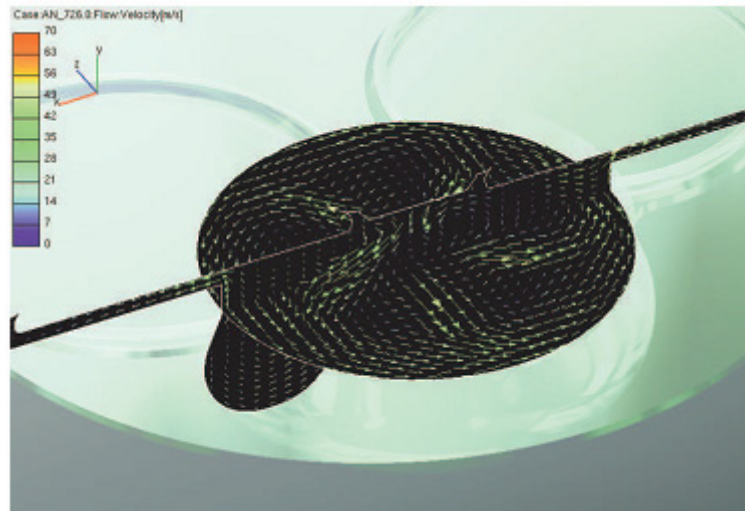


**Figure 3.20:** Bowl velocity field – 6 CAATDC



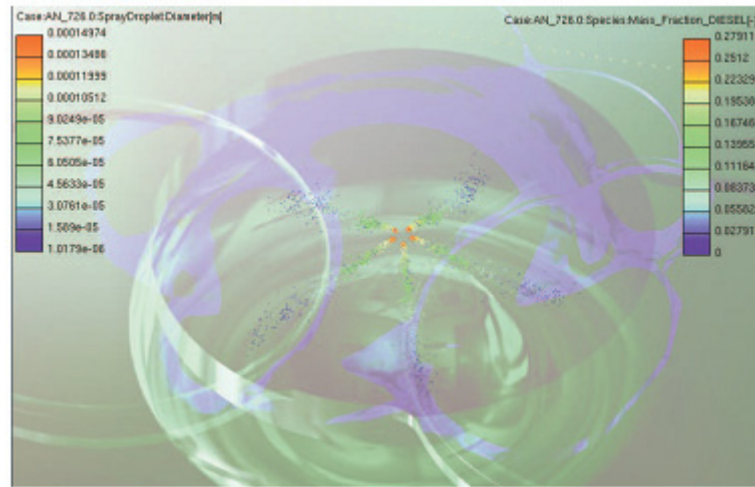


**Figure 3.21:** Spray droplet diameter - Diesel mass fraction isosurface (0.001) – 6 CAATDC

The fuel/air mass fraction (0.001) of Fig.3.21 is located at a large distance from the spray cones, as the mixture building is going on. At this crank angle, the first half of the injected mass is evaporated (Fig.3.21). At 12 CAATDC, the flow velocity field show that the mixture is outgoing from the bowl (Fig.3.22).

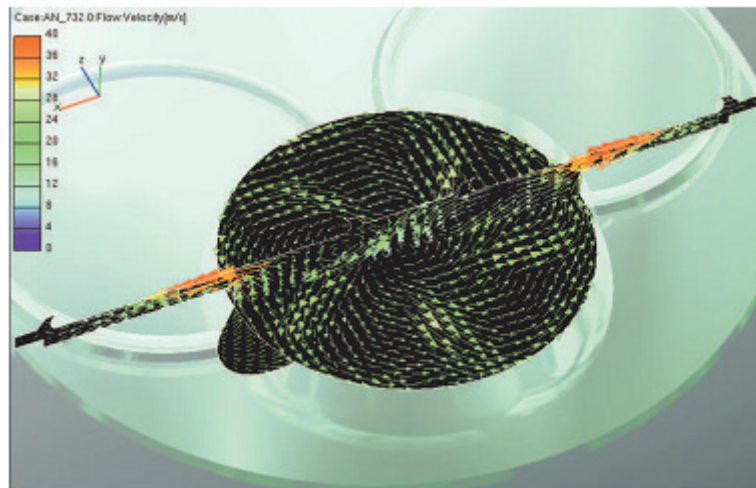


**Figure 3.22:** Bowl velocity field – 12 CAATDC

In order to evaluate the influence of the 'nozzle interface' on the spray break-up, a second calculation run has been performed. In such a run (case 2), the 'nozzle interface' has been disabled: it means that the results of the nozzle flow simulation have been neglected and the fuel injection has been modelled directly on the basis of the fuel flow rate law (Fig.3.7). In case 2, a different evaporation rate has been observed. Differences in the spray penetration, spray cone angle, droplet diameter,

mixture building and wall impingement have been highlighted by the comparison between Figs.3.23, 3.24. In the second case, the spray cone angle is almost completely undeveloped. These qualitative differences can be quantitatively evaluated in Fig.3.25, in which the evaporated fuel mass is depicted. In case 2, the droplet vaporisation shows a delay of about 3 CA. Then the vaporisation rate becomes faster, but at 20 CAATDC the amount of evaporated fuel is the 94% of the total. Figures 3.26 and 3.27 represent the hole to hole penetration curves. The differences between the curves could be caused by the chamber flow field characteristics and by the mesh grid influence [27]. The spray cone penetration has quantitatively a different behaviour; a relevant increment, of about 25% at 10 CAATDC, is shown in the second simulation. On the other hand, penetration curves coming from case 1 (Fig.3.26) have an evident slope change in the initial phase of injection, corresponding to a penetration depth of 0.01 m. In correspondence to this point, the SMD curve (Fig.3.29) of case 1 presents a relevant slope change, too. About the SMD curves of both simulations, the values at the beginning of the injection are significantly different (20%). This feature reflects the different vaporisation behaviour between the two solutions. A shape agreement between the obtained results and the experimental measurements of spray cone investigations [28] has been obtained (Fig.3.28).



**Figure 3.23:** Spray droplet diameter- Diesel mass fraction isosurface (0.0065) – TDC

Measurements are referred to a hydraulic electronic unit injector, with pressure of  $77 \cdot 10^6$  Pa, duration of  $2.25 \cdot 10^{-3}$  s, nozzle hole diameter  $0.190 \cdot 10^{-3}$  m. The spray penetration results from case 1 seem to be closer to the measured data, because of the discussed slope change. Figure 3.28 indicates that the ambient pressure affects the spray penetration significantly.

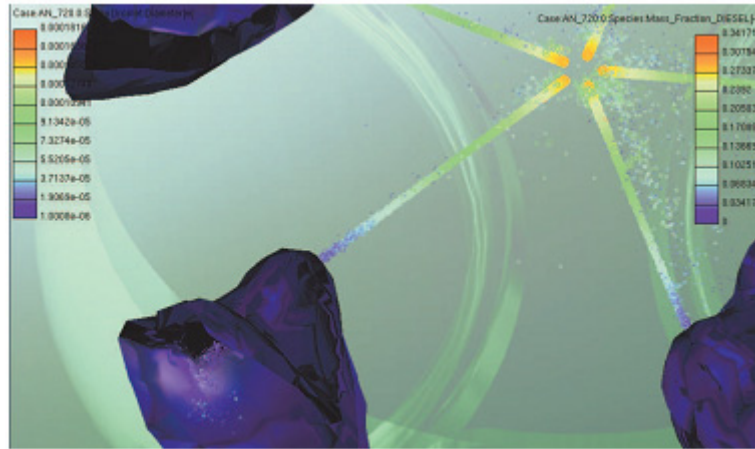


**Figure 3.24:** Diesel mass fraction isosurface (0.0065) – TDC - Deactivated nozzle interface

The penetration after 1 ms decreases of about 25% when ambient pressure increases of about 37%. Quantitatively, a direct comparison between Figs.3.26, 3.27 and 3.28 show a significant difference of penetration, probably due to the different injection conditions: the predicted results (Figs.3.26, 3.27) correspond to an ambient pressure in the range of  $40\div 45 \cdot 10^6$  Pa, and this, together with the simulated nozzle hole diameter, is expected to be a significant cause of predicted penetration decrease.

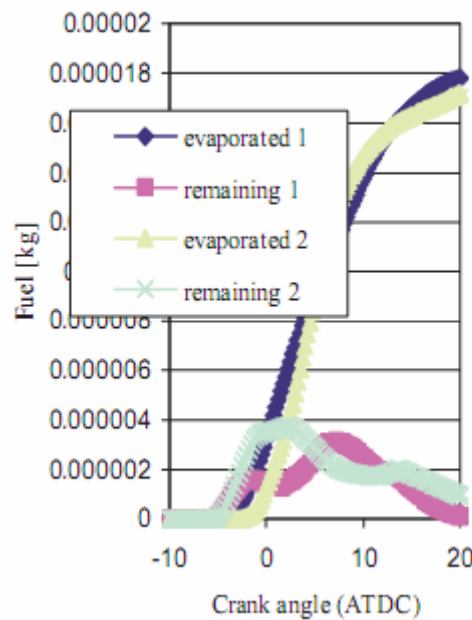


**Figure 3.25:** Different results obtained with activated nozzle interface (case 1) and deactivated nozzle interface (case 2), respectively.

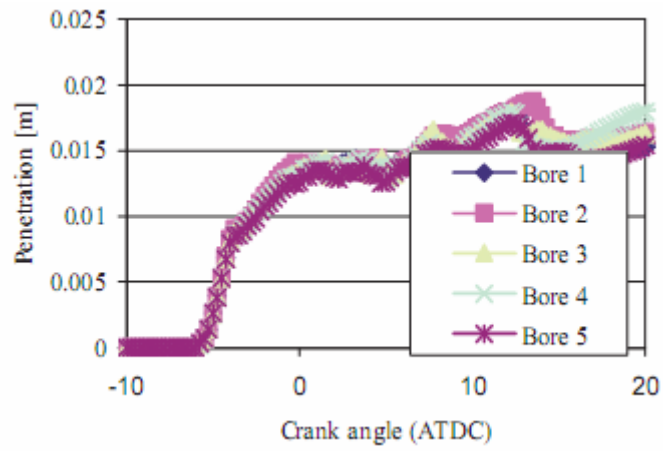


**Figure 3.26:** Hole to hole penetration of the spray, case 1

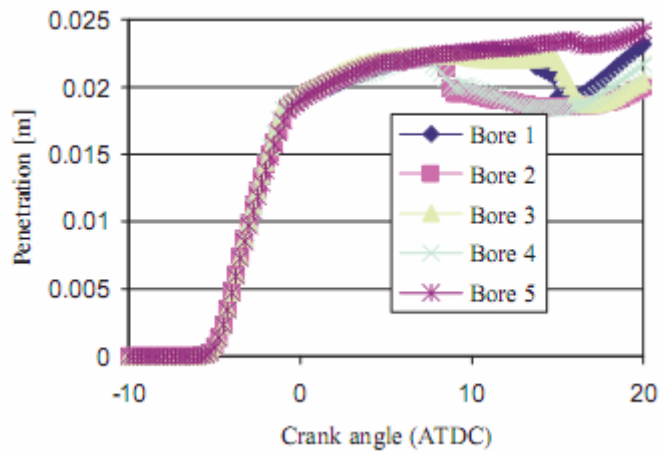


**Figure 3.27:** Hole to hole penetration of the spray, case 2

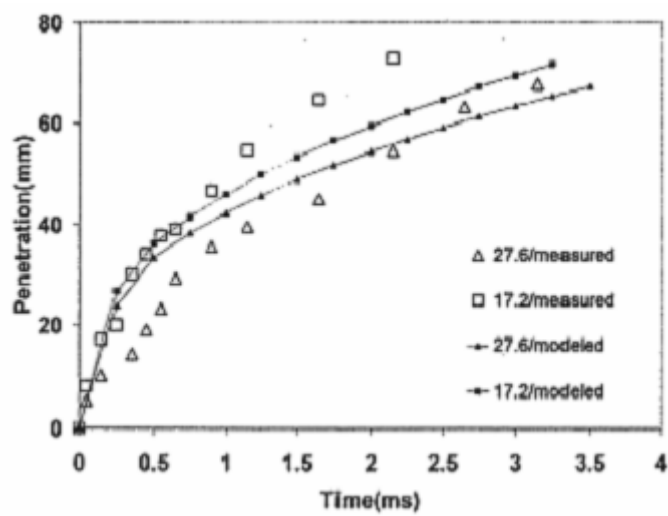


**Figure 3.28:** Correlation between measured and modelled spray penetration [28]

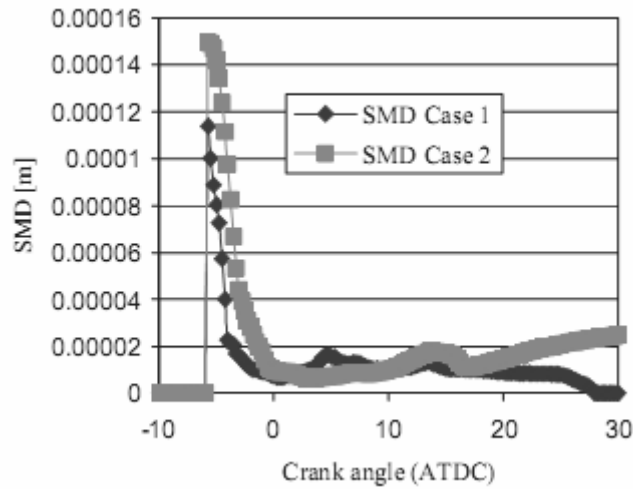


**Figure 3.29:** SMD in case 1 and case 2

**3.6 Concluding remarks.** A comprehensive computational tool in which two different codes are coupled has been presented, with the aim of predicting the performance of the entire injection system, the spray characteristics, the interaction among spray-cones, chamber flows and geometry. The injection system simulation has been the first step of the modelling procedure: the obtained results, concerning needle lift injection and flow rate time evolution have been used to initialize the nozzle flow simulation. The dynamic CFD analysis on the nozzle flow has been performed to investigate the effect of the cavitating flow regime on the primary break-up. The following features have been pointed out: -the vapour region grows from the inlet corner of the hole and extends downstream. Initially the nozzle exit is not significantly involved and the vapour/liquid volume fraction does not exceed the limit of 0.6 in the core; subsequently, such a value decreases to the minimum and the region reaches the nozzle exit. The cavitating behaviour holds up during the whole process; -the flow velocity is in the range of 80÷120 m/s at the beginning. The flow velocity increases (max. value 300÷320 m/s) and, at 0.865 ms ASOI, it is still in the range of 180÷220 m/s; -the injector flow 3D streamlines reveal the presence of a helicoidal motion which characterizes the vapour region during the process. Agreement with the experimental investigations concerning cavitation inception and its development has been pointed out. Finally, a spray model has been used, by means of the 'nozzle flow interface'. In comparison with an experimental spray cones visualization, the predicted spray features have shown agreement. From the comparison between two simulation settings (case 1 and case 2), relevant differences have been found;

- in case 2, the droplet vaporisation shows a delay of about 3 CA respect to the case 1;
- at 20 CAATDC (case 2) the amount of evaporated fuel is 94% of the case 1;

- spray cone penetration in case 2 is more relevant than case 1 (about 25% at 10 CAATDC)
- wall impingement happens in case 2, only;
- spray cone angle in case 2 is undeveloped;
- the SMD curves of both simulations have significantly different initial values;
- shape agreement between results and experimental measurements is shown.

### 3.7 Nomenclature

$A_i^m$  = interfacial area density

CAA = Crank Angle After

CAB = Crank Angle Before

$D_b$  = bubble diameter

$C_{CR}$  = condensation reduction factor

$C_D$  = drag coefficient

$C_E$  = Egler coefficient

$C_{TD}$  = drag turbulent coefficient

EOI = End Of Injection

$M_c$  = vapor phase momentum

$M_d$  = liquid phase momentum

$N_0^m$  = initial bubble number density

$N^m$  = number density

$R$  = bubble radius

$Re_b$  = bubble Reynolds number

SOI = Start Of Injection

TDC= Top Dead Centre

We = Weber number

$k_c$  = vapor phase turbulence kinetic energy

$p_{sat}$  = saturation pressure

$\mathbf{v}_c$  = vapor velocity

$\mathbf{v}_d$  = liquid phase velocity

$\mathbf{v}_r$  = relative velocity

#### Greek symbols

$\Gamma_c$  = vapor phase mass

$\Gamma_d$  = liquid phase mass

$\Delta p$  = pressure difference

$\alpha_d$  = liquid phase volume fraction

$\rho_c$  = vapor phase density

$\rho_d$  = liquid phase density

$\rho_2$  = liquid density

### 3.8 References

- [1] Mulemane, A., Han, J.S., Lu, P.H., Yoon, S.Y. and Lai, M.C., "Modelling Dynamic Behavior of Diesel Fuel Injection Systems", SAE Paper No. 2004-01-0536.
- [2] Chiavola, O. and Giulianelli, P., "Modelling and Simulation of Common-Rail Systems", SAE Paper No. 2001-01-3183.
- [3] Stiesch, G., "Modelling Engine Sprays and Combustion Processes", Springer Verlag, Berlin, 2003.
- [4] Benajes, J., Payri, R., Molina, S. and Soare, V., "Investigation of the Influence of Injection Rate Shaping on the Spray Characteristics in a Diesel Common Rail System Equipped with a Piston Amplifier", J. Fluids Eng., 127, 1102-1110, 2005.
- [5] Morgan, R., Wray, J., Kennaird, D.A., Crua, C. and Heikal, M. R., "The Influence of Injector Parameters on the Formation and Break-up of a Diesel Spray", SAE Paper No. 2001-01-0529.
- [6] Lim, J. and Min, K., "The Effects of Spray Angle and Piston Bowl Shape on Diesel Engine Soot Emissions Using 3-D CFD Simulation", SAE Paper No. 2005-01-2117.
- [7] Nehmer, D. A. and Reitz, R. D., "Measurements of the Effect of the Injection Rate and Split Injections on Diesel Spray", SAE Paper No. 940668.
- [8] Adomeit, P., Lang, O., Schulz, R. and Weng, V., "CFD Simulation of Diesel Injection and Combustion", SAE Paper No. 2002-01-0945.
- [9] Imagine AMESim v4.2 Tutorial and User Guide, AMESim Technical Bulletins.
- [10] Ueki, H., Ishida, M. and Sakaguchi, D., "Investigation of Droplet Disintegration in Diesel Spray Core by Advanced Laser 2-Focus Velocimeter", SAE Paper No. 2005-01-1238.
- [11] FIRE v8.4 Manuals AVL List GmbH.
- [12] FIRE v8.4 Multiphase Manual AVL List GmbH.
- [13] Lee, S.J., Lahey, R.T., Jr. and Jones, O.C., Jr., "Japanese J. Multiphase Flow", 3, 335, 1989.
- [14] Hinze, J.O., "Turbulence", 2<sup>nd</sup> ed., McGraw-Hill, New York, 1975.
- [15] Franklin, R.E. and McMillan, J., "Noise Generation in Cavitating Flows", J. Fluids Eng., 106, 336-341, 1984.
- [16] Ishii, M. and Mishima, K., "Nucl. Eng. & Design", 8, 107, 1984.
- [17] Su, T.F., Patterson, M.A., Reitz, R.D. and Farrell, P.V., "Experimental and Numerical Studies of High Pressure Multiple Injection Sprays", SAE Paper No. 960861.
- [18] Tatschl, R., v. Künsberg-Sarre, C., Alajbegovic, A. and Winklhofer, E., "Diesel Spray Modelling Including Multidimensional Cavitation Nozzle Flow Effects", Proc. of ILASS Europe Conference, Sept. 11-13, Darmstadt, Germany, 2000.
- [19] Patterson, M.A. and Reitz, R.D., "Modeling the Effects of Fuel Spray Characteristics on Diesel Engine Combustion and Emissions", SAE Paper No. 980131.
- [20] O'Rourke, P.J. and Bracco, F.V., "Modelling of Drop Interactions in Thick Sprays and a Comparison With Experiments", IMECHE, 1980.
- [21] Dukowicz, J.K., "A Particle-Fluid Numerical Model for Liquid Sprays", J. Comp. Physics, 35, 229-253, 1980.
- [22] O'Rourke, P.J., "Statistical Properties and Numerical Implementation of a Model for Droplet Dispersion in Turbulent Gas", J. Comput. Physics, 83, 345, 1989.
- [23] Naber, J.D. and Reitz, R.D., "Modelling Engine Spray/Wall Impingement", SAE Paper No. 880107.
- [24] Dukowicz, J.K., "Quasi-steady droplet change in the presence of convection", informal report Los Alamos Scientific Laboratory", LA-7997-MS, 1979.

- [25] Roth, H., Gavaises, M. and Arcoumanis, C., "Cavitation Initiation, Its Development and Link with Flow Turbulence in Diesel Injector Nozzles", SAE Paper No. 2002-01-0214.
- [26] Han, J.S., Lu, P.H., Xie, X.B., Lai, M.C. and Henein, N.A., "Investigation of Diesel Spray Primary Break-up and Development for Different Nozzle Geometries", SAE Paper No. 2002-01-2775.
- [27] Peng Karrholm, F. and Nordin, N., "Numerical Investigation of Mesh/Turbulence/Spray Interaction for Diesel Application", SAE Paper No. 2005-01-2115.
- [28] Wang, T.C., Han, J.S., Xie, X.B., Lai, M.C., Henein, N.A., Schwarz, E. and Bryzik, W., "Parametric Characterization of High-Pressure Diesel Fuel Injection Systems", J. Engineering in Gas Turbine & Power, 125, 412-426, 2003.



## 4. Multi-step Modeling of Fuel Influence on Common Rail Injection System Performance

**4.1 Injection system.** The whole system model has been built in AMESim environment; all the hydraulic components have been represented, namely high pressure reciprocating pump, relief valve, pipelines, high pressure rail and injectors. Figure 4.1 shows the system sketch in the code environment.

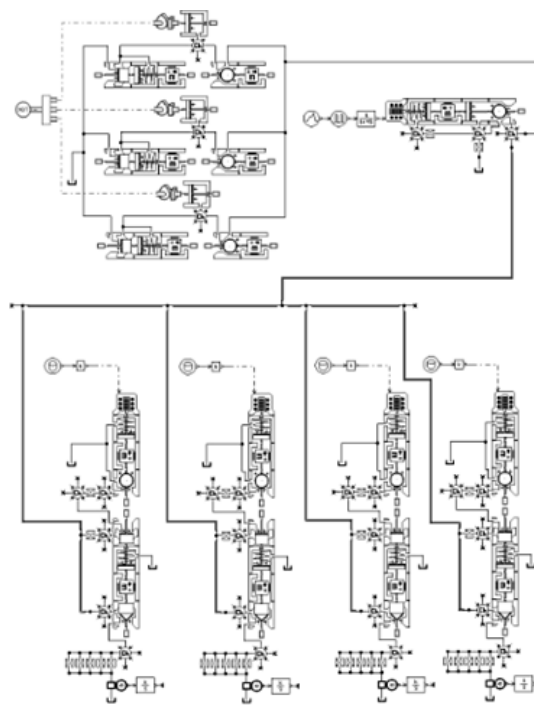


**Figure 4.1:** Injection system sketch

Two elemental units represent the high pressure injector, the nozzle unit and the solenoid; the former one contains the purely hydraulic part, the latter one contains the solenoid valve and the control devices. The short pipe that characterizes and connects the described parts of the common rail injectors has been represented by a hydraulic line and two dead volumes; a throttle valve governs the transient flow phenomena. Pipelines and dead chambers models take variable volumes and pressure dynamics into account. As the interest has been focused on the hydraulic aspects of the system and the engine regime has been kept steady during the runs [11], the injection control signals have been imposed so that pressure and energizing time are the same for the three considered fuels (Tab. 4.3).

The adopted mesh represents a minisac type injector, and it has been obtained connecting two elemental mesh grids. The former one is the needle grid, with polar symmetry, the latter one is the nozzle hole mesh (Fig. 4.2).

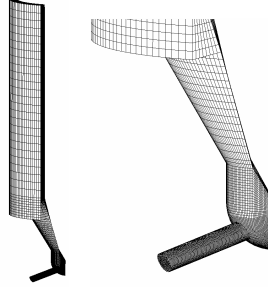


**Figure 4.2:** Injector mesh

In order to individuate an appropriate cell dimension, able to guarantee the independence of the obtained flow fields on the adopted mesh, preliminary tests have been performed. Figure 4.3 shows the comparison between the velocity maps obtained with mesh 'a' (101500 cells) and mesh 'b' (677362 cells). The calculation has been performed considering kerosene fuel at the injection pressure of 110 MPa and the maximum value of needle lift. In the frame of the integrated modeling strategy, the most refined mesh has not been selected, due to the non-substantial differences between the obtained flow conditions, allowing a reduction of the computational effort.

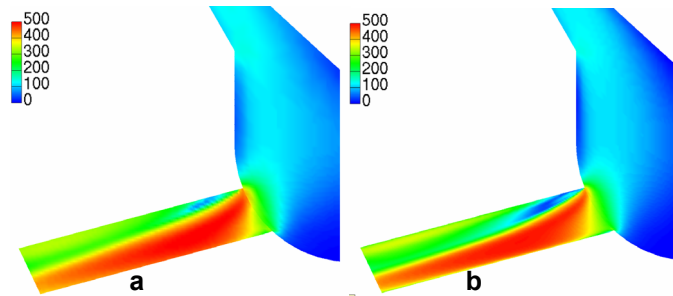


**Figure 4.3:** Scalar velocity [m/s]; a, mesh 'a'; b, mesh 'b'

Three kinds of fuel have been considered in the simulations: diesel fuel, kerosene and biodiesel (the properties of the adopted fuels have been reported in Table 4.1).

fuel type	density [kg/m <sup>3</sup> ]	dynamic viscosity [Pa s]	bulk modulus [Pa]
diesel	850	0.00365	$1.3 \cdot 10^9$
kerosene	800	0.002	$1.3 \cdot 10^9$
biodiesel	880	0.00485	$1.55 \cdot 10^9$

**Table 4.1:** Fuel properties

The features of diesel fuel represent the European standard; kerosene fuel has been modeled on the basis of a dodecane hydrocarbon and biodiesel fuel has been derived by the diesel fuel model, modifying the values of density, viscosity and bulk modulus in order to match the characteristics of a representative blend. It should be noted that several kind of different bio-blends are available in the market having different features.

Three needle displacements, respectively for diesel fuel, kerosene and biodiesel, have been obtained as data files coming from the injection system simulations (Fig.4.5) and have been imposed to the needle meshes.

In order to perform the nozzle flow simulations, three injection pressure laws have been imposed to the inlet surface of the injector mesh. Such laws (Fig.4.6), as the needle lift time traces, come from the injection system simulation. In this way, the coupling between the nozzle flow simulation in FIRE code and the injection system results from AMESim has been realized. At the exit of the nozzle, a constant pressure of 4.6·10<sup>6</sup> Pa has been imposed; such a value is the mean chamber pressure calculated during the injection period.

**4.2 Spray and chamber flow simulation.** All the models used to represent the spray formation are available in FIRE [9] environment and they have been described in the following. The calculation is based on the Discrete Droplet Method (DDM) and the k-ε closure for a RANS approach has been adopted.

*Primary break-up:* nozzle flow interface and diesel blob injection integration. The coherent liquid jet introduced in the chamber is represented by series of large blobs whose diameter is subsequently reduced according to the mass detachment rate calculated from the primary break-up model. The model used to represent the primary atomization phenomena is based on the evaluation of the competing effects of aerodynamic, cavitation and turbulence induced break-up processes [14] and it needs the nozzle interface data file. The aerodynamic break-up rate is evaluated on the basis of the WAVE model [15-17] in which a characteristic droplet radius and a break-up time have been chosen,  $r_A$  and  $\tau_A$  respectively. The calculation is referred to Eq. 13, where the symbol  $r$  denotes the actual droplet radius.

$$\frac{dR}{dt} = \frac{r - C_1 r_A}{C_2 \tau_A} \quad (13)$$

Break-up time and characteristic droplet radius can be adjusted by means of the model constants  $C_1$  and  $C_2$ .

Turbulent length scale  $r_T$  (14) and turbulent time scale  $\tau_T$  (15) are used to calculate the turbulent break-up (16).

$$r_T = C_\mu^{0.75} \frac{k^{1.5}}{\varepsilon} \quad (14)$$

$$\tau_T = C_\mu \frac{k}{\varepsilon} \quad (15)$$

$$\frac{dR}{dt} = \frac{r - C_3 r_T}{C_4 \tau_T} \quad (16)$$

Similar to WAVE model, product droplets are also generated within this model and they get an additional radial velocity taken from aerodynamic respectively turbulent break-up mechanism; as consequence, the spray angle is calculated immediately from atomization physics. The turbulence induced break-up is evaluated by an additional equation for the turbulence kinetic energy and its dissipation rate within the liquid fuel core. Source terms in the turbulence model are used to describe the effect of the collapsing bubbles on the primary break-up. The turbulence and cavitation induced break-up competes with the aerodynamic one until, at a certain distance far from the nozzle exit, the aerodynamic process becomes dominant. The considered turbulence equations for the liquid fuel core are (17,18):

$$\frac{dk}{dt} = -\varepsilon + S_k \quad (17)$$

$$\frac{d\varepsilon}{dt} = -C \cdot \frac{\varepsilon}{k} \cdot (\varepsilon - S_k) \quad (18)$$

where  $k$  is the turbulence kinetic energy,  $\varepsilon$  the dissipation rate,  $C$  a model constant, and  $S_k$  the cavitation source term. By means of the Rayleigh Plesset equation (19), a description of the bubble radius and its rate evolution can be represented:

$$\frac{p_b(t) - p_\infty(t)}{\rho_2} = R \cdot \frac{d^2 R}{dt^2} + \frac{3}{2} \left( \frac{dR}{dt} \right)^2 + \frac{4 \cdot \nu_2}{R} \cdot \frac{dR}{dt} + \frac{2 \cdot \sigma}{\rho_2 \cdot R} \quad (19)$$

where  $p_b$  is the pressure in the bubble,  $p_\infty$  the environment pressure,  $\rho_2$  the liquid density,  $\nu_2$  the cinematic viscosity of the liquid and  $\sigma$  the surface tension. The velocity  $v$  surrounding the bubble at position  $R_L$  is derived from (20).

$$v(R_L) = \left( \frac{R}{R_L} \right)^2 \cdot \dot{R} \quad (20)$$

The total kinetic energy of the liquid around the bubble can be expressed as (21):

$$E_k = \frac{m \cdot v^2}{2} = \frac{1}{2} \cdot \int_{R_L=R}^{R_L=\infty} \left( \frac{R}{R_L} \right)^4 \cdot \dot{R}^2 \cdot 4 \cdot \pi \cdot \rho_2 \cdot R_L^2 \cdot dR_L = 2\pi \rho_2 \cdot R^3 \cdot \dot{R}^2 \quad (21)$$

The disturbance caused by the collapsing bubbles is assumed to be proportional to the change of the kinetic energy the source term  $S_k$  (22):

$$S_k = C_B \cdot \frac{dE_k}{dt} \cdot \frac{n_L}{m_L} \quad (22)$$

where CB is a model constant,  $m_L$  is the liquid mass of the ligament and  $n_L$  is the number of bubbles in the ligament. According to the presented model, the boundary conditions required for the primary break-up are obtained from the results of the two-phase nozzle flow calculation. The nozzle flow results provide the relevant information on the local fuel velocity, turbulence intensity and fuel vapor mass fraction at the nozzle exit. It must be noted that the injected blobs have the same diameter of the nozzle orifice; their position is randomly chosen within the exit orifice area and each particle gets the data of the nearest cell face. The number of blobs introduced per time step is adjusted by the model in order to fit the flow rate time trace. The primary break-up model is activated together with a separate secondary break-up model. However, primary and secondary break-up do not act at the same time on the parcels, but subsequently. In the present approach, the criterion for switching from primary to secondary break-up is a check on Weber number  $< 500$  and checks on stable or minimum diameter [14].

*Secondary breakup:* WAVE model [15-17] has been used to simulate the droplet secondary break-up process, assuming that the growth of an initial perturbation on a liquid surface is linked to its wavelength and to other physical and dynamic parameters of the injected fuel and the fluid domain.

*Turbulent dispersion model:* the model presented by O'Rourke [18] has been adopted, in order to take the interaction between the particles and the turbulent eddies into account.

*Particle interaction model:* the model based on the statistical approach proposed by O'Rourke [19] has been adopted.

*Wall interaction model:* Walljet2 model, based on the work of Naber and Reitz [20], has been considered.

*Evaporation model:* The model originally derived by Dukowicz [21] has been used to represent the heat and mass transfer processes.

Figure 4.4 shows the engine computational mesh at 5 CABTDC. The calculations have been performed in the crank angle domain 135 CABTDC - 117 CAATDC. The initial flow conditions in the chamber have been imposed according to the results of a cylinder head flow simulation in order to take into account the manifold effects [6].

As suggested in spray simulation [22], in order to reduce the calculation grid dependency, the necessary computation measures have been taken: the turbulence length scale has been limited to the jet diameter within the jet region and the grid arrangement tends to realize a perpendicular cell penetration.

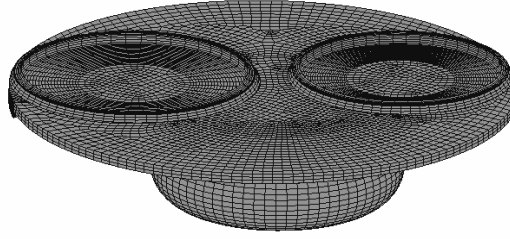


**Figure 4.4:** Engine mesh at 5 CABTDC

**4.3 Results.** The simulations have been performed on a four cylinder diesel industrial engine whose main features have been listed in Tab.4.2.

displacement [m <sup>3</sup> ]	401.3*10 <sup>-6</sup>
bore x stroke [m]	0.082 x 0.076
compression ratio	20.3:1
fuel injection system	HPCR
injector nozzle diameter [m]	0.154*10 <sup>-3</sup>
injector nozzle length [m]	0.72*10 <sup>-3</sup>
sac volume [m <sup>3</sup> ]	1.589*10 <sup>-10</sup>
number of nozzles	5

**Table 4.2:** Main characteristics of the diesel engine

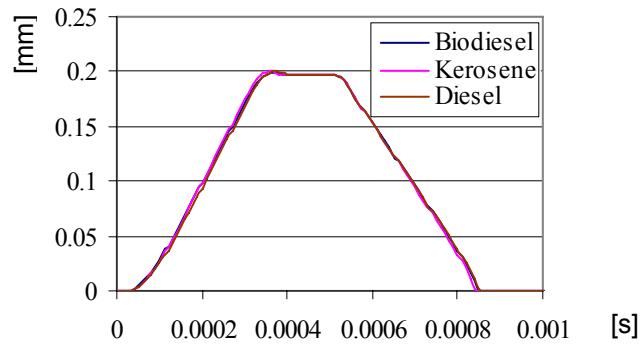
The simulations refer to the following conditions (Tab.4.3).

engine speed [Hz]	50
start of injection CABTDC	6
nominal rail pressure [MPa]	100
rail volume [m <sup>3</sup> ]	3*10 <sup>-5</sup>
high pressure pump displacement [m <sup>3</sup> ]	0.65*10 <sup>-6</sup>
energizing time [s]	0.5*10 <sup>-3</sup>
diesel injected mass [kg] (result)	1.94*10 <sup>-5</sup>
kerosene injected mass [kg] (result)	1.87*10 <sup>-5</sup>
biodiesel injected mass [kg] (result)	1.99*10 <sup>-5</sup>

**Table 4.3:** Simulation conditions

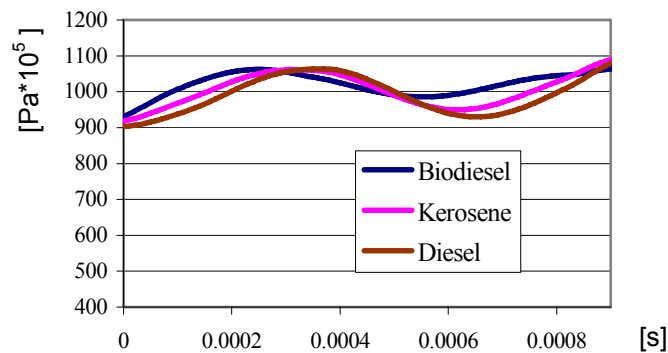
**4.4 Injection characteristics.** The following figures show the needle lift traces (Fig.4.5), the injection pressure trends (Fig.4.6) and the injection flow rate curves (Fig.4.7) respectively. In each figure, the comparison among the results regarding the three different fuels is presented.

Referring to the needle lift (Fig.4.5), it can be observed that no appreciable differences are highlighted in the traces behavior, both during the opening and the closing phases.



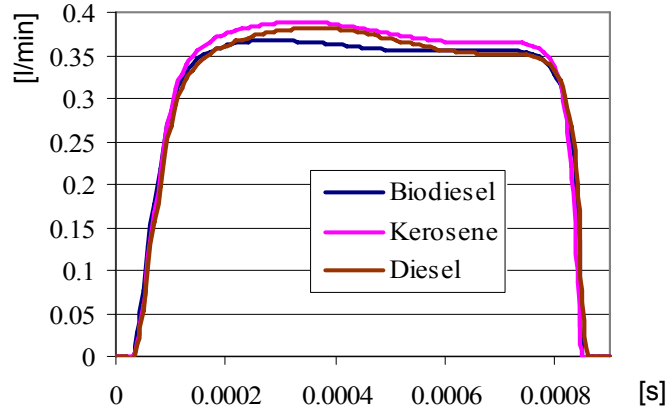
**Figure 4.5:** Poppet lift

Figure 4.6 represents the pressure curves referred to the drift injector chamber. The lines are characterized by almost the same trend; a delay can be observed in both kerosene and diesel traces, as regards biodiesel one, whose values are in a narrower range.



**Figure 4.6:** Injection pressure

The results of Fig.4.7 show that biodiesel volumetric flow rate reaches the lowest values, namely it remains below the other graphs. It must be noted that the highest percentage difference between the maximum (kerosene) and minimum (biodiesel) flow rate values doesn't exceed the value of 5%. Biodiesel curve appears flat compared to the others, highlighting an almost constant value during the injection. The most important differences appear during the first half of the injection; diesel and biodiesel fuels tend to have the same trace in the second phase, while kerosene fuel lies over them.



**Figure 4.7:** Injection flow rate

The opening ramps show a lower slope than the closing ramps, and they have the same behavior for the different fuels. In order to check the nozzle flow results, the total injected mass has been computed, in terms of fuel flow rate time integral at the nozzle exit.

**4.5 Injector flows.** The nozzle flow features have been evaluated on the basis of flow velocity and vapor region observation. The obtained results have been arrayed in synoptic way, in order to ease the comparisons among the figures. All graphs have been referred to the mid cut surface containing the nozzle hole axis.

Figure 4.8 shows the velocity fields at 0.1 ms ASOI. The maps behave in a similar way concerning their shapes, but differences of intensity can be found. The lowest values correspond to the diesel fuel (Fig.4.8b), where the stream that goes through the sac and the nozzle does not overcome the limit of 190 m/s; biodiesel fuel (Fig.4.8c) reaches the threshold of 198 m/s, that grows up to 235 m/s dealing with kerosene (Fig.4.8a). Cavitating regions are not present, but a hardly visible inception point is located at the inlet nozzle corner in kerosene flow, highlighted by the black circle of Fig.4.12a. At 0.2 ms ASOI, kerosene flow (Fig.4.9a) is about 6% faster than diesel one (Fig.4.9b) and it reaches values in the order of 460 m/s. Biodiesel flow velocities (Fig.4.9c) present an intermediate behavior, with a maximum value of 442 m/s. Cavitating regions characterize the flow in all cases. The inlet nozzle corner acts as inception point and vapor extends downstream to reach the nozzle exit (Fig.4.13). The exit conditions, in terms of volume fraction, have the same values (about 0.5) for the three fuels, but the core regions show different lengths; kerosene region (Fig.4.13a) has the longest full vapor core that extends beyond the first nozzle half.

At 0.4 ms ASOI the needle lift is much increased (Fig.4.5) and the injection pressure differences among the three curves are bounded in a range of 3MPa (Fig.4.6). At intermediate lifts, the flow is accelerated by the narrowed passage in correspondence of the needle seat and it generates a well structured stream, visible in



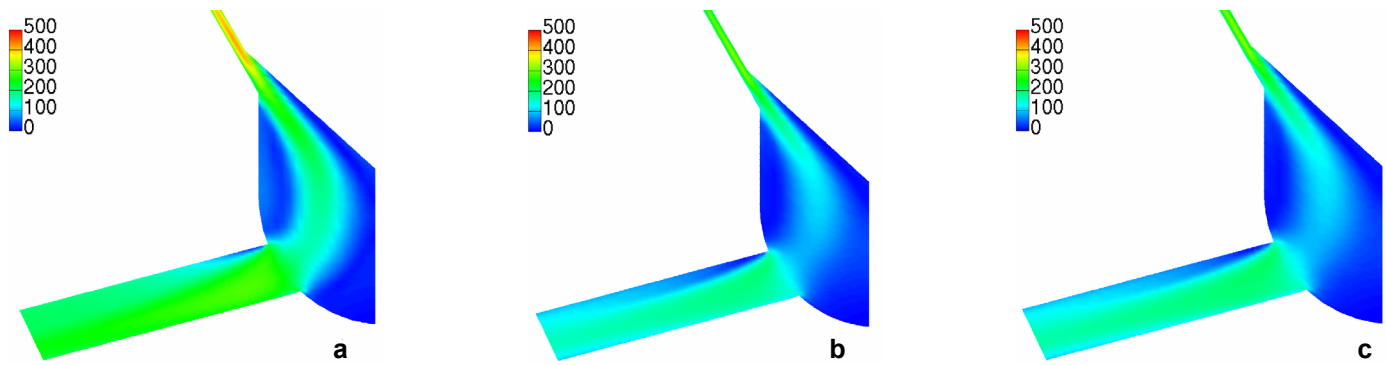


**Figure 4.8:** Scalar velocity [m/s], 0.1 ms ASOI; **a**, kerosene; **b**, diesel; **c**, biodiesel

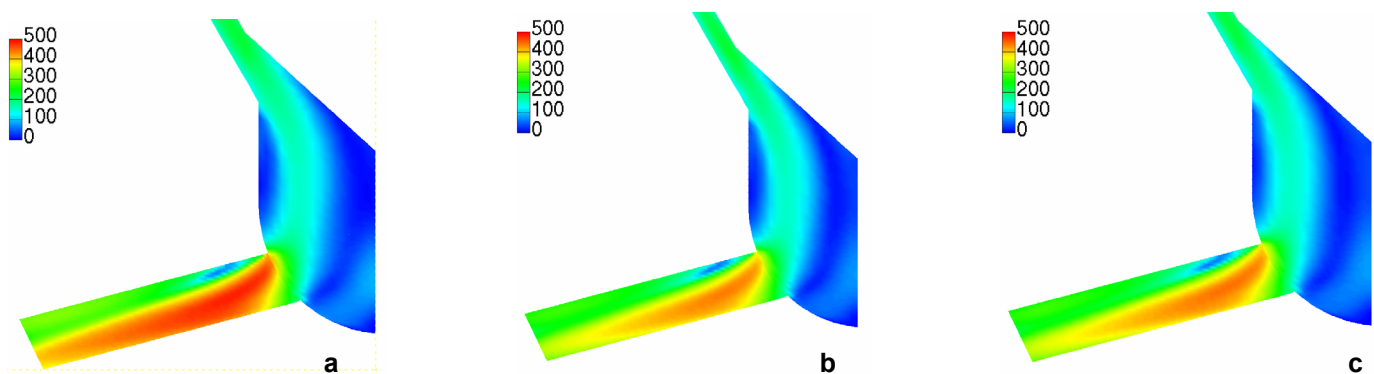


**Figure 4.9:** Scalar velocity [m/s], 0.2 ms ASOI; **a**, kerosene; **b**, diesel; **c**, biodiesel

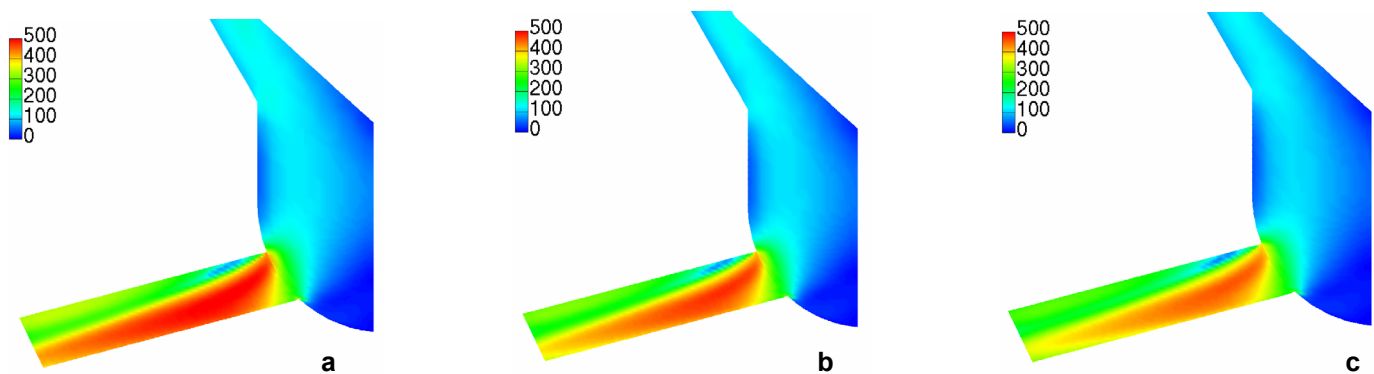


**Figure 4.10:** Scalar velocity [m/s], 0.4 ms ASOI; **a**, kerosene; **b**, diesel; **c**, biodiesel

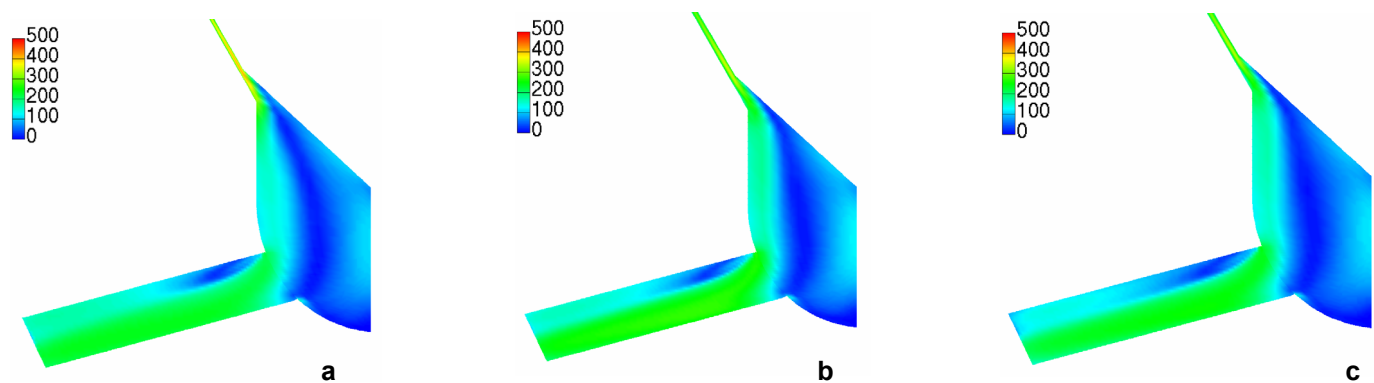


**Figure 4.11:** Scalar velocity [m/s], 0.8 ms ASOI; **a**, kerosene; **b**, diesel; **c**, biodiesel

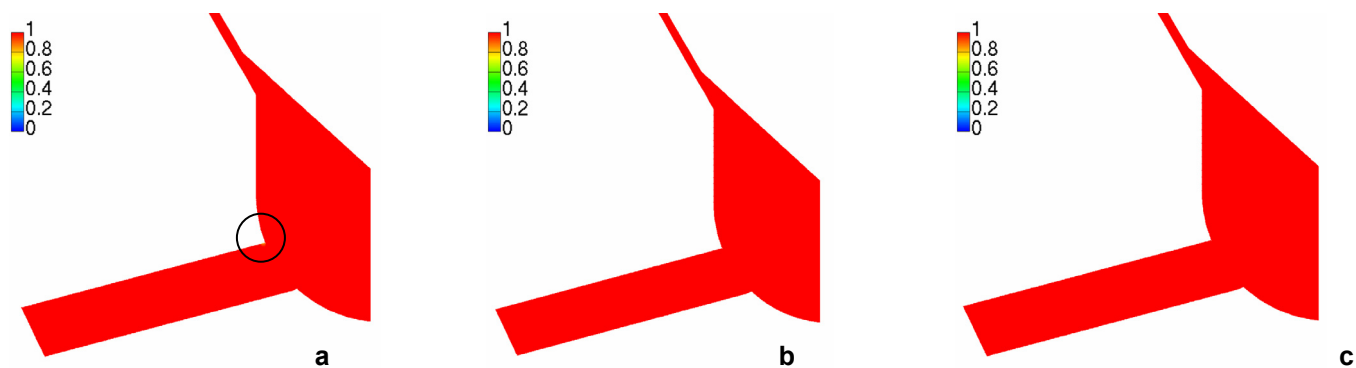


**Figure 4.12:** Liquid-vapor volume fraction, 0.1 ms ASOI; **a**, kerosene; **b**, diesel; **c**, biodiesel

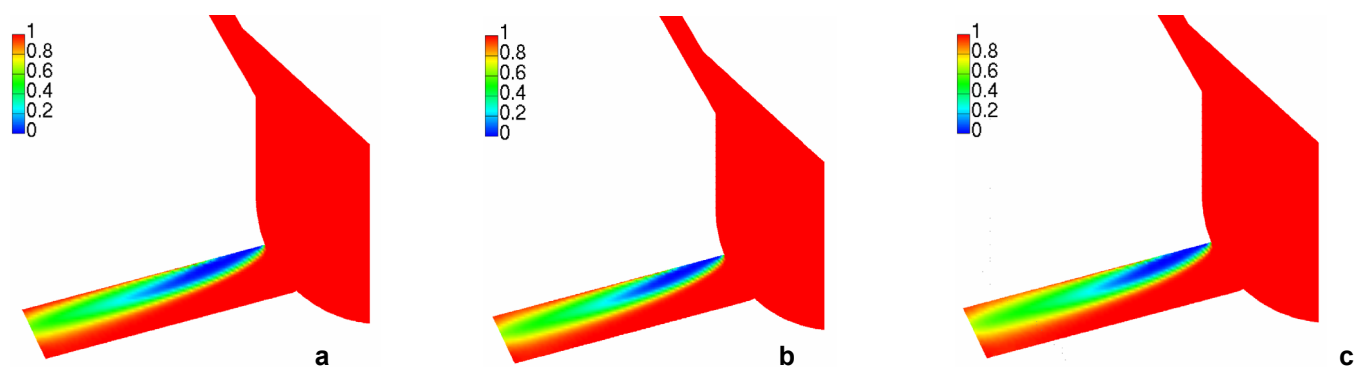


**Figure 4.13:** Liquid-vapor volume fraction, 0.2 ms ASOI; **a**, kerosene; **b**, diesel; **c**, biodiesel

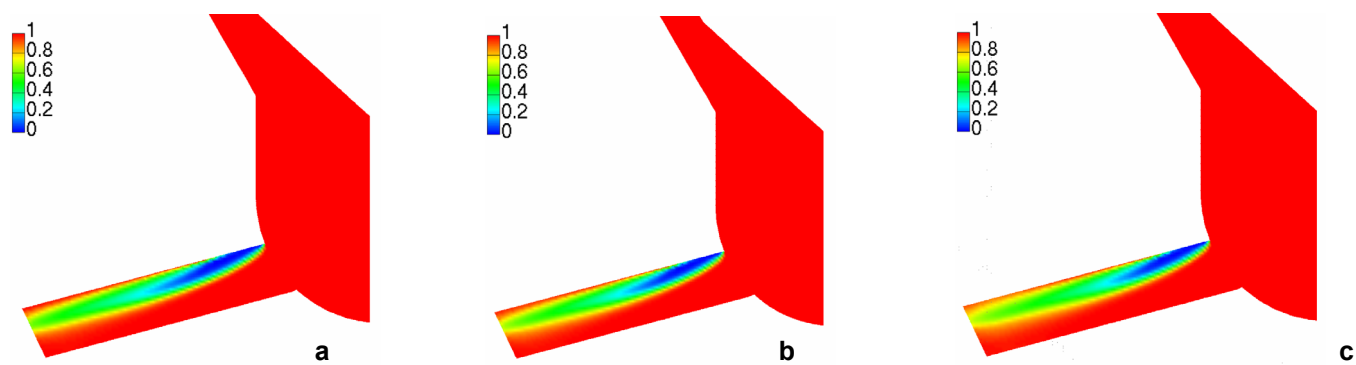


**Figure 4.14:** Liquid-vapor volume fraction, 0.4 ms ASOI; **a**, kerosene; **b**, diesel; **c**, biodiesel

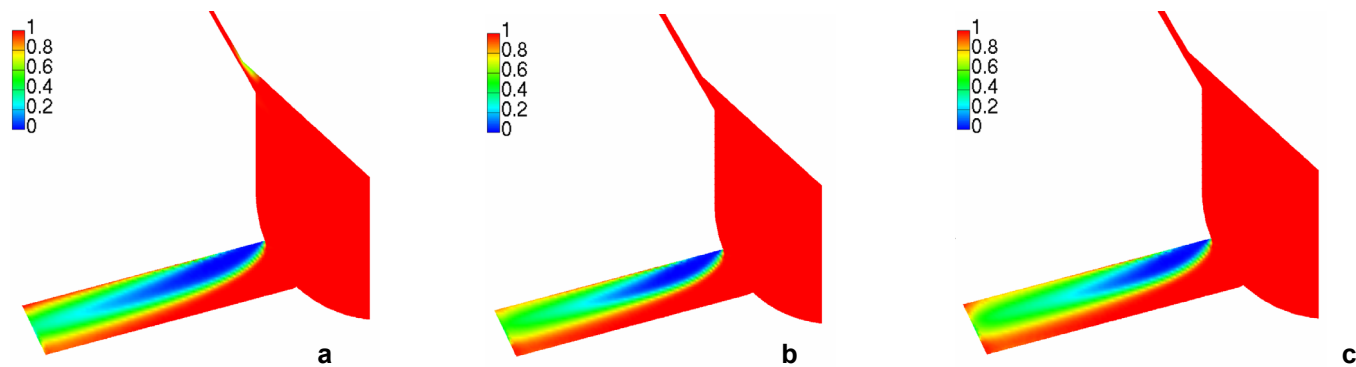


**Figure 4.15:** Liquid-vapor volume fraction, 0.8 ms ASOI; **a**, kerosene; **b**, diesel; **c**, biodiesel

the sac (Figures 4.9a-c); on the contrary, full lift keeps relatively slow the sac flows (Figures 4.10a-c). Kerosene fuel reaches the velocity of 485 m/s immediately followed by diesel (475 m/s); biodiesel flows slower than the others, and it does not overcome the limit of 455 m/s. Focusing on the cavitating regions (Figures 4.14a-c), a core area size reduction can be observed, although the nozzle flow speed is higher compared to the previous visualization; such a condition can be related to the current sac flow field, characterized by low speed and little cross sectional velocity components at the nozzle inlet. The closing phase seems to confirm the described behavior; the results referred to 0.8 ms ASOI (Figures 4.11a-c) show the presence of a fast stream, produced by the narrowing of the passage, that initially flows along the peripheral sac wall; suddenly, it is forced to turn the inlet corner: the velocity results reveal an evident stream contraction and the Figures 4.15a-c point out an increment of vapor region size. Kerosene fuel shows the largest cavitating zone that involves the nozzle outlet section for a relevant part of its area.

**4.6 Spray features.** Figure 4.16 shows the SMD curves calculated for each considered fuel. The obtained time traces reveal a similar behavior during the beginning of injection process, although a slight initial droplet diameter difference between kerosene and diesel fuel can be observed; anyway, all the initial computed SMDs are in the same length order, namely they are about 10-15% smaller than the nozzle hole diameter. The SMD decreases with the same rate until 3 CABTDC, where biodiesel curve starts showing a hardly visible slope reduction and then it remains below the other traces. In 3CABTDC-TDC interval, according to the default break-up model available in FIRE code, the velocity values and the chemical-physical properties of biodiesel fuel are responsible for its highest break-up. After TDC, a similar shape characterizes the results.

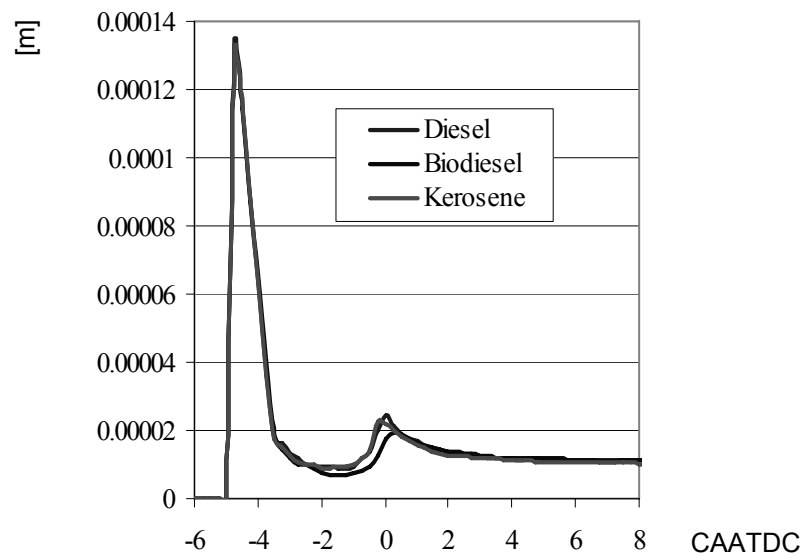


**Figure 4.16:** SMD referred to the three fuel spray simulations

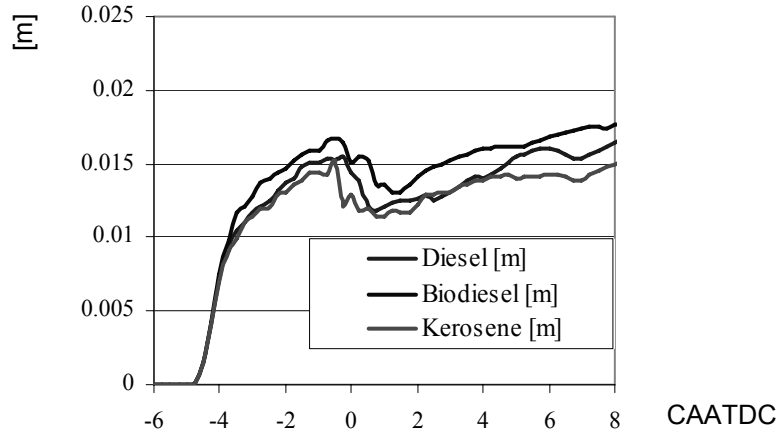


**Figure 4.17:** Mean hole penetration of the three fuel sprays

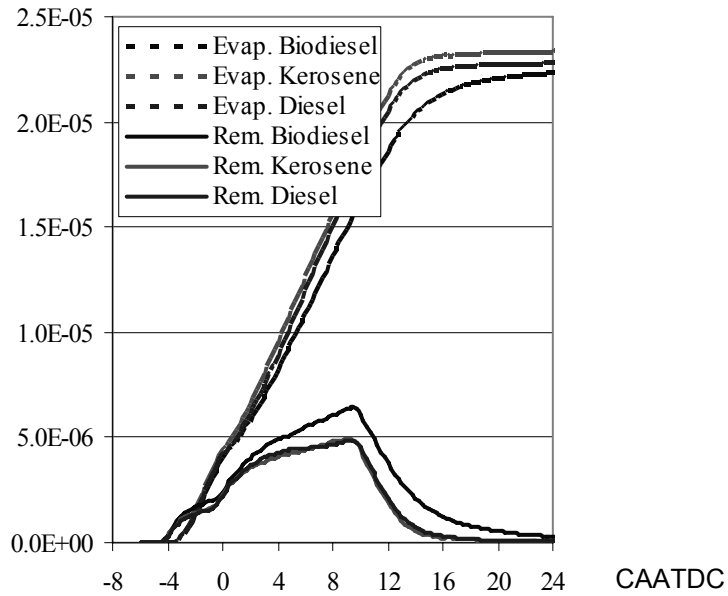


**Figure 4.18:** Evaporated and remaining fuel volume [l]

In Fig.4.17, the hole-averaged spray penetration curves have been depicted; biodiesel fuel is the most penetrating, followed by the diesel and kerosene traces. During the first millimeters of penetration, which means 1 CAD or 55  $\mu$ s in terms of time at 3000 rpm, the traces behave in the same way. Afterwards, a deeper penetration characterizes biodiesel case and, starting from 2 CABTDC, different trends can be observed for all fuels. A sudden slope inversion happens just before TDC, when penetration lengths reach the max values; at such a crank angle value, the chamber flow structures, in terms of swirl and squish effects, gain a strong intensity and the produced mixing effect tends to keep the spray cones bounded inside the piston bowl; during the expansion phase, penetration

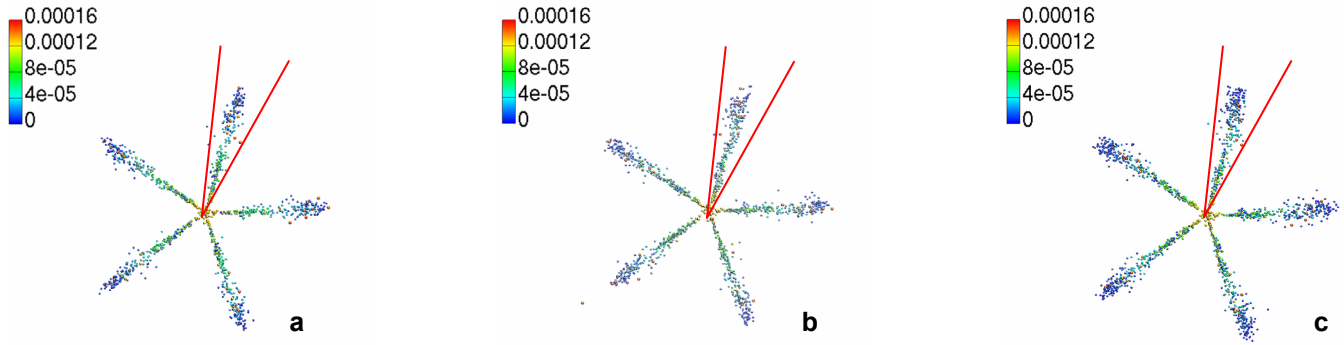


**Figure 4.19:** Droplet diameter [m], 3 CABTDC; **a**, kerosene; **b**, diesel; **c**, biodiesel

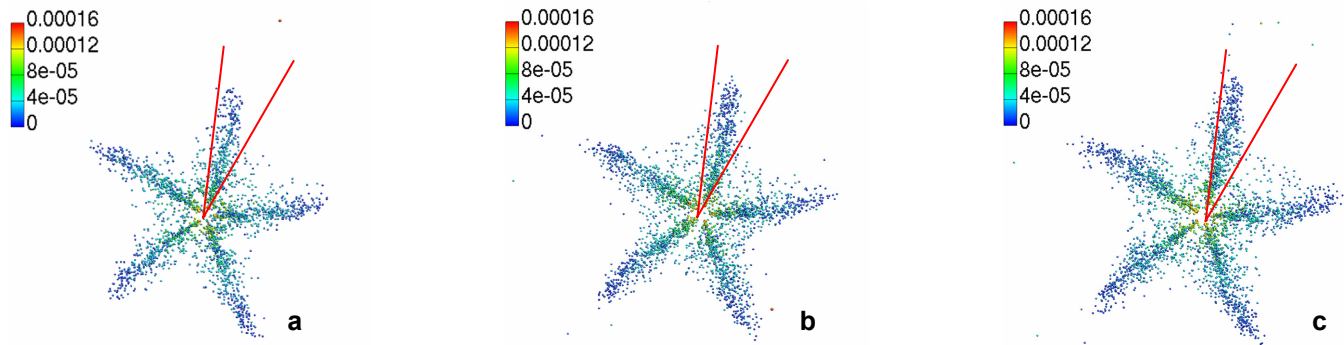


**Figure 4.20:** Droplet diameter [m], 2 CAATDC; **a**, kerosene; **b**, diesel; **c**, biodiesel

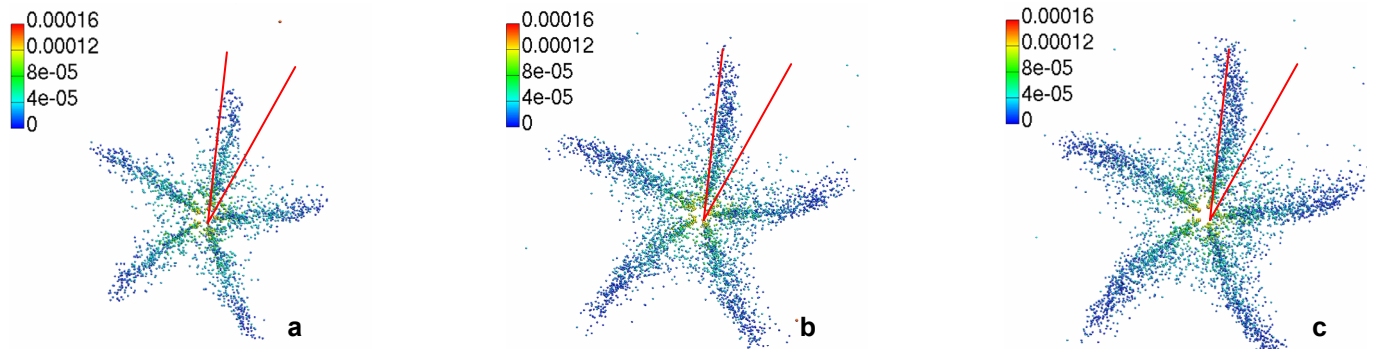


**Figure 4.21:** Droplet diameter [m], 5 CAATDC; **a**, kerosene; **b**, diesel; **c**, biodiesel

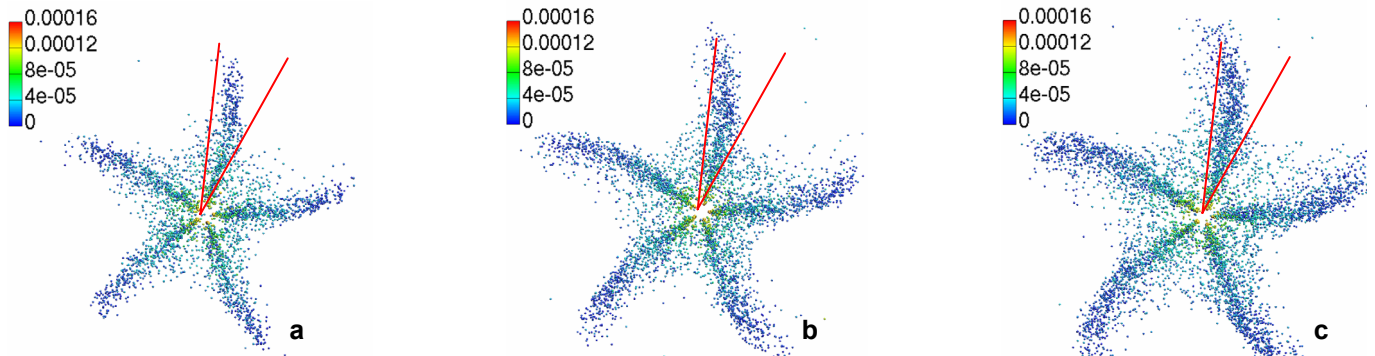


**Figure 4.22:** Droplet diameter [m], 8 CAATDC; **a**, kerosene; **b**, diesel; **c**, biodiesel

is enhanced again (wall impingement phenomena do not happen). Respect to the experimental results in test ambient [22,23], shape agreement can be observed, except for the described slope change, but in such experiments the initialization of chamber flow conditions is not produced.

Figure 4.18 compares the evaporated and remaining fuel volumes; kerosene and diesel fuels are characterized by almost the same evaporation rate, but they differ about the maximum value (see also Tab.4.3). From Fig. 4.16 it appears that, close to TDC, the mean droplet diameter in biodiesel spray is lower compared to diesel and kerosene ones; such a feature does not lead to a ready evaporation due to the high boiling temperature of the fuel assumed as representing biodiesel.

At 16 CAATDC, 99% of injected kerosene is evaporated; biodiesel curve has the lowest slope of the considered fuels; the different behavior starts at TDC and it becomes more evident in the subsequent CAs; the end of the process, highlighted by the horizontal trend of the curve, is considerably delayed.

The visualization of the spray cone results is based on the same array used for the nozzle flows. A red mark is added to the figures to better evaluate the observed geometries. Figures 4.18a-c represent the spray condition at 3 CABTDC. Kerosene and diesel fuels have a similar cone shape; biodiesel cones show a higher droplet presence far from the nozzles and a deeper penetration.

At 2 CAATDC (Figg.4.20a-c), the highlighted initial differences become more evident: injected kerosene forms short jets with a relatively little plume. On the contrary, biodiesel droplets persist for longer time in the chamber and tend to be conveyed by the swirl flow. During the subsequent phases of injection (5 CAATDC-Figg.4.21a-c), all the visualizations show the enhance of a droplet cloud surrounding the nozzles. Biodiesel cones penetrate deeper and a wide plume shape characterizes its development. At this CA, kerosene and diesel evaporation rate are faster compared to biodiesel one, and a larger number of droplets remains liquid conveyed by the swirl stream. In the last visualized phases (Figg.4.22a-c), the described behavior, concerning the presence of several biodiesel droplets at long distance from the nozzles, is still visible.

The qualitative spray features, highlighted in this section, seem to be in agreement with the experimental results in which diesel and biodiesel fuel sprays have been tested [5].

**4.7 Concluding remarks.** A model based on the integration of two commercial codes has been used in order to analyze the influence of different fuels on the injection performances. Such a model is based on a two step procedure. In the first one, the complete injection system is analyzed by means of AMESim code and the obtained needle lift, pressure and flow rate time traces are used in the second step to initialize the CFD investigations of nozzle flow and spray formation, allowing to adopt a detailed break-up model able to take the effect of the cavitating flow regime into account. Differences concerning fuel injected masses have been pointed out; in detail, kerosene shows the minimum injected mass. From the comparison among the flow rate traces,

similar transient phases have been observed; in all cases, the most relevant differences have been found in the first half of the curves.

The 3D models implemented in FIRE environment have highlighted the nozzle flow features and the spray behavior. The nozzle transient flow phenomena and the fuel tendency toward cavitation have been observed: kerosene fuel has shown the fastest flows and the largest cavitating regions. The effects of the needle closing phase on the sac flow features have been highlighted: the narrowing of the fuel passage has accelerated the stream and it has influenced its direction; such a transient has been related to the observed vapor region enhancement during the last part of injection process.

Focusing on fuel jet characteristics, a comparison among the jet feature has been presented (spray cone penetration, breakup rate and cone angles). The main conclusions have been resumed in the following:

- high density fuels enhance spray cone penetration;
- spray cone angles do not reveal significant differences;
- biodiesel spray plumes appear the most developed;
- fuel properties have influence on vaporization rate;
- qualitative shape agreement can be found comparing the simulated results with experimental spray visualizations available in literature.

#### 4.8 Nomenclature

$A_i''$	=	interfacial area density
CAA	=	Crank Angle After
CAB	=	Crank Angle Before
$D_b$	=	bubble diameter
$C$	=	constant
$C_{CR}$	=	condensation reduction factor
$C_D$	=	drag coefficient
$C_E$	=	Egler coefficient
$C_{TD}$	=	drag turbulent coefficient
$C_{1-4}$	=	Wave model constant
$E_k$	=	kinetic energy
EOI	=	End Of Injection
$M_c$	=	vapor phase momentum
$M_d$	=	liquid phase momentum
$N_0''$	=	initial bubble number density
$N'''$	=	number density
$R$	=	bubble radius
$Re_b$	=	bubble Reynolds number
$S_k$	=	cavitation source term
SOI	=	Start Of Injection
TDC	=	Top Dead Centre

$We$  = Weber number  
 $k_c$  = vapor phase turbulence kinetic energy  
 $m_L$  = liquid mass of a ligament  
 $n_L$  = number of bubbles in a ligament  
 $r$  = actual droplet radius  
 $r_A$  = characteristic droplet radius  
 $r_T$  = turbulent length scale  
 $p_{sat}$  = saturation pressure  
 $p_b$  = pressure in a bubble  
 $p_\infty$  = environment pressure  
 $v_c$  = vapor velocity  
 $v_d$  = liquid phase velocity  
 $v_r$  = relative velocity

#### **Greek symbols**

$\Gamma_c$  = vapor phase mass  
 $\Gamma_d$  = liquid phase mass  
 $\Delta p$  = pressure difference  
 $\alpha_d$  = liquid phase volume fraction  
 $\nu_2$  = liquid cinematic viscosity  
 $\rho_c$  = vapor phase density  
 $\rho_d$  = liquid phase density  
 $\rho_2$  = liquid density  
 $\sigma$  = surface tension  
 $\tau_A$  = characteristic break-up time  
 $\tau_T$  = turbulent time scale

#### **4.9 References**

- [1] Fimml, W., Fuchs, C., Jank, T. and Wimmer, A., "Optical Analysis and Simulation of Diesel Sprays in a High Pressure and High Temperature Spray Box", ICES2006 ASME Paper No. 1376.
- [2] Fezzaa, K., Lee, W.K., Cheong, S., Powell, C.F., Wang, J., Li, M., and Lai, M.C., "High Pressure Diesel Injection Studied by Time-Resolved X-Ray Phase Contrast Imaging", ICES2006 ASME Paper No. 1409.
- [3] Su, T.F., Patterson, M.A., Reitz, R.D. and Farrell, P.V., "Experimental and Numerical Studies of High Pressure Multiple Injection Sprays", SAE Paper No. 960861.
- [4] Ueki, H., Ishida, M. and Sakaguchi, D., "Investigation of Droplet Disintegration in Diesel Spray Core by Advanced Laser 2-Focus Velocimeter", SAE Paper No. 2005-01-1238.



- [5] Grimaldi, C. and Postrioti, L., "Experimental Comparison Between Conventional and Bio-derived Fuels Spray from a Common Rail Injection System", SAE Paper No. 2000-01-1252.
- [6] Chiavola, O. and Palmieri, F., "Coupling Codes for Nozzle Flow Modeling in Diesel Injection Systems", ICES2006 ASME Paper No. 1414.
- [7] Imagine AMESim v4.2 Tutorial and User Guide, AMESim Technical Bulletins.
- [8] FIRE v8.4 CFDWM Guide, AVL List GmbH.
- [9] FIRE v8.4 Spray Manual, AVL List GmbH.
- [10] FIRE v8.4 Multiphase Manual, AVL List GmbH.
- [11] Chiavola, O. and Giulianelli, P., "Modeling and Simulation of Common-Rail Systems", SAE Paper No. 2001-01-3183
- [12] Hinze, J.O., "Turbulence", 2<sup>nd</sup> ed., McGraw-Hill, New York, 1975.
- [13] Franklin, R.E. and McMillan, J., "Noise Generation in Cavitating Flows", J. Fluids Eng., 106, 336-341, 1984.
- [14] Tatschl, R., v.Kuensberg Sarre, E. and v.Berg, E., "IC-Engine Spray Modeling – Status and Outlook", acts of Int. Multidimensional Engine Modeling User's Group Meeting at SAE W. Congress, 2002.
- [15] Su, T.F., Patterson, M.A., Reitz, R.D. and Farrell, P.V., "Experimental and Numerical Studies of High Pressure Multiple Injection Sprays", SAE Paper No. 960861.
- [16] Tatschl, R., v. Künsberg-Sarre, C., Alajbegovic, A. and Winklhofer, E., "Diesel Spray Modeling Including Multidimensional Cavitation Nozzle Flow Effects", Proc. of ILASS Europe Conference, Sept. 11-13, Darmstadt, Germany, 2000.
- [17] Patterson, M.A. and Reitz, R.D., "Modeling the Effects of Fuel Spray Characteristics on Diesel Engine Combustion and Emissions", SAE Paper No. 980131.
- [18] O'Rourke, P.J., "Statistical Properties and Numerical Implementation of a Model for Droplet Dispersion in Turbulent Gas", J. Comput. Physics, 83, 345, 1989.
- [19] O'Rourke, P.J. and Bracco, F.V., "Modeling of Drop Interactions in Thick Sprays and a Comparison With Experiments", IMECHE, 1980.
- [20] Naber, J.D. and Reitz, R.D., "Modeling Engine Spray/Wall Impingement", SAE Paper No. 880107.
- [21] Dukowicz, J.K., "Quasi-steady droplet change in the presence of convection", informal report Los Alamos Scientific Laboratory", LA-7997-MS, 1979.
- [22] Stiesch, G., "Modeling Engine Sprays and Combustion Processes", Springer Verlag, Berlin, 2003.
- [23] Wang, T.C., Han, J.S., Xie, X.B., Lai, M.C., Henein, N.A., Schwarz, E. and Bryzik, W., "Parametric Characterization of High-Pressure Diesel Fuel Injection Systems", J. Engineering in Gas Turbine & Power, 125, 412-426, 2003.

## 5. Injector Dynamic and Nozzle Flow Features in Multiple Injection Modeling

**Introduction.** The aim of the numerical investigation is to capture the behavior of the multiple injections, in terms of electro-injector dynamic and nozzle flow development. In detail, the multiple injection investigation focuses on the transient phenomena of the injector, in order to evaluate their role on the definition of two aspects of the injection strategy, the fuel rate time evolution and their influence on the nozzle flow features. The model is based on the integration of two different commercial codes. In the simulations, a 0/1-D code has been used to analyze the complete injection system. The results obtained from the injection system simulation, in terms of injection needle lift, injection flow rate, pressure time evolution, have been used as boundary conditions for the 3-D CFD computation tool, in which the numerical investigation of the internal injector flow has been performed. Such an investigation is thought to highlight the exit flow features that play a significant role in the break-up process.

The present section is placed in the described integrated modeling strategy but it is restricted to the first and second simulation steps; at first, the attention is focused on the system dynamics, highlighting the interactions between two consecutive injection events due to the pressure wave propagation that happen in a second generation solenoid type common rail system. In detail, the dwell time dependence of the injection duration is highlighted by the 0/1-D model and the transient behavior that characterizes the pressure in the injector drift chamber is used to simulate the internal nozzle flows; in such a frame, the results coming from AMESim model (pressure and needle lift time traces) are used to initialize the 3D-CFD nozzle flow simulation and the comparison between the behavior of pre-injection and main-injection is presented. As the dwell time dependence causes noticeably fuel amount variations (energizing time being the same), simulations are then devoted to evaluate its influence on the flow field characteristics.

**5.1 Injection system.** The model of a second generation common rail layout (solenoid-actuated) is built on the basis of the AMESim libraries; the system consists of high pressure reciprocating pump, relief valve, pipelines, control valves and injectors. Figure 5.1.1, shows the coupled schemes of the needle and the control plunger, whereas in Fig. 5.1.2 the scheme of the pilot valve is presented; as visible, the mobile equipment is made of two units, the anchor and the pin. The anchor unit is allowed to swing in respect to the pin when it reaches the displacement limit, damping the pin counterstroke and preventing unwanted oscillations.

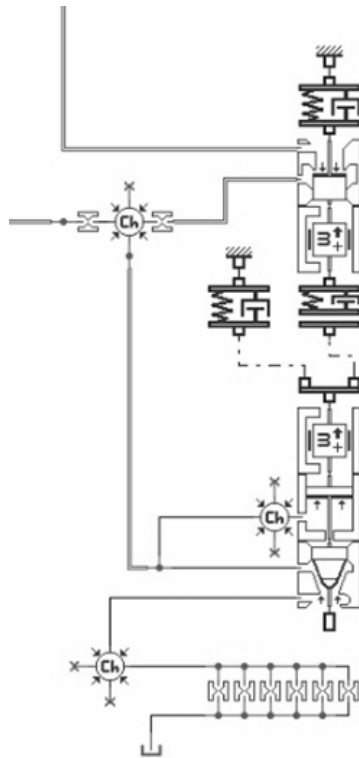


**Figure 5.1.1:** Needle and plunger model

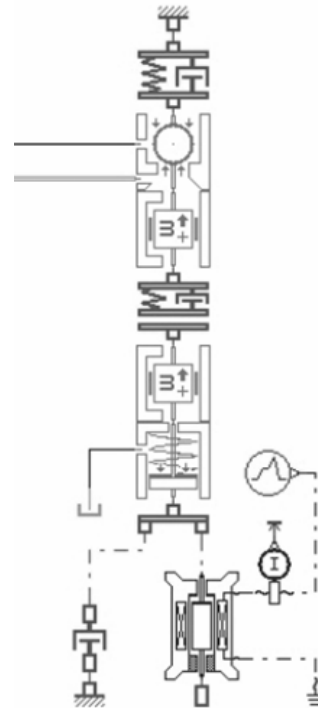


**Figure 5.1.2:** Pilot valve model sketch

The electromagnetic force acting on the pilot valve is represented by means of a solenoid circuit model available in AMESim library. Figure 5.2 represents the time distribution of the force acting on the anchor.

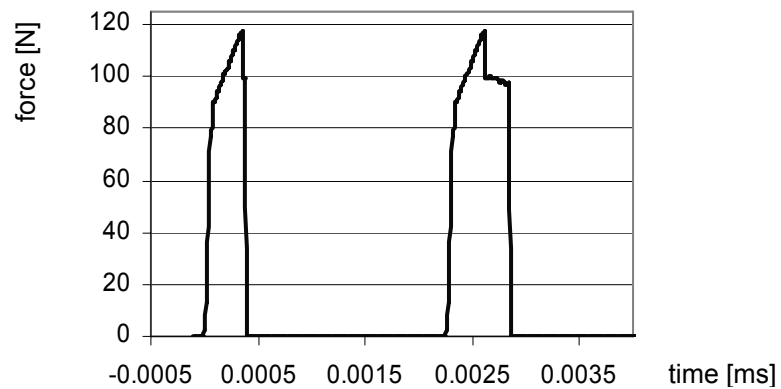


**Figure 5.2:** Electromagnetic forces for a multi-event injection

The hydraulic network of the system is a combining of chamber volumes and pipe elements. Pressure and temperature in lumped volume elements are just time dependent, whereas the pipeline models are based on a one-dimensional approach; in such a case,

the solution of wave equation is used to represent the effects of inertia, friction and compressibility; in detail, AMESim library contains a sub-model capable to represent the influence of the frequency dependent friction [20-21].

The building up of the complete model is based on the knowledge of the component characteristics and on the choice of appropriated physical models, in order to represent the behavior of the considered injection system.

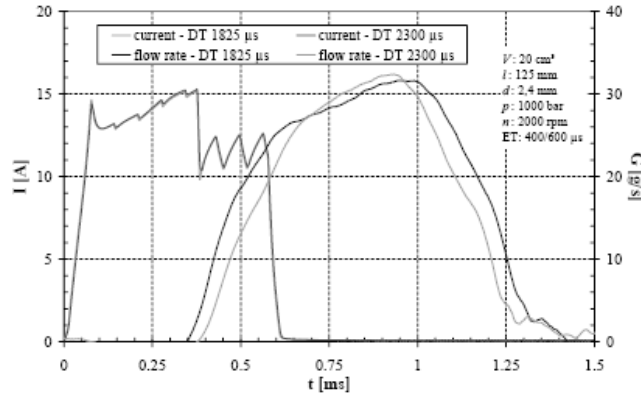


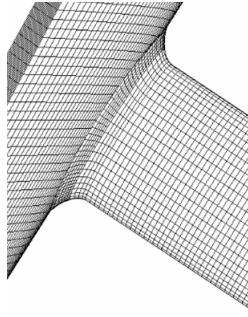
**Figure 5.3:** Comparison between injected flow rates for different dwell time and same energizing time [3]

A preliminary computation phase has been performed in order to assess the model performance in predicting mass flow rate, needle lift and the effect of dwell time on injection profile. The comparison of the obtained results (e.g. Figure 5.10) with those referred to a similar system, available in the literature (e.g. Fig. 5.3) [3], whose validation has been extensively discussed [4], has been made; the general agreement among the curves shows the satisfactory representation of the typical injection phenomena.

**5.2 Injector features and nozzle type.** The transient nozzle flow simulation is performed evaluating the influence of the injector features on the development of two phase cavitating flows.

The analysis is focused on a VCO type nozzle; Figure 5.4 shows the detail of the inlet edge of the hole, characterized by a rounded shape (even if it is not constant, the length of the minimum inlet radius is in the order of 30  $\mu\text{m}$ ). The computational grid is made of two structured elements (body volume and nozzle) separately generated and then connected. The whole mesh is formed by 57708 hexahedral cells.

The simulation of the injection event is based on the generation of a mesh set that reproduces the needle movement. The lift of the needle is computed as a time function in the AMESim model and it is then imposed to the needle surface. The FAME ENGINE environment (included in FIRE code) operates the generation of the mesh set that represents the opening-closing movement.



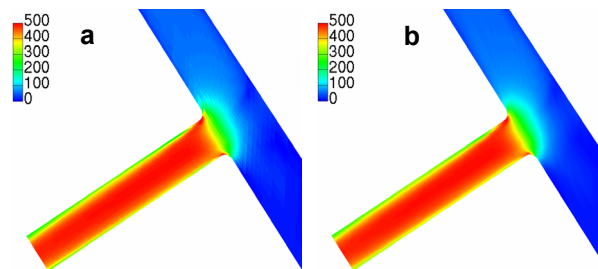
**Figure 5.4:** Detail of the edge inlet

Figure 5.9 shows the needle lift time traces, in which the opening for a double shot injection is actuated. The injection system model gives also the boundary condition at the mesh inlet surface, in terms of pressure time evolution within the needle drift chamber (Fig. 5.8). At the exit of the nozzle, a constant pressure of  $4.6 \cdot 10^6$  Pa has been imposed, in agreement with the 0-1D model. Table 5.1 resumes the injector geometrical features.

injector nozzle diameter [m]	$0.14 \cdot 10^{-3}$
injector nozzle length [m]	$0.7 \cdot 10^{-3}$
needle length [m]	$40 \cdot 10^{-3}$
number of nozzles	6

**Table 5.1:** Injector features

Preliminary tests are devoted to find a convenient mesh refinement. Figure 5.5 shows the comparison between the velocity scalar field obtained with mesh 'a' (57708 cells) and mesh 'b' (461664 cells).



**Figure 5.5:** Scalar velocity [m/s]; a, mesh 'a'; b, mesh 'b'

The calculation considers diesel fuel at the constant injection pressure of 100 MPa at maximum value of needle lift. The results show limited differences between the two computation; the difference evaluation in the predicted mass flow rate (slightly lower in case of the finest grid) and the analysis of the magnitude deviation of the local

pressure values make possible the selection of mesh 'a', reducing the computational effort.

### 5.3 Results

**5.3.1 Injection System.** The injection system model is used to simulate a multi event injection, characterized by two energizing signals, whose lengths are 400 microseconds for the pre-injection and 600 microseconds for the main-injection. Such a couple of values is implemented in two modalities, defined by two different widths of dwell time, being the energizing times equal. For the sake of simplicity, these two simulation conditions are named DT1 and DT2, whose details are listed in Tab.5.2.

nominal rail pressure [MPa]	100
high pressure pump displacement [m <sup>3</sup> ]	$0.65 \cdot 10^{-6}$
rail volume [m <sup>3</sup> ]	$2 \cdot 10^{-5}$
pre-injection energizing time [ $\mu$ s]	400
main-injection energizing time [ $\mu$ s]	600
DT1, dwell time of 1 <sup>st</sup> simulation [ $\mu$ s]	1825
DT2, dwell time of 2 <sup>nd</sup> simulation [ $\mu$ s]	1785

**Table 5.2:** Injection features and conditions

In the following, the influence of the dwell time width on the injection process is discussed. Figure 5.6 shows the pressure time trace at injector inlet during the whole injection process (DT1). As visible, the pre-injection shot induces a considerable perturbation that forces the pressure to oscillate. Evidently, such a pressure behavior has the capability to influence the next injection, due to the amplitude of the pressure fluctuations, that tend to be damped, but not enough to disappear before the next injection shot.

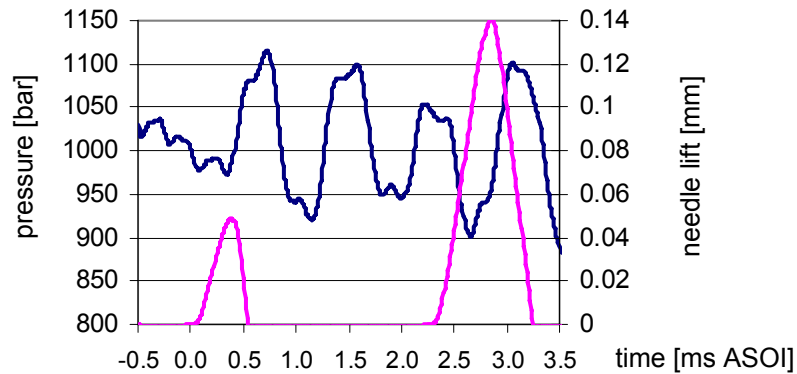


**Figure 5.6:** DT1, pressure trace at injector inlet — , needle lift —

Concerning the frequency of the pressure ripple at injector inlet, a discussion on its nature has been extensively produced in the literature and it has been highlighted that the system oscillation frequency depends on geometrical and physical features of the system; more in detail, without introducing hydraulic dissipative elements, the injector-supplying pipe design (e.g. length to diameter ratio) is shown to be a key factor in the definition of amplitude and frequency of the pressure oscillations, whereas the dynamic of the pressure wave is shown to be virtually independent of the rail size (in presence of pressure regulator) [3,2].

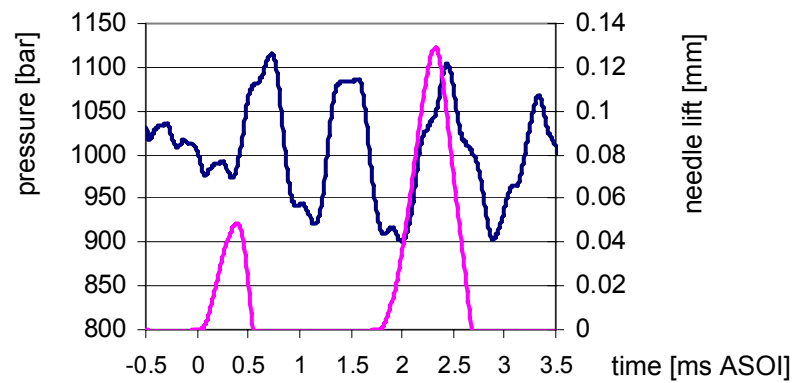


**Figure 5.7:** DT2, pressure trace at injector inlet — , needle lift —

In detail, the dwell time width plays a relevant role in the definition of the boundary conditions that characterize the main injection, namely the actions that induce the lift of the needle and influence the pressure history during the fuel injection. Figure 5.7 shows the pressure history of the second simulation (DT2); the narrower dwell time causes the injector opening to be at a lower pressure in respect to the DT1 case. Figure 5.8 shows in detail the pressure traces of the needle drift chamber during the main injections, for the considered simulations (DT1 and DT2). The wider dwell time of DT1 is responsible for opening and closing pressures that are considerably higher than those of DT2 case.

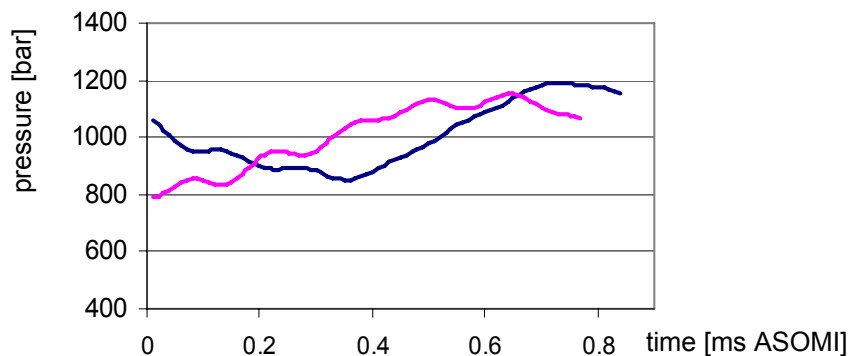


**Figure 5.8:** Pressure trace within needle drift chamber, DT1 — , DT2 —

Such a condition induces different net forces acting on the needle surfaces, causing a modified needle lift response, that is shown in Fig. 5.9; the maximum value of the lift trace in DT1 case is higher than the one of DT2 and the duration of the whole process is longer, too. The macroscopic difference due to the considered injection conditions pertains to the injected fuel amounts. As shown in Fig. 5.10, the injected flow rate time trace of DT1 has a steeper trend during the beginning of the process, a longer duration and it defines a larger area, even though it shows a lower maximum value if compared to DT2 case.

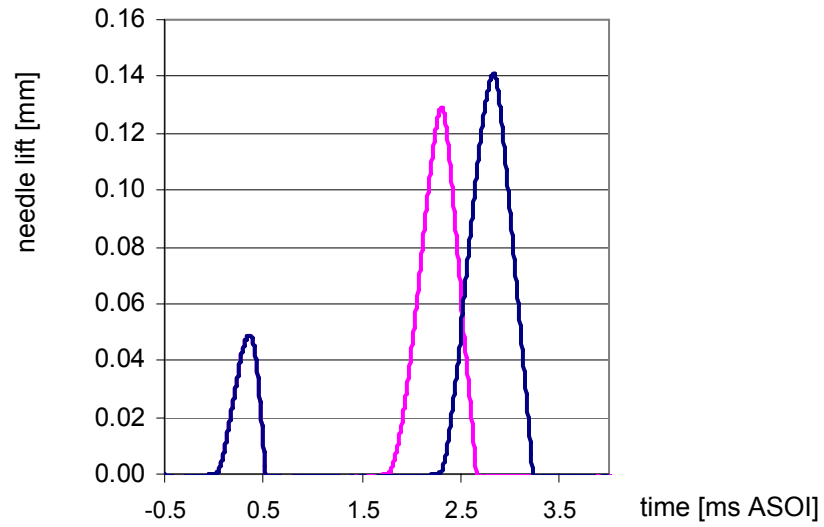


**Figure 5.9:** Needle lift comparison, DT1 — , DT2 —

The traces of Fig.5.8 highlight the agreement with the flow rate results of Fig. 5.10. In Fig. 5.8, the trend of the curves can be divided in three parts, separated by the two points in which the traces are intersected, alternating their prevalence each other.

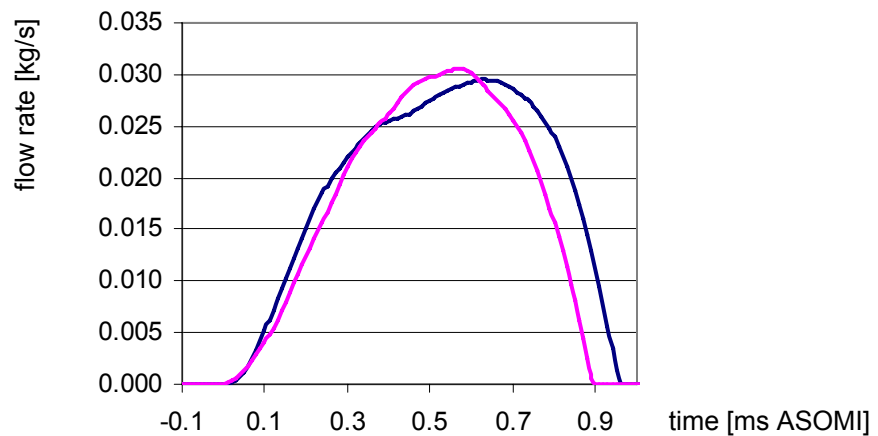


**Figure 5.10:** Fuel flow rate, DT1 — , DT2 —



The flow rate traces (Fig. 5.10) have the same behavior, so that two intersection points are visible in turn. When the injection pressure of DT1 is below the values of DT2, the flow rate is lower, too. In DT1 case, the injected fuel amount is  $18.55 \cdot 10^{-3}$  mg, whereas  $16.41 \cdot 10^{-3}$  mg is the fuel mass of DT2; the difference is in the order of 10%, and it is clear that such a difference is due not simply to the injection pressure value, but to its time history and to the influence on the conditions that define the needle lift; DT1 injection is characterized by a pressure dynamics that induces the needle to be faster during the opening and to remain open for a longer time.

**5.3.2 Nozzle flow.** In order to clarify the 3-D simulation step, it must be pointed out that a computation with completely closed injector is meaningless; a minimum lift position is established, and in the present case it is limited at  $10 \mu\text{m}$ . Such a value is subtracted to the lift trace that is used for the moving mesh generation, in order to take into account the initial minimum displacement. In the case of pilot injection, the lift at the start of simulation is in the order of 20% of the maximum lift (0.01/0.05 ratio); such a condition, in agreement with other numerical investigations available in the literature [14], on the one hand represents a weakness in the modeling of the low lifts, on the other hand, it depends on the impossibility to reduce the opening gap at pleasure.

The picture sequence of Fig. 5.12 displays the scalar velocity time evolution along the whole pre-injection process and, in order to better visualize the flow features, the results are displayed on a couple of cut planes mutually perpendicular and one of them containing the injector axis (see Appendix). The influence of the hole edge, that causes a considerable stream acceleration, is clearly visible at the nozzle inlet; the flow velocity, despite the high fuel pressure level, takes a relatively long time to reach the maximum value, but it must be pointed out that the pre-injection is characterized by relatively little value of needle lift, as Fig.5.9 highlights; such a feature causes the opening of a narrow passage for the fuel, that tends to limit the flow rate; moreover, the velocity distribution within the nozzle remains poorly uniform for the whole process.

The visualization of the streamlines gives an indication on the flow behavior; in the early initial phase (0.05 ms ASOI), when the fuel rate is still very low, the tangential component of velocity is not present; such a condition evolves as the process goes on and the streamlines assume a helicoidal shape, as the picture shows at 0.28 ms ASOI.

Concerning the flow tendency towards the cavitation, Fig.5.13 shows the characteristics of the vapor formation. In the initial part of the process, fuel does not cavitate, except for the presence of some hardly visible inception points that collapse just after their formation.

As the flow velocity increases, stable cavitation is formed at the hole edge. On the cut plane that contains the injector axis, the visualization shows that the highest part of the inlet edge behaves as the main inception zone, even though fuel vapor is formed at side also, especially in the closing phase. By means of an iso-surface that represents the vapor/liquid volume fraction at the value of 0.6, the shape of the cavitating region can be better understood; it is clearly visible that the vapor zone is attached to the hole surface.

The visualization highlights the shape of the inception zone, that involves the top half of the inlet edge. After its formation, the cavitating region tends to be conveyed by the fuel stream and to be detached from the hole surface after the initial third of the nozzle; such a behavior seems to be in agreement with the helicoidal motion of the flow.

Main-injection is characterized by longer duration and higher lift; results of Fig.5.14 show the different features in respect to the pre-injection; fuel flow is faster and it is characterized by a more uniform velocity profile during the whole process, due to the higher lift value.

The streamline visualization points out the influence of the needle lift on the flow features. At 0.04 ms ASOI a helicoidal motion is visible already, whereas in the previous case the flow lines look parallel. In the central phase of the process (0.4 ms ASOI and maximum lift) the flow tends to loose the tangential component of velocity, so that the shape of the lines becomes weakly helicoidal.

The visualization of the vapor zones (Fig.5.15) reveals the different behavior of cavitation; as pointed out, the faster needle lift is responsible for higher flow velocity from the early phase already; such a feature induces an anticipated cavitation inception, that becomes well visible at 0.06 ms ASOI; the vapor formation is sustained by the faster stream and it tends to be longer than the one of pre-injection; even though the vapor reaches and passes the half of the nozzle length, in this case it remains well attached to the nozzle wall. Such a behavior is also visible looking at the iso-surfaces for 0.4 ms ASOI; even cavitation maintains the inception at the inlet edge, its development remains close to the nozzle wall; indeed the iso-surface with 0.6 volume fraction, compared to the one of pre-injection, shows an “open” shape, whereas, to obtain the same shape of pre-injection it is necessary to display the volume fraction 0.9.

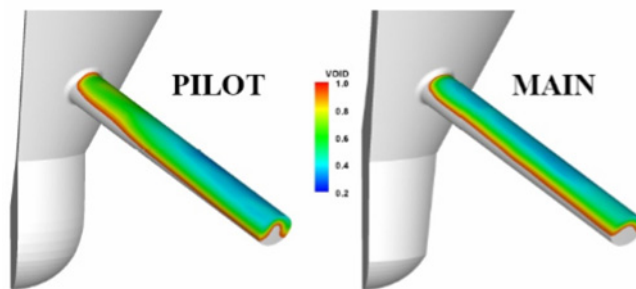


**Figure 5.11:** Void fraction distribution at mid-pilot and mid-main injection point for VCO nozzle [14]

Figure 5.11 shows a comparison of the void fraction distribution for pilot and main injection, as obtained in the detailed investigation of reference [14]; in such a case, the authors obtained visible differences in the cavitation regimes, so at lower needle lifts (pilot injections), cavitation structures seem to stretch towards the exit of the nozzle hole. Even if the injection conditions are not directly comparable and despite the different modeling approach presented in [14], the global trend of model reliability is tracked.

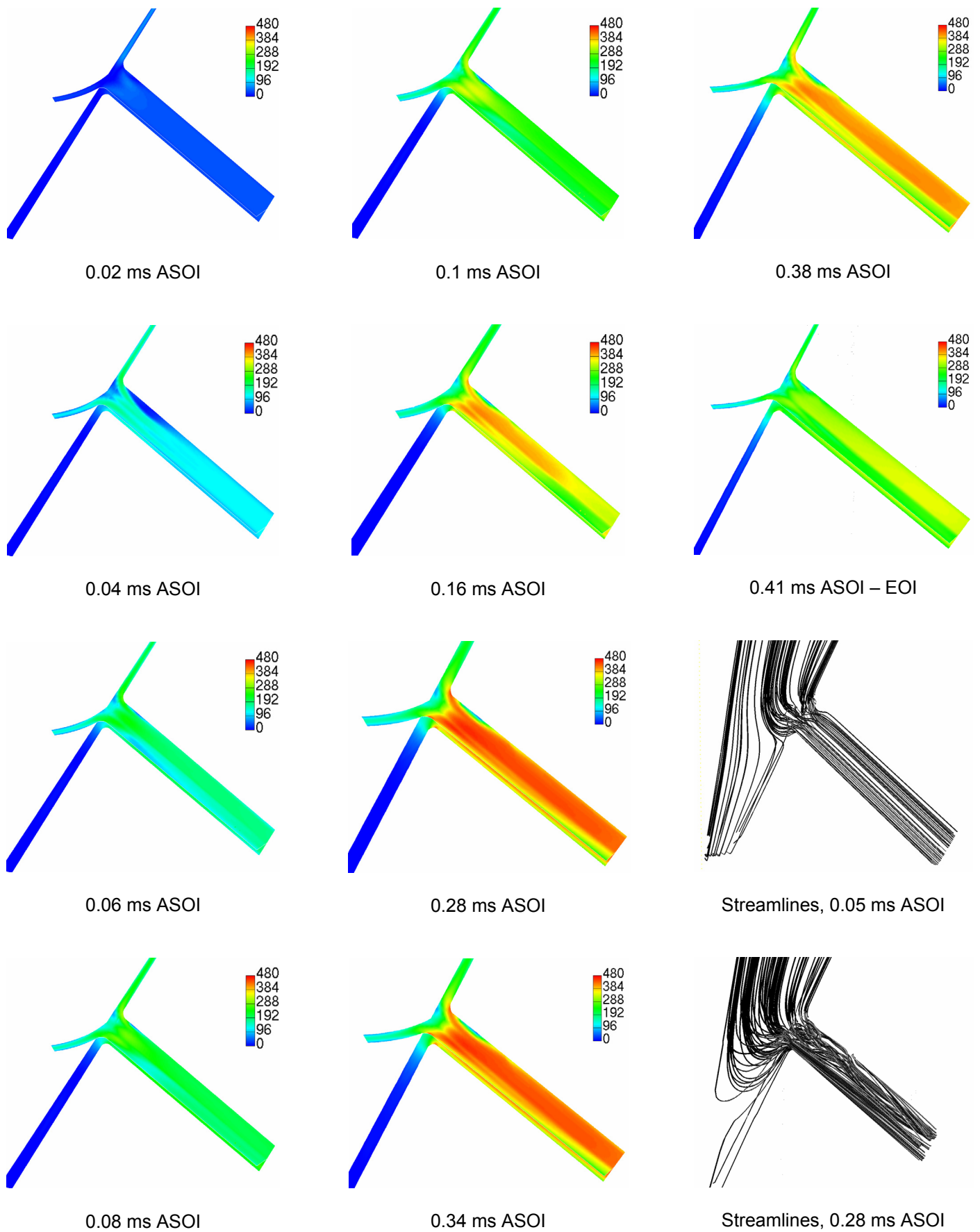


**Figure 5.12:** Pre-injection – Fuel scalar velocity [m/s]

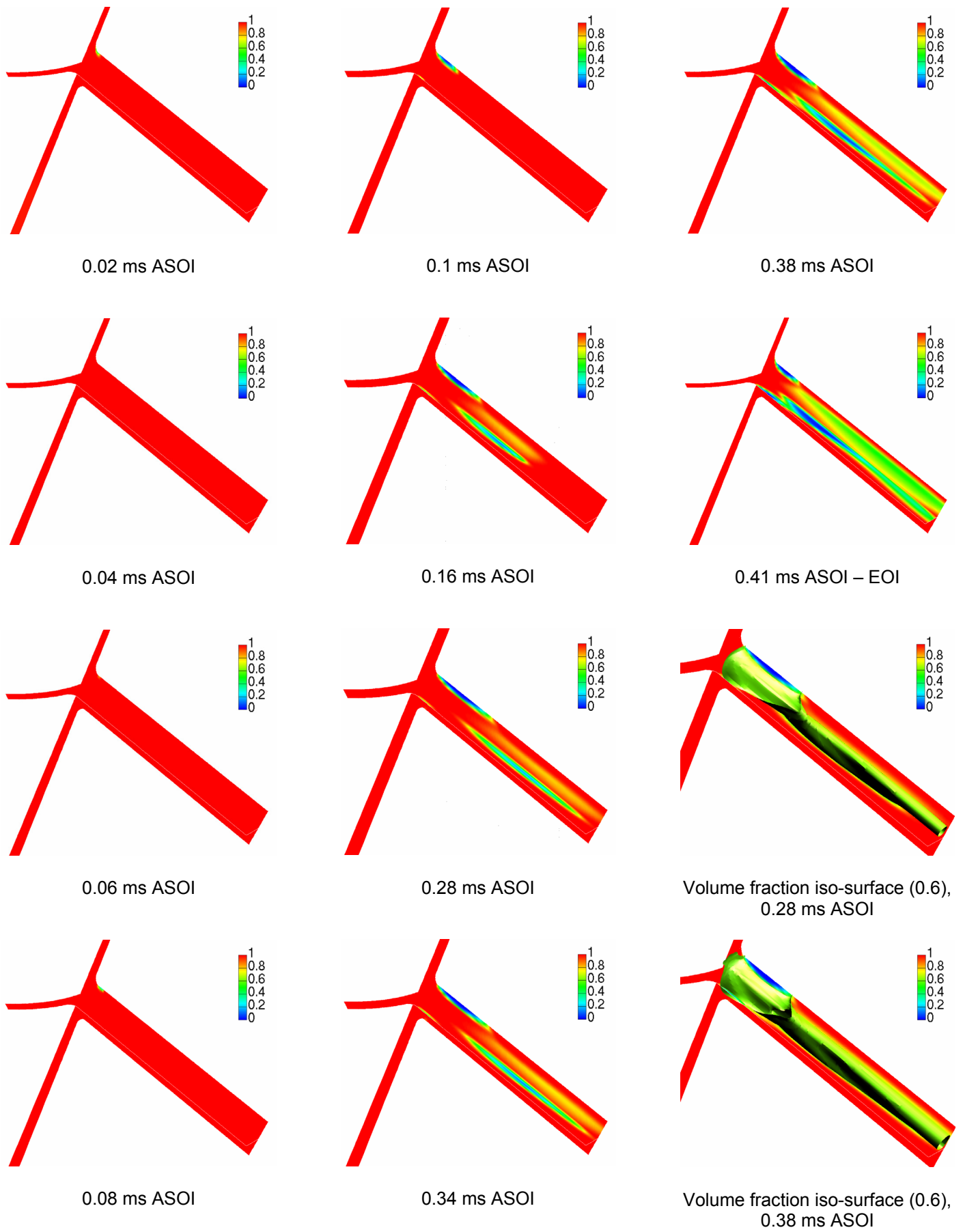


**Figure 5.13:** Pre-injection - Liquid vapor volume fraction [-]

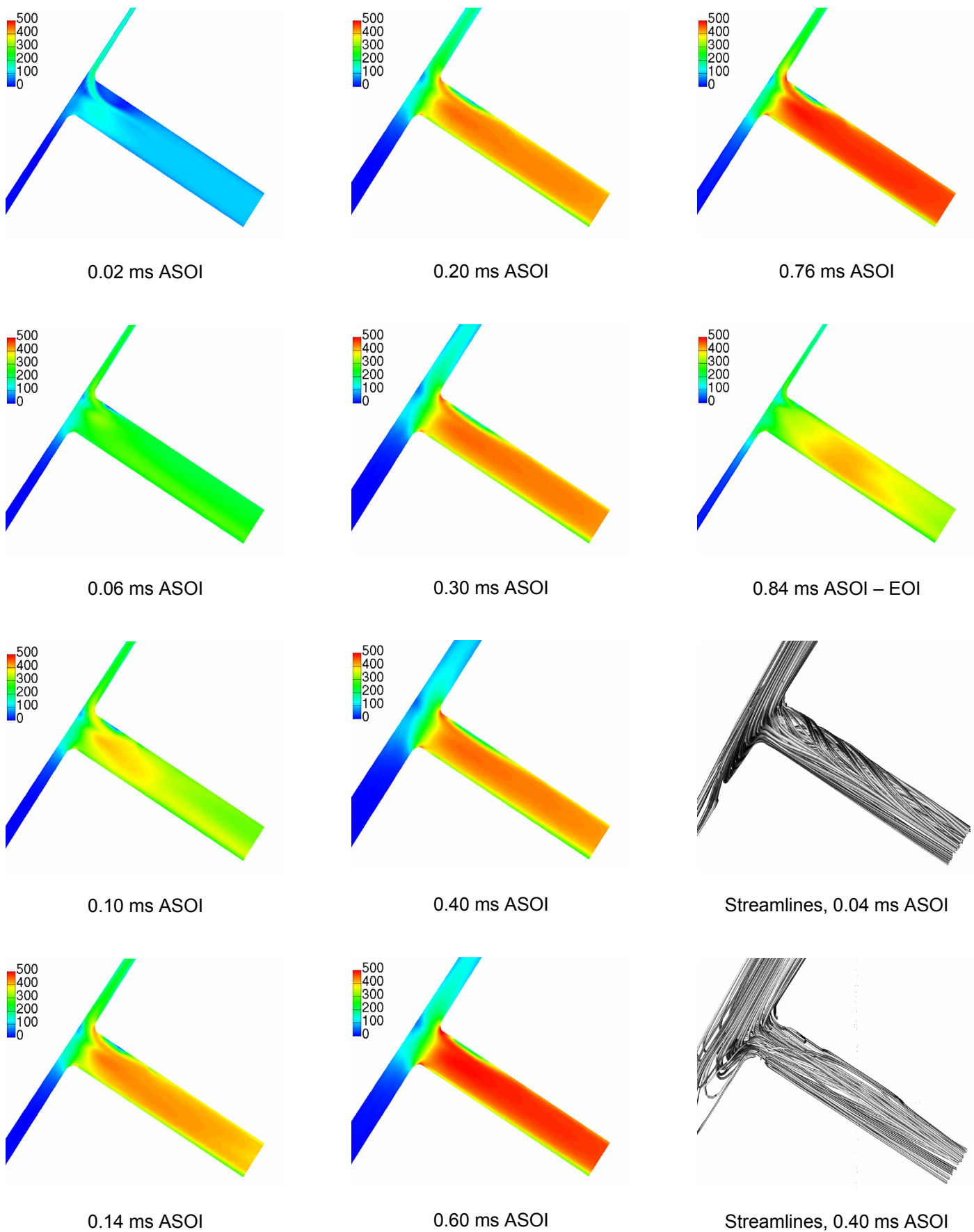


**Figure 5.14:** DT1, Main-injection – Fuel scalar velocity [m/s]

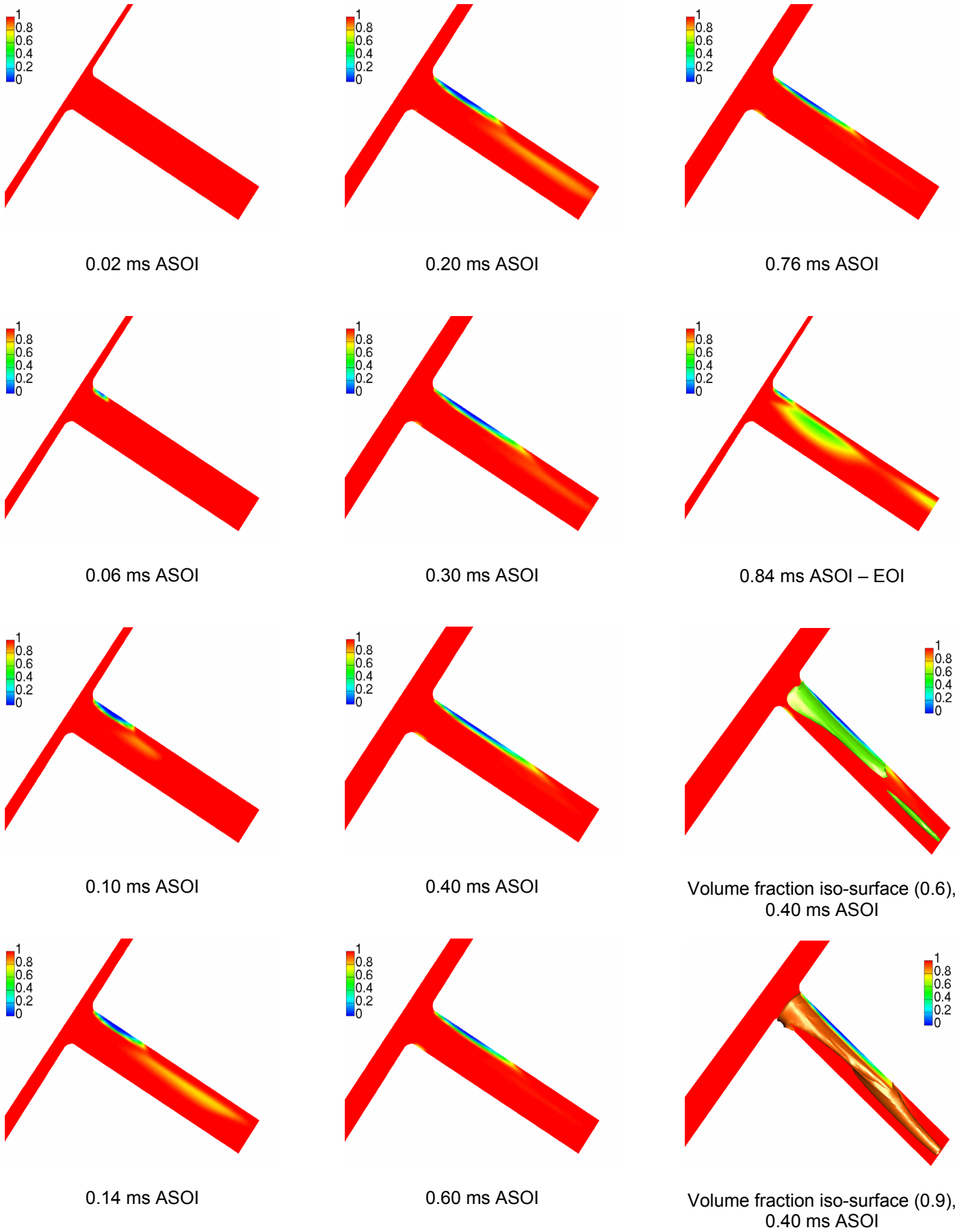


**Figure 5.15:** DT1, Main-injection - Liquid vapor volume fraction [-]

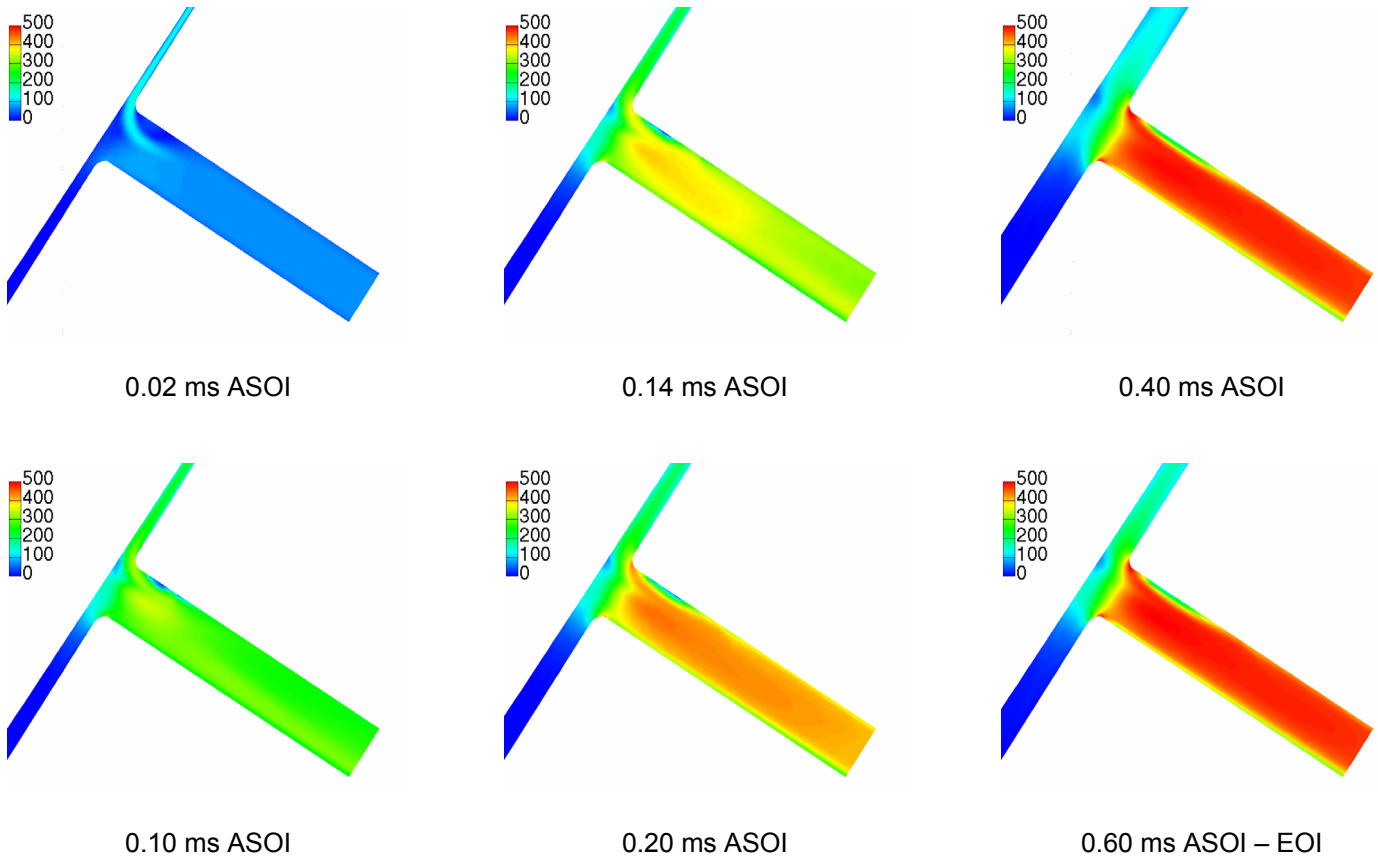


**Figure 5.16:** DT2, Main-injection – Fuel scalar velocity [m/s]

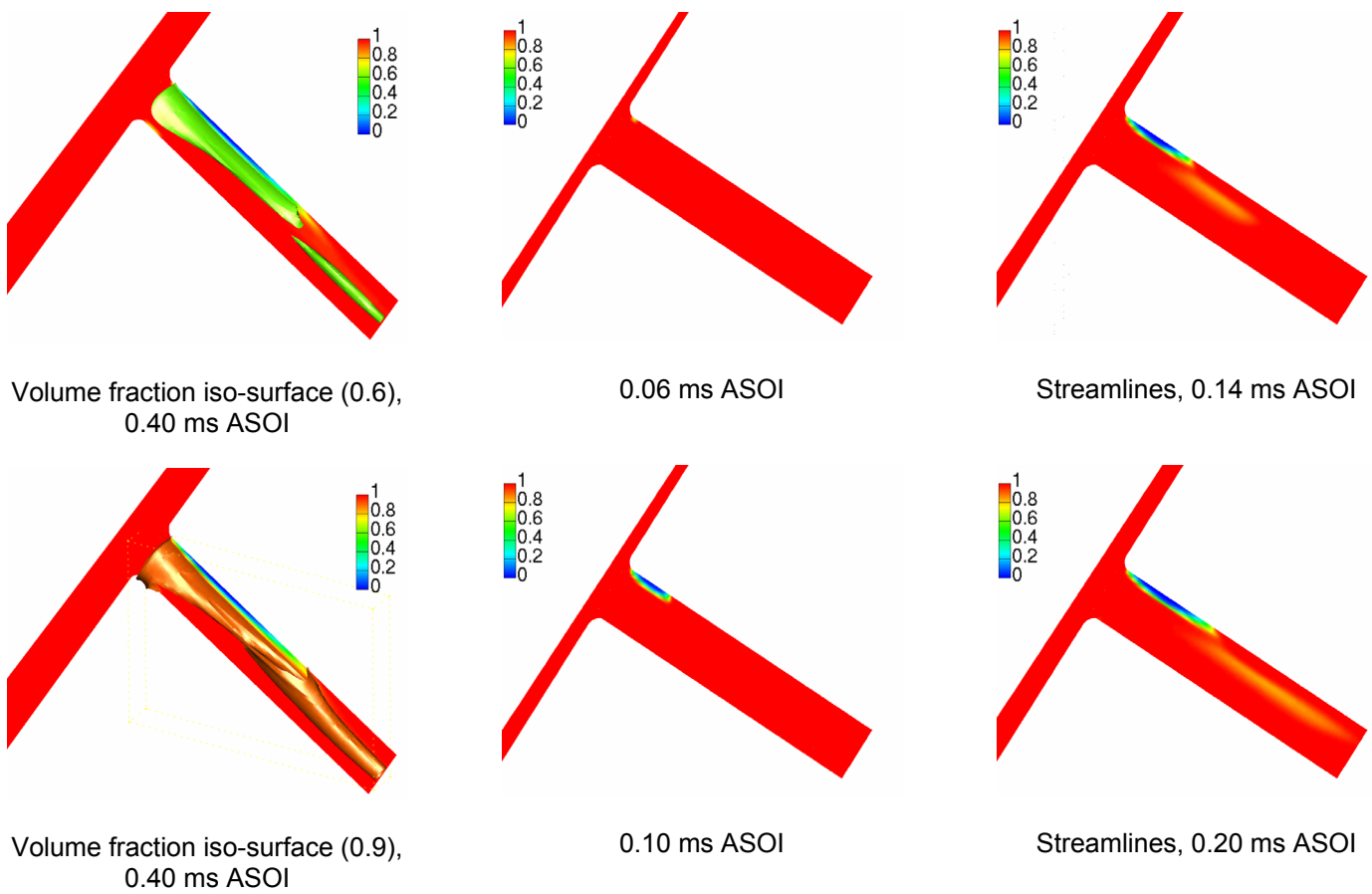


**Figure 5.17:** DT2, Main-injection – Left, iso-surfaces; Centre and Right, liquid vapor volume fraction [-]

Focusing the attention on the DT2 simulation (Fig.5.16), a relatively slower flow characterizes the initial phase of the injection, as the visualizations at 0.02 and 0.1 ms ASOI point out. As needle lift increases, flow field tends to be similar to the one of DT1. The different behavior of the opening phase influences the cavitation inception timing (Fig.5.17); in DT1 simulation the early vapor development is visible at 0.06 ms ASOI, whereas in this case vapor is not formed. At 0.2 ms ASOI the extension of vapor is almost the same of DT1 simulation. The central phase of injection shows negligible differences with the previous case, as the iso-surfaces at 0.40 ms ASOI highlight.

**5.4 Concluding remarks.** The operation characteristic of injection systems is certainly ordered by the design features of each component; these define the system size, the peculiarities of the performance, the operating pressure range and the fuel amount that can be handled. Beside the characterization of the system components, it has to be considered the aspect that comes from the interaction among the single elements; such effects assume particular relevance in the definition of the injection strategies, due to their highlighted influence on the flexibility. The interaction among the components is based on the role of the highly unsteady dynamics that characterize the pressure wave propagation through the fuel. By means of lumped/one dimensional tools, the modeling of these phenomena is possible and it can be useful in the injection strategies definition and development. Moreover, with a unitary point of view, the indications given by these models can be completed by 3-D investigations, in order to evaluate their influence on the nozzle flow features and, consequently, on the properties of the liquid jet that enters the combustion chamber. In this frame of reference, an integrated simulation, based on a multi-step procedure, is applied to model the multiple injection features of a common rail system. The first step of the simulation points out the influence of the pressure oscillation on a train of two consecutive injection shots; in detail, the effect generated by the pre-injection on the main event shows a relevant dependence on the dwell time. The 3-D investigation, performed in the second simulation step, shows its capability to help the analysis of two facets of injection strategy; on one hand, it offers the possibility of evaluating the differences between two consecutive injection events, concerning the fuel flow features and the behavior towards cavitation phenomena; on the other hand, the influence of the transient condition details, like the perturbation due to the dwell time width, can be modeled and considered. Appreciable deviations are found between pre and main shots, in terms of fuel flow field evolution and cavitation development. Differently, the comparison between the two main injection events highlights an overall similarity concerning the dynamic of the flows, suggesting a quantitatively similar influence on the subsequent atomisation process, in despite of the distinct injected fuel amount.

## 5.5 Nomenclature

$A_i''$	=	interfacial area density
$D_b$	=	bubble diameter



$C_{CR}$	=	condensation reduction factor
$C_D$	=	drag coefficient
$C_E$	=	Egler coefficient
$C_{TD}$	=	drag turbulent coefficient
$M_c$	=	vapor phase momentum
$M_d$	=	liquid phase momentum
$N_0'''$	=	initial bubble number density
$N'''$	=	number density
$R$	=	bubble radius
$Re_b$	=	bubble Reynolds number
SOI	=	Start Of Injection
$k_c$	=	vapor phase turbulence kinetic energy
$p_{sat}$	=	saturation pressure
$\mathbf{v}_c$	=	vapor velocity
$\mathbf{v}_d$	=	liquid phase velocity
$\mathbf{v}_r$	=	relative velocity

#### Greek symbols

$\Gamma_c$	=	vapor phase mass
$\Gamma_d$	=	liquid phase mass
$\Delta p$	=	pressure difference
$\alpha_d$	=	liquid phase volume fraction
$\rho_c$	=	vapor phase density
$\rho_d$	=	liquid phase density

**5.6 Appendix.** Figure 5.18 clarifies the position of the cut planes used to display the results in pre-injection. The pink plane contains both the injector axis and the nozzle axis.

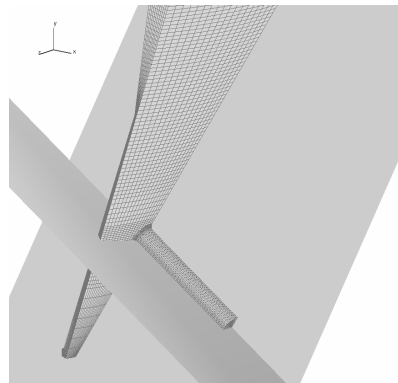


**Figure 5.18:** Cut planes used to display the nozzle results (green and pink)

## 5.7 References

- [1] Catania, A., Ferrari, A. and Spessa, E., "Numerical-Experimental Study and Solutions to Reduce the Dwell Time Threshold for Fusion-Free Consecutive Injections in a Multijet Solenoid-Type C.R. System", ICES2006 ASME Paper No. 1369.
- [2] Baratta, M., Catania, A. and Ferrari, A., "Hydraulic Circuit Design Keys to Remove the Dependence of the Injected Fuel Amount on Dwell Time in Multi-Jet C.R. Systems ", ICES2006 ASME Paper No. 1426.
- [3] Catania, A., Ferrari, A., Manno, M. and Spessa, E., "Experimental Investigation of Dynamics Effects on Multiple-Injection Common Rail System Performance", ICES2005 ASME Paper No. 1108.
- [4] Catania, A., Ferrari, A. and Manno, M., "Development and Application of a Complete Common-Rail Injection System Mathematical Model for Hydrodynamic Analysis and Diagnostics", ICES2005 ASME Paper No. 1018.
- [5] Mulemane, A., Han, J.S., Lu, P.H., Yoon, S.Y. and Lai, M.C., "Modelling Dynamic Behavior of Diesel Fuel Injection Systems", SAE Paper No. 2004-01-0536.
- [6] Wang, T.C., Han, J.S., Xie, X.B., Lai, M.C., Henein, N.A., Schwarz, E. and Bryzik, W., "Parametric Characterization of High-Pressure Diesel Fuel Injection Systems", J. Engineering in Gas Turbine & Power, 125, 412-426, 2003.
- [7] Chiavola, O. and Giulianelli, P., "Modeling and Simulation of Common-Rail Systems", SAE Paper No. 2001-01-3183.
- [8] Roth, H., Gavaises, M. and Arcoumanis, C., "Cavitation Initiation, Its Development and Link with Flow Turbulence in Diesel Injector Nozzles", SAE Paper No. 2002-01-0214.
- [9] Arcoumanis, C., Flora, H., Gavaises, M. and Kampanis, N., "Investigation of Cavitation in a Vertical Multi-Hole Injector", SAE Paper No. 1999-01-0524.
- [10] Gavaises, M. and Andriotis, A., "Cavitation Inside Multi-hole Injectors for Large Diesel Engines and Its Effects on the Near-nozzle Spray Structure", SAE Paper No. 2006-01-1114.
- [11] Fezzaa, K., Lee, W.K., Cheong, S., Powell, C.F., Wang, J., Li, M. and Lai, M.C., "High Pressure Diesel Injection Studied by Time-Resolved X-Ray Phase Contrast Imaging", ICES2006 ASME Paper No. 1409.
- [12] Han, J.S., Lu, P.H., Xie, X.B., Lai, M.C. and Henein, N.A., "Investigation of Diesel Spray Primary Breakup and Development for Different Nozzle Geometries", SAE Paper No. 2002-01-2775
- [13] Tatschl, R., v. Künsberg-Sarre, C., Alajbegovic, A. and Winklhofer, E., "Diesel Spray Modeling Including Multidimensional Cavitation Nozzle Flow Effects", Proc. of ILASS Europe Conference, Sept. 11-13, Darmstadt, Germany, 2000.
- [14] Giannadakis, E., "Modelling of Cavitation in Automotive Fuel Injector Nozzles", PhD thesis, Imperial College London, UK 2006.
- [15] Chiavola, O. and Palmieri, F., "Coupling Codes for Nozzle Flow Modeling in Diesel Injection Systems", ICES2006 ASME Paper No. 1414.
- [16] Chiavola, O., Palmieri, F. and Chiatti, G., "Integrated Modeling of Fuel Influence on Common Rail Injection System Performance", ICEF2006 ASME Paper No. 1556.
- [17] Chiavola, O. and Palmieri, F., "Modeling Needle Motion Influence on Nozzle Flow in High Pressure Injection System", SAE Paper No. 2007-01-0250.
- [18] Imagine AMESim v4.2 Tutorial and User Guide, AMESim Technical Bulletins.
- [19] FIRE v8.4 CFDWM Guide, AVL List GmbH.
- [20] Zielke W., "Frequency-dependent friction in transient pipe flow", Trans. ASME J. Basic Engng, 90, 109-115, 1968.

- [21] K. Samada, C.W. Richards, et al., "A finite element model of hydraulic pipelines using an optimized interlacing grid system", ImechE, 1993.
- [22] FIRE v8.4 Multiphase Manual, AVL List GmBH.
- [23] Hinze, J.O., "Turbulence", 2<sup>nd</sup> ed., McGraw-Hill, New York, 1975.
- [24] Franklin, R.E. and McMillan, J., "Noise Generation in Cavitating Flows", J. Fluids Eng., 106, 336-341, 1984.

## 6. Diesel VCO Injector: Geometric Layout and Operating Condition influence. Nozzle Flow Modeling and 3D in-Cylinder Simulation

**6.1 Injection system.** The model of the injection system is built in AMESim environment and it is referred to a second generation common rail layout, that consists of high pressure reciprocating pump, relief valve, pipelines, high pressure rail and solenoid type injectors.

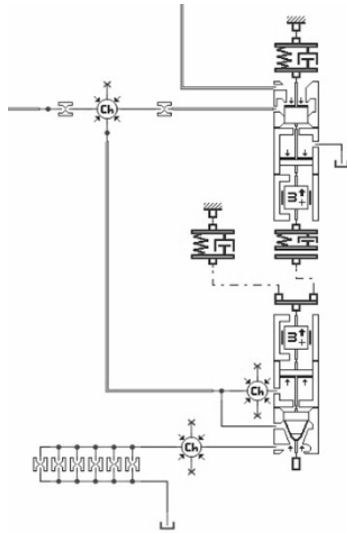


**Figure 6.1:** Needle and plunger model

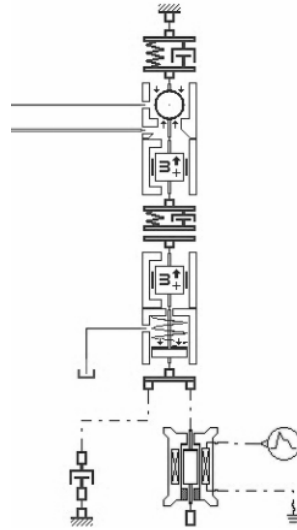


**Figure 6.2:** Pilot valve model

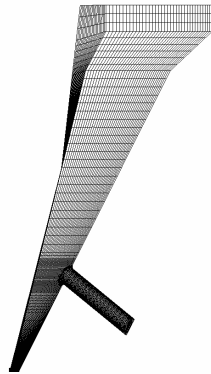
*Electromagnetic Circuit Model.* The electromagnetic force acting on the anchor is represented by means of a solenoid circuit model available in AMESim library.

*Mechanical Model.* A detailed injector mechanical model is built on the basis of the AMESim libraries; Figure 6.1, shows the coupled schemes of the needle and the control plunger. Figure 6.2 shows the scheme of the pilot valve; as visible, it is made of two units, the pin and the so called anchor, whose swing motion in respect to the pin is allowed, when it reaches the displacement limit.

*Thermo Fluid Dynamic Model.* The hydraulic network of the system is made of chamber volumes and pipe elements. Concerning the volumes, pressure and temperature are just time dependent, according to the lumped parameter model. On the other hand, the used pipeline model follows a one-dimensional approach, based on wave equation solution and it is able to take into account compressibility, inertia and friction effects in which a frequency dependent function is included [21,22].

The injection control signal is imposed in term of voltage time trace to the solenoid coil and it is characterized by an ET of 1085 microseconds.

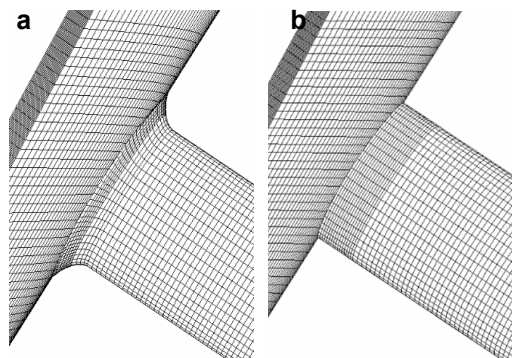
**6.2 Injector geometry and configuration.** The 3D calculations are performed with the aim of evaluating the influence of the injector features on the development of two phase cavitating flows. The considered geometry represents a VCO type injector; the computation grid is obtained by connecting two elemental meshes, the former one is the needle grid, with polar symmetry, the latter one is the nozzle hole mesh (Fig.6.3).



**Figure 6.3:** VCO injector mesh

The needle lift is simulated by means of a mesh set generation. The time dependent displacement is obtained as a data file (Fig.6.12) coming from the injection system simulation (in AMESim environment) and then it is imposed to the meshes. The boundary condition at the mesh inlet surface, namely the fuel pressure time trace, comes from the AMESim simulation, too (Fig.6.10).

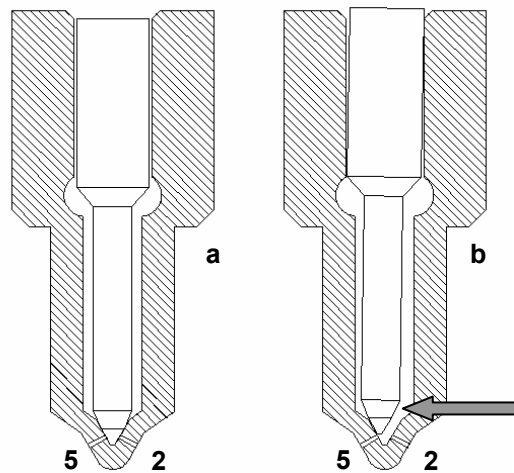
In order to explore the effects of the hole geometry on the nozzle flow, two different meshes are adopted for the simulations; Figure 6.4 shows the details of the two considered geometries, in which a rounded off inlet edge (in accordance to the hydro-grinding processes) is compared to a sharp edge hole.



**Figure 6.4:** VCO injector mesh: **a**, rounded inlet; **b**, sharp inlet

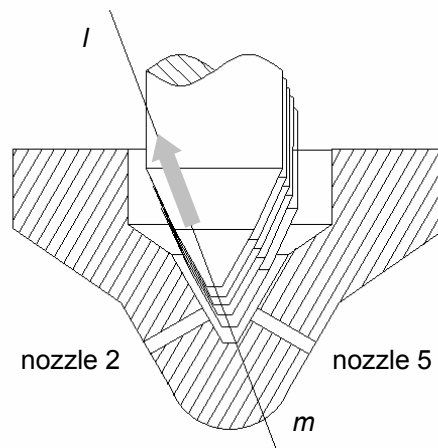
The needle lift is simulated by means of a mesh set generation. The time dependent displacement is obtained as a data file (Fig.6.12) coming from the injection system simulation (in AMESim environment) and then it is imposed to the meshes. The boundary condition at the mesh inlet surface, namely the fuel pressure time trace, comes from the AMESim simulation, too (Fig. 6.10).

A second investigation is devoted to the evaluation of the influence that needle eccentricity can exert on the hole to hole flow rate deviations. As a clearance characterizes the diameter of the cylindrical needle guide in respect to needle diameter, the radial displacement of the needle tip allowed by the clearance is evaluated, as Fig. 6.5 shows.



**Figure 6.5:** Needle configuration schemes: **a**, closing position; **b**, full lift position

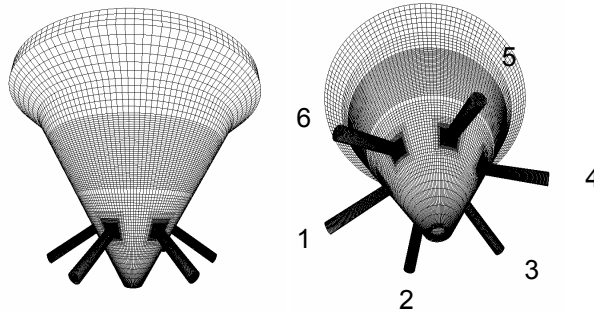
The displacement of the needle is imposed along a deviated direction, so that the calculated maximum radial displacement is reached at full lift.



**Figure 6.6:** Needle displacement scheme; *l-m* is the displacement direction

The needle lift time trace coming from AMESim model is imposed to the needle surface of the computational grid along the straight line in the plane that cuts in half nozzles n.2 and n.5 (such a direction is identified by the trace *l-m* in Fig.6.6). As can be argued by the given description, the evaluation of the radial displacement is based on the rotation allowed by the cylindrical constraint of the needle: taking into account that the entity of the angular displacement is very small, the movement of the needle tip is assumed to be regarded as a simple translation. The radial displacement at maximum needle lift is in the order of 0.04 mm.

Figure 6.7 shows the computational mesh used to simulate the eccentric needle displacement; it is derived from the rounded inlet single hole mesh; it is made of 643464 cells.



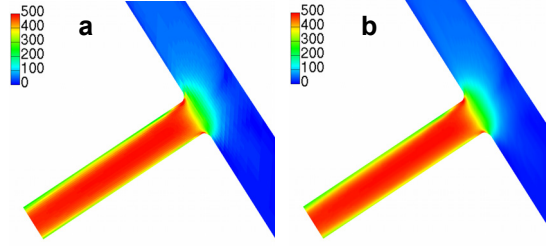
**Figure 6.7:** Injector mesh: left, front view; right, bottom view; injector holes are numbered from 1 to 6

Table 6.1 resumes the injector geometrical features.

injector nozzle diameter [m]	$0.14 \cdot 10^{-3}$
injector nozzle length [m]	$0.7 \cdot 10^{-3}$
needle length [m]	$40 \cdot 10^{-3}$
needle cylindrical guide length [m]	$12 \cdot 10^{-3}$
number of nozzles	6

**Table 6.1:**Injector features

The preliminary phase of the computation is aimed to identify an adequate cell dimension that guarantees the independence of the obtained flow fields on the adopted mesh. Figure 6.8 shows the comparison between the velocity maps obtained with mesh 'a' (98500 cells) and mesh 'b' (590000 cells). In the calculation, diesel fuel at the injection pressure of 105 MPa and the maximum value of needle lift are imposed. The most refined mesh is not selected, due to the non-substantial differences between the obtained flow conditions, allowing a reduction of the computational effort.



**Figure 6.8:** Scalar velocity [m/s]; a, mesh 'a'; b, mesh 'b'

**6.3 Spray and chamber flow simulation.** FIRE environment provides all the submodels used to perform the in-chamber simulations [26]; the spray calculation is based on the Discrete Droplet Method in the frame of a RANS  $k$ - $\varepsilon$  solution. In the following, a description of the models is presented.

*Primary break-up: nozzle flow interface and diesel blob injection integration.* Series of large blobs represent the liquid jet introduced in the cylinder volume. A primary break-up model is used to calculate the mass detachment rate that reduces the diameter of the blobs. Such a model is based on the evaluation of the competing effects of three different atomization mechanisms, namely the aerodynamic, cavitation and turbulent induced break-up processes [14] and it needs the 'nozzle interface' data file.

The calculation of the aerodynamic break-up rate is based on the WAVE model [27,28], where a characteristic droplet radius and a break-up time are chosen,  $r_A$  and  $\tau_A$  respectively. Eq. 13 is used to evaluate the bubble radius time evolution, where the symbol  $r$  denotes the actual droplet radius.

$$\frac{dR}{dt} = \frac{r - C_1 r_A}{C_2 \tau_A} \quad (13)$$

The constants  $C_1$  and  $C_2$  are used to adjust the break-up time and the characteristic droplet radius.

The evaluation of the turbulent break-up is based on equation (14), in which the turbulent length scale  $r_T$  (15) and the turbulent time scale  $\tau_T$  (16) appear.

$$\frac{dR}{dt} = \frac{r - C_3 r_T}{C_4 \tau_T} \quad (14)$$

$$r_T = C_\mu^{0.75} \frac{k^{1.5}}{\varepsilon} \quad (15)$$



$$\tau_T = C_\mu \frac{k}{\varepsilon} \quad (16)$$

The product droplets are generated within this model and their velocity is combined with the additional radial velocity taken from aerodynamic and turbulent break-up mechanisms; it has to be pointed out that such a model feature makes the calculation of the spray angle from the atomization physics possible.

The effect of the collapsing bubbles on the primary break-up is taken into account by means of the presence of source terms in the turbulence model. During the computation, the turbulence and cavitation induced break-up competes with the aerodynamic one until the aerodynamic process becomes dominant. The considered turbulence equations for the liquid fuel core are (17,18):

$$\frac{dk}{dt} = -\varepsilon + S_k \quad (17)$$

$$\frac{d\varepsilon}{dt} = -C \cdot \frac{\varepsilon}{k} \cdot (\varepsilon - S_k) \quad (18)$$

where  $k$  is the turbulence kinetic energy,  $\varepsilon$  the dissipation rate,  $C$  a model constant and  $S_k$  the cavitation source term. The Rayleigh-Plesset equation (19), describes the bubble radius and its rate evolution:

$$\frac{p_b(t) - p_\infty(t)}{\rho_2} = R \cdot \frac{d^2 R}{dt^2} + \frac{3}{2} \left( \frac{dR}{dt} \right)^2 + \frac{4 \cdot \nu_2}{R} \cdot \frac{dR}{dt} + \frac{2 \cdot \sigma}{\rho_2 \cdot R} \quad (19)$$

where  $p_b$  is the pressure in the bubble,  $p_\infty$  the environment pressure,  $\rho_2$  the liquid density,  $\nu_2$  the cinematic viscosity of the liquid and  $\sigma$  the surface tension. Equation (20) is used to derive the velocity  $v$  surrounding the bubble at position  $R_L$ :

$$v(R_L) = \left( \frac{R}{R_L} \right)^2 \cdot \dot{R} \quad (20)$$

The total kinetic energy of the liquid around the bubble can be expressed as (21):

$$\begin{aligned} E_k &= \frac{m \cdot v^2}{2} = \\ &= \frac{1}{2} \cdot \int_{R_L=R}^{R_L=\infty} \left( \frac{R}{R_L} \right)^4 \cdot \dot{R}^2 \cdot 4 \cdot \pi \cdot \rho_2 \cdot R_L^2 \cdot dR_L = 2\pi \rho_2 \cdot R^3 \cdot \dot{R}^2 \end{aligned} \quad (21)$$

The disturbance caused by the collapsing bubbles is assumed to be proportional to the change of the kinetic energy in  $S_k$  source term (22):

$$S_k = C_B \cdot \frac{dE_K}{dt} \cdot \frac{n_L}{m_L} \quad (22)$$

where  $C_B$  is a model constant,  $m_L$  is the liquid mass of the ligament and  $n_L$  is the number of bubbles in the ligament. The presented model implies the use of boundary conditions obtained from the results of the two-phase nozzle flow calculation. The nozzle flow results contains the values of local fuel velocity, turbulence intensity and fuel vapor mass fraction at the nozzle exit. The injected blobs have the same diameter of the nozzle orifice; their position is randomly chosen within the exit orifice area and each particle gets the data of the nearest cell face. The number of blobs introduced per time step is adjusted by the model in order to fit the flow rate time trace. The primary break-up model is activated together with a separate secondary break-up and they act in sequence on the parcels, governed by a switching criterion based on Weber number. The change from primary to secondary break-up must satisfy the check on Weber number (500 is the threshold) and the checks on stable or minimum diameter.

*Secondary breakup.* WAVE model is used to simulate the droplet secondary break-up process. It assumes that the growth of an initial perturbation on a liquid surface is linked to its wavelength and to other physical and dynamic parameters of the injected fuel and the fluid domain.

*Turbulent dispersion model.* The model presented by O'Rourke [29] is adopted, in order to take the interaction between the particles and the turbulent eddies into account.

*Particle interaction model.* The model based on the statistical approach proposed by O'Rourke [30] is adopted.

*Wall interaction model.* Walljet2 model, based on the work of Naber and Reitz [31], is considered.

*Evaporation model.* The model originally derived by Dukowicz [32] is used to represent the heat and mass transfer processes.

The simulation is performed in the crank angle domain 140 CABTDC - 120 CAATDC. Figure 6.9 shows a view of the engine computational mesh at TDC

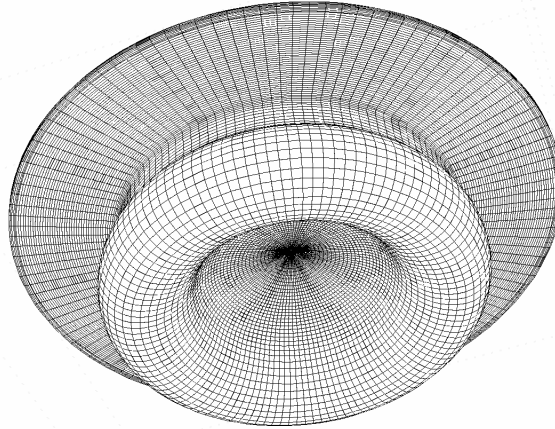


**Figure 6.9:** Bottom view of engine mesh at TDC

In order to reduce the calculation grid dependency, the necessary computation measures are taken, as suggested in spray simulation problems [33].

**6.4 Results.** The considered diesel engine is a supercharged four cylinder unit, whose features and operating conditions are listed in Tab.6.2.

bore x stroke [m]	0.083 x 0.0978
compression ratio	16:1
fuel injection system	HPCR
engine speed [rpm]	1500
start of injection CABTDC	5
nominal rail pressure [MPa]	100
high pressure pump displ.nt [m <sup>3</sup> ]	$0.65 \cdot 10^{-6}$
rail volume [m <sup>3</sup> ]	$2 \cdot 10^{-5}$
energizing time [s]	$1.085 \cdot 10^{-3}$
fuel injected mass [kg]	$5.6 \cdot 10^{-5}$

**Table 6.2:** Engine features and operating conditions

**6.4.1 Injection System.** Figures 6.10-12 show the common rail injection system performance, obtained for a nominal rail pressure of 100 MPa and an energizing time of 1.085 ms. The diagram of Fig.6.10 reports the pressure time history in the needle drift chamber; the initial value of about 950 kPa, lower than the nominal rail pressure of 1000 kPa, is due to the depression event that happens in the needle control valve as the electro-actuated pilot valve opens (a red line highlights the start of the needle lift). The pressure time trace is then characterized by an oscillating behavior that is the result of the complex interaction among needle lift effects, control volumes modifications due to the influence surface displacements and pressure waves travelling through the pipelines.

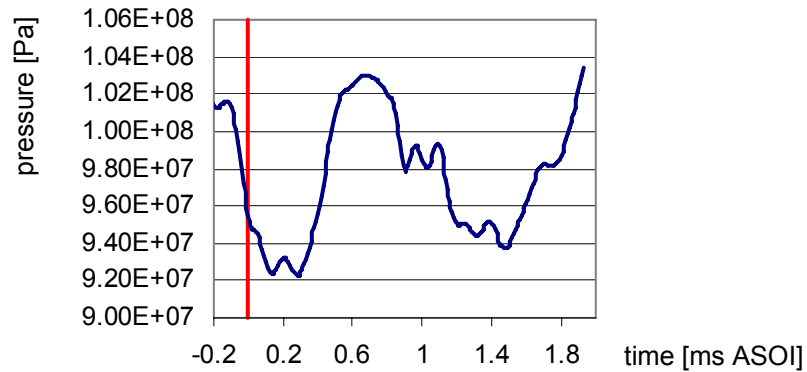


**Figure 6.10:** Pressure time trace at injector inlet; red line indicates the lift start

The pressure time trace is imposed to the 3D computation grids in order to perform the aforementioned coupling between the codes. Figure 6.11 shows the comparison between the nozzle flow mean velocity (evaluated by means of the orifice lumped model) and the nozzle flow mean velocity at the hole exit coming from the 3-D model in FIRE environment (the 3-D simulation is referred to the rounded edge hole mesh). The shape agreement between the curves is an indication of the consistency of the coupling. It has to be noted that the origin of the graph indicates the beginning of the 3-D simulation, in which the flow rate value cannot be equal to zero.

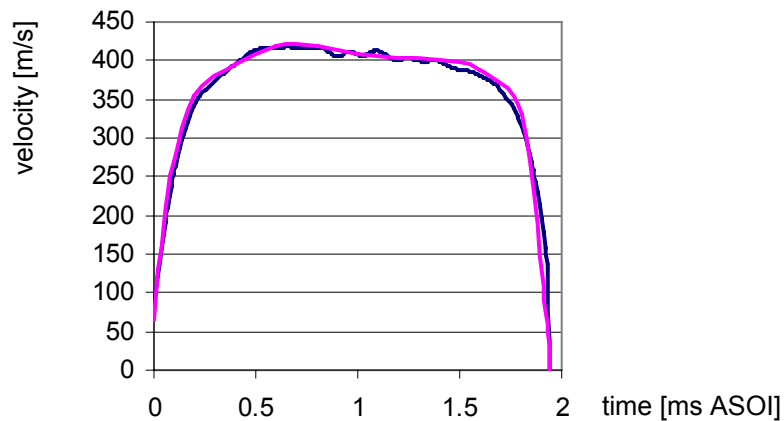


**Figure 6.11:** Nozzle mean velocity: 0/1-D model —; 3-D model —

The temporal extension of the injection phase comes through the energizing time, due to the different needle response in respect to the current rise-drop.

In Fig.6.12 two needle lift traces are visible; blue line is the lift coming from the injection system model: it reaches the value of 0.43 mm at full opening. As the 3-D simulation with completely closed injector is meaningless, a minimum lift position is established, and in the present case it is 10  $\mu\text{m}$ . Such a value is subtracted to the lift

trace that is used for the moving mesh generation (violet line), to take into account the initial minimum displacement.

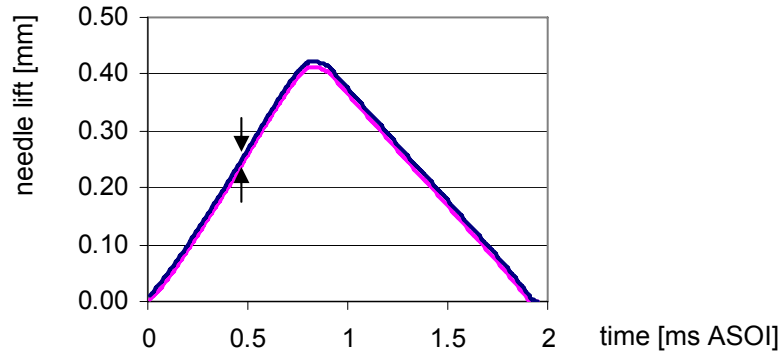


**Figure 6.12:** Needle lift trace —, needle lift trace used to generate the moving mesh set — (10 $\mu$ m shift)

**6.4.2. Nozzle Flow.** The flow regimes that characterize the injection process are evaluated in terms of flow velocity and vapor region observation. The first series of results concerns the rounded edge hole (Figs. 6.13-14); as described above, they are referred to the injection pressure of Fig. 6.10. The outcome of a further investigation on a sharp edge hole is shown in Figs. 6.15 and 6.16; such results are obtained with the same boundary conditions of the previous case, in order to evaluate the role of the geometry details on the flow development. Finally, an evaluation of the needle eccentricity influence on the process is outlined.

The image sequence of Fig. 6.13 shows the flow behavior on the mid-cut surface that contains the nozzle axis. The edge geometry is responsible of a relatively low velocity gradient at the inlet of the hole; more in detail, the fuel feeds the hole with a similar behavior both from up-to-down and down-to-up directions; this condition becomes evident looking at the volume fraction results (Fig. 6.14). As suggested by the maps, the cavitating areas tends to remain close to the hole surface, bounded in the peripheral zone of the nozzle; nonetheless, the needle lift influences the cavitation development: in the central phases of injection both the inlet corners play the role of inception point on the mid-cut plane; on the contrary, in the opening and closing phases, a single inception point characterizes the flow, due to the (weak) prevalence of the up-to-down current at the hole inlet. In the volume fraction maps related to low lift conditions (opening and closing), the presence of a vapor region is highlighted, whose inception is not related to the aforementioned corners; these zones, in which the liquid fraction is relatively high (in the range of 0.6 – 1), reveal that the inception of the cavitation is located along the hole edge and it tends to involve a relatively wide portion of the nozzle inlet; hence, in Figs 6.17 and 18, the results (referred to the closing phase, at 1.8 ms ASOI) are displayed on a plane that cuts the inlet edge and highlights the position of the cavitation inception region.

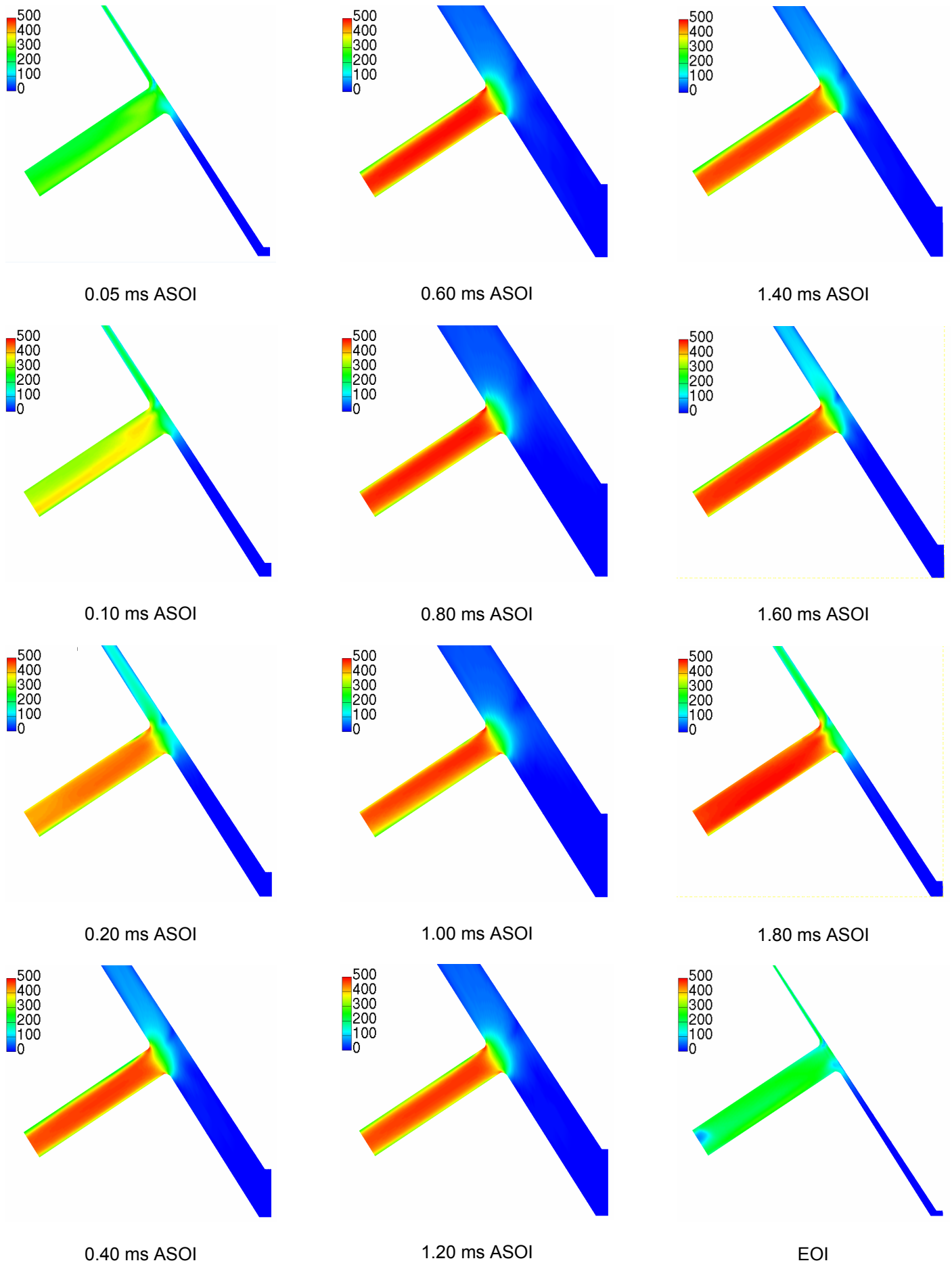


**Figure 6.13:** Fuel scalar velocity for rounded edge hole [m/s]

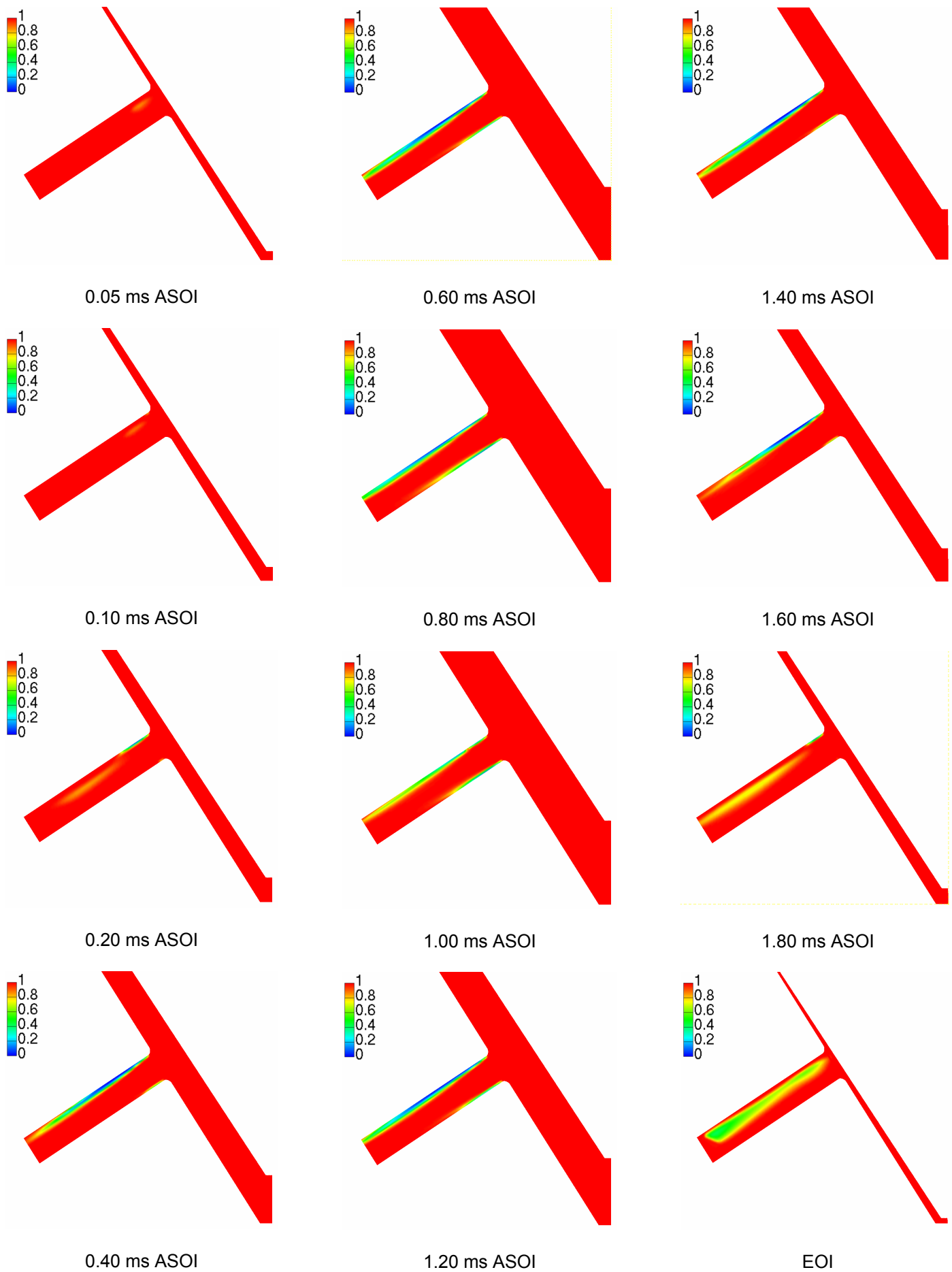


**Figure 6.14:** Liquid vapor volume fraction for rounded edge hole

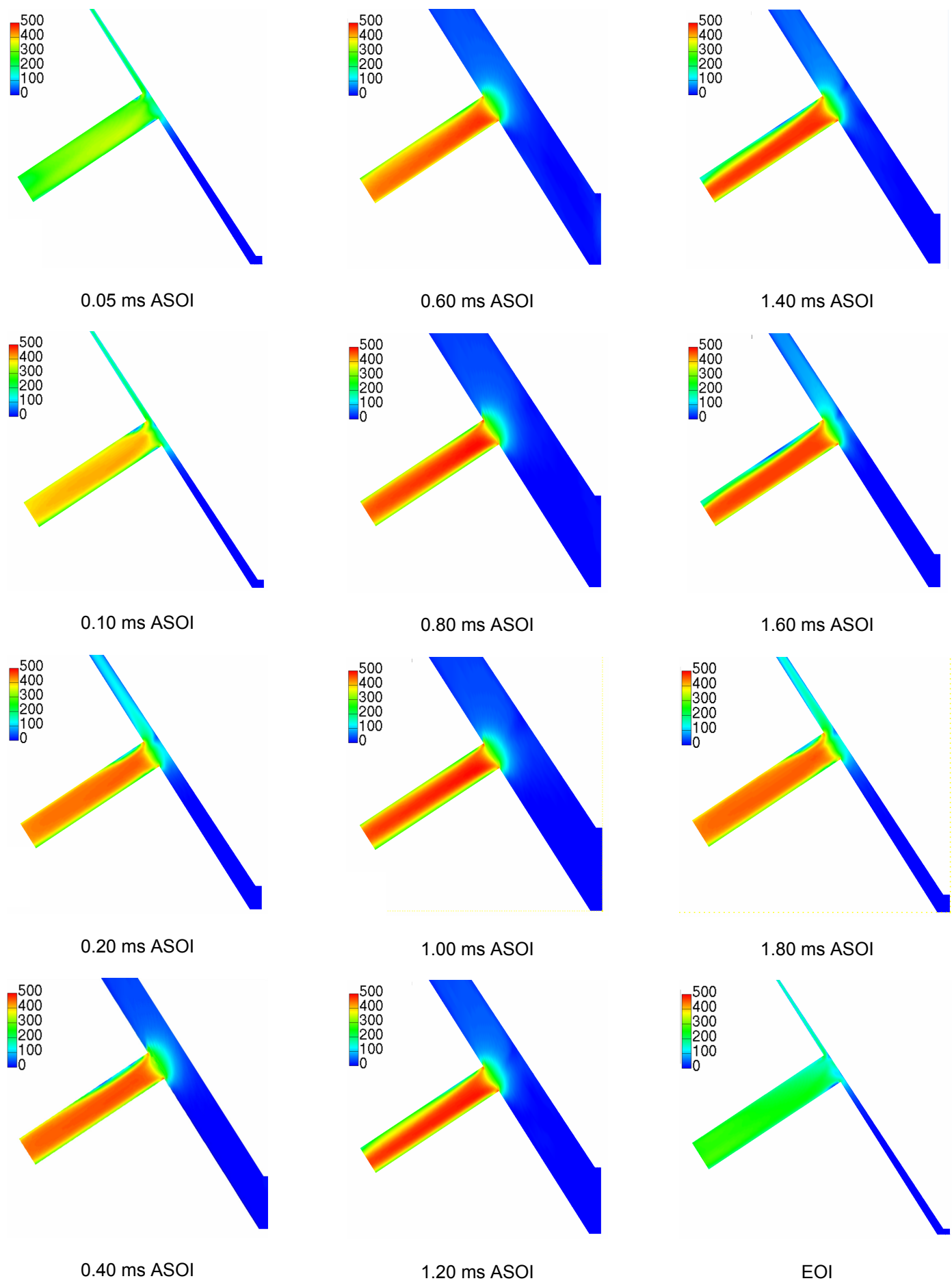


**Figure 6.15:** Fuel scalar velocity for sharp edge hole [m/s]



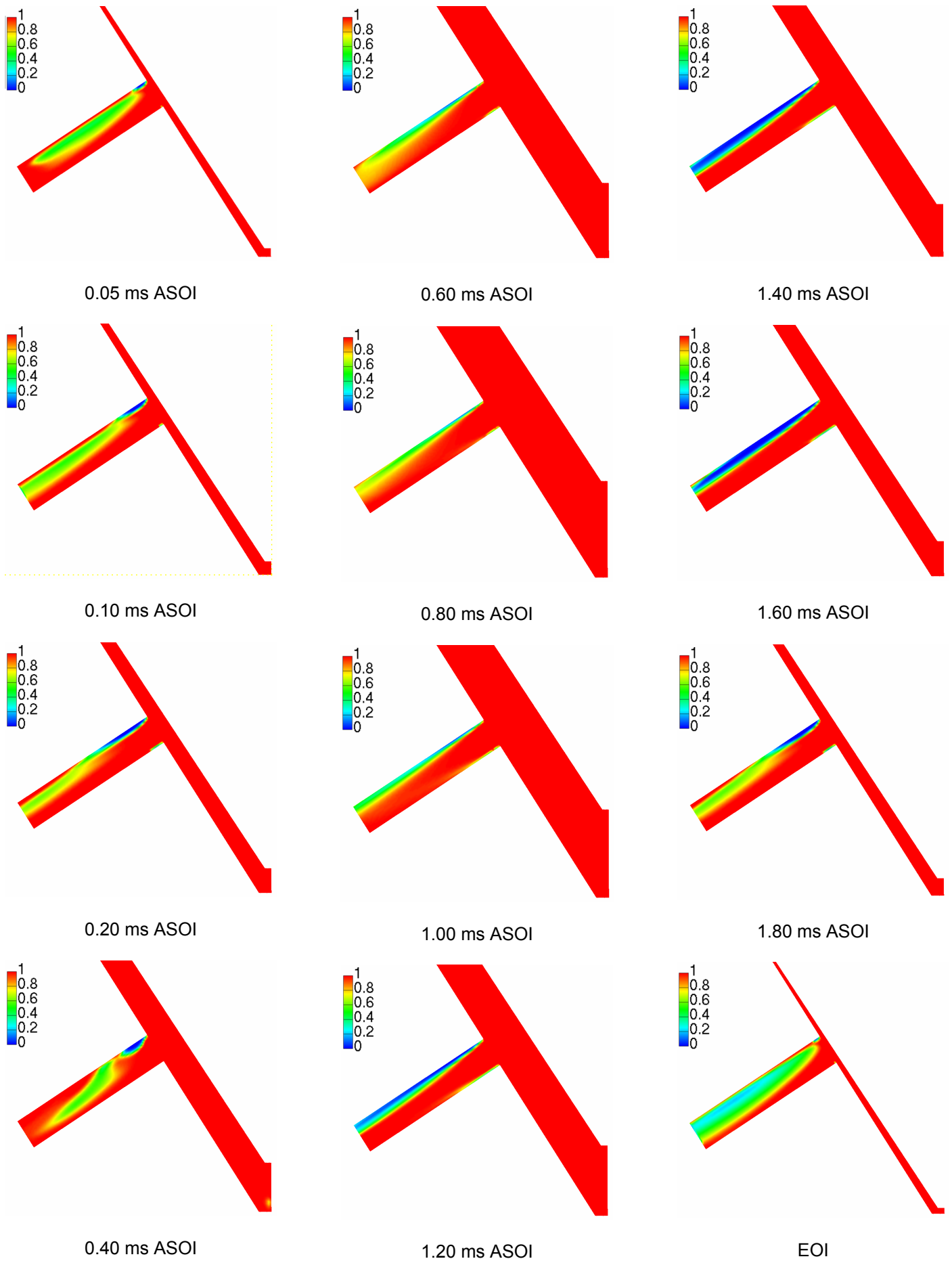


**Figure 6.16:** Liquid vapor volume fraction for sharp edge hole

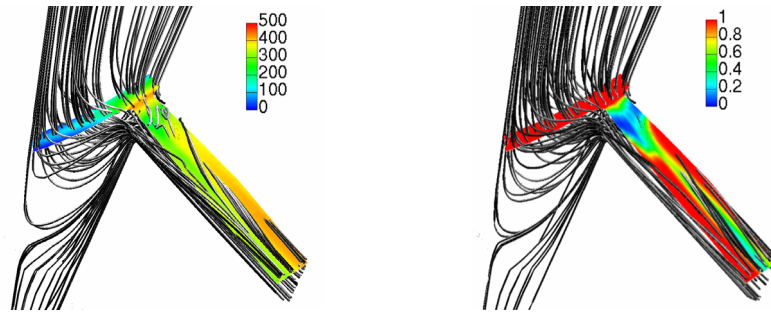


**Figure 6.17 (left):** Streamlines and velocity for rounded edge hole [m/s], 1.8 ms ASOI

**Figure 6.18 (right):** Streamlines and volume fraction for rounded edge hole; 1.8 ms ASOI

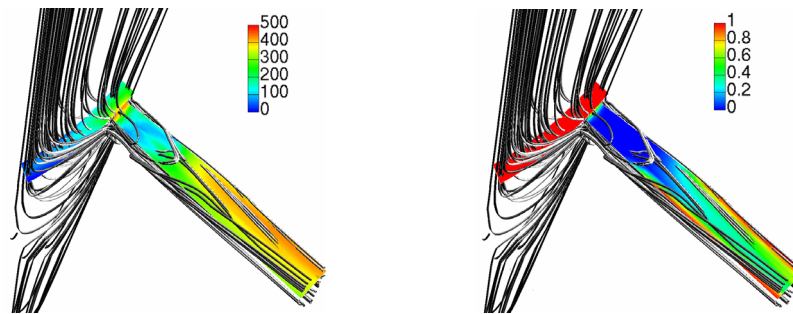


**Figure 6.19 (left):** Streamlines and velocity for sharp edge hole [m/s]; 1.8 ms ASOI

**Figure 6.20 (right):** Streamlines and volume fraction for sharp edge hole; 1.8 ms ASOI

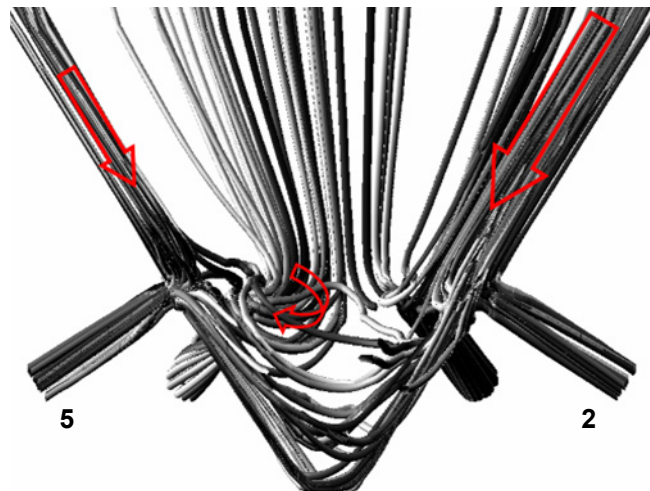


**Figure 6.21:** Flow streamlines, 1 ms ASOI

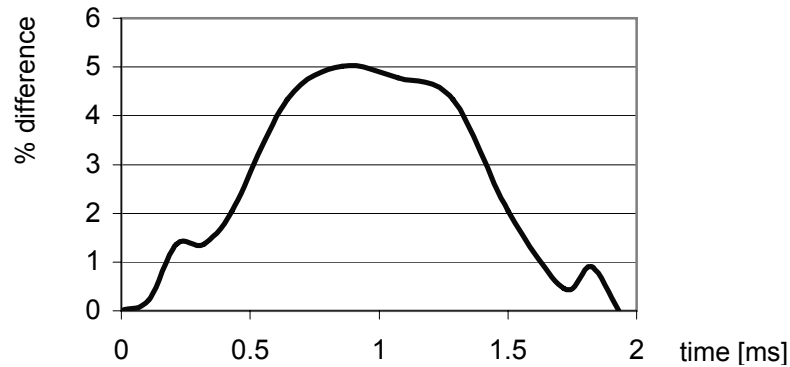


**Figure 6.22:** % nozzle mean outlet velocity difference between nozzles 2 and 5

Due to the helicoidal shape of the streamlines, the cavitating regions tend to spread or to be conveyed by the main flow.

The flow behavior in case of sharp edge hole is displayed by means of Figs 6.15 and 16, in which the sequence of the injection process is presented. The sharpness of the edge plays a relevant role on the fuel stream in terms of velocity distribution and, consequently on the cavitation behavior. The differences in respect to the round edge case can be summarized in various aspects. Concerning the cavitation inception time, vapor regions are quickly formed as they are observable at 0.05 ms ASOI. The recirculation zones downstream the inlet up corner are wider and thus the size of the cavitating region is also generally enhanced, at low lifts and at high lifts as well. Figures 6.19 and 6.20 complete the description of the flow features; as easily visible, the flow across the edge is strongly modified; the velocity amplitude shows a considerable variation and the cavitation inception appears evident, strong and well defined.

**6.4.3 Chamber Flow/Spray.** By means of cut surfaces it is possible to visualize the in-cylinder flow condition when the piston is close to the TDC and the injection process begins. A sequence of three figures (6.23-6.25) shows the flow field evolution on a plane that contains the cylinder axis. The velocity vectors of Fig.6.23 show the presence of the early fuel jets; their penetration is initially weak and the squish eddies remain undisturbed; looking at the same visualization for TDC, the traces of the diesel jets are evident and induce a strong acceleration of the surrounding air. The process goes on as shown in the last picture (Fig.6.25).

In Fig.6.26, the hole-averaged spray penetration curve is depicted; maximum penetration length is slightly over 0.03 m, that is the order length of the piston bowl radius; the slope of the curve tends to become flat towards the end of the process.

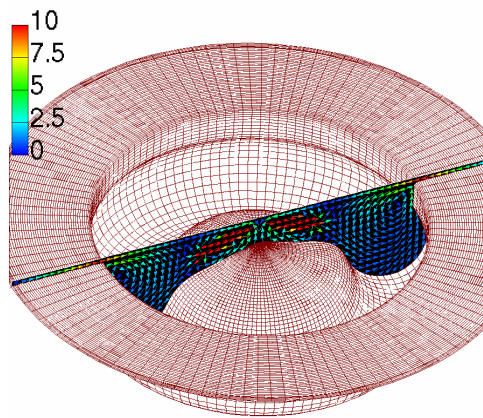


**Figure 6.23:** Cylinder velocity field [m/s] – 4 CABTDC

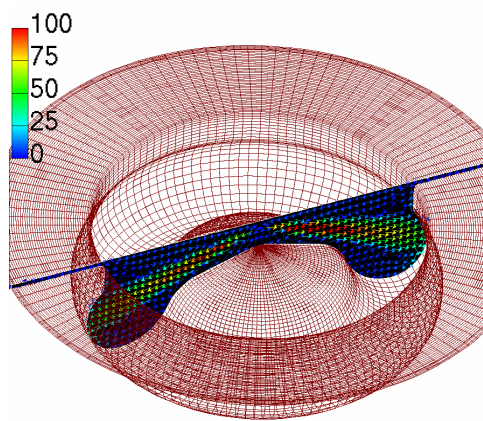


**Figure 6.24:** Cylinder velocity field [m/s]– TDC

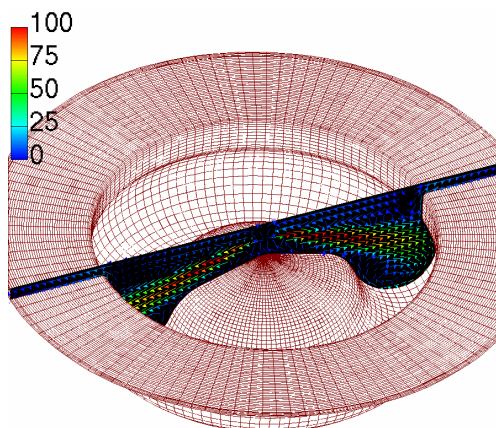


**Figure 6.25:** Cylinder velocity field [m/s] – 6 CAATDC

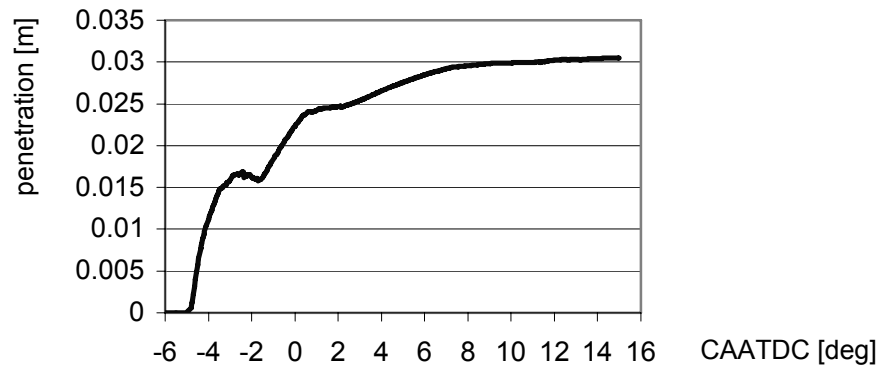


**Figure 6.26:** Mean penetration curve [m]

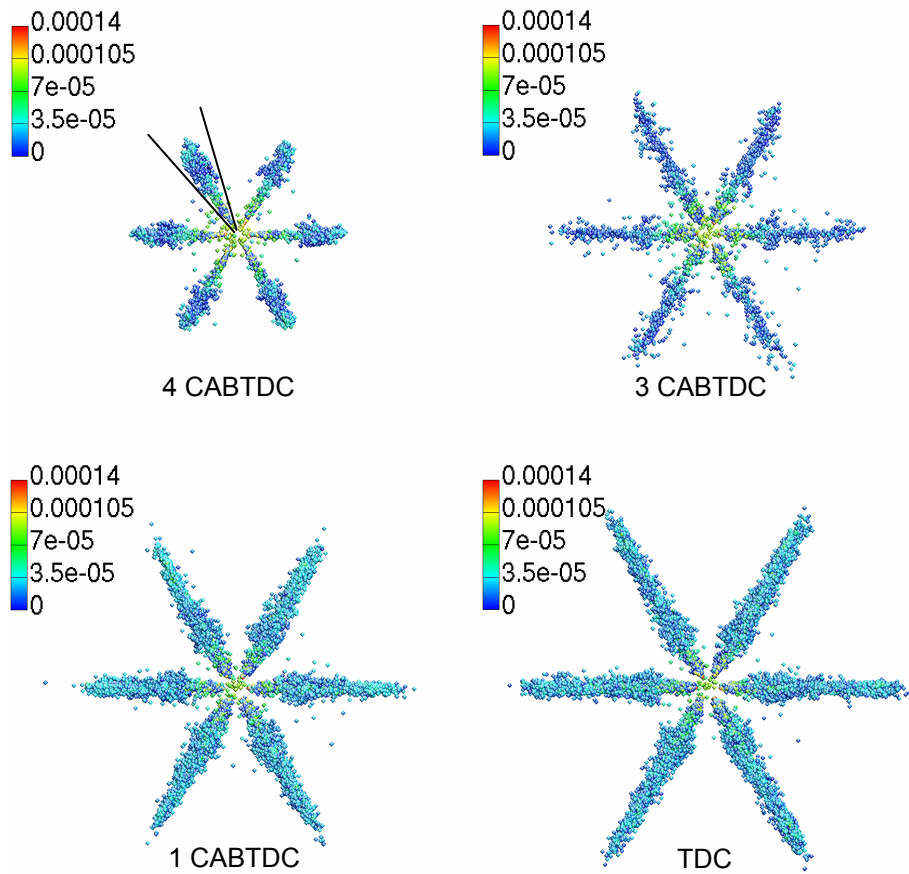


**Figure 6.27:** Spray droplet diameter visualization [m]

The visualization of the spray cone results, based on the FIRE spray post processor, is depicted in Fig.6.27, that shows a sequence of the fuel atomization process.

The color-bar represents the droplet diameter, whose start value is initialized to be exactly at the nozzle diameter, so that the effect of the brake up model is immediately visible; particles cover a very short path being red, due to their tendency to form smaller units. The spray plumes appear compact and characterized by a cone angle in the range of 20÷25 degrees.

**6.5 Concluding remarks.** The introduction of the fuel in the combustion chamber is the result of the correct integration of the roles played by several components. The modern layout of the high pressure injection systems is conceived to deeply match the engine features, in order to obtain well suited components that form an efficient single whole. The coupled use of two different codes seems to be in agreement with the need for an integrated simulation approach, in which the performance of the entire injection system, the nozzle flow characteristics and the air-fuel mixing process can be evaluated. Even 0/1-D modeling allows for a detailed representation of the transient phenomena that define the injection rate shape and the injected quantities, other indications are needed to complete the characterization of the system, like the nozzle flow features. The presented model points out the contribution that a 3-D CFD analysis can give to the development of the high pressure systems; the hole flow model plays a double role in the numerical investigation: on one hand, it gives a 3-D representation of the initially predicted flow rates, that helps the development of the convenient layout features of the nozzles; on the other hand, such a simulation works as link for the break-up modeling. In detail, the predicted flow regimes can be translated into indications that allow the use of detailed fuel atomisation sub-model: as shown in the last step of the simulation, the numerical investigation can be extended to the mixing process in the combustion chamber. The presented modeling approach can be summarized as follows:

- the first step of the modeling procedure highlights the complex pressure dynamics of the transient phenomena, and the obtained results, as the needle lift time evolution, are used to initialize the nozzle flow simulation;
- the dynamic CFD analysis on the nozzle shows its attitude to point out the behavior of the flow streams, the formation of the cavitating zones and the role of geometrical details like the inlet edge hole (further analysis is devoted to investigate the influence of the needle eccentricity on the hole to hole velocity variations);
- finally, by means of the 'nozzle interface' activation, the spray modeling can take into account the nozzle exit flow data, allowing for a complete and unitary representation of the injection process.

## 6.6 Nomenclature

$A_i''$	=	interfacial area density
CAA	=	Crank Angle After
CAB	=	Crank Angle Before
$D_b$	=	bubble diameter
C	=	constant

$C_{CR}$	=	condensation reduction factor
$C_D$	=	drag coefficient
$C_E$	=	Egler coefficient
$C_{TD}$	=	drag turbulent coefficient
$C_{1-4}$	=	Wave model constant
$E_k$	=	kinetic energy
EOI	=	End Of Injection
$M_c$	=	vapor phase momentum
$M_d$	=	liquid phase momentum
$N_0^m$	=	initial bubble number density
$N^m$	=	number density
$R$	=	bubble radius
$Re_b$	=	bubble Reynolds number
$S_k$	=	cavitation source term
SOI	=	Start Of Injection
TDC	=	Top Dead Centre
We	=	Weber number
$k_c$	=	vapor ph. turb. kinetic energy
$m_L$	=	liquid mass of a ligament
$n_L$	=	number of bubbles in a ligament
$r$	=	actual droplet radius
$r_A$	=	characteristic droplet radius
$r_T$	=	turbulent length scale
$p_{sat}$	=	saturation pressure
$p_b$	=	pressure in a bubble
$p_\infty$	=	environment pressure
$\mathbf{v}_c$	=	vapor velocity
$\mathbf{v}_d$	=	liquid phase velocity
$\mathbf{v}_r$	=	relative velocity

#### **Greek symbols**

$\Gamma_c$	=	vapor phase mass
$\Gamma_d$	=	liquid phase mass
$\Delta p$	=	pressure difference
$\alpha_d$	=	liquid phase volume fraction
$\nu_2$	=	liquid cinematic viscosity
$\rho_c$	=	vapor phase density
$\rho_d$	=	liquid phase density
$\rho_2$	=	liquid density
$\sigma$	=	surface tension
$\tau_A$	=	characteristic break-up time
$\tau_T$	=	turbulent time scale

## 6.7 References

- [1] Catania, A., Ferrari, A. and Spessa, E., "Numerical-Experimental Study and Solutions to Reduce the Dwell Time Threshold for Fusion-Free Consecutive Injections in a Multijet Solenoid-Type C.R. System", ICES2006 ASME Paper No. 1369.
- [2] Baratta, M., Catania, A. and Ferrari, A. "Hydraulic Circuit Design Keys to Remove the Dependence of the Injected Fuel Amount on Dwell Time in Multi-Jet C.R. Systems ", ICES2006 ASME Paper No. 1426.
- [3] Catania, A., Ferrari, A., Manno, M. and Spessa, E., "Experimental Investigation of Dynamics Effects on Multiple-Injection Common Rail System Performance", ICES2005 ASME Paper No. 1108.
- [4] Catania, A., Ferrari, A. and Manno, M. "Development and Application of a Complete Common-Rail Injection System Mathematical Model for Hydrodynamic Analysis and Diagnostics", ICES2005 ASME Paper No. 1018.
- [5] Mulemane, A., Han, J.S., Lu, P.H., Yoon, S.Y. and Lai, M.C., "Modelling Dynamic Behavior of Diesel Fuel Injection Systems", SAE Paper No. 2004-01-0536.
- [6] Wang, T.C., Han, J.S., Xie, X.B., Lai, M.C., Henein, N.A., Schwarz, E. and Bryzik, W., "Parametric Characterization of High-Pressure Diesel Fuel Injection Systems", J. Engineering in Gas Turbine & Power, 125, 412-426, 2003.
- [7] Chiavola, O. and Giulianelli, P., "Modeling and Simulation of Common-Rail Systems", SAE Paper No. 2001-01-3183.
- [8] Roth, H., Gavaises, M. and Arcoumanis, C., "Cavitation Initiation, Its Development and Link with Flow Turbulence in Diesel Injector Nozzles", SAE Paper No. 2002-01-0214.
- [9] Arcoumanis, C., Flora, H., Gavaises, M. and Kampanis, N., "Investigation of Cavitation in a Vertical Multi-Hole Injector", SAE Paper No. 1999-01-0524.
- [10] Gavaises, M. and Andriotis, A., "Cavitation Inside Multi-hole Injectors for Large Diesel Engines and Its Effects on the Near-nozzle Spray Structure", SAE Paper No. 2006-01-1114.
- [11] Fezzaa, K., Lee, W.K., Cheong, S., Powell, C.F., Wang, J., Li, M., and Lai, M.C., "High Pressure Diesel Injection Studied by Time-Resolved X-Ray Phase Contrast Imaging", ICES2006 ASME Paper No. 1409.
- [12] Han, J.S., Lu, P.H., Xie, X.B., Lai, M.C. and Henein, N.A., "Investigation of Diesel Spray Primary Breakup and Development for Different Nozzle Geometries", SAE Paper No. 2002-01-2775.
- [13] Tatschl, R., v. Künsberg-Sarre, C., Alajbegovic, A. and Winklhofer, E., "Diesel Spray Modeling Including Multidimensional Cavitation Nozzle Flow Effects", Proc. of ILASS Europe Conference, Sept. 11-13, Darmstadt, Germany, 2000.
- [14] Tatschl, R., v.Kuensberg Sarre, E. and v.Berg, E., "IC-Engine Spray Modeling – Status and Outlook", acts of Int. Multidimensional Engine Modeling User's Group Meeting at SAE W. Congress, 2002.
- [15] Giannadakis, E., "Modelling of Cavitation in Automotive Fuel Injector Nozzles", PhD thesis, Imperial College London, UK 2006.
- [16] Chiavola, O. and Palmieri, F., "Coupling Codes for Nozzle Flow Modeling in Diesel Injection Systems", ICES2006 ASME Paper No. 1414.
- [17] Chiavola, O., Palmieri, F. and Chiatti, G., "Integrated Modeling of Fuel Influence on Common Rail Injection System Performance", ICEF2006 ASME Paper No. 1556.
- [18] Chiavola, O. and Palmieri, F., "Modeling Needle Motion Influence on Nozzle Flow in High Pressure Injection System", SAE Paper No. 2007-01-0250.
- [19] Imagine AMESim v4.2 Tutorial and User Guide, AMESim Technical Bulletins.



- [20] FIRE v8.4 CFDWM Guide, AVL List GmbH.
- [21] Zielke W., "Frequency-dependent friction in transient pipe flow", Trans. ASME J. Basic Engng, 90, 109-115, 1968.
- [22] K. Samada, C.W. Richards, et al., "A finite element model of hydraulic pipelines using an optimized interlacing grid system", ImechE, 1993.
- [23] FIRE v8.4 Multiphase Manual, AVL List GmbH.
- [24] Hinze, J.O., "Turbulence", 2<sup>nd</sup> ed., McGraw-Hill, New York, 1975.
- [25] Franklin, R.E. and McMillan, J., "Noise Generation in Cavitating Flows", J. Fluids Eng., 106, 336-341, 1984.
- [26] FIRE v8.4 Multiphase Manual, AVL List GmbH.
- [27] Su, T.F., Patterson, M.A., Reitz, R.D. and Farrell, P.V., "Experimental and Numerical Studies of High Pressure Multiple Injection Sprays", SAE Paper No. 960861.
- [28] Patterson, M.A. and Reitz, R.D., "Modeling the Effects of Fuel Spray Characteristics on Diesel Engine Combustion and Emissions", SAE Paper No. 980131.
- [29] O'Rourke, P.J., "Statistical Properties and Numerical Implementation of a Model for Droplet Dispersion in Turbulent Gas", J. Comput. Physics, 83, 345, 1989.
- [30] O'Rourke, P.J. and Bracco, F.V., "Modeling of Drop Interactions in Thick Sprays and a Comparison With Experiments", IMECHE, 1980.
- [31] Naber, J.D. and Reitz, R.D., "Modeling Engine Spray/Wall Impingement", SAE Paper No. 880107.
- [32] Dukowicz, J.K., "Quasi-steady droplet change in the presence of convection", informal report Los Alamos Scientific Laboratory", LA-7997-MS, 1979.
- [33] Stiesch, G., "Modeling Engine Sprays and Combustion Processes", Springer Verlag, Berlin, 2003

## **7. Mini-sac Injector: Needle Motion Influence on Nozzle Flow in High Pressure Injection System**

This section deals with the numerical investigation of a diesel engine high pressure DI system in which the influence of needle motion characteristics on the internal injector flows is evaluated; a radial perturbation of the axial needle motion has been imposed to analyze its role over the nozzle flow features. The developed model is based on the coupling of two computational tools. With the former one, AMESim code, the injector has been modeled; the results obtained from the injector simulation, in terms of injection needle lift time evolution, have been used to initialize the latter computation tool, FIRE code, in which 3D flow numerical investigation of the internal injector flows has been performed. Details of the adopted modeling strategy are presented and the results of each simulation step are shown.

**7.1 Introduction.** In the investigation of injection systems, modeling plays a significant role due to its ability of catching and highlighting the aspects characterizing the fuel injection process. On the one hand, great relevance is attributed to the study of all parameters affecting the quantity of injected fuel, the mass flow trend and the flexibility of injection strategy [1,2]; on the other hand, all aspects concerning the air-fuel mixture formation are important alike [3,4]. Investigations have been aimed at evaluating the role that nozzle flow features can play in the break-up processes and therefore in the air-fuel mixing behavior [5-8]. Since a deep link characterizes the injection modality and the subsequent processes in combustion chamber, the development of both experimental and numerical activities, aimed at improving the driving factors understanding, is encouraged [9]. In the frame of numerical simulation activities, a comprehensive approach in the system analysis seems to be significant, due to the concatenation of the injection peculiar sub processes.

On such a subject, some works of the author [10,11] highlight the advantages deriving from the coupling of two different codes, allowing a three step simulation procedure. According to the adopted strategy, by means of AMESim code [12-14], a zero/one-dimensional model representing the whole injection system is realized; such a model provides the relevant indications about the injection process. The investigation goes into more depth concerning the nozzle flow condition in the second step of the simulation: results coming from AMESim model (flow rate, pressure and needle lift time traces) are used to initialize 3D CFD nozzle flow simulation, with the aim of evaluating the flow features at the exit section of the injection hole, in terms of turbulence, cavitation and velocity; these values are used in the third computation step in the modeling of the fuel spray formation, in which a detailed submodel representing the liquid fuel primary break-

up mechanism can be adopted, just through the flow exit condition evaluation [15]. Both the second and the third simulation steps are performed in FIRE environment [16]. Some interesting works point out the effect of the nozzle geometry on the flow features; experimental and numerical investigations have been performed in order to characterize the role of typical parameters like injection hole shape, inlet corner grinding degree and sac type; moreover, concerning penetration length of fuel spray cones, hole to hole deviations have been detected and they have been ascribed to needle radial displacements affecting lift motion [17]. Recently developed visualization techniques based on X-ray technology enable the observation of the injector needle during the injection process; in detail, it has been highlighted the capability of evaluating any possible radial displacement as well as the axial one [18].

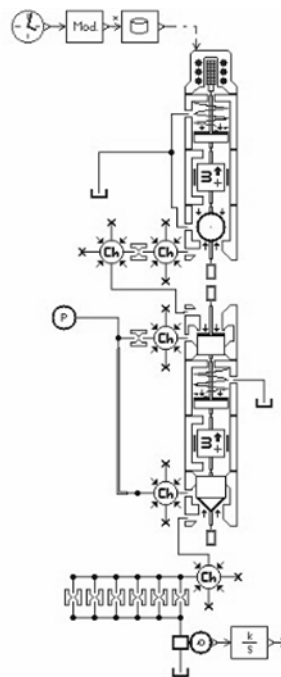


**Figure 7.2:** Injection system sketch

The present section can be placed in the multi-step modeling strategy and it represents a deepening of the second simulation step; the attention is focused on the influence that a radial component in the needle lift can exercise on nozzle flow features. Investigations are referred to a HPCR system in which six holes minisac injectors are used. As above introduced, two models of the injector have been built, the former one in AMESim environment, the second one by means of FIRE code. The coupling between the two models is based on the needle lift time trace coming from the zero-dimensional model, which is used to simulate the needle displacement on the 3D computational grid. The 3D injector model is conceived to simulate the fuel flow through the opening passage between needle surface and seat edge, through the sac volume and through the nozzles. By means of a mesh representing the injector tip, the consequences of a presumed

needle eccentricity on flow fields are evaluated; the attention is focused on flow field velocities, fuel tendency to cavitation and exit flow velocity. The modeling of the eccentric needle displacement is based on the needle lift time trace coming from AMESim model, but the lift direction has been deviated from the axis of the needle guide; this condition induces the radial displacement component to grow linearly as regards the lift value.

**7.2 Injector model.** Figure 7.2 shows the injector sketch as appears in AMESim environment. The model is made of two sub units, the former one is hydraulic, representing the needle in its guide, the latter one is electro-hydraulic, modeling the solenoid and the hydraulic control valve.

The short pipe that characterizes and connects the described parts of the common rail injectors has been represented by a hydraulic line and two dead volumes; a throttle valve governs the transient flow phenomena. Pipelines and dead chambers models take variable volumes and pressure dynamics into account.

In the present approach, unlike the previous works, the injector model has been fed by an ideal pressure source instead of injection radial pump, relief valve and rail volume; such a choice has been made in order to focus the attention just on the injector internal flow and, at the same time, to contain the modeling effort. The simulation conditions are listed in Table 1

fuel injector	HPCR type
injection pressure [MPa]	110
energizing time [s]	$0.5 \cdot 10^{-3}$

**Table 7.1:** Simulation conditions

**7.3 Injector flow modeling.** A clearance characterizes the diameter of the cylindrical needle guide in respect to needle diameter; in detail, the values of 4 mm and 4.018 mm have been considered for the simulations. Subsequently, the maximum radial displacement of the needle tip allowed by the clearance has been calculated, as Fig.7.3 shows.

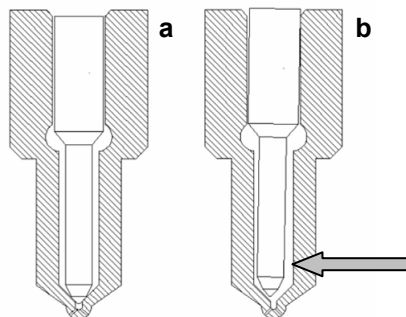


**Figure 7.3:** Needle configuration schemes: **a**, closing position; **b**, full lift position

The eccentric displacement of the needle is modeled considering a deviated direction so that the calculated maximum radial displacement is reached at full lift. In accordance with such a criterion, the needle lift time trace coming from AMESim model is imposed to the needle surface of the computational grid along a straight line in the plane that cuts in half nozzles n.2 and n.5; such a direction is identified by the trace k-j in Fig.7.4. Even though the evaluation of the eccentric displacement is based on the rotation allowed by the cylindrical constraint of the needle, the entity of the angular displacement is so small that the movement of the needle tip is considered as a translation.

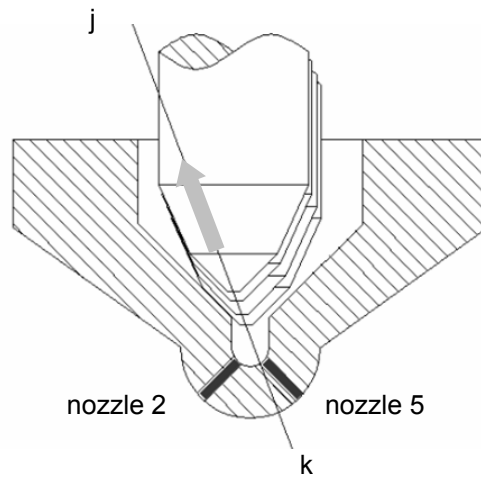


**Figure 7.4:** Needle lift deviation scheme; k-j is the displacement direction

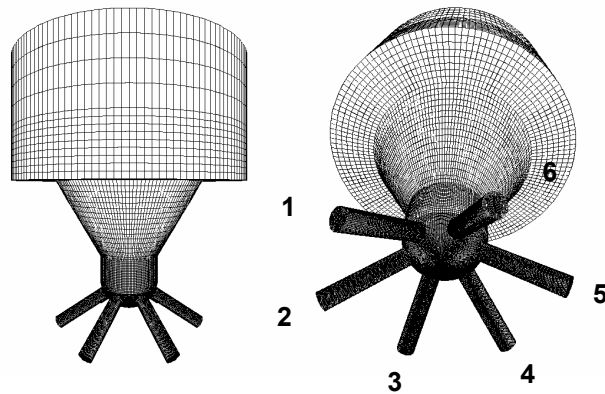


**Figure 7.5:** Injector mesh: left, front view; right, bottom view; injector holes are identified by numbers 1 to 6

The radial displacement in correspondence of maximum needle lift is 0.04 mm. Figure 7.5 shows two views of the adopted computational mesh; it is obtained connecting two elemental mesh grids. The former one is the needle grid, with polar symmetry cells arrangement, the latter one is the nozzle hole mesh; they are both structured grids; the complete mesh is made of 501144 cells.

The inlet hole edges are rounded off, avoiding a sharp corner geometry, in accordance to the hydro grinding production processes, as Fig.7.6 shows.

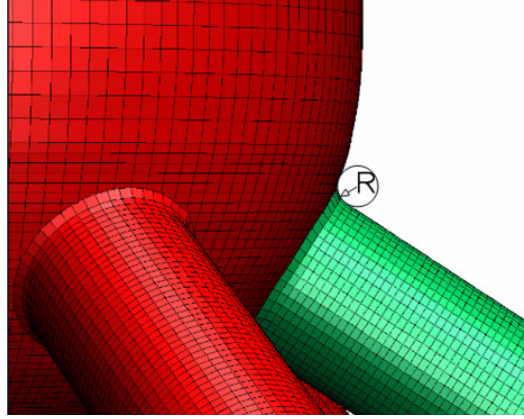


**Figure 7.6:** Particular of injector mesh; in evidence the rounded inlet hole edge

The solution of the nozzle flow is based on the FIRE Multiphase Module [15], in which the Euler-Euler simulation can be performed by means of the 'Multifluid sub module'; details of the model have been discussed in chapter 4 and in a work of the author, as well [11]; the k- $\epsilon$  closure for a RANS approach has been adopted. Central issues in the modeling of cavitation phenomena are the mass transfer between phases and the interfacial momentum source. The mass transfer is represented by relation (1), in which the radius length  $R$  with its time derivative, the liquid density  $\rho_d$  and the bubble number density  $N'''$  appear.

$$\Gamma_c = \rho_d N''' 4R^2 \dot{R} = -\Gamma_d \quad (1)$$

$N'''$  is calculated using the Rayleigh equation (2).

$$R\ddot{R} + \frac{3}{2}\dot{R}^2 = \frac{\Delta p}{\rho_c} \quad (2)$$

By linearizing equation (1) and neglecting the inertial term, equation (3) can be obtained:

$$\Gamma_c = \frac{1}{C_{CR}} \text{sign}(\Delta p) 3.85 \frac{\rho_d}{\sqrt{\rho_c}} N'''^{\frac{1}{3}} \alpha_d^{\frac{2}{3}} |\Delta p|^{\frac{1}{2}} = -\Gamma_d \quad (3)$$

The term  $\Delta p$  represents the effective pressure difference (4),

$$\Delta p = p_{sat} - \left( p - C_E \frac{2}{3} \rho_c k_c \right) \quad (4)$$

in which the Egler coefficient  $C_E$  depends on the local turbulence level [19]. The empirical formula (5) is used to compute  $N'''$ , where  $N_0'''$  represents the initial bubble density [20].

$$N''' = \begin{cases} N_0''' & \alpha_d \leq 0.5 \\ 2(N_0''' - 1)(1 - \alpha_d) + 1 & \alpha_d > 0.5 \end{cases} \quad (5)$$

The number density is constrained by the (6).

$$N''' = \max \left( N''', \frac{6\alpha_d}{\pi D_{b,\max}^3} \right) \quad (6)$$

$D_{b,\max}$  is a function of geometry and it represents the maximum bubble diameter. The bubble diameter  $D_b$  is then related (7) to the volume fraction and to the number density  $N'''$ .

$$D_b = \left( \frac{6\alpha_d}{\pi N'''} \right)^{\frac{1}{3}} \quad (7)$$

Relation (8) represents the interfacial momentum source, including drag and turbulent dispersion actions.

$$M_c = C_D \frac{1}{8} \rho_c A_i'' |\mathbf{v}_r| \mathbf{v}_r + C_{TD} \rho_c k_c \nabla \alpha_d = -M_d \quad (8)$$

Relations (9) and (10) are used to calculate the relative velocity  $\mathbf{v}_r$  and the interfacial area  $A_i'''$

$$\mathbf{v}_r = \mathbf{v}_d - \mathbf{v}_c \quad (9)$$

$$A_i'' = \pi D_b^2 N''' = (36\pi)^{\frac{1}{3}} \alpha_d^{\frac{2}{3}} \quad (10)$$

Number density,  $N'''$ , is obtained from the cavitation mass exchange model. Drag coefficient,  $C_D$ , depends on the bubble Reynolds number,  $Re_b$ , defined by relation (11):

$$Re_b = \frac{v_r D_b}{\nu_c} \quad (11)$$

A correlation (12), valid for bubbles, is adopted [7]:

$$C_D = \begin{cases} \frac{192}{Re_b} (1 + 0.10 Re_b^{0.75}) & Re_b \leq 1000 \\ 0.438 & Re_b > 1000 \end{cases} \quad (12)$$

The modeling of the closure terms of the turbulence kinetic energy involves the following assumptions [19]:

- the interfacial interaction between phases is neglected;
- the turbulence level of the dispersed phase is assumed to be equal to the continuous phase turbulence level.

In Tab.2, the injector geometrical features are presented. To guarantee the independence of the obtained flow fields on the adopted mesh, preliminary runs have been performed and an appropriate cell dimension has been individuated.

injector nozzle diameter [m]	$0.15 \cdot 10^{-3}$
injector nozzle length [m]	$0.7 \cdot 10^{-3}$
sac volume [m <sup>3</sup> ]	$1.8 \cdot 10^{-10}$
needle length [m]	$40 \cdot 10^{-3}$
needle cylindrical guide length [m]	$12 \cdot 10^{-3}$
number of nozzles	6

**Table 7.2:** Injector characteristics

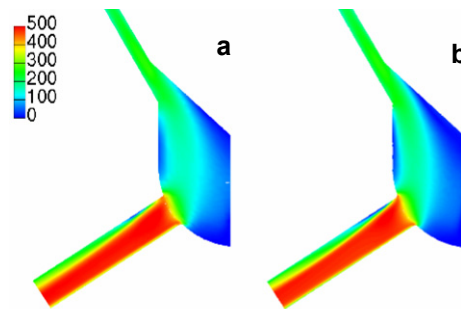


**Figure 7.7:** Scalar flow velocity [m/s]; mesh **a**, 86232 cells; mesh **b**, 576960 cells

Figure 7.7 shows the comparison between the velocity maps obtained with mesh 'a' (86232 cells) and mesh 'b' (576960 cells). The calculation has been performed at the injection pressure of 110 MPa and maximum value of needle lift. The most refined mesh has not been selected, due to the non-substantial differences between the obtained flow conditions, allowing a reduction of the computational effort.

**7.4 Results.** Figure 7.8 shows the needle lift time trace coming from AMESim model. As described above, such a curve has been adopted to simulate the needle displacement, namely to create the computation mesh in FIRE environment.

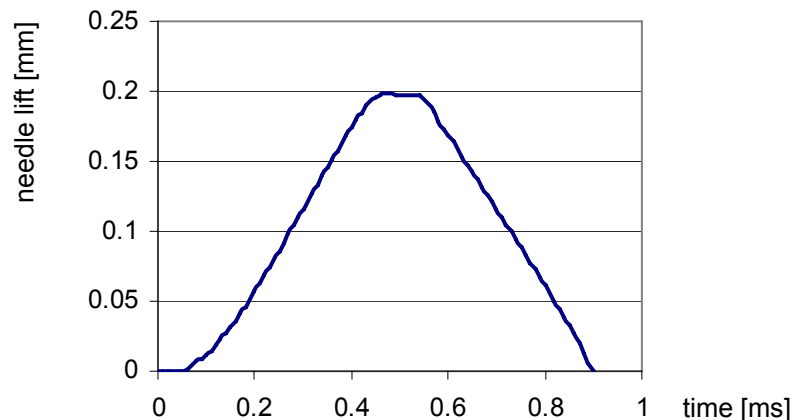


**Figure 7.8:** Needle lift



The nozzle flow features have been evaluated on the basis of flow velocity and vapor region observation. The obtained results have been arrayed in a single picture, and all graphs have been referred to the mid cut surface containing the axes of nozzles 2 and 5 (Figs. 7.9,7.10).

From the beginning of injection process until 0.10 ms ASOI, flow velocities do not show relevant differences in the nozzle; quickly, as shows the image referred to 0.15 ms ASOI, flow becomes faster and the eccentric needle displacement starts having an influence on the velocity field. An easily visible, fuel stream feeding nozzle 2 is present in the sac volume, generated by the eccentric position of the needle that narrows the opening in respect to the nozzle 5 and widens the opposite gap. At 0.20 ms ASOI, velocities become faster and stronger nozzle imbalances appear, in terms of velocity field shape. The intensity of the imbalances is due to the velocity difference of the two fuel streams passing through the opening section. Hole 2 is still fed by a preferential well structured fuel sub stream, but the main characteristic is that at the inlet of the holes fuel flows through the nozzles with different directions; an up to down flow path characterizes the inlet of nozzle 2; on the contrary, fuel in nozzle 5 passes the inlet section from down to up. Moreover, nozzle 2 flow is quite faster than the other one. At 0.25 ms ASOI, the scalar velocity field does not change its behavior, but a general speed increment is observable. The flow features in the sac volume previously described and the flow velocities in the nozzles are enhanced. At 0.30 ms ASOI, the scalar velocity field does not change its structure, even a speed increment is observable. The previous velocity distribution inside the sac volume is maintained. The effect of the needle radial displacement tends to decrease heading toward the maximum lift. The gap between needle and conical seat is wide enough to limit its accelerating effect on the flow and it causes a reduction of the flow asymmetry, as the pictures referred to 0.40-0.50 ms ASOI highlight. At these lift conditions, the differences of the two nozzle flows are at the minimum value: the inlet flow direction of nozzle 5 is almost parallel to the hole axis. During the closing phase, the flow features look like the results of the opening stage. Results referred to 0.70 ms are similar to the flow visualization at 0.25 ms ASOI; in detail, the closing flows appear slightly faster, needle lift being equal.

The presented results show that needle eccentricity plays a role if it causes a considerable perturbation on the flow symmetry. In the present case, such a condition takes place until the conical surface of the needle keep close to the seat edge; the radial displacement of the needle narrows and widens at the same time two opposite flow sections (related to holes 5 and 2 in the simulation) altering the velocity field in the sac volume and, consequently, the nozzle flows. Pictures of Fig.7.10 show the cavitation inception and its development at the same instants of the velocity results, in order to point out the relation between fuel velocity and its tendency to vapor formation. Initial cavitating zones appear during the range 0.15/0.20 ms ASOI, when the fuel flow reaches a relevant

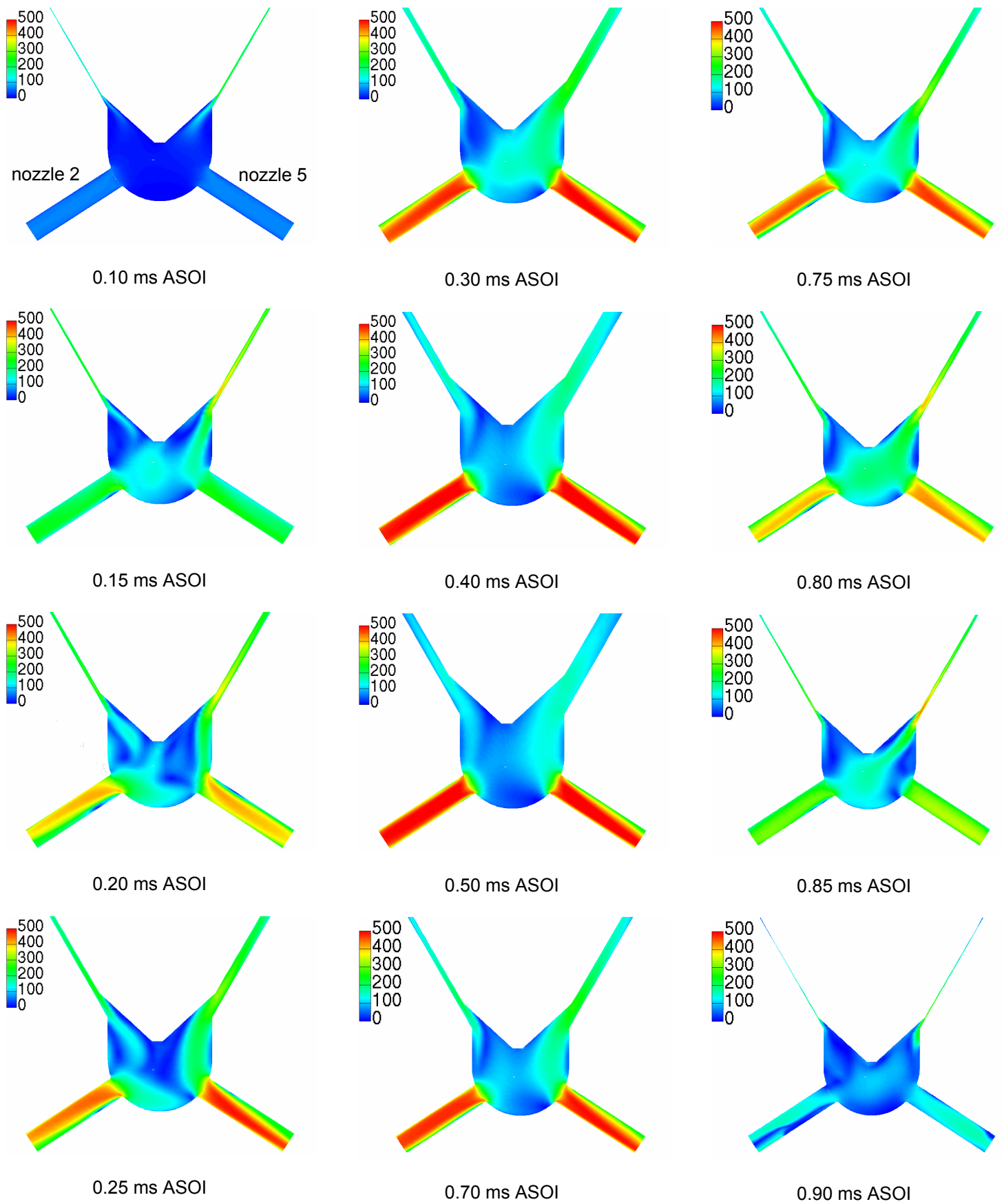


**Figure 7.9:** Fuel scalar velocity [m/s]

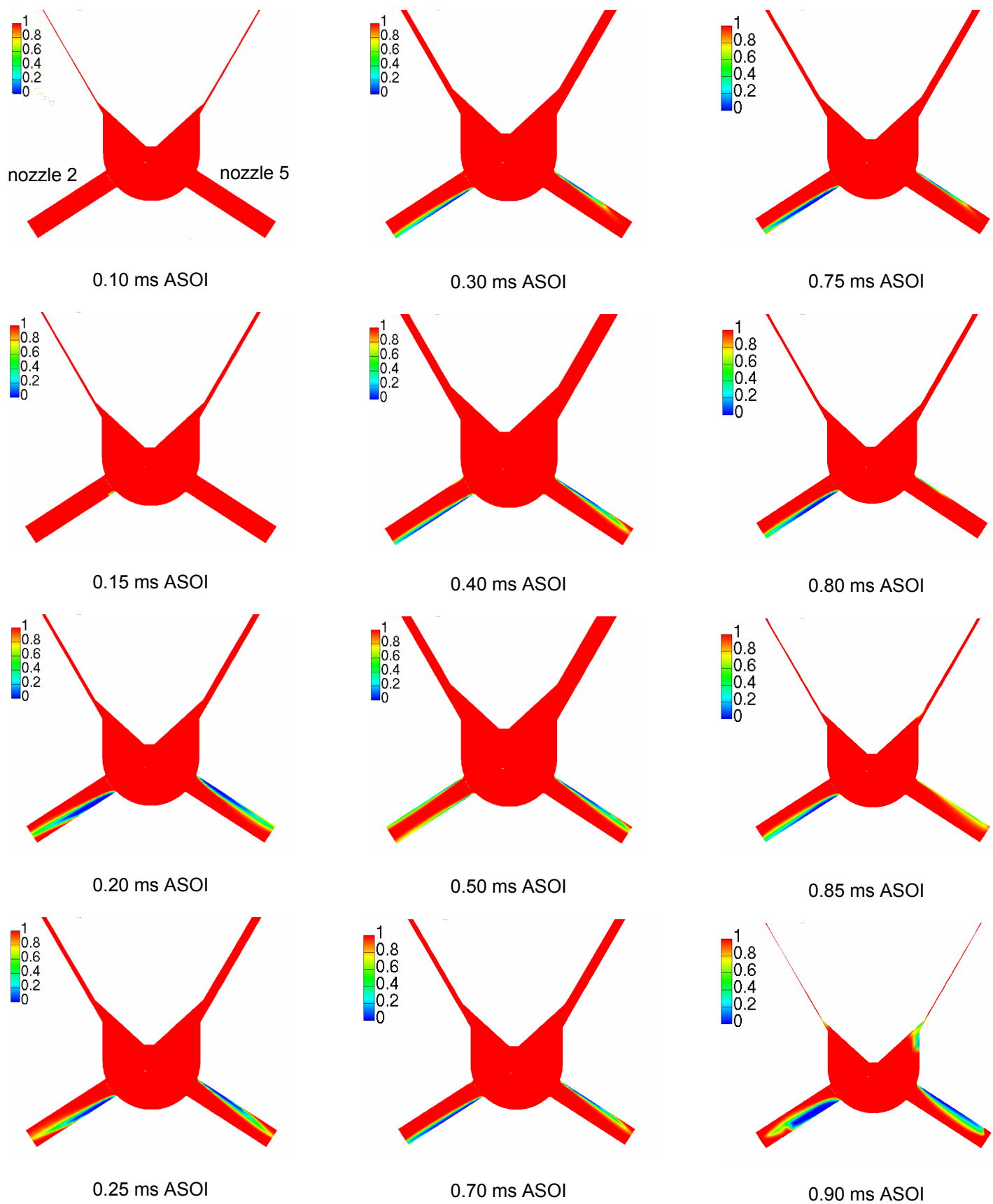


**Figure 7.10:** Liquid vapor volume fraction

speed, showing different shapes: in nozzle 5, vapor tends to move towards the hole axis and it reaches a central position at the outlet section; in nozzle 2 the cavitation bubbles appear well bounded by the main liquid stream. During the time interval 0.25-0.40 ms ASOI, cavitation areas show a general reduction, without varying the shape features, but later, at 0.50 ms ASOI in hole 5, vapor formation is characterized by two inception points; such a behavior is in agreement with the inlet flow direction discussed above. The closing phase is characterized by narrow and wall close-fitting cavitating regions. Quite useful in interpreting the flow pattern, are the streamlines inside the sac volume, presented in Figs. 7.11-13. At 20 ms ASOI it is evident that the flow is characterized by a vortex on the left side of the sac; such a vortex seems to be induced by the fast stream coming from the right-hand side; the stream is strong enough to influence the whole sac flow and to generate the previously described flow imbalance. The vortex tends to deteriorate to a slighter perturbation of the flow pattern as the lift goes on.

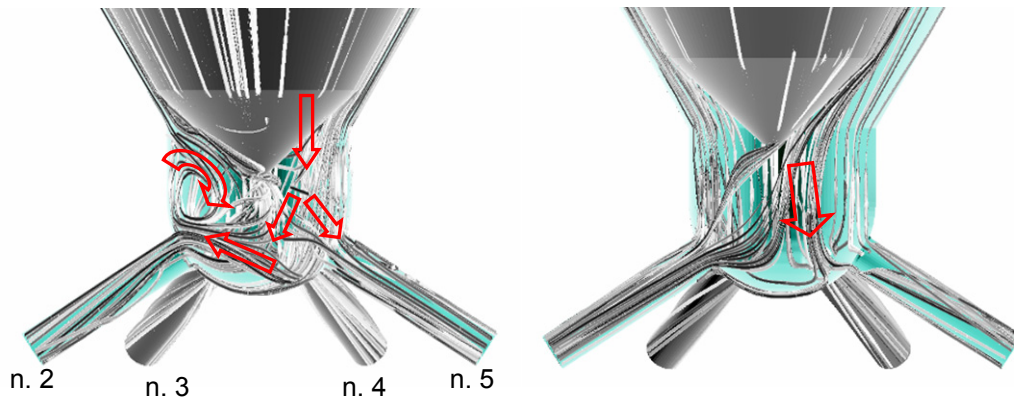


**Figure 7.11 (left):** Flow streamlines, 0.2 ms ASOI

**Figure 7.12 (right):** Flow streamlines, 0.5 ms ASOI

Indeed, at 50 ms ASOI (Fig.7.12), the streamlines are still deflected but eddy zones are not present; the full lift condition leads to the formation of an eccentric stagnation point on the bottom of the sac whose influence is lower than in the opening-closing phases. Figure 7.13 shows the closing behavior: the stagnation point is still present and the flow imbalance is enhanced again. The flow line visualisation highlights the hole to hole variation of the helicoidal shape of the lines. It is another facet of the effects due to the needle eccentricity that can play a role in the spray formation.

In order to better outline the flow features inside the injector, another cut plane has been considered; the flow of fuel through a plane perpendicular to the one displayed in Figs 7.9-13 is shown in Figs. 7.14 and 7.15. The flow fields highlight a symmetric behavior, both for little and high needle lifts.

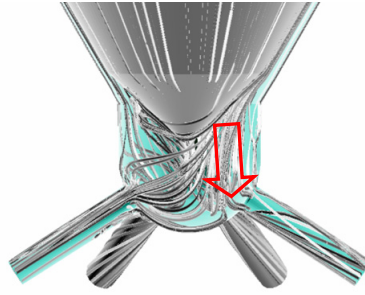


**Figure 7.13:** Flow streamlines, 0.75 ms ASOI

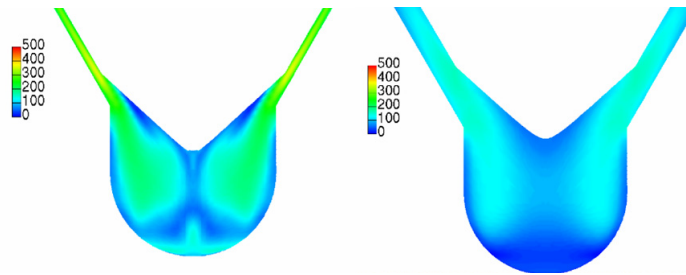


**Figure 7.14 (left):** Fuel velocity, 0.2 ms ASOI

**Figure 7.15 (right):** Fuel scalar velocity, 0.5 ms ASOI

Mean flow velocities have been evaluated at each nozzle exit. Figure 7.16 shows the percentage mean outlet velocity difference between nozzles 2 and 5; the main differences can be observed during the opening phase; at 0.20 ms the exit mean velocity of hole 2 is 8% higher than that one of hole 5. At maximum needle lift, low or negligible differences characterize the exit mean velocities. Figure 7.17 shows the trends related to the rest of the injection holes. These results give an indication of the needle eccentricity effect on the whole injector flow; the flow velocities in the holes beside nozzle 2 are faster than those of the opposite couple.

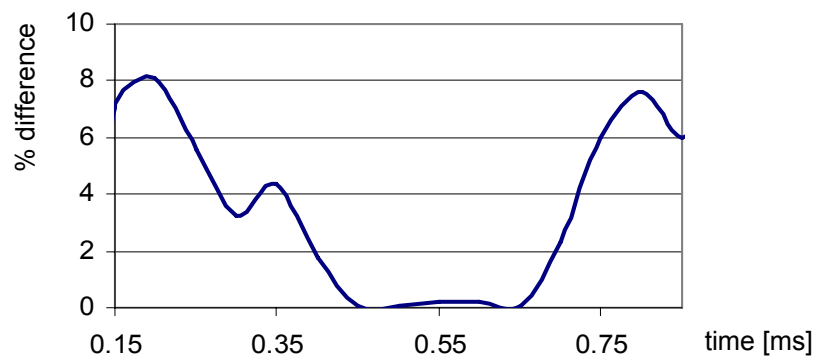


**Figure 7.16:** % nozzle mean outlet velocity difference between nozzles 2 and 5

Low (in the range of the computation accuracy) velocity differences between the values of each couple are visible, due to the flow symmetry respect to the plane in which needle moves (shown in Figs 7.14 and 7.15). The highlighted hole to hole differences in the exit flow velocities are worthy to be considered to cause spray asymmetries, in terms of penetration length and cone angle development.

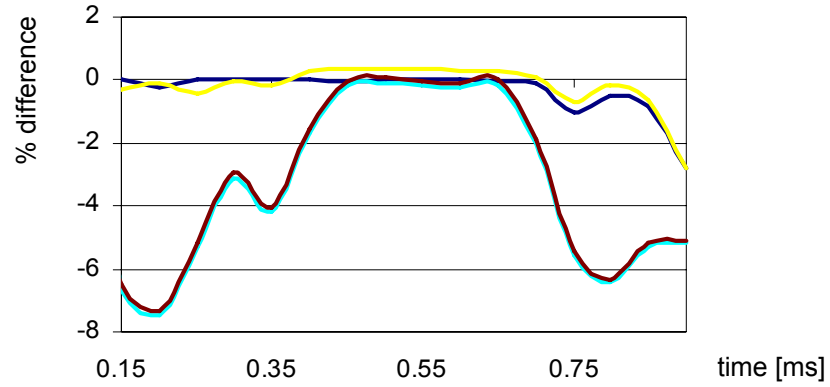


**Figure 7.17:** % nozzle mean outlet velocity difference between nozzles 2 and 1 — , 3 — , 4 — , 6 —

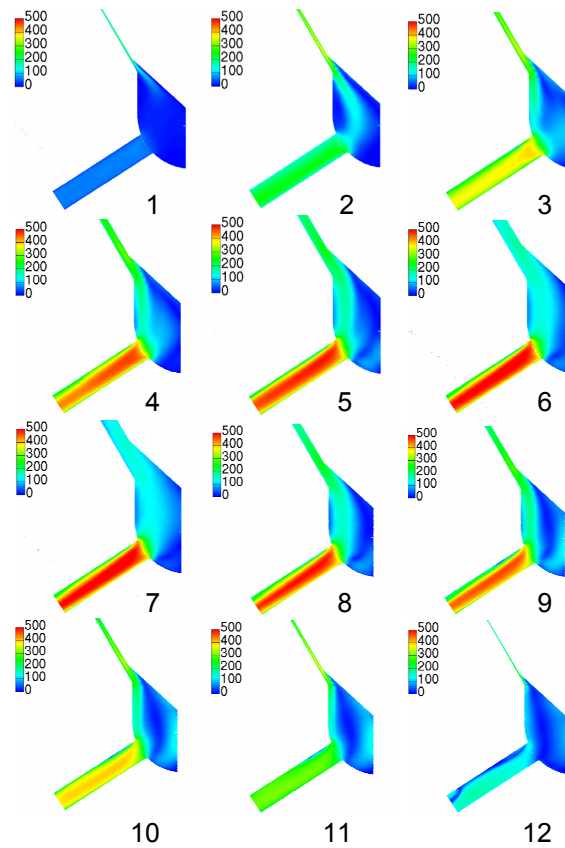


**Figure 7.18:** Fuel scalar velocity (centered case)

The presented results can be compared to the results referred to another simulation in which a simple axial displacement is imposed. Figures 7.18 and 7.19 show the scalar velocity flow field and the liquid-vapor volume fraction of nozzle 5. The sac volume is characterized by a symmetric flow, and each hole behaves in the same way. Cavitating regions have the same shape and the inception points are located at the high inlet corner.

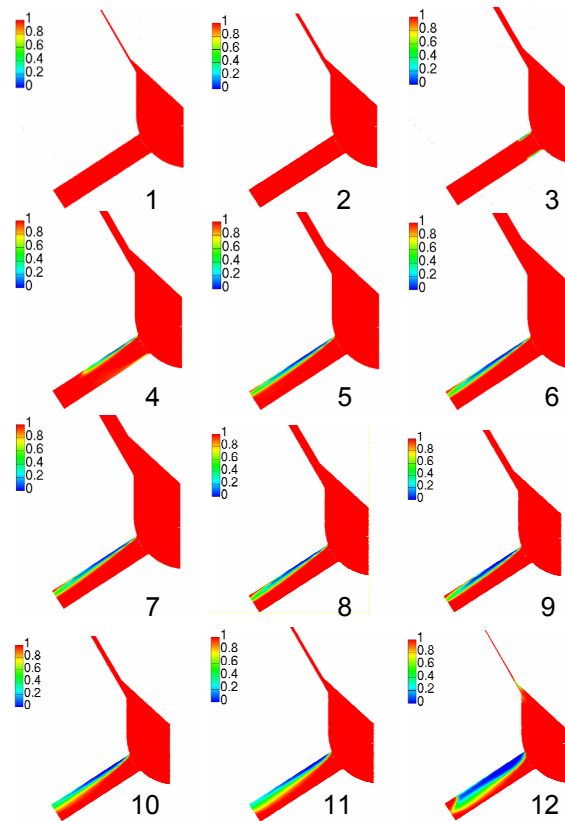


**Figure 7.19:** Liquid vapor volume fraction (centered case)

It is evident that the simple axial displacement does not induce flow imbalances among the nozzles, so that, at the exit of the holes, the same features characterize the fuel in terms of fuel velocity and vapor fraction.

**7.5 Concluding remarks.** A numerical model aimed at investigating the details of injector fuel flows has been presented; the attention has been focused on the nozzle flows characteristics, in order to evaluate the influence of a radial component on the needle displacement. Velocity flow fields, cavitation behavior and mean outlet velocities have been computed during the injection process. A comparison with a fully axial needle simulation has been performed. The following conclusions can be outlined:

- The radial component of the needle displacement is responsible for significant differences among the nozzle flow conditions: the eccentricity affects velocity field characteristics and vapor regions behavior and wideness.
- The location of cavitation inception points and the consequent vapor development depend on the inlet flow conditions, which are the consequence of the sac flow field features. The eccentric needle displacement is responsible for the imbalance of the flow passing through the injector opening whose effect is an asymmetric flow generation in the sac volume.
- The injection hole, that is more approached by the needle, is characterized by the lowest flow velocities; making a comparison with the flow features of the opposite hole, mean velocity difference reaches the percentage value of 8%; the minimum flow divergences among the nozzles are observed in correspondence to the maximum needle lift, when the conical injector surface is at the highest distance from the seat edge. Without modifying the opening and closing phases, it can be concluded that the longer is the duration of injection the lower is the relevance of eccentricity on the flow.

## 7.6 Nomenclature

$A_i''$	=	interfacial area density
$D_b$	=	bubble diameter
$C_{CR}$	=	condensation reduction factor
$C_D$	=	drag coefficient
$C_E$	=	Egler coefficient
$C_{TD}$	=	drag turbulent coefficient
$M_c$	=	vapor phase momentum
$M_d$	=	liquid phase momentum
$N_0''$	=	initial bubble number density
$N'''$	=	number density
$R$	=	bubble radius
$Re_b$	=	bubble Reynolds number
SOI	=	Start Of Injection
$k_c$	=	vapor phase turbulence kinetic energy
$p_{sat}$	=	saturation pressure
$\mathbf{v}_c$	=	vapor velocity
$\mathbf{v}_d$	=	liquid phase velocity
$\mathbf{v}_r$	=	relative velocity
<b>Greek symbols</b>		
$\Gamma_c$	=	vapor phase mass



$\Gamma_d$	=	liquid phase mass
$\Delta p$	=	pressure difference
$\alpha_d$	=	liquid phase volume fraction
$\rho_c$	=	vapor phase density
$\rho_d$	=	liquid phase density

## 7.7 References

- [1] Catania, A., Ferrari, A. and Spessa, E., "Numerical-Experimental Study and Solutions to Reduce the Dwell Time Threshold for Fusion-Free Consecutive Injections in a Multijet Solenoid-Type C.R. System", ICES2006 ASME Paper No. 1369.
- [2] Baratta, M., Catania, A. and Ferrari, A. "Hydraulic Circuit Design Keys to Remove the Dependence of the Injected Fuel Amount on Dwell Time in Multi-Jet C.R. Systems ", ICES2006 ASME Paper No. 1426.
- [3] Fimml, W., Fuchs, C., Jank, T. and Wimmer, A., "Optical Analysis and Simulation of Diesel Sprays in a High Pressure and High Temperature Spray Box", ICES2006 ASME Paper No. 1376.
- [4] Ueki, H., Ishida, M. and Sakaguchi, D., "Investigation of Droplet Disintegration in Diesel Spray Core by Advanced Laser 2-Focus Velocimeter", SAE Paper No. 2005-01-1238.
- [5] Tatschl, R., v.Kuensberg Sarre, E. and v.Berg, E., "IC-Engine Spray Modeling – Status and Outlook", acts of Int. Multidimensional Engine Modeling User's Group Meeting at SAE W. Congress, 2002.
- [6] Morgan, R., Wray, J., Kennaird, D.A., Crua, C. and Heikal, M. R., "The Influence of Injector Parameters on the Formation and Break-up of a Diesel Spray", SAE Paper No. 2001-01-0529.
- [7] Tatschl, R., v. Künsberg-Sarre, C., Alajbegovic, A. and Winklhofer, E., "Diesel Spray Modeling Including Multidimensional Cavitation Nozzle Flow Effects", Proc. of ILASS Europe Conference, Sept. 11-13, Darmstadt, Germany, 2000.
- [8] Roth, H., Gavaises, M. and Arcoumanis, C., "Cavitation Initiation, Its Development and Link with FlowTurbulence in Diesel Injector Nozzles", SAE Paper No. 2002-01-0214.
- [9] Stiesch, G., "Modeling Engine Sprays and Combustion Processes", Springer Verlag, Berlin, 2003.
- [10] Chiavola, O. and Palmieri, F., "Coupling Codes for Nozzle Flow Modeling in Diesel Injection Systems", ICES2006 ASME Paper No. 1414.
- [11] Chiavola, O., Palmieri, F. and Chiatti, G., "Integrated Modeling of Fuel Influence on Common Rail Injection System Performance ", ICEF2006 ASME Paper No. 1556.
- [12] Imagine AMESim v4.2 Tutorial and User Guide, AMESim Technical Bulletins. Chiavola, O. and Giulianelli, P., "Modeling and Simulation of Common-Rail Systems", SAE Paper No. 2001-01-3183.
- [13] Wang, T.C., Han, J.S., Xie, X.B., Lai, M.C., Henein, N.A., Schwarz, E. and Bryzik, W., "Parametric Characterization of High-Pressure Diesel Fuel Injection Systems", J. Engineering in Gas Turbine & Power, 125, 412-426, 2003.
- [14] FIRE v8.4 Multiphase Manual, AVL List GmbH.
- [15] FIRE v8.4 CFDWM Guide, AVL List GmbH.

- [16] Han, J.S., Lu, P.H., Xie, X.B., Lai, M.C. and Henein, N.A., "Investigation of Diesel Spray Primary Breakup and Development for Different Nozzle Geometries", SAE Paper No. 2002-01-2775.
- [17] Fezzaa, K., Lee, W.K., Cheong, S., Powell, C.F., Wang, J., Li, M., and Lai, M.C., "High Pressure Diesel Injection Studied by Time-Resolved X-Ray Phase Contrast Imaging", ICES2006 ASME Paper No. 1409.
- [18] Hinze, J.O., "Turbulence", 2<sup>nd</sup> ed., McGraw-Hill, New York, 1975.  
Franklin, R.E. and McMillan, J., "Noise Generation in Cavitating Flows", J. Fluids Eng., 106, 336-341, 1984.

## 8. Flow Features in Reduced Dwell Time Diesel Injector

The research and development activities on diesel injection systems have focused some key-factors that improve the solenoid actuated injector performance, especially in the frame of the multi-event injection strategies. This section deals with a 3-D numerical investigation that highlights the nozzle flow features of different injector layouts. A comparison between a last generation standard injector and an optimized unit characterized by an improved dynamics, different number of holes and reduced maximum lift is performed. By means of transient numerical simulations, the behavior of the fuel flows, the tendency to cavitation development and the response to the deviation from the standard operating conditions (highlighted by introducing a radial perturbation on the lift motion) are investigated.

**8.1 Introduction.** At present, considerable efforts are made at improving the features of the automotive engines, both diesel and gasoline. The main areas of interest concern on one side the pollutant emissions, on the other side the parameters that influence the engine operation, like fun to drive, noise, harshness and fuel economy (key-factors in the automotive market). Moreover, due to the evolution of emission standard and regulation, it is often necessary to modify or reconsider the trade-off among the aspects that define the main features of the vehicle. Certainly, as regards diesel engine (here considered), the performance improvement is related to the injection strategy; system layout, degree of development and operation logic exert a strong influence on injection, in terms of each needle opening dynamics and interaction among each fuel shot.

Some authors [1-3], by means of rigorous investigation, have clarified the driving factors of injection dynamics; the determining role of the high transient fuel pressure phenomena has been pointed out and its influence on the opening-closing strokes of the needle has been understood. At the same time, such investigations have traced the guideline to improve the injector performances (solenoid-actuated), especially towards multi-shot and HCCI applications; for example, the recent insight into fuel pressure allows to reassess the role of the rail, deeply innovating the usual *common rail* layout [4]. Another interesting issue is related to the injector performance improvement, in particular concerning the reduction of dwell time wideness; in the latest investigations on such a topic [5], the authors propose to limit the dwell time by means of a consistent reduction of the needle stroke, in conjunction with an increased number of holes in order to preserve the same fuel injection capability.

In this way, it is possible to achieve a relevant improvement of injector dynamics; moreover, such a modification is extremely easy to realize, very cost effective or, at least, inexpensive at all. Comparing the standard injector with the modified one, it is

spontaneous to pose a question about the onset of possible secondary consequences on the fuel flow (driven by the restriction of the needle lift); as an example, fuel is forced to pass through narrower passages upstream the holes, flow rate being equal.

The present section deals with a numerical investigation that highlights the internal flow features of injectors with restricted needle lift, in comparison with the standard layout. As previously mentioned, the attention is focused on a second generation common rail system, that means equipped with solenoid actuated pilot valves; the investigation is made of two steps: the former one represents the preliminary stage; it consists in the 0/1-D modeling of the whole injection system, by means of the commercial code AMESim [6]. Moving from the standard injector layout, the performance of the modified version is modeled and the differences in respect to the initial one (flow rate, dwell time, needle lift, etc.) are highlighted. The 1-D model is used to obtain the pressure time-history in the nozzle as boundary condition for the latter investigation step, which is the 3-D analysis of the nozzle fluid dynamics. It is devoted to understand the consequences on the fuel flow induced by the modification of the standard injector. Such a phase represents the main purpose of the investigation; it is based on a CFD simulation tool (FIRE [7]) and it is divided into two more parts. On one hand, a comparison between the standard and the dwell time reduced injector is performed. On the other hand, the response to a radial perturbation of the needle lift is evaluated, for both the injector layouts; even if it is difficult to understand and characterize the needle real motion [8], it is quite reasonable that a simplified analysis [9] can be able to provide interesting hints, or trends at least, about the magnitude of the flow rate deviations and about the asymmetries caused by needle eccentricity.

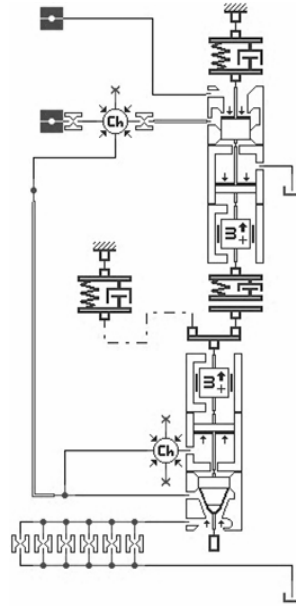
**8.2 0/1-D injection system model.** As described in the introductory section, the present investigation is referred to a second generation common rail system. On condition that layout and features of each component of the system is known, it is possible to choose physical models capable to represent the system operation. The system consists of high pressure reciprocating pump, relief valve, pipelines, control valves and injectors.

Figure 8.1 represents the detail of injector scheme in the modeling environment; it is made of two components mechanically coupled, the needle and the plunger.

The pilot valve is mechanically modeled by a mobile equipment made of two units, anchor and pin; as in the real layout, the swing of the anchor in respect to the pin is possible when it reaches the displacement limit, with the effect of damping the pin counterstroke and preventing oscillations. The electromagnetic force acting on the pilot valve is represented by means of a solenoid circuit model, whose energizing signal is given as external input, as shown in Fig.8.2.

The hydraulic network of the system is a combination of chamber volumes and pipe elements, whose modeling is based on different approaches; pressure and temperature in lumped volume elements are just time dependent, whereas the pipeline models are based on a one-dimensional scheme; in the latter case, the solution of wave equation is

used to represent the effects of inertia, friction and compressibility; in detail, AMESim library contains a sub-model capable to represent the influence of the frequency dependent friction [10-11]. The whole building up of the model is based on the libraries provided by AMESim environment. In order to evaluate the model performance in predicting the effect of injector layout on the needle dynamic, a preliminary computation phase has been performed.



**Figure 8.1:** Needle and plunger sketch in 0/1-D simulation environment

Preliminary simulations are devoted to identify the convenient computation setting and mesh refinement, in order to obtain results at least in qualitative agreement with the results available in the literature.

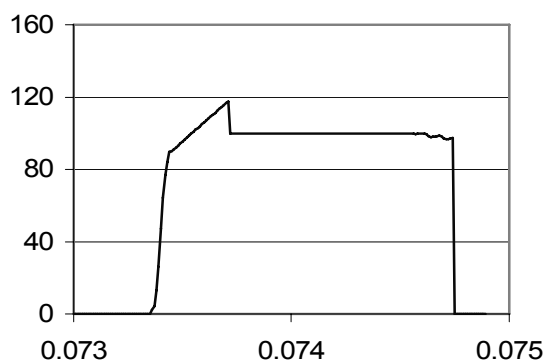


**Figure 8.2:** Energizing current signal, ET 1.150 ms

Concerning the mesh refinement, the number of computational cells used to discretize a 1/6<sup>th</sup> of the injector sector has been varied from about 100.000 to 600.000. The results are evaluated in terms of predicted mass flow rate, magnitude deviation of the local pressure values and velocity field features; such a preliminary phase allows to choose a satisfactory grid refinement, bounding the computational effort without compromise the meaning of the results.

**8.3 Injector features and lift modeling.** Calculations have been referred to two types of VCO injector, having the same geometrical layout, but different number of holes and maximum lift value (Fig.8.4).

In the following, the standard injector, with 6 holes and lift of 0.43 mm is indicated with *Injector1*, whereas the modified injector, with 7 holes and maximum lift of 0.2 mm is called *Injector2*. In both cases the hole drilling (k-factor = 0.0) and the rounded shape of the inlet edge (radius length in the order of 30 microns) remain the same.

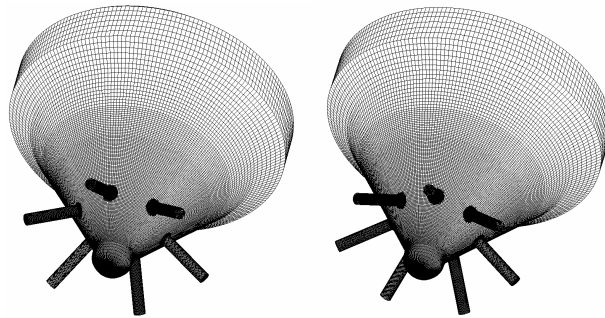


**Figure 8.3:** Left, bottom view of *Injector1* mesh (6 holes); right, *Injector2* (7 holes)

Five 3-D CFD computation cases are considered, that are further divided into two groups, one is formed of a couple of simulations, the other is a set of three simulations; Table 8.1 shows the computation conditions of the first group, whereas Tab.8.2 is referred to the group number 2.

energizing time [ms]	1.150
nominal injection pressure [bar]	1250
back pressure (constant) [bar]	46
type of displ. Injector1 [-]	nominal (axial)
type of displ. Injector2 [-]	nominal (axial)

**Table 8.1:** Computation conditions of 1<sup>st</sup> simulation group

energizing time [ms]	1.150
nominal injection pressure [bar]	1250
back pressure (constant) [bar]	46
type of displ. <i>Injector1</i> [-]	nominal – <i>eccentric1</i>
type of displ. <i>Injector2</i> [-]	reduced – <i>eccentric1</i>
type of displ. <i>Injector2</i> [-]	reduced – <i>eccentric2</i>

**Table 8.2:** Computation conditions of 2<sup>nd</sup> simulation group

As visible in Tab.8.1, the same boundary condition at the hole exit is considered for all cases, represented by a constant pressure value of 4.6 MPa. On the contrary, the inlet condition comes from the 0/1-D computation; it means that the pressure time evolution in the needle delivery chamber during the injection is computed by AMESim model and then it is imposed to the inlet surface of the mesh, performing a transient simulation; two different pressure traces are computed for the two injectors. Table 8.2 indicates that the simulations of the 2<sup>nd</sup> group are characterized by an eccentric lift of the needle; such a condition is imposed in order to evaluate the injector response to a radial perturbation of needle motion; it is worthy to be highlighted that such a deviated direction of the lift is intended to provide indications regarding its effect on the fuel flow, rather than to represent the real needle displacement; in detail, the interest is focused on the hole flow rate variations and on the flow asymmetries in general.

The value of the radial displacement is quantified considering the features of the mechanical coupling between needle and guide; the clearance that characterizes the diameter of the cylindrical guide in respect to needle diameter is used to evaluate the maximum allowed radial displacement of the needle tip, as Fig.8.5 shows (in detail, the values of 4.018 mm and 4 mm have been considered, respectively).

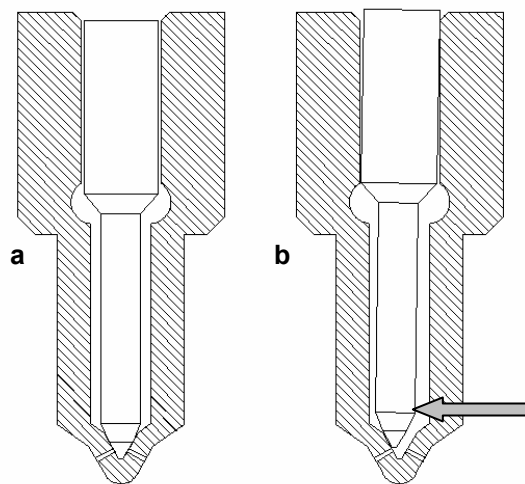


**Figure 8.4:** Needle configuration schemes: **a**, closing position; **b**, full lift position (eccentric)

The eccentric displacement of the needle is modeled considering a deviated direction so that the calculated maximum radial displacement is reached at full lift. Therefore, the needle lift time traces coming from AMESim model are imposed to the needle surface of the computational grid, along a straight line in the plane that cuts in half two opposite nozzles (in case of 6 hole injector); such a direction is identified by the trace *l-m* in Fig.8.5. Even if the evaluation of the lift radial component is based on the needle rotation allowed by the cylindrical constraint, the angular displacement is so small that the movement of the needle tip can be considered as a translation. Concerning the case of *Injector2*, the deviated lift is modeled in two different ways, so distinct radial perturbations can be compared. With *eccentric1* (see Tab.8.2) the same deviated direction used for *Injector1* is adopted; as *Injector 2* has a lower stroke end, a proportional reduction of eccentricity is obtained when the needle is opened. On the contrary, considering *eccentric2*, the lift direction is modified in order to reach the maximum radial displacement (*the same of Injector1*) when the needle is at full lift (Fig. 8.5).

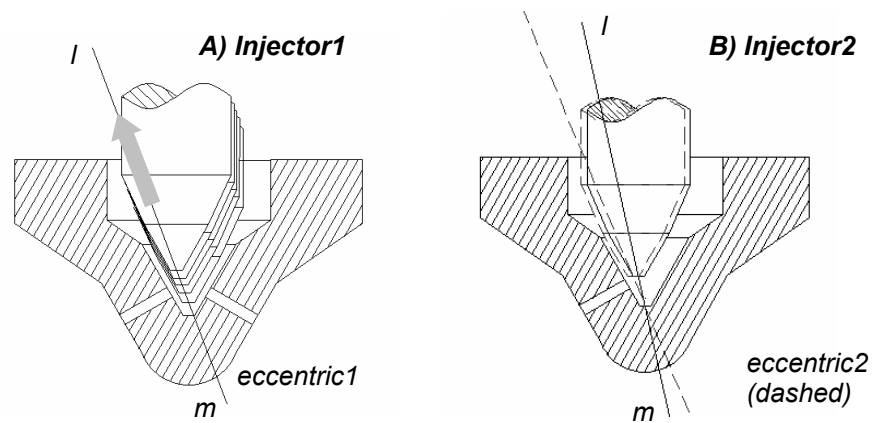


**Figure 8.5:** A) Needle displacement scheme; *l-m* is the displacement direction (*eccentric1*)  
B) Needle displacement scheme; two directions of displacement are alternatively adopted (*eccentric1* and *eccentric2*)

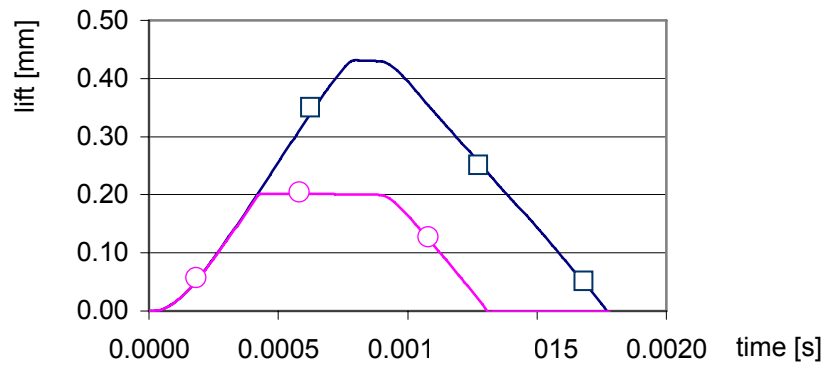
**8.4 Results.** The result paragraph is divided in two sections which are referred to the 0/1-D model and to the 3D-CFD simulation, respectively.

Figure 8.6 shows the needle lift time traces for the two considered injectors, highlighting the maximum stroke end difference; the main effect induced by the reduction of the lift is represented by the relevant decrease of the opening time (in the percentage range of 25-30%); such a circumstance is an advantage in case of multi-event and contiguous injections, in which the reduction of the injection fusion threshold plays a crucial role. The



wider phase in which the needle is at maximum lift can be considered as a positive aspect, because it limits the range in which the nozzle closing delay has a linear dependence on ET. In fact, the larger ET, the longer is the distance covered by needle during its opening lift; therefore, the time employed by the needle to come back to its closure position is longer. However, when ET lasts enough to let the needle reach its mechanical stroke-end (i.e. 0.2 mm for *Injector2*), a further increase in ET does not raise NCD more.

The traces of Fig.8.6 are used to create the dynamic meshes in FIRE environment; it must be mentioned that the 3-D simulation requires the setting of a minimum lift position; in the present case, the value of 10  $\mu\text{m}$  is considered and then subtracted to the lift trace used for the moving mesh generation.



**Figure 8.6:** Needle lift comparison [mm], *Injector1* —□—, *Injector2* —○—

The reaching of the needle stroke end is visible observing the pressure traces, too (Fig. 8.7). The traces represent the pressure time evolution within the needle delivery chamber; the colored arrows point out the maximum lifts, with the resulting onset of relatively high frequency pressure oscillation. As the end of the needle stroke of *Injector1* is delayed in respect to the other; a phase difference affects the two pressure waves, showing the same fundamental frequency and harmonic components anyway. More in detail, the high frequency components are due to the pressure wave propagation in the internal fuel duct between injector inlet and delivery chamber volume. The traces of Fig.8.7 are used as transient boundary conditions at the inlet section of the 3-D meshes.

The injection flow rate produced by the two injectors is depicted in Fig.8.8. As easily visible, the shorter injection length of *Injector2* is in good part balanced by the increased number of nozzle in respect to the case of *Injector1*; the percentage difference of injected volume is bounded below 20%, roughly. The results of Fig.8.8 are compared with those available in literature (Fig.8.9) [5], that are referred to a similar model [3], extensively validated against experimental data. The different injection rate patterns of Fig.8.9 are computed by modifying the mechanical stroke-end values of injector ( $L$ ,  $0.46L$  and  $0.7L$ , where  $L = 0.43$  mm is the value of the mechanical stroke-end for the reference injector).

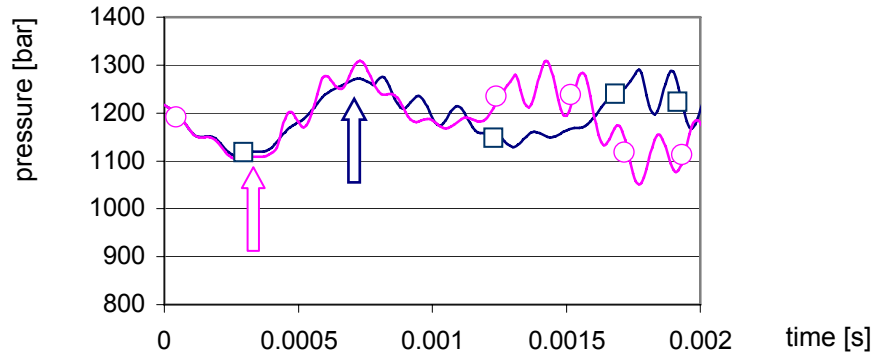


**Figure 8.7:** Pressure [bar] in injector delivery chamber, *Injector1* —□—, *Injector2* —○—

The curves are referred to a double-shot injection; it is visible that a lower mechanical stroke-end, diminishing the maximum needle lift, reduces NCD and produces two fusion free consecutive injections

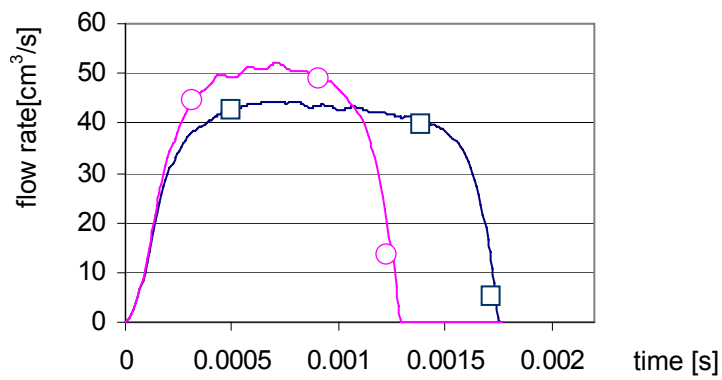


**Figure 8.8:** Injection flow rate [ $\text{cm}^3/\text{s}$ ], *Injector1* —□—, *Injector2* —○—

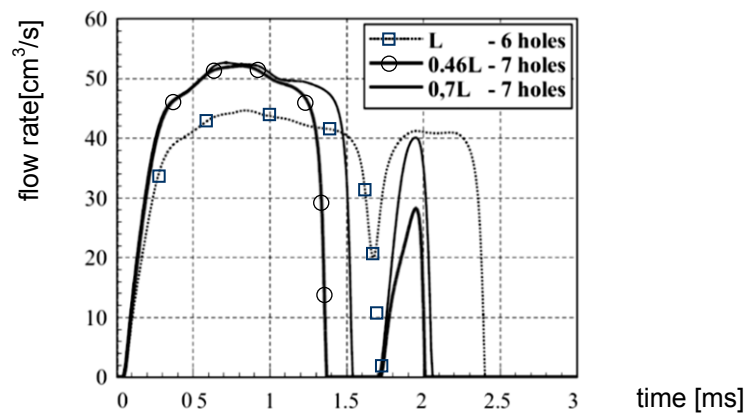


**Figure 8.9:** Needle mechanical stroke-end effect on injection fusion threshold [5]

Results of Fig.8.8 show a good agreement with the main injection traces of Fig.8.9, indicating a satisfactory representation of the typical injection phenomena.

From here on, the indications obtained by the 3-D CFD models are shown; initially the results referred to the pure axial needle stroke are discussed (1<sup>st</sup> simulation group); afterwards, the attention moves to those in which the lift of the needle is affected by a radial perturbation; the comparison among three different cases is then outlined (2<sup>nd</sup> simulation group). In Fig.8.10, the six-hole injector (*Injector1*) is opened at stroke-end; the picture shows the scalar velocity field (on the left) and the map of the liquid/vapor volume fraction (on the right). In analogous way, Fig.8.11 shows the results obtained in case of the seven-hole injector (*Injector2*), whose stroke-end is evidently lower. Comparing the figures, it is possible to observe the features of each fuel flow, pointing out the main differences. The reduction of the needle stroke makes narrow the cross section of the opening (passage between conical needle surface and seat) as highlighted by the arrows of Figs.8.10-8.11; such a condition makes faster the fuel upstream the holes for all the injection process, influencing the flow features at the inlet of the nozzles. Therefore, the flow that enters the hole of *Injector2* seems to turn with more difficulties in respect to that of *Injector1*, as shows the presence of a recirculation zone downstream the hole inlet (dashed arrow in Fig.8.11). The shape of the cavitating regions reflects the described effect; in *Injector1*, the vapor inception is localized along the whole nozzle edge, so that in Fig.8.10, from both the inlet corners a vapor plume arises; it attests (in accordance with the direction of velocity vectors – not shown here) that the entering flow is almost parallel to the axis of the nozzle.

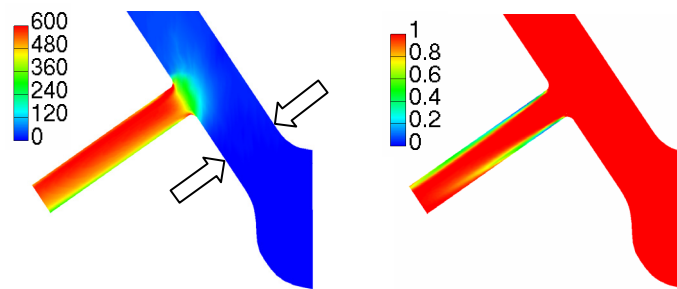


**Figure 8.10:** *Injector1* at full lift. Left, scalar velocity field [m/s]; right, liquid/vapor volume fraction

In *Injector2*, the inception of cavitation is localized in correspondence of the higher part of the inlet edge and the vapor development seems to be more intense, as the liquid/vapor volume fraction within the cavitating region reaches smaller values compared to those of *Injector1*. Such a flow difference characterizes all the central phase of injection, in which the needle of *Injector2* is at full lift.

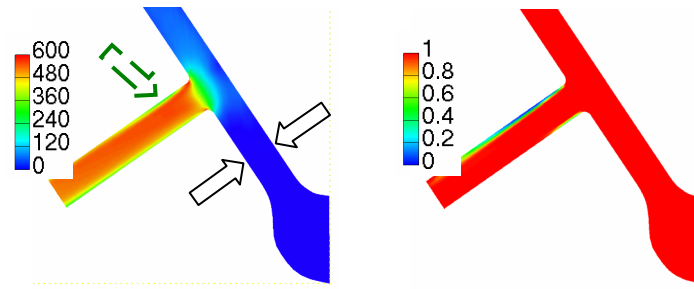


**Figure 8.11:** *Injector2* at full lift. Left, scalar velocity field [m/s]; right, liquid/vapor volume fraction

The response to the radial perturbations in each of the considered configurations (2<sup>nd</sup> simulation group) is observed from different points of view; a qualitative estimation is provided through the observation of velocity fields, streamline shape and cavitation behavior; a quantitative characterization is then outlined by taking into account the mean exit flow velocity and computing the hole to hole variations.

Concerning the standard injector (*Injector1*), Fig.8.12 shows a sequence that gives an idea of the time evolution of fuel injection. The asymmetry of velocity field characterizes the flow during the whole process, as visible in each image of the figure; the effects of the asymmetry appear in the nozzle holes mainly, in terms of flow direction and speed, which is slowed down by the narrowing of the passage and accelerated at opposite side. The perturbation induced by the asymmetry involves the localisation of the cavitation inception points; in the present case, the hole that is more approached by the needle is characterized by a flow that enters almost parallel to the hole axis, whereas the opposite hole is fed by an up to down stream, mainly. Such a flow field structure is responsible for different positions of the cavitation inception points (highlighted by arrows at 0.45 & 0.90 ms ASOI, Fig.8.12) within the opposite holes: top inlet corner in case of right side hole, diffused along the whole edge concerning the hole that is most approached by the needle. The streamline representation of Fig.8.15 (referred to *Injector1*) is useful to better understand the flow field structure; downstream the right side hole, the presence of an eddy contributes to the formation of a fuel stream that, from the bottom of the tip, rises towards the opposite hole, influencing the direction of the entering fuel. Two pictures of Fig.8.12 are devoted to show the flow field on a plane that cuts the injector axis; besides the asymmetries of the scalar velocity field, no negligible differences in the location of cavitation inception points are visible, being worthy to be deeply analyzed in further investigations.

The attention is now moved to the results that refer to *Injector2* (Fig.8.13), in which the lift keeps the same deviated direction of the previous case (*eccentric1*). Clearly, hole number being odd, the radial component of the lift is on a plane that contains just the axis of one nozzle (the most approached by the needle in the present case), so the

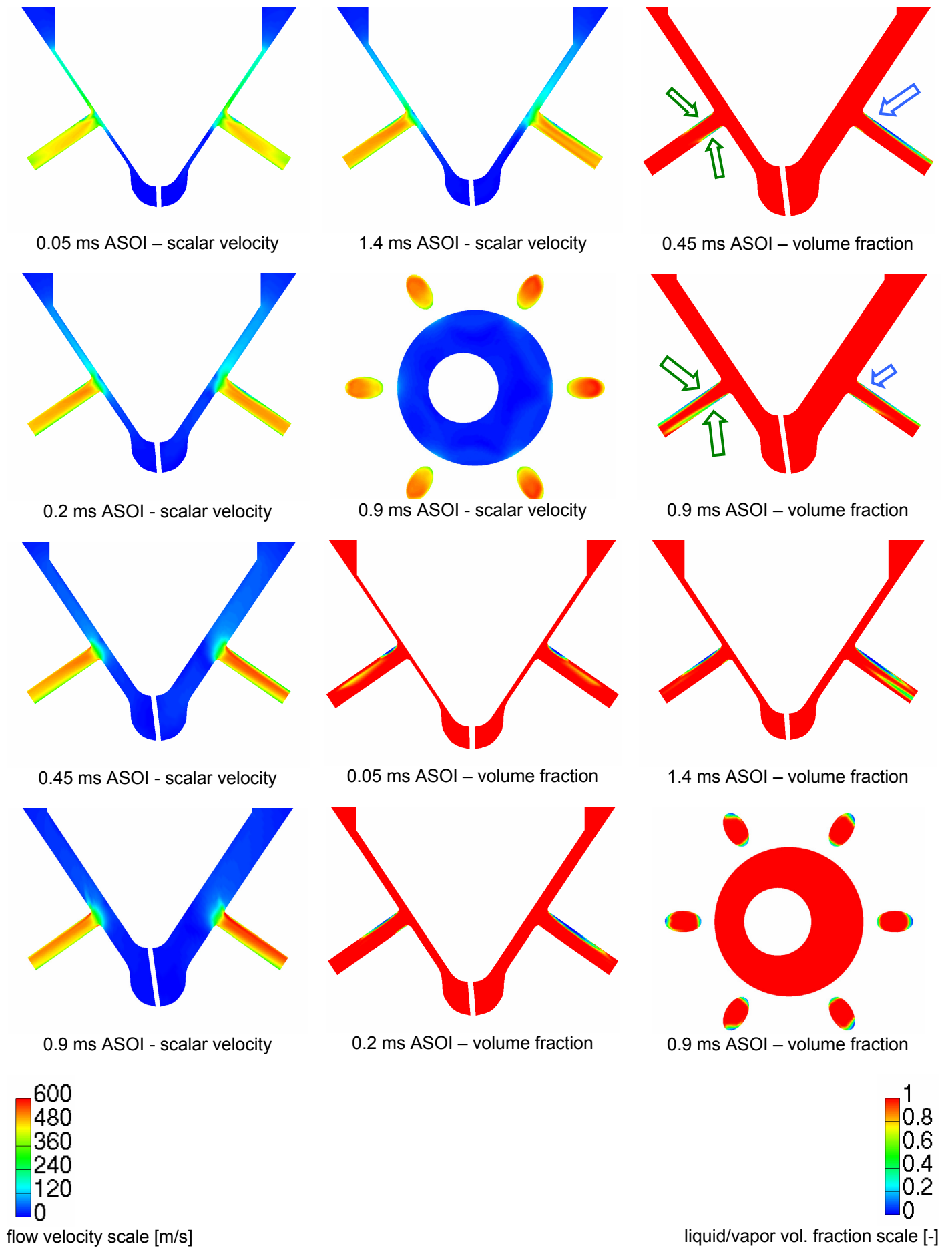


**Figure 8.12:** *Injector1*, 3D results referred to *eccentric1* lift

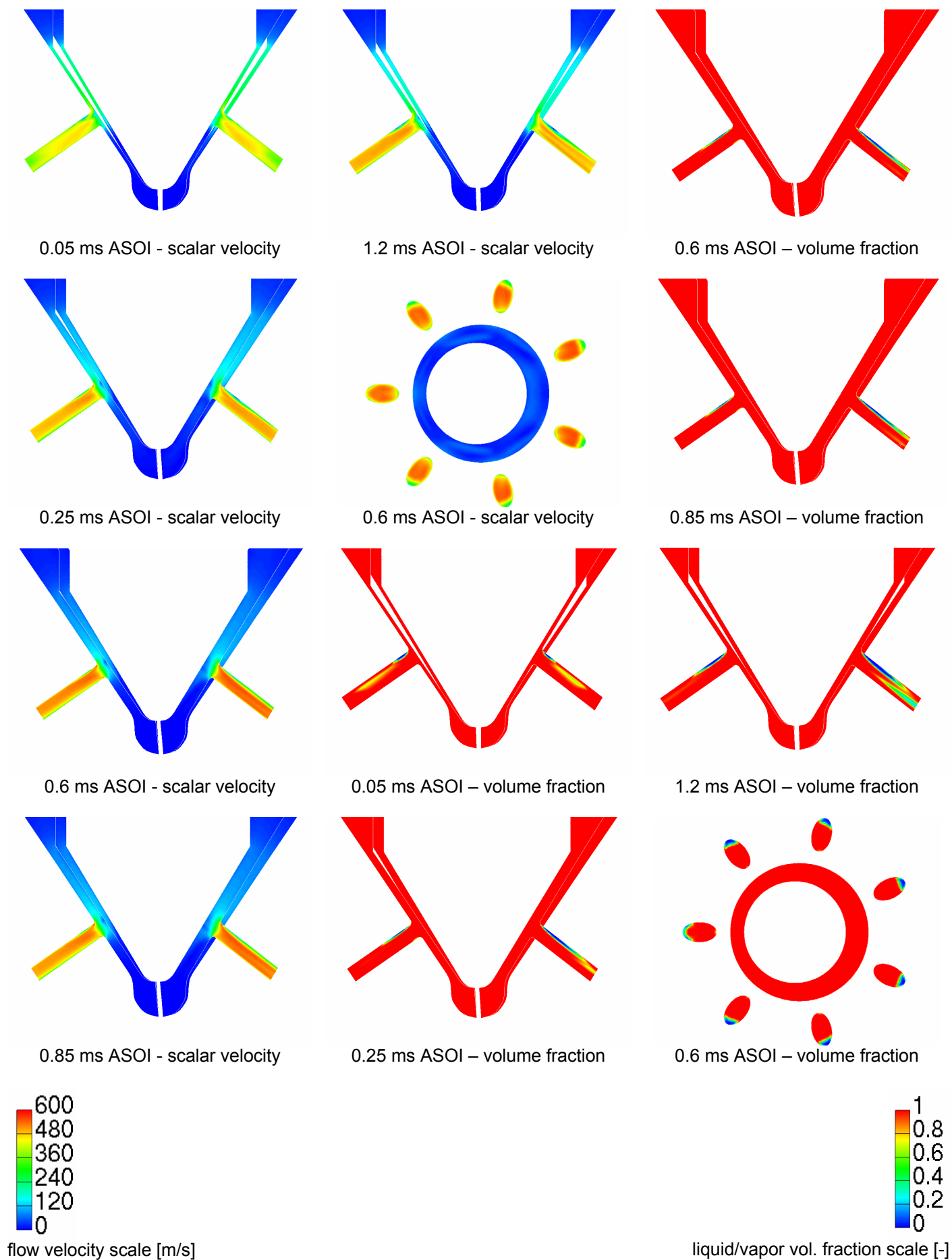


**Figure 8.13:** *Injector2*, 3D results referred to *eccentric1* lift

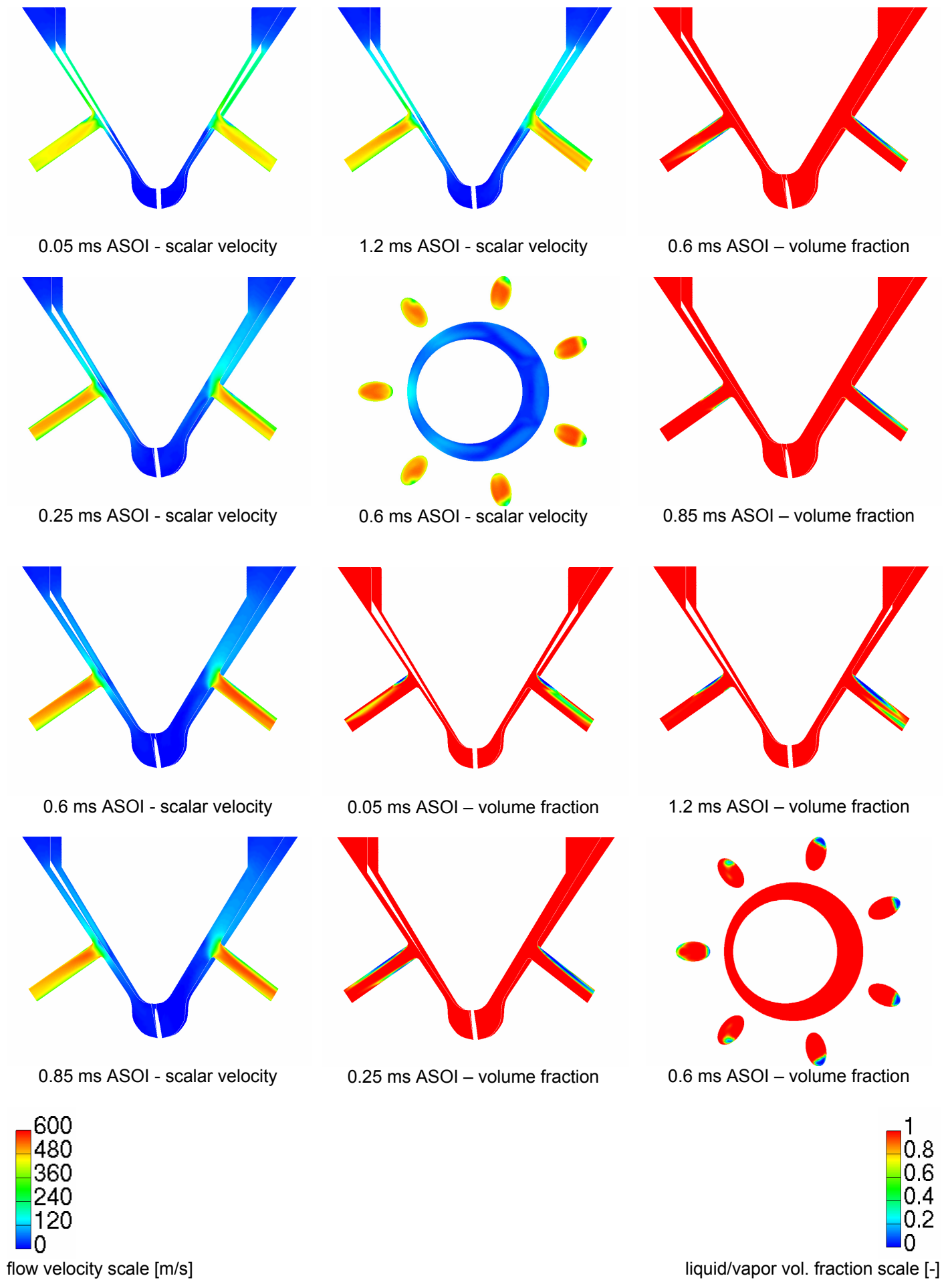


**Figure 8.14:** *Injector2*, 3D results referred to *eccentric2* lift



**Figure 8.15 (left):** *Injector1* at full *eccentric 1* lift, streamlines

**Figure 8.16 (right):** *Injector2* at full *eccentric 1* lift, streamlines

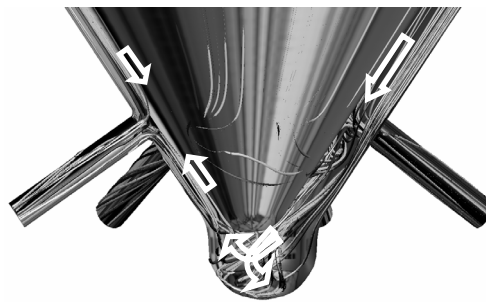


**Figure 8.17:** *Injector2* at full *eccentric 2* lift, streamlines

results are now displayed on a couple of different planes. The lower stroke-end value goes with a proportional reduction of the eccentricity at full lift; a general decrease of the hole to hole differences is visible. The shape of the scalar flow field within the two opposite holes shows closer behaviors; it is interesting to note that the lower lift tends to accelerate the fuel in the seat passage, whose influence on the flow direction at the nozzle inlet has been discussed already. Therefore, fuel streams turn less easily and such a condition is reflected, in turn, by the shape of the vapor zones, even in this case; so, the inception zones are visible on the top corners of both visualized nozzles. The flow line trend is depicted in Fig.8.16; it gives a more complete description of the flow, showing the presence of two main streams that roughly turn to enter the holes; macroscopic eddies are not present and the flow around the needle tip is not promoted, as in the previous case.

Finally the behavior of the last injector configuration (*Injector2 – eccentric2*) is analyzed; if compared to the previous two cases, the obtained results are characterized by intermediate characteristics (Fig.8.14); the effects due to the restriction of the stroke-end (*Injector2 – eccentric1*) are now weakened by the rise of the lift radial component, that has the capability to influence the flow condition at nozzle inlet, as previously highlighted. Focusing the attention on the scalar velocity field, a just slightly accelerated flow passes through the widest passage, in contrast with the opposite (left) side (the eccentricity effect



weights more in respect to the previous case). The inception of cavitation involves more easily the bottom of the inlet edge, during the central phase of the process. Looking at Fig.8.17, as pointed out by the arrows, a behavior that resemble the first case can be found; a fraction of the flow rate coming from the wider side moves around the needle tip, matching the flow that enters the opposite hole. However, in this case, eddies are no longer formed due to the small lift value, reasonably.

With the aim to provide a quantitative indication about the discussed results, for each of the considered configurations of the 2<sup>nd</sup> simulation group, the mean fuel velocities at the outlet section of the nozzles are collected; the hole to hole difference of each considered couple (Fig.8.18) is then evaluated.

Making a comparison among the traces of Fig.8.18, besides the quantitative evaluation of the flow imbalances produced by the three modeled cases, it is possible to consider two further facets. The former one is that the modified injector layout tends to decrease the hole to hole velocity variations (blue vs. pink and green curves); moreover, the higher radial component the higher is the flow imbalance (pink and green curves to be compared). The latter facet is that, in any considered case, flow imbalance seems to grow whether lift grows (especially as regards *Injector1*); such a feature is turned out to be in contrast with the behavior of minisac injectors, whose response to radial perturbation has been investigated by the authors in a previous work [9] (% velocity difference tends to zero in the central phase of injection, being in the order of 8% during early opening and closing phases). An explanation for such a different response can be found in the fact that VCO injectors do not have an intermediate volume (between conical seat and nozzle) capable of attenuating flow asymmetries; on the contrary, nozzles are fed *directly* by the flow passing along the conical seat, being more sensitive to any flow perturbation.

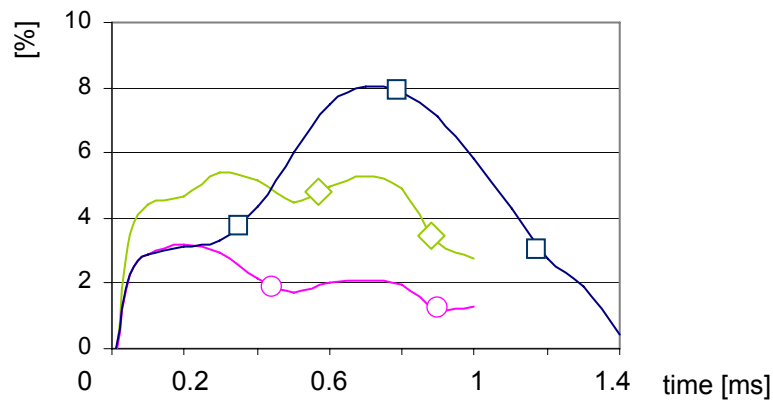


**Figure 8.18:** % nozzle mean outlet velocity difference  
*Injector1 eccentric1* —□—, *Injector2 eccentric1* —○—, *Injector2 eccentric2* —◇—

**8.5 Concluding remarks.** A 3-D CFD analysis of nozzle fluid dynamics is carried out, in order to evaluate the flow field and cavitation in the VCO nozzle of an injector with reduced maximum needle lift and one additional nozzle hole, in comparison to the standard layout. The effect of a radial perturbation of the needle lift is evaluated for both injector layouts, too.

The operating differences between the standard injector and the modified one are shown by the 0/1-D model of injection system. The obtained results are used to perform a (transient) 3-D CFD investigation, providing a deep insight into the nozzle flow features. The 3-D model highlights the fuel flow features inside the injectors. The reduction of the lift influences the localization of cavitation inception zones, forcing the flow to turn roughly to enter the holes. The modified injector retains an improved response to radial perturbation, showing a smaller hole to hole velocity variation. Concerning the value of eccentricity, the higher radial component the higher results the flow imbalance.

### 8.6 Nomenclature

$A_i''$	=	interfacial area density
$D_b$	=	bubble diameter
$C_{CR}$	=	condensation reduction factor
$C_D$	=	drag coefficient
$C_E$	=	Egler coefficient
$C_{TD}$	=	drag turbulent coefficient
ET	=	Energizing Time
$M_c$	=	vapor phase momentum
$M_d$	=	liquid phase momentum
$N_0''$	=	initial bubble number density
$N'''$	=	number density
NCD	=	Needle Closing Delay
$R$	=	bubble radius
$Re_b$	=	bubble Reynolds number
SOI	=	Start Of Injection
$k_c$	=	vapor phase turbulence kinetic energy
$p_{sat}$	=	saturation pressure
$\mathbf{v}_c$	=	vapor velocity
$\mathbf{v}_d$	=	liquid phase velocity
$\mathbf{v}_r$	=	relative velocity

### Greek symbols

$\Gamma_c$	=	vapor phase mass
$\Gamma_d$	=	liquid phase mass
$\Delta p$	=	pressure difference
$\alpha_d$	=	liquid phase volume fraction

$\rho_c$  = vapor phase density  
 $\rho_d$  = liquid phase density

## 8.7 References

- [1] Baratta, M., Catania, A. and Ferrari, A., "Hydraulic Circuit Design Keys to Remove the Dependence of the Injected Fuel Amount on Dwell Time in Multi-Jet C.R. Systems ", ICES2006 ASME Paper No. 1426.
- [2] Catania, A., Ferrari, A., Manno, M. and Spessa, E., "Experimental Investigation of Dynamics Effects on Multiple-Injection Common Rail System Performance", ICES2005 ASME Paper No. 1108.
- [3] Catania, A., Ferrari, A. and Manno, M., "Development and Application of a Complete Common-Rail Injection System Mathematical Model for Hydrodynamic Analysis and Diagnostics", ICES2005 ASME Paper No. 1018.
- [4] Catania, A., Ferrari, A., Mittica, A. and Spessa, E., "Common Rail without Accumulator: Development, Theoretical-Experimental Analysis and Performance Enhancement at a DI-HCCI Level of a new Generation FIS", SAE Paper No. 2007-01-1258.
- [5] Catania, A., Ferrari, A. and Spessa, E., "Numerical-Experimental Study and Solutions to Reduce the Dwell Time Threshold for Fusion-Free Consecutive Injections in a Multijet Solenoid-Type C.R. System", ICES2006 ASME Paper No. 1369
- [6] Imagine AMESim v4.2 Tutorial and User Guide, AMESim Technical Bulletins.
- [7] FIRE v8.5 CFDWM Guide, AVL List GmbH.
- [8] Fezzaa, K., Lee, W.K., Cheong, S., Powell, C.F., Wang, J., Li, M. and Lai, M.C., "High Pressure Diesel Injection Studied by Time-Resolved X-Ray Phase Contrast Imaging", ICES2006 ASME Paper No. 1409.
- [9] Chiavola, O. and Palmieri, F., "Modeling Needle Motion Influence on Nozzle Flow in High Pressure Injection System", SAE Paper No. 2007-01-0250.
- [10] Zielke W., "Frequency-dependent friction in transient pipe flow", Trans. ASME J. Basic Eng, 90, 109-115, 1968.
- [11] Samada, C.W. Richards, et al., "A finite element model of hydraulic pipelines using an optimized interlacing grid system", ImechE, 1993.
- [12] Giannadakis, E., "Modelling of Cavitation in Automotive Fuel Injector Nozzles", PhD thesis, Imperial College London, UK 2006.
- [13] Giannadakis, E., Papoulias, D., Gavaises, M., Arcoumanis, C., Soteriou, C. and Tang, W., "Evaluation of Predictive Capability of Diesel Nozzle Cavitation Models", SAE Paper No. 2007-01-0245.
- [14] FIRE v8.4 Multiphase Manual, AVL List GmbH.
- [15] Tatschl, R., v. Künsberg-Sarre, C., Alajbegovic, A. and Winklhofer, E., "Diesel Spray Modeling Including Multidimensional Cavitation Nozzle Flow Effects", Proc. of ILASS Europe Conference, Sept. 11-13, Darmstadt, Germany, 2000.
- [16] Hinze, J.O., "Turbulence", 2<sup>nd</sup> ed., McGraw-Hill, New York, 1975.  
 Franklin, R.E. and McMillan, J., "Noise Generation in Cavitating Flows", J. Fluids Eng., 106, 336-341, 1984.

## **9. Inline Pump Internal Flow Characterization For Optimized Diesel Injection – 3D-CFD Evaluation of Pump Passages Discharge Coefficients**

**9.1 Introduction.** Small diesel engines are largely used in industry and agriculture. Reliability and cost effectiveness are often key features of such a kind of engines. In several applications, sophisticated electronic or electric devices (common in automotive field) cannot be used; furthermore, especially for the smaller units, battery lack is often necessary or recommended (e.g. manual start). If reliability is preferred to absolute performance, these engines are equipped with relatively simple auxiliary components. Nonetheless, the pollutant emission standards define limits that must be strictly satisfied. Therefore, simple engine layouts do not mean obsolete technology; on the contrary, accurate research and development activities are required to match reliability, cost effectiveness and emission standard accordance. As exhaust-gas after-treatment systems cannot be easily used (for the already described reason), the in-chamber pollutant formation control is pre-eminent. In such a frame of reference, fuel-air mixing process plays a major role and it is deeply influenced by the injection strategy. More in detail, the engine performance is widely influenced by the ensemble inline pump-delivery valve; as known, injected fuel amounts, fuel pressure level and process length are reciprocally related. Engine operation is controlled by the positioning of the helicoidal groove, whose rotation angle defines engine load, injection phase and pressure evolution. Interesting investigations, available in literature [1-3], focus the transient phenomena due to the delivery valve displacement, in terms of fuel pressure oscillation. Moreover, undesired phenomena like injector needle re-opening and in-pipe cavitation can affect negatively the system operation; on such a topic, some authors [4] show the influence of the component design on the fuel injection process. Numerical analyses evidence the design optimization effect on cavitation onset and needle dynamics; in this case [4], the authors found the investigation on a lumped/1D injection system model. The model is based on the indications obtained by a fluid-dynamic characterization of the most influencing components (in terms of discharge coefficient evaluation). In the present paper, the attention is focused on a single-cylinder diesel engine. It is equipped with a fully mechanical injection system, composed of spring-injector, inline pump, delivery valve and high pressure pipe. The aim of the work is to evaluate the influence of fuel characteristics on the system operation (in terms of fuel rate time evolution and injected amount). On the basis of the indications obtained by 3D CFD investigations, a lumped/1D model of the complete system is built; indeed, the discharge coefficients needed by the lumped approach are evaluated by means of 3D numerical experiments, allowing for a detailed component characterization. The results predicted by the complete system

model (line-pressure time evolution) are compared to experimental data (referred to a conventional diesel fuel – named diesel1). The lumped model, validated against experimental data, is then used to predict the effect of the fuel characteristics on the process; as in the previous case, preliminary 3D CFD investigations are devoted to characterize discharge coefficients for the second fuel, whose properties are chosen to match those of bio-diesel (named diesel2 for the sake of simplicity).

**9.2 Fuel injection system.** The main technical data of the fuel injection system under investigation are summarized in Tab.9.1. It is made up of an inline pump, a minisac nozzle-hole type injector and connecting high pressure pipe. Fuel pump is equipped with a delivery valve; the system is designed to reach a nominal injection pressure of 800 bar at maximum load and power. Table 9.2 shows the main features of the considered engine.

type	cam-driven system
pump plunger diameter [mm]	7
plunger stroke [mm]	8
number of nozzle holes	5
diameter of nozzle holes [mm]	0.159

**Table 9.1:** Specifications of fuel injection system

type	direct injection
bore [mm]	82
stroke [mm]	76
max engine speed [rpm]	3000

**Table 9.2:** Specifications of diesel engine

**9.3 Lumped/1D approach.** The lumped/1D modeling of a real system is related to many interesting issues; a valid sketch of the system has to be identified, highlighting the operating role of each considered component. Each element of the system has to be successively represented by means of a physical model; such a model must have the capability to give an adequate representation of the meaningful element operation phenomena; physical models are finally translated to mathematical equations, whose solution provides the results. By using commercial computation codes, such a procedure is often made easier by the availability of rich software libraries; pre-defined elemental components like valves, springs, pistons, masses and orifices are associated to a wide class of physical sub-models that help the modeling of the system. In the adopted scheme, pressure and temperature in lumped volume elements are just time dependent, whereas the high pressure pipeline model is based on a one-dimensional scheme in which wave equation is used to account for inertia, friction and compressibility effects.

Beside the possibility of quickly identifying a valid physical model of the system and of solving the related equations, the correct use of constants and parameters seems to be crucial; in the mechanic-hydraulic modeling, a typical issue concerns the correct choice of the discharge coefficients; indeed, they have a relevant influence on the flow evaluation through fixed or variable orifices.

**9.3.1 Flow through orifices modeling.** The mathematical description of the flow through orifices is based on Bernoulli's equation; it leads to the form

$$Q = C_d A \sqrt{\frac{2|\Delta p|}{\rho}} \text{sign}(\Delta p) \quad (1)$$

where  $C_d$  is the discharge coefficient, whose value varies with orifice geometry and Reynolds number; indeed, for sufficiently small pressure differences flow is laminar, which means that  $C_d$  is not constant. More in detail, the adopted simulation code represents the variation of  $C_d$  by means of the following hyperbolic function [5,6,7]

$$C_d = C_{dm} \tanh\left(\frac{2\lambda}{\lambda_{crit}}\right) \quad (2)$$

in which appear the constants  $C_{dm}$ ,  $\lambda_{crit}$  and the dimensionless number  $\lambda$ , defined as follows

$$\lambda = \frac{D_h}{\mu} \sqrt{\frac{2|\Delta p|}{\rho}} \quad (3)$$

As the experimental investigations show that, for high values of  $\lambda$ ,  $C_d$  is approximately constant,  $C_{dmax}$  indicates the limiting value of  $C_d$ . The constant  $\lambda_{crit}$  is defined as the value of the dimensionless number  $\lambda$  when  $C_d$  is 96% of  $C_{dmax}$ . In order to use such a modeling scheme for the flow rate evaluation, it is necessary to know the values of the two constants  $C_{dm}$  and  $\lambda_{crit}$ . In principle, the values can be obtained through experimental activities, on the basis of the data available in the literature or by means of numerical investigations; in the present case, a 3D CFD code [8] is used to model the flows through the most influencing fuel passages (in detail, delivery valve, plunger spill port, and nozzle orifices are simulated), aiming at drawing the function  $C_d = C_d(\lambda)$  for the considered components (fuel pump, delivery valve and nozzle holes). Concerning fixed orifices, dimensionless number  $\lambda$  is considered as a function of the pressure difference,  $D_h$  being univocally defined; therefore, numerical investigations for nozzle holes are made for different pressure levels, characterizing the discharge coefficient value versus pressure difference. In case of variable orifices or passages (like those of inline pump and delivery valve), dimensionless number  $\lambda$  is considered to be a function of pressure and geometry; therefore, numerical experiments are made varying both pressure difference and orifice opening; even for variable orifices, the adopted model (eq.2) requires to use a single representative value for  $C_{dmax}$  and  $\lambda_{crit}$ .

At each time step (and for the actual geometric configuration of the variable orifice), the solution procedure of the lumped/1D model [5] allows the computation of the

dimensionless value of  $\lambda$  from eq. (3); then  $C_d$  is evaluated according to eq. (2) in order to finally use eq. (1) and compute the flow rate.

Figure 9.1 shows the injection system sketch in AMESim environment.

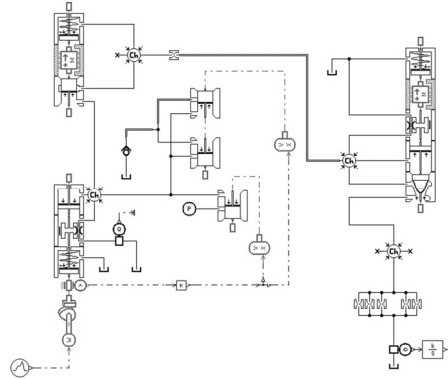


**Figure 9.3:** Injection system sketch in AMESim environment

**9.3.2 3D flow analysis.** Computations are based on RANS approach and standard  $k-\epsilon$  closure is adopted. Cavitation effects are taken into account by means of an Euler-Euler model (two-fluid method). It is a *mechanical* model, based on the assumption that cavitation is a mechanically driven phenomenon, initiated by the presence of nuclei able to grow to form bubbles. Fuel is treated as incompressible, and each phase, liquid and vapor, is governed by a set of conservation equations. Details of the model are provided by “Appendix A” section.

In order to obtain both reliable results and bound computational effort, a preliminary computing phase comes before the 3D flow characterization. Simulations are devoted to identify the convenient computation setting and mesh refinement; spatial cell arrangement influence (e.g. local refinements) is evaluated, too. For each considered component, different grid refinements are tested in the preliminary phase and the results are compared in terms of predicted mass flow rate, magnitude deviation of local pressure values and velocity field features. The tested grid types together with the min/max and adopted cell number are listed in Tab.9.3.

component/mesh type	min. cell number	max. cell number	<b>adopted</b> cell number
delivery valve/hexahedral-structured	25000	500000	120000
plunger spill port/ hexahedral-unstructured	32000	600000	250000
nozzle/ hexahedral-structured	12000	360000	86000

**Table 9.3:** Grid properties and adopted refinements

Moreover, other preliminary computations are performed in order to point out the coupling influence of the 3-D simulation of the fuel passages with the lumped system-based model. Results and more details of the system-based model without the use of the 3-D CFD data are shown in “Appendix B” section.

The results of the next sub-section show the behavior of each component in meaningful operating conditions, in terms of pressure differences and geometric arrangement.

**9.3.3 Discharge coefficient evaluation.** In the following, the discharge coefficient traces obtained by the 3D simulations are summarized; for each component, the results referred to the two considered fuels are shown; Tab.9.4 reports the property differences.

fuel type	density [kg/m <sup>3</sup> ]	bulk modulus [bar]	dynamic viscosity [Pa s]
diesel1	800	15000	0.00172
diesel2	850	19000	0.00425

**Table 9.4:** Fuel properties

Figure 9.2 shows the delivery valve discharge coefficient traces; the values are computed by varying the opening of the valve (expressed as fraction of the maximum opening stroke in the abscissa axis), pressure difference being constant; equation (1) is used and the coefficients are referred to a fixed reference “A” cross section. The computation is made for three different values of pressure difference, as the caption suggests. Pressure values are chosen aimed at simulating realistic operating conditions of the component. In case of diesel1 fuel, discharge coefficient is slightly dependent of pressure difference; the three group of results are almost coincident and they can be easily be represented by the single continuum line of Fig.9.2; such a trace is then used to indicate the maximum discharge coefficient and the critical dimensionless number  $\lambda_{crit}$ , required by the lumped sub-models for flow rate computation.

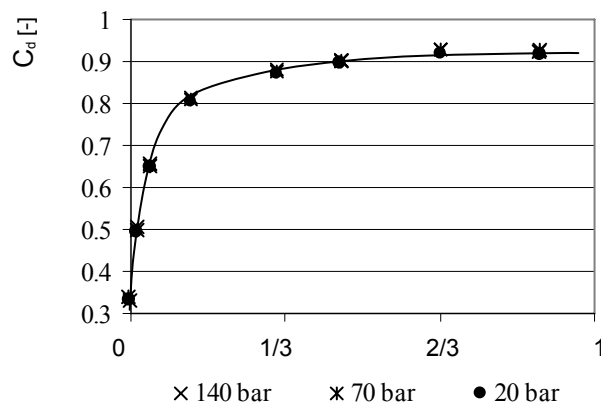


**Figure 9.2:** Delivery valve discharge coefficients vs. opening stroke fraction, diesel1 fuel



Results of Fig.9.3 are referred to diesel2 fuel; they are affected by a more appreciable dependence on the pressure difference, due to the higher value of viscosity; results are resumed through a continuum line, whose position is conceived as representative of a weighted intermediate behavior among the found trends. In respect to the diesel1 fuel, a lower maximum discharge coefficient is obtained, which is bound to 0.9. Figure 9.4 shows the sectioned delivery valve computation grid (it is represented at full lift condition).

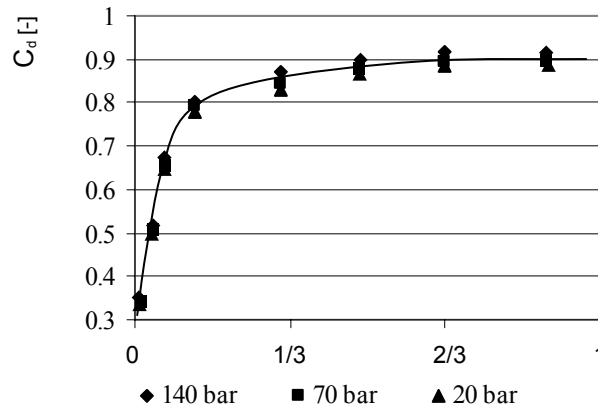


**Figure 9.3:** Delivery valve discharge coefficients vs. opening stroke fraction, diesel2 fuel

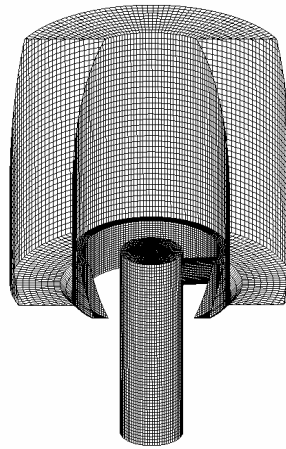


**Figure 9.4:** Delivery valve computation grid

Figures 9.5 and 9.6 are referred to the pump spill port discharge coefficients; as in the previous case, they are evaluated according to equation (1) and are referred to a fixed reference section “ $\tilde{A}$ ”. Simulations are made for a relatively wide range of pressure differences (from 5 to 500 bar). During the early instants of the port opening, spill hole and plunger grooves (shown in Fig.9.7) are characterized by the maximum pressure difference at boundary (the opening of the spill port is used to cut the fuel delivery). Clearly, pressure difference drops quickly to null during the opening. Discharge coefficient are evaluated for different opening conditions of the port (expressed as fraction of the

maximum opening stroke in abscissa axis), pressure level being equal. Results produce three groups of solutions for each considered fuel like in the previous case. Figure 9.5 shows the behavior induced by the diesel1 fuel. In respect to the values of Fig.9.6 (diesel2 fuel), it is visible a lower dependence on pressure difference; taking into account such a feature, the trends are summarized so that maximum discharge coefficient assumes a weakly higher value as regards diesel1 fuel.

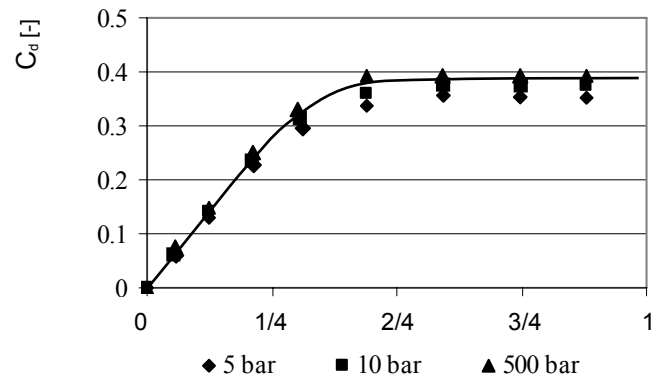


**Figure 9.5:** Pump spill port discharge coefficients vs. opening stroke fraction, diesel1 fuel

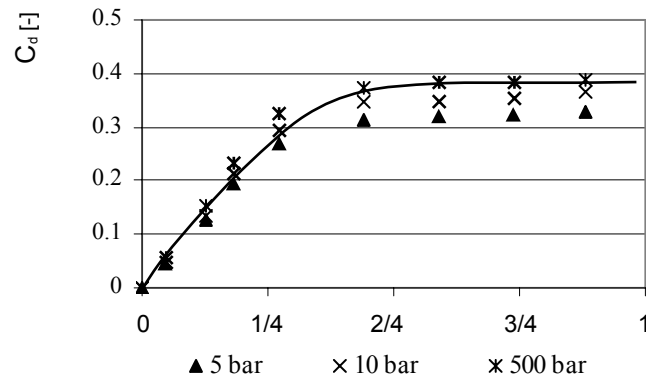


**Figure 9.6:** Pump spill port discharge coefficients vs. opening stroke fraction, diesel2 fuel

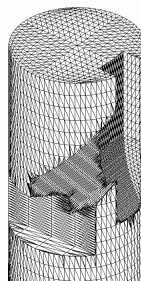


**Figure 9.7:** View of the plunger grooves on plunger surface

Concerning the flow characterization of the nozzle holes (fixed orifices), simulation are performed by varying the boundary pressure (from 50 to 600 bar). In Fig.9.8, discharge coefficients are plotted versus dimensionless number  $\lambda$ ; in case of diesel1 fuel, discharge coefficients are higher, in agreement with the previously observed results.

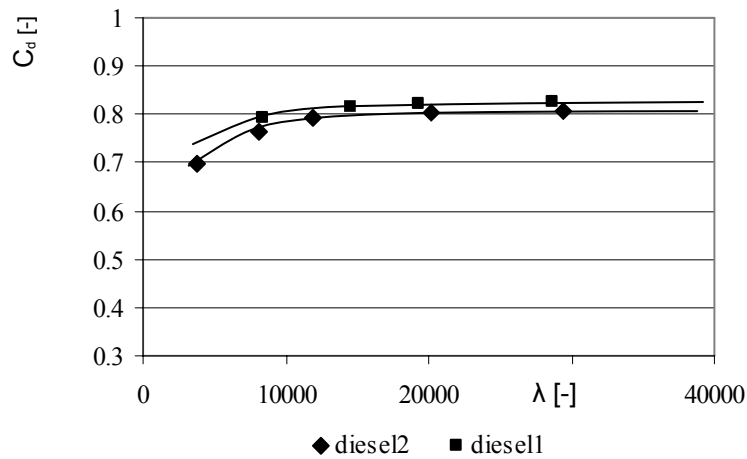


**Figure 9.8:** Nozzle hole discharge coefficients

**9.4 Simulated system performance.** From here on, the results obtained by the lumped system model (with the use of the CFD data) are discussed. Figure 9.9 shows a comparison between the experimental measured line-pressure and the numerical one (the curves are referred to diesel1 fuel). Line-pressure is measured at a distance of 25mm from the injector inlet (engine at 3000rpm, maximum load). Predicted pressure and experimental one are characterized by very good agreement. Figure 9.10 is referred to the same comparison of Fig.9.9, but it differs from the previous about engine speed (2200rpm); a good agreement between the traces is visible in this case, too; reasonably, pressure trace at 2200rpm differs from the one at 3000rpm, showing lower peak and slope.

After the comparison against the measured pressure trends, the model is used in predictive manner, in order to evaluate the influence of fuel properties on the injection process. Injected amounts and injection time evolution are considered to be representative of the process behavior.

Curves of Fig.9.11 show the comparison between line-pressure, simulating diesel1 and diesel2 fuels; diesel2 (characterized by higher bulk modulus) induces a steeper pressure rising; peak value is higher, too (~750 bar vs. ~680 bar). Such differences have influence on the process; looking at the same figure (9.11) it is possible to observe the needle lift time trace, whose behavior reflects the pressure history. In case

of diesel2 fuel, injection process starts in advance; even if the needle closure is anticipated, the duration of the process is longer.

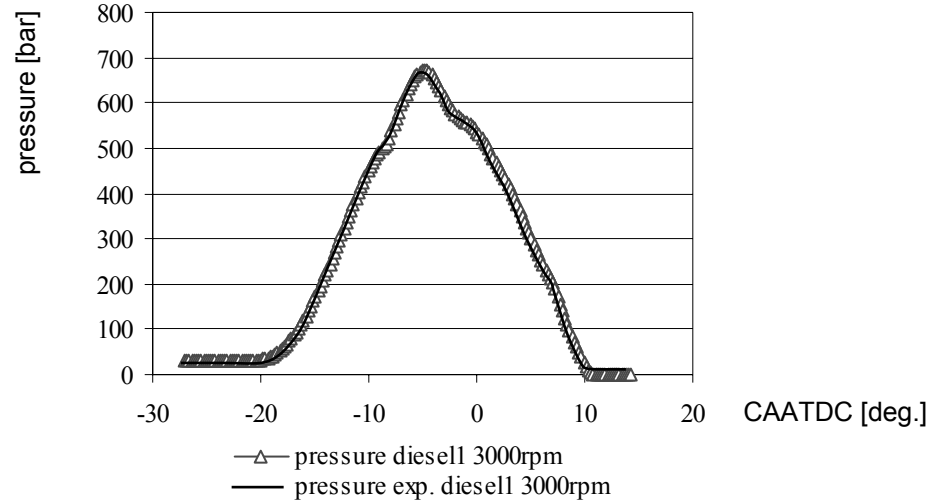


**Figure 9.9:** Line-pressure at 3000rpm, comparison between experimental and numerical results

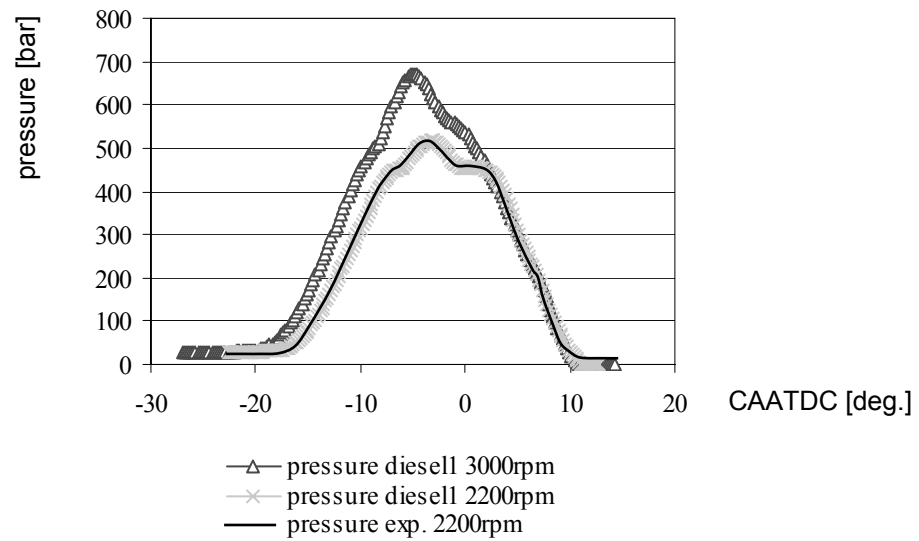


**Figure 9.10:** Line-pressure at 2200rpm, comparison between experimental and numerical results

The injected flow rate time evolution is represented by curves of Fig.9.12; their shape is closely related to the pressure evolution and they point out the prevalence of the diesel2

injection over the other fuel; higher peak value and longer process are due to the combined effect of injection pressure and needle opening.

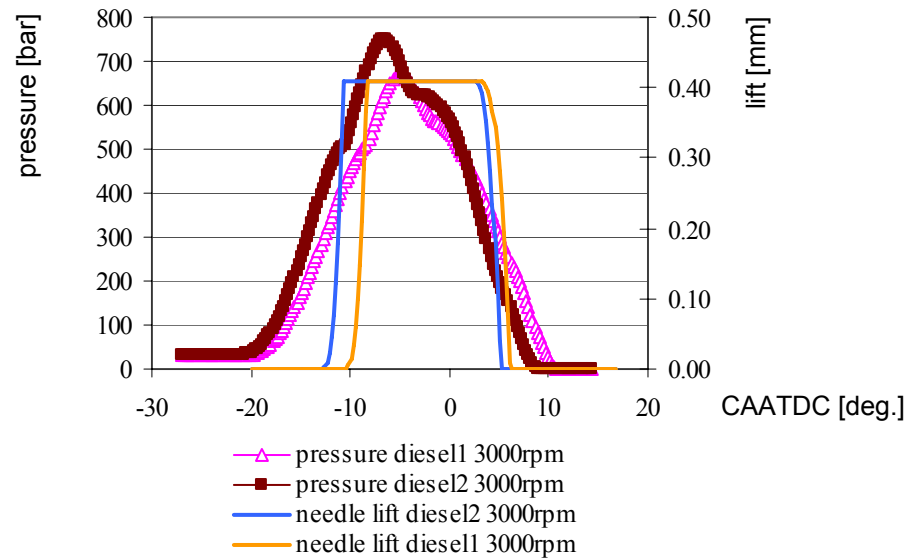


**Figure 9.11:** Simulated line-pressure at 3000rpm and needle lift; influence of fuel

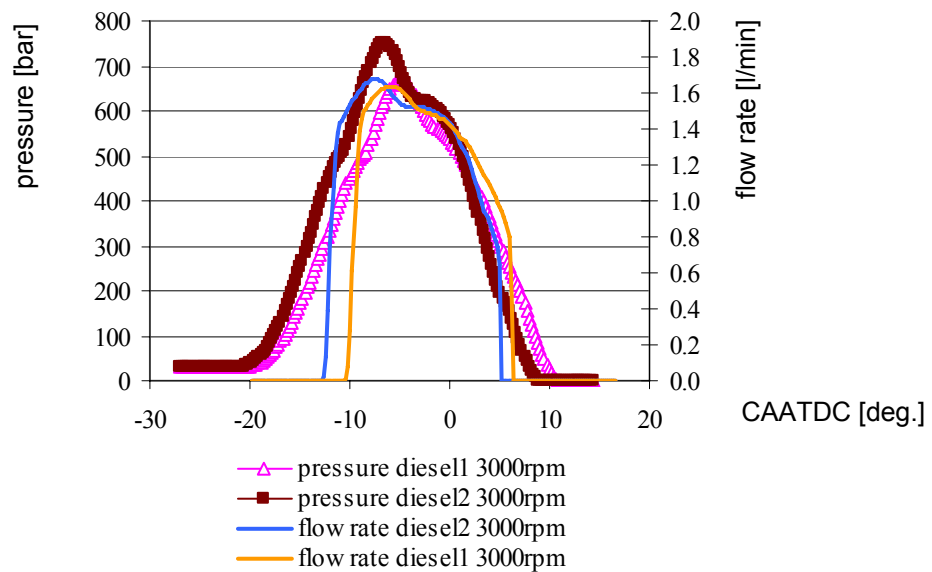


**Figure 9.12:** Simulated line-pressure at 3000rpm and volumetric flow rate; influence of fuel

Figures 9.13 and 9.14 refer to the second operation condition, namely engine at 2200rpm; the effect of bulk modulus is still evident; injection pressure traces of Fig. 9.13 have different slope and maximum value, as in the previous case; the difference between peaks is bound below ~50 bar, and the curve slope of diesel2 fuel is similar to that

obtained at 3000rpm with diesel1 (pink trace, Fig.9.13). The pressure decrease phases are substantially alike, inducing the same needle closure phasing for the two fuels.

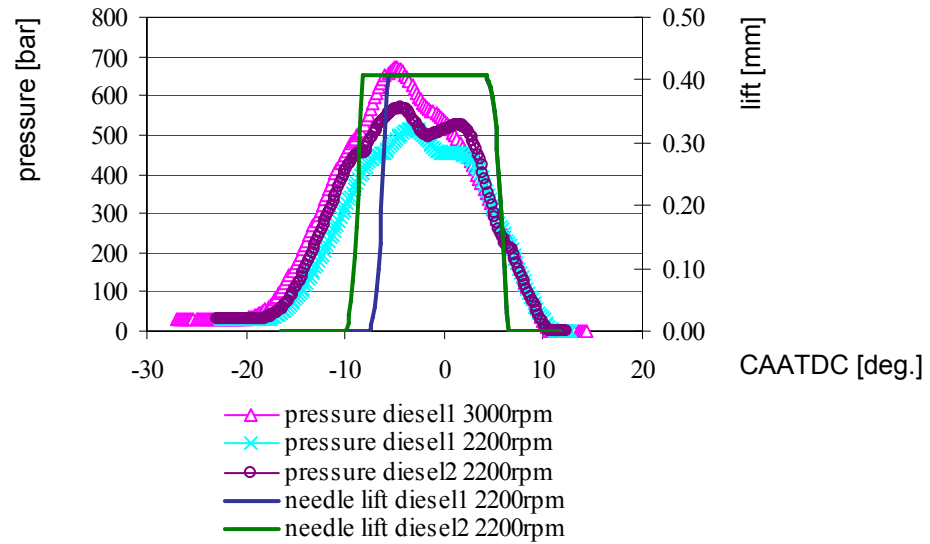


**Figure 9.13:** Simulated line-pressure at 2200rpm and needle lift; influence of fuel

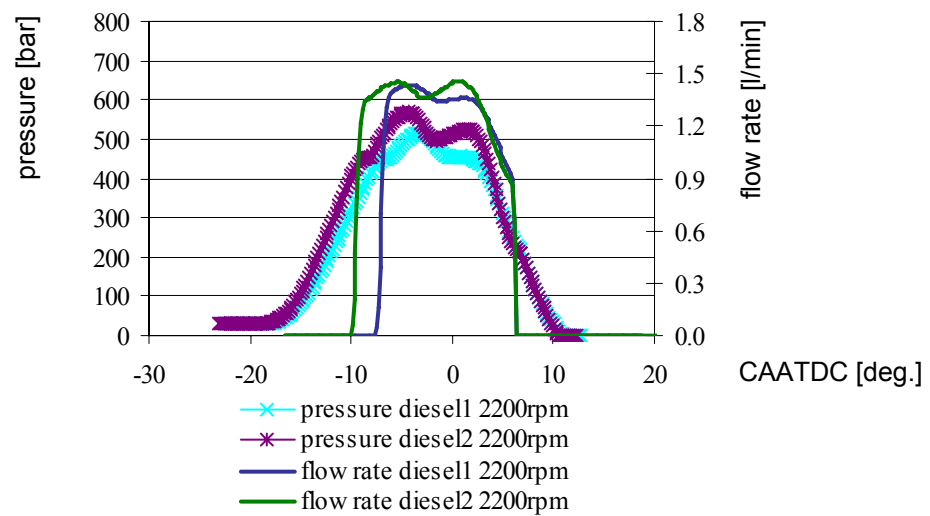


**Figure 9.14:** Simulated line-pressure at 2200rpm and volumetric flow rate; influence of fuel

A meaningful difference is observed between the opening phases of the needle; the use of different fuels induces stronger differences on the injection at 2200rpm than those at 3000rpm. Looking at Fig.9.14, such a different behavior can be viewed in terms of injected flow rate; in case of diesel2 fuel, the process is 2-3 crank angle degrees longer;

moreover, it is worthy to be pointed out that, beside the difference of the process length (and consequently the injected volume amount), the whole process timing results to be advanced.

**9.5 Concluding remarks.** A complete and detailed lumped/1D model of mechanical-hydraulic injection system is built and set up, taking into account the flow condition through the influencing components of the inline pump, like spill passages and delivery valve. The flow features inside the fuel pump and nozzle holes are evaluated by means of a 3D CFD characterization of the discharge coefficients; such a numerical investigation represents an important step in the modeling procedure, due to the need to properly lump the parameters.

Preliminarily, the model results are validated against the available experimental data; successively, the model is used with a predictive approach, in order to explore the influence of fuel properties on the injection process; due to the interesting capability to draw useful indications about the injection system, the used modeling approach is very helpful in advanced system design and development. The fine modeling of fuel delivery process is directly tied to the description accuracy of combustion processes; therefore, it represents a key factor during the engine optimization in the matter of performance and emission reduction.

**9.6 Appendix A - Multiphase flow modeling.** The adopted FIRE Multiphase module [9,10] is based on an Euler-Euler approach to model cavitating flows, with a two-fluid method. Bubble dynamics is used to calculate the mass transfer rate from one phase to the other. The mass transfer, is modeled by relation (1), in which the radius length  $R$  with its time derivative, the liquid density  $\rho_d$  and the bubble number density  $N'''$  appear.

$$\Gamma_c = \rho_d N''' 4R^2 \dot{R} = -\Gamma_d \quad (1)$$

$N'''$  is calculated by means of equation (2)

$$R\ddot{R} + \frac{3}{2}\dot{R}^2 = \frac{\Delta p}{\rho_c} \quad (2)$$

The linearization of Equation (1) and the drop of the inertial term give equation (3):

$$\Gamma_c = \frac{1}{C_{CR}} \text{sign}(\Delta p) 3.85 \frac{\rho_d}{\sqrt{\rho_c}} N'''^{\frac{1}{3}} \alpha_d^{\frac{2}{3}} |\Delta p|^{\frac{1}{2}} = -\Gamma_d \quad (3)$$

$\Delta p$  represents the effective pressure difference (4),

$$\Delta p = p_{sat} - \left( p - C_E \frac{2}{3} \rho_c k_c \right) \quad (4)$$

in which the Egler coefficient,  $C_E$ , depends on the local turbulence level [11].

The reduction of the initial bubble density  $N_0'''$ , is taken in to account by an empirical formula (5), used to calculate  $N'''$  [12].

$$N''' = \begin{cases} N_0''' & \alpha_d \leq 0.5 \\ 2(N_0''' - 1)(1 - \alpha_d) + 1 & \alpha_d > 0.5 \end{cases} \quad (5)$$

Number density is limited by relation (6).

$$N''' = \max \left( N''', \frac{6\alpha_d}{\pi D_{b,\max}^3} \right) \quad (6)$$

The maximum bubble diameter,  $D_{b,\max}$ , is a function of geometry, whereas the bubble diameter  $D_b$  is related (7) to the volume fraction and number density  $N'''$ .

$$D_b = \left( \frac{6\alpha_d}{\pi N'''} \right)^{\frac{1}{3}} \quad (7)$$

The modeling of the interfacial momentum source is given by equation (8). It represents the dynamics taking into account the effects of drag and turbulent dispersion.

$$M_c = C_D \frac{1}{8} \rho_c A_i'' |\mathbf{v}_r| \mathbf{v}_r + C_{TD} \rho_c k_c \nabla \alpha_d = -M_d \quad (8)$$

To calculate the relative velocity  $\mathbf{v}_r$  and the interfacial area  $A_i'''$ , relations (9) and (10) are used.

$$\mathbf{v}_r = \mathbf{v}_d - \mathbf{v}_c \quad (9)$$

$$A_i'' = \pi D_b^2 N''' = (36\pi)^{\frac{1}{3}} \alpha_d^{\frac{2}{3}} \quad (10)$$

Number density,  $N'''$ , is obtained from the cavitation mass exchange model. Drag coefficient,  $C_D$ , is a function of bubble Reynolds number,  $Re_b$ , defined by relation (11):

$$Re_b = \frac{v_r D_b}{\nu_c} \quad (11)$$

Correlation (12), valid for bubbles, is adopted [10]:

$$C_D = \begin{cases} \frac{192}{Re_b} (1 + 0.10 Re_b^{0.75}) & Re_b \leq 1000 \\ 0.438 & Re_b > 1000 \end{cases} \quad (12)$$

In addition, the following assumptions are considered [11]:

- the interfacial interaction between phases is neglected;
- the turbulence level of the dispersed phase is assumed to be equal to the continuous phase turbulence level.

**9.7 Appendix B –  $C_d$  setting influence.** Pointing out the influence of the  $C_d$  setting on the results, flow rate traces of the system-based model without the use of the 3-D CFD data are shown in Fig.9.15. In detail  $C_{d\max} = 0.7$  is assumed as default value for the considered orifices. The comparison highlights a noteworthy difference between the curves (in terms of flow rate peak and process duration), that induces an injected amount difference in the order of 20%.



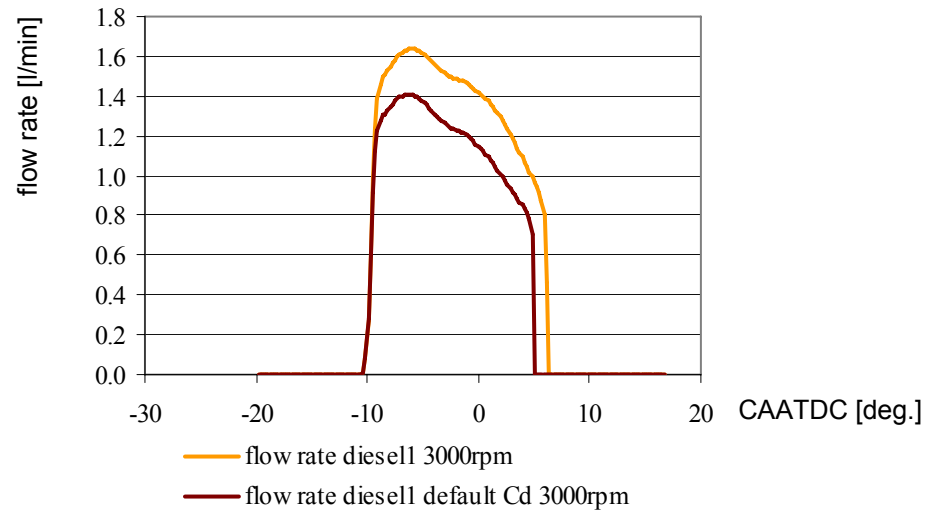


**Figure 9.15:**  $C_d$  setting influence on flow rate results

## 9.8 Nomenclature

$Q$	=	flow rate
$A$	=	cross sectional area
$D_h$	=	hydraulic diameter
$C_d$	=	discharge coefficient
$C_{dmax}$	=	maximum discharge coefficient
$A_i''$	=	interfacial area density
$D_b$	=	bubble diameter
$C_{CR}$	=	condensation reduction factor
$C_D$	=	drag coefficient
$C_E$	=	Egler coefficient
$C_{TD}$	=	drag turbulent coefficient
$M_c$	=	vapor phase momentum
$M_d$	=	liquid phase momentum
$N_0''$	=	initial bubble number density
$N'''$	=	number density
$R$	=	bubble radius
$Re_b$	=	bubble Reynolds number
$k_c$	=	vapor phase turbulence kinetic energy
$p_{sat}$	=	saturation pressure

$\mathbf{v}_c$	=	vapor velocity
$\mathbf{v}_d$	=	liquid phase velocity
$\mathbf{v}_r$	=	relative velocity

#### **Greek symbols**

$\Gamma_c$	=	vapor phase mass
$\Gamma_d$	=	liquid phase mass
$\Delta p$	=	pressure difference
$\alpha_d$	=	liquid phase volume fraction
$\lambda$	=	flow number
$\lambda_{crit}$	=	critical flow number
$\rho_c$	=	vapor phase density
$\rho_d$	=	liquid phase density

#### **9.9 References**

- [1] Catania, A.E., Dongiovanni, C., and Mittica, A., "Implicit Numerical Model of a High Pressure Injection System", Journal of Engineering for Gas Turbines and Power, 114, pp. 534-543, 1992.
- [2] Catania, A.E., Dongiovanni, C., and Mittica, A., "Numerical Analysis Versus Experimental Investigation of a Distributor-Type Diesel Fuel-Injection System", Journal of Eng. for Gas Turbines and Power, 116, pp. 814-830, 1994.
- [3] Catania, A.E., Dongiovanni, C., and Spessa, E., "Delivery-Valve Effects on the Performance of an Automotive Diesel Fuel-Injection System", SAE Paper No. 1999-01-0914.
- [4] Kim, D-H., Kim, H-W., Kim, B-S., Ghal, S-H., Ha, J-S., "A Design Modification of the Delivery Valve and the Constant Pressure Valve in a Medium Speed Diesel Engine Fuel Injection System for the Prevention of Cavitation Damage and Secondary Injection", ASME Paper IMECE2005-80730.
- [5] AMESim Tutorial and User Guide, AMESim Technical Bulletins, LMS.
- [6] McCloy, D., "Discharge Characteristics of Servo Valve Orifices", Fluid International Conference, pp. 43-50, 1968.
- [7] AMESim Hydraulic Library Manual, LMS.
- [8] FIRE v8.5 CFDWM Guide, AVL List GmbH.
- [9] FIRE v8.5 Multiphase Manual, AVL List GmbH.
- [10] Tatschl, R., v. Künsberg-Sarre, C., Alajbegovic, A. and Winklhofer, E., "Diesel Spray Modeling Including Multidimensional Cavitation Nozzle Flow Effects", Proc. of ILASS Europe Conference, Sept. 11-13, Darmstadt, Germany, 2000.
- [11] Hinze, J.O., "Turbulence", 2<sup>nd</sup> ed., McGraw-Hill, New York, 1975.
- [12] Franklin, R.E. and McMillan, J., "Noise Generation in Cavitating Flows", J. Fluids Eng., 106, 336-341, 1984.

## 10. Multi-Step Lumped Parameter Fuel Injection and Vaporization Modeling for Diesel Engine Performance Analysis

**10.1 Introduction.** The activity aims at developing and setting up a model able to predict the diesel spray evolution to be integrated into a complete thermodynamic model of the engine. Previous papers have been devoted to realize a numerical model for the injection system, in which a lumped parameter + one-dimensional approach is employed. Such a model has been now enhanced by introducing a quasi-dimensional model for fuel break up, diffusion and penetration processes. A self-developed heating sub-model is included in the model, which enables the evaluation of the influence of the fuel properties on the evaporation process. As a result, the injection system simulation model gives indications on the spray formation process and it is used into a lumped parameter model of the combustion process. Results concerning the influence of fuel properties on the evaporation process are presented and discussed, pointing out its effect on engine performance.

**10.2 Fuel injection system.** To set the necessary frame of reference, a concise description of the injection system is given. The fully mechanical operation is based on an in-line high pressure pump. The pump feeds a spring injector, whose operation is controlled by the interposition of a delivery valve. The considered system is tailored for relatively small size single-cylinder diesel units. Reliability and cost effectiveness are key features of such a kind of engines, largely used in industry and agriculture.

type	cam-driven system
pump plunger diameter [mm]	7
plunger stroke [mm]	8
number of nozzle holes	5
diameter of nozzle holes [mm]	0.159

**Table 10.1:** Specifications of fuel injection system

type	direct injection
bore [mm]	86
stroke [mm]	86
max engine speed [rpm]	3000

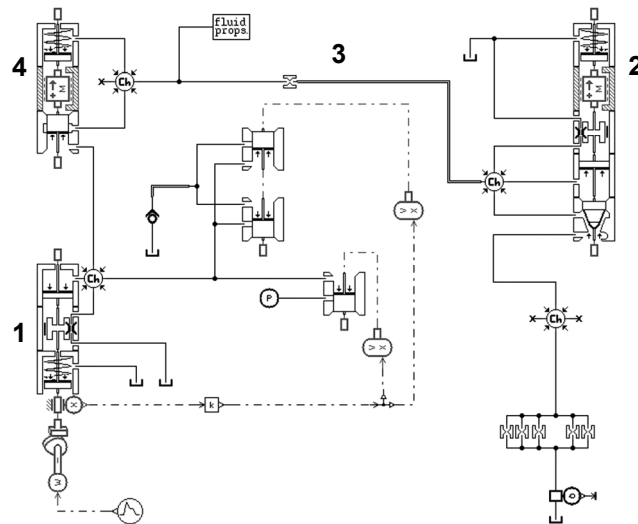
**Table 10.2:** Specifications of diesel engine

Table 1 summarizes the technical data of the system, designed to reach a nominal injection pressure of 800 bar at maximum load and power. The main features of the single cylinder engine are shown in Table 2.

### 10.3 Injection system modeling - I Simulation Module. Lumped/1D approach

The mechanical-hydraulic model of the system is implemented according to the approach used in a previous work of the authors [1]; in that case, a complete model of an analogous system is built and set up, taking into account the flow condition through the influencing components of the inline pump, like spill passages and delivery valve. More in detail, in order to properly lump the parameters, the flow features inside the fuel pump and nozzle holes are evaluated by means of a 3D CFD characterization of the discharge coefficients. In the adopted scheme, pressure and temperature in lumped volume elements are just time dependent, whereas the high pressure pipeline model is based on a one-dimensional scheme in which wave equation is used to account for inertia, friction and compressibility effects.

Figure 10.1 shows the injection system sketch in AMESim environment [2], in which the inline pump (1), a minisac nozzle-hole type injector (2) and connecting high pressure pipe (3) are visible. As mentioned, fuel pump is equipped with a delivery valve (4).



**Figure 10.4:** Injection system sketch in AMESim environment

Fuel modeling - Three different fuels are simulated; these are diesel fuel and two pure hydrocarbons, namely the alkanes n-dodecane and n-hexadecane. The chemical-physical properties of the diesel fuel are provided by the AMESim internal data base, whereas the characteristics of the mentioned alkanes are gathered from the specific literature [3-5] and then arranged to be read by the software. From a practical point of

view, the fuel properties modeling requires the data storing in a system file. In the adopted scheme, density and bulk modulus are defined from a reference density at corresponding pressure and from a set of tables of speed of sound values against pressure. Each table applies for a given temperature. The table data is then used to create a new table of bulk modulus values. The fluid viscosity is also given in an input file once the density and the bulk modulus are defined. The absolute viscosity is defined from tables which applies for a given temperature, too. Temperature values are chosen in a range that is representative of the engine operation.

#### 10.4 Fuel spray dynamics – II Simulation Module. Spray penetration

A quasi-dimensional approach is adopted to model the fuel spray penetration, based on empirical correlations. More in detail, a generalized form of the known Hiroyasu & Arai correlation [6] is considered. Such a generalization is proposed by Jung & Assanis [7] and it is developed to extend its validity to the cases in which nozzle flows are characterized by any discharge coefficient. Indeed, the correlations in the original work of Hiroyasu & Arai are suited for the specific nozzle discharge coefficient that was used during the experimental activity. The presented correlations are widely used in spray modeling by independent researchers, too [8,11]. The spray tip penetration ( $S$ ) before breakup is expressed by

$$S = C_D \left( \frac{2\Delta P}{\rho_l} \right)^{0.5} t \quad 0 < t < t_b \quad (1)$$

whereas after breakup, the following equation is used

$$S = 2.95 \left( \frac{\Delta P}{\rho_a} \right)^{0.25} (d_n t)^{0.5} \quad t_b \leq t \quad (2)$$

where  $\Delta P$  is the pressure drop through the nozzle hole;  $\rho$  is the density;  $d_n$  is nozzle hole diameter; and subscript  $l$  and  $a$  denote liquid fuel and ambient gas, respectively. Breakup time, ( $t_b$ ), is given by (3)

$$t_b = 4.351 \frac{\rho_l d_n}{C_D^2 (\rho_a \Delta P)^{0.5}} \quad (3)$$

Spray angle: the two most commonly used correlations for spray angle have been implemented into the second computation module. The former correlation is [6]:

$$\theta = 2 \cdot 0.025 \left( \frac{\rho_a \Delta P d_n^2}{\mu_a^2} \right)^{0.25} \quad (4)$$

where  $\mu_a$  is the viscosity of ambient gas. The latter one [12], which in some cases appears to yield predictions in better agreement with experimental data [13], is:

$$\tan(\theta) = \frac{1}{A} 4\pi \left( \frac{\rho_a}{\rho_l} \right)^{0.5} \frac{\sqrt{3}}{6} \quad (5)$$

where

$$A = 3.0 + 0.28 \left( \frac{l_n}{d_n} \right) \quad (6)$$

Spray breakup – droplet diameter - Following breakup, all droplets are assumed to have the same initial diameter, equal to the Sauter Mean Diameter (SMD). The following equations [14] give the SMD,  $d_{32}$ , in the zone located along the spray centerline.

$$\frac{d_{32}}{d_n} = \max \left( \frac{d_{32}^{LS}}{d_n}, \frac{d_{32}^{HS}}{d_n} \right) \quad (7)$$

$$\frac{d_{32}^{LS}}{d_n} = 4.12 \text{Re}^{0.12} \text{We}^{-0.75} \left( \frac{\mu_l}{\mu_a} \right)^{0.54} \left( \frac{\rho_l}{\rho_a} \right)^{0.18} \quad (8)$$

$$\frac{d_{32}^{HS}}{d_n} = 0.38 \text{Re}^{0.25} \text{We}^{-0.32} \left( \frac{\mu_l}{\mu_a} \right)^{0.37} \left( \frac{\rho_l}{\rho_a} \right)^{-0.47} \quad (9)$$

where  $\mu_l$  is the viscosity of liquid and  $\sigma_l$  is the surface tension. By using the above equations initial diameter of liquid fuel droplets right after the breakup time is calculated.

**10.5 Droplet evaporation – III Simulation Module.** A wide literature is available on the topic of fuel droplet vaporization. Experimental studies and numerical models continue to be accomplished by several authors, due to the challenge to improve the understanding and the role of the various phenomena and interactions involved in the process. On the field of theoretical modeling, a reference contribution is represented by the approach proposed by Godsave & Spalding (known as  $d^2$  law), which gives the basis for the subsequent model improvements, proposed in the course of time by many authors. Among others, the contributions of Faeth [15-17] and Law. [18,19] improve upon the transient phenomena modeling, taking into account the heat-up period of the droplet, the convective effects on evaporation (relative motion between the drop and the surrounding gas) and other distinctive features of real fuel composition (modeled as multi-component mixtures). Further contributions on convective effect and its role on thermal exchange come from the works of Sirignano et Al. [20-22]; such a topic is originally related to the development of empirical correlations to adjust the spherical symmetry models. Moving from spherical symmetry schemes into the axial one [23-25,27], the effect of the fuel circulation within the droplet and the role of the finite fuel thermal conductivity are investigated. Other deepening concerns the effect of air ambient condition (high temperature) and the improvement of evaporation models [28-31]. More recently [32-46], a detailed modeling approach (the effects of thermal radiation are considered, as well) is proposed, having the advantage of being computationally not expensive; due to completeness and effectiveness, the contributions of Sazhin et Al., together with those of Varanasi [47] and Lefebvre [48] are adopted as main reference for the implementation of the third computation module. In the adopted approach, due to the typical range of droplet size in the current engine, the relative velocity between the drop

and the surrounding gas is assumed to be constant [20]; the forced convective heat transfer regime is modeled through the use of the Ranz-Marshall correlation. Concerning the modeling of the liquid phase heating and evaporation, two approaches are compared; the former one is based on the assumption that the droplet thermal conductivity is infinite, whereas in the latter scheme, a finite conductivity is hypothesized. Three different zones are distinguished in the evaporation model structure, these are:

1. Ambient - The gaseous ambient in which the droplet vaporization takes place is air. Obviously, temperature, pressure and specie concentrations are time-dependent, but in the present case they are modeled as permanent, due to the relatively small amplitude of evaporation timescale, that makes the approximation possible.
2. Gas-vapor interface - Quasi-permanent conditions are assumed to represent the gas-vapor interface; in fact, as demonstrated by Faeth [16] (for 10-100  $\mu\text{m}$  diameter droplets and 10-100m/s relative velocity), the gas flow follows the boundary and droplet diameter variation with a characteristic timescale in the range of 0.1-10 $\mu\text{s}$ ; such values are substantially below the droplet lifetime, which is in the order of 10ms. According to the Rault's law, during the droplet heating, the interface specie concentrations vary due to the surface temperature and to the liquid molar concentration within the droplet. In the subsequent phase (vaporization), the droplet temperature remains constant and the specie concentrations vary due to the liquid molar concentration within the droplet, essentially.

Liquid - Unsteady conditions are considered for the liquid. During the droplet heating, both droplet temperature and specie concentration vary. In the subsequent phase, when the molecular diffusion coefficient (Spalding coefficient) equals the thermal diffusion coefficient, droplet temperature is assumed to remain constant; clearly, molar concentrations continue varying when a mixture of two components with different vaporization rate is considered. As previously mentioned, in the modeling of the liquid phase, two different approaches are used and the results are compared. In the former one, thermal conductivity is considered to be infinite; in the latter one, a finite value (fuel/component dependent) is adopted. Infinite conductivity model - Droplet temperature rises during the heating phase being uniform within the droplet.

Finite conductivity model - During the heating transient, temperature within the droplet varies and its profile is not uniform. The solution of the droplet thermal profile is obtained according to the Dombrovsky-Sazhin theory on the parabolic thermal profile [49]. The details of the solution procedure used in the third simulation module are shown in "Appendix A" section.

Injected fuel combustion - In order to simulate the in-cylinder combustion, the fuel vaporization module is integrated in a self-developed single-zone thermodynamic model. At each time-step, injection flow rate and SMD time traces (coming from the first and second simulation modules) are used to compute the number of incoming droplets in combustion chamber; step by step, the mass of available fuel vapor is computed and on its basis the heat release is modeled. The heat release is modeled taking into account the

combustion conditions (premixed and diffusion controlled); premixed combustion is assumed to occur until the amount of fuel evaporated at the end of ignition delay period is consumed [7]. The ignition delay is evaluated using a correlation that accounts of fuel cetane number, explicitly [53].

**10.6 Comparison among models and validation.** With the aim of evaluating the model capability, a preliminary vaporization test is performed and the obtained results are compared to those available in the related literature. The time evolution of a n-heptane droplet is modeled. The droplet initial state is resumed in Table.3.

fuel type	n-heptane
droplet diameter [mm]	0.2
initial surface temperature [K]	300
fuel density [kg/m <sup>3</sup> ]	744
ambient pressure [Pa]	101325
ambient temperature [K]	800

**Table 10.3:** N-heptane droplet initial state

A comparison among the following models is performed:

1. elemental  $D^2$  model
2. modified  $D^2$  model [48]
3. infinite conductivity model (author's)
4. finite conductivity model (author's)

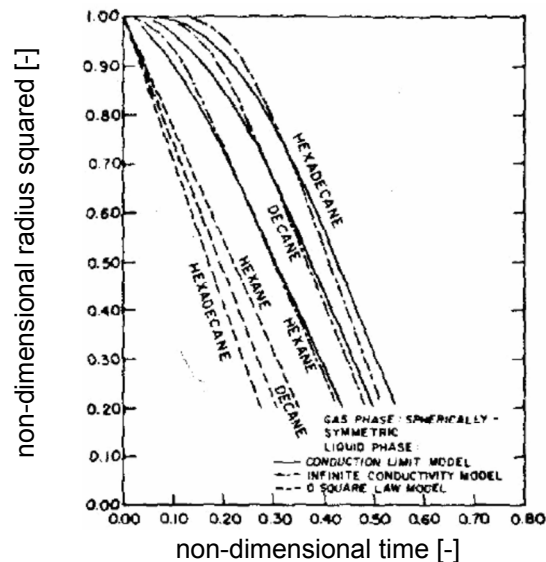


**Figure 10.2:** Vaporization behavior provided by different modeling approaches for different fuels [26]



In Fig.10.2 the discrepancies among the models are evident. The comparison highlights the behavior of the  $D^2$  law model that tends to underestimate the process duration, due to the complete neglecting of the droplet heating transient. Modified  $D^2$  law model estimates such a transient with an elementary representation. Differences are certainly more evident when high boiling point fuels are considered, (e.g. n-hexadecane), that show a relatively long heating phase. In such cases,  $D^2$  law models are incapable of detailed predictions (the higher is the fuel boiling point, the higher is the  $D^2$  law underestimation of the heating transient). In Fig.10.3, the results coming from the preliminary computation (author's finite conductivity model) are compared with the traces obtained by other authors and validated with experimental data [52]. A good agreement with both the measured and modeled vaporization behavior is visible.

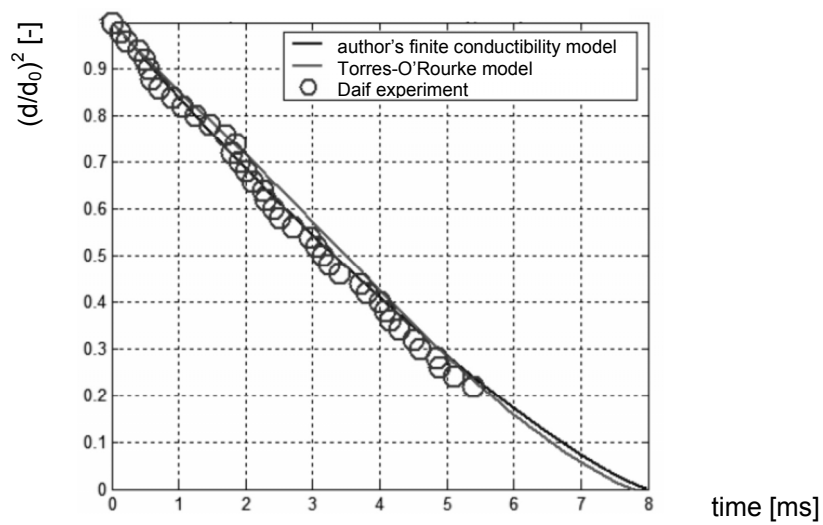


**Figure 10.3:** Validation of finite conductivity model

**10.7 Results.** The results obtained by the mechanical-hydraulic model are discussed. Figure 10.4 shows a comparison between the experimental line pressure and the numerical one, referred to diesel fuel.

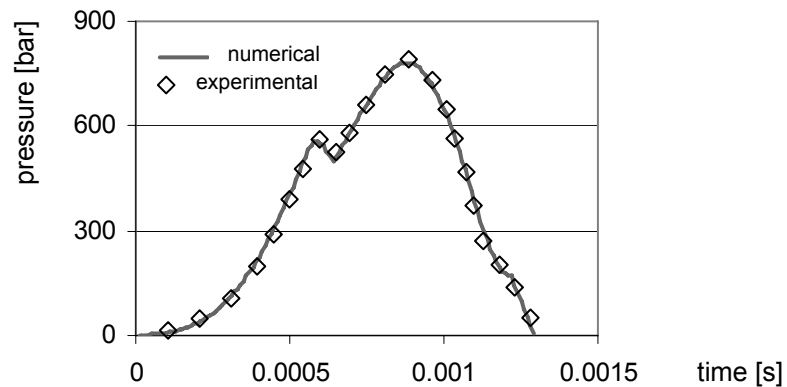


**Figure 10.4:** Line-pressure trend comparison

Line-pressure is measured at a distance of 25mm from the injector inlet. Predicted pressure and experimental one are characterized by good agreement, concerning maximum value, process duration and trend slope. After the comparison against the measured pressure trend, the model is used in predictive manner, in order to evaluate the injection process and the influence of fuel properties. Figure 10.5 shows, on a single diagram, a comparison among the pressure time traces referred to the three considered fuels.

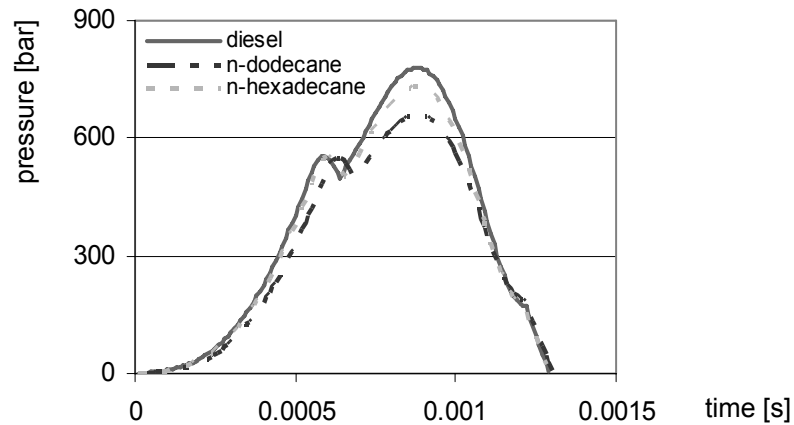


**Figure 10.5:** Line pressure time trace

Simulating diesel fuel, the maximum peak pressure is reached; n-hexadecane and n-dodecane are characterized by lower peak values.

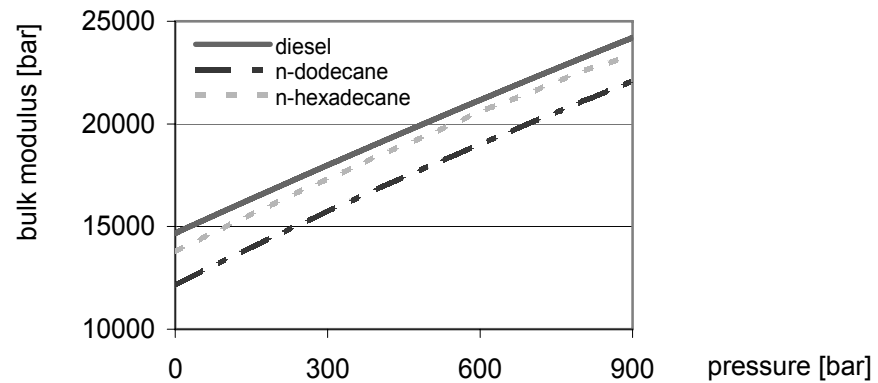


**Figure 10.6:** Fuel bulk modulus vs. Pressure

Such a behavior is mainly due to the different bulk modulus, which is maximum in case of diesel fuel and minimum considering n-dodecane. From a quantitative point of view, the line pressure difference between diesel and n-dodecane is in the order of 120 bar. It is

interesting to point out that n-hexadecane induces a pressure time evolution closer to the diesel one.

For each fuel, bulk modulus vs. pressure trends are shown in Fig.10.6; as the values of the couple diesel-hexadecane are closer than the others, the n-hexadecane line pressure is closer to the diesel one than to the n-dodecane one.

The different line pressure behaviors induced by the considered fuels are observed looking at the needle opening-closing stroke (Fig.10.7). Both n-hexadecane and n-dodecane show the presence of time delay in the needle opening phase. Dealing with n-hexadecane, the entity of delay is relatively small; such a feature is in agreement with the pressure rising during the needle opening, whose trend closely resemble the diesel one. Quantitatively, the opening delay represents the 1-2% of the whole injection length.

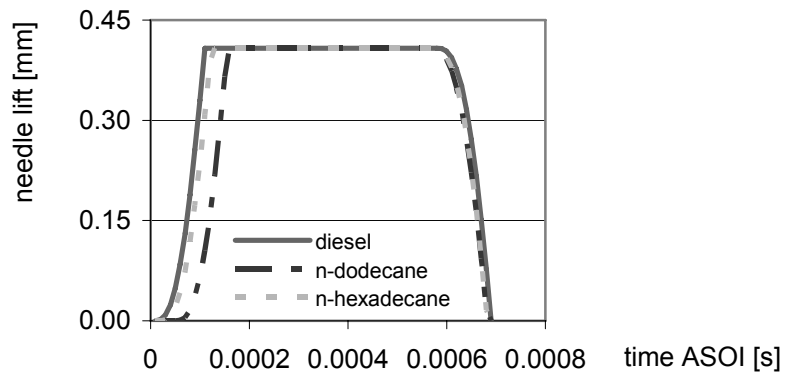


**Figure 10.7:** Simulated needle lift

N-dodecane fuel induces a more deviating injection timing if compared to the diesel case. The lower slope in line pressure rising causes a more evident opening delay, which represents a significant reduction of the process duration (in the order of 10% in respect to the diesel injection).

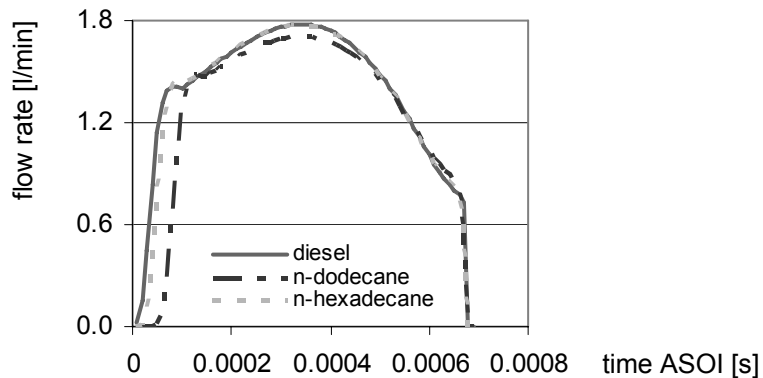


**Figure 10.8:** Simulated volumetric flow rate

The injected flow rate curves are compared in Fig.10.8; as visible, the trend shape is directly influenced by the pressure time evolution. A fast rising phase is followed by an evident slope decrement as the needle reaches the stroke end. Peak flow rate is slightly over 1.75 l/min in case of diesel fuel and n-hexadecane, whereas n-dodecane is characterized by lower value.

**10.8 Fuel spray model.** The behavior of fuel jet penetration is discussed in the following. Looking at Fig.10.9 it is possible to observe that the fuels having higher density show a weak prevalence in penetration depth. The traces of Fig.10.9 are referred to the same injection velocity, namely 262 m/s, which is a relatively high value reached by all the three considered fuels.

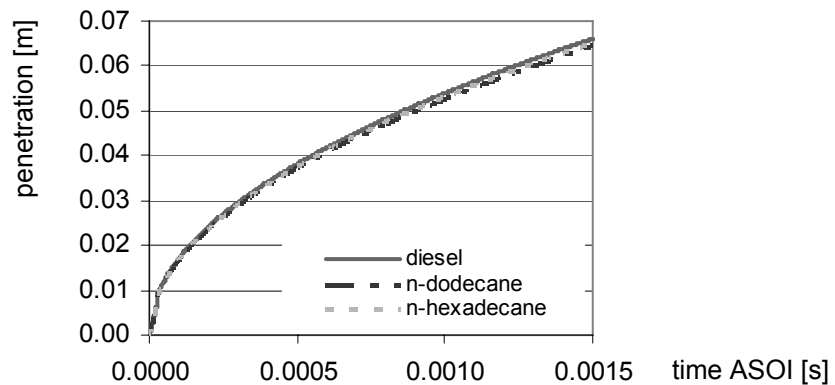


**Figure 10.9:** Simulated fuel jet penetration

In order to better evaluate the role of fuel density, Fig.10.10 shows the density trace vs. pressure for each fuel. Even if the higher is fuel density the deeper is penetration, it must be pointed out that the difference among the results is relatively light, in the order of few percent points in respect to the maximum penetration length (~0.07m after 1.5 ms). Therefore, according to the used penetration model, it is possible to conclude that the use of both n-hexadecane and n-dodecane does not influence the jet penetration significantly.

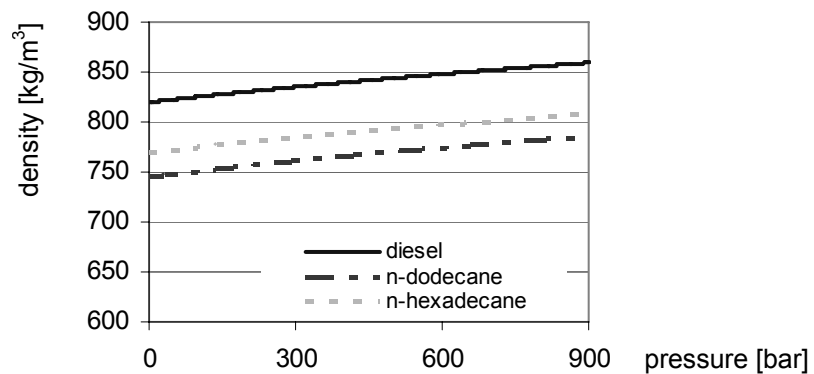


**Figure 10.10:** Fuel density vs. pressure

The atomization behavior of the three considered fuels is characterized by appreciable differences. Figure 10.11 shows the evolution of SMD during the injection process. Clearly, at the early phase of injection, fuel velocity is still low (injection velocity is provided by the first simulation module) and the formation of relatively big droplets is modeled. As fuel velocity increases (it happens quickly after the start of injection), each fuel atomizes according to its chemical-physical features.

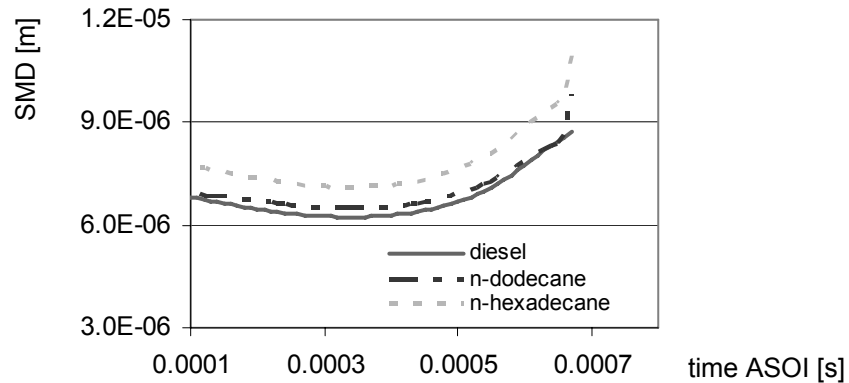


**Figure 10.11:** SMD traces

Among the features that exert an influence on the atomization process, it is necessary to highlight that viscosity, surface tension and density of fuel play a fundamental role, whose values define We and Re numbers that appear in the used SMD empirical correlations (7-9); Table 4 resumes these features for each fuel. Even though n-dodecane is characterized by the lowest injection velocities (Fig.10.8) during the process, SMD values are close to those of diesel fuel. Comparing the n-hexadecane behavior to the SMD of diesel, the same injection velocity corresponds to a quite different atomization quality.

density [kg/m <sup>3</sup> ]	diesel	821.5
	n-dodecane	746.9
	n-hexadecane	771.3
absolute viscosity [cP]	diesel	3.317
	n-dodecane	1.398
	n-hexadecane	3.184
surface tension [kg/s <sup>2</sup> ]	diesel	0.02
	n-dodecane	0.0235
	n-hexadecane	0.02747

**Table 10.4:** Fuel properties

Comparing the computed spray cones (Fig.10.12), diesel fuel is characterized by the widest angle; the value is over twenty degrees, slightly over that of n-hexadecane. N-dodecane cone angle is narrower and it remains on the limit of twenty degrees.

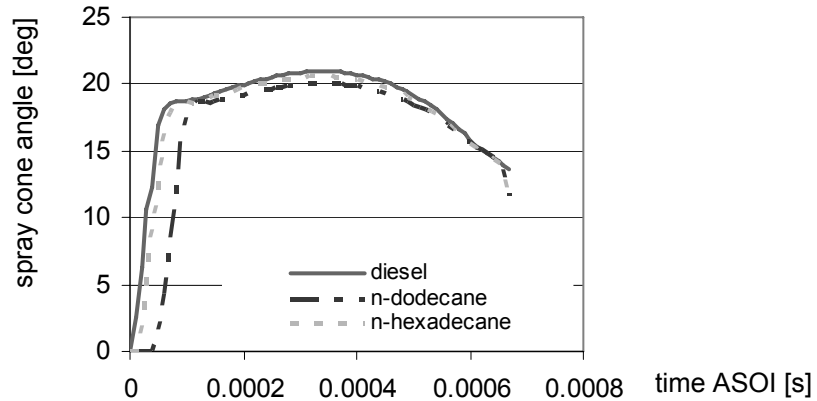


**Figure 10.12:** Spray angle results (model [6])

The obtained time trends are completely congruent to the fuel flow rates (Fig.10.8), so the higher is the velocity, the wider is the cone angle. Table 5 resumes the cone angle values obtained by the Reitz&Bracco correlation. Obviously such values are time independent, as they do not depend on the transient flow conditions (negligible differences characterize the results).

diesel	5.9 [deg.]
n-dodecane	6.2 [deg.]
n-hexadecane	6.1 [deg.]

**Table 10.5:** Spray angle results (model [12])

**10.9 vaporization model.** From here on, the results referred to the fuel evaporation are discussed. More in detail, the vaporization of a single fuel droplet is analyzed. Such a droplet is considered to be in an evaporation ambient at high temperature (800K) and high pressure (30 bar); a 10 $\mu$ m droplet initial diameter is assumed. Figure 10.13 shows the droplet vaporization process for n-hexadecane, n-dodecane and a mixture of them (50% in volume). The low boiling point fuel (n-dodecane) shows a faster evaporation rate if compared to the high boiling point one (n-hexadecane). More in detail, n-hexadecane requires a twenty percent longer time to completely evaporate. Such a behavior is worthy to be related to the different injection phasing induced by these fuels. Even if the injection of n-dodecane is delayed, the higher vaporization rate tends to balance its effect. Fuel mixture shows an intermediate behavior; obviously the complete evaporation of the droplet requires a time interval that is comprised between those of pure fuels.

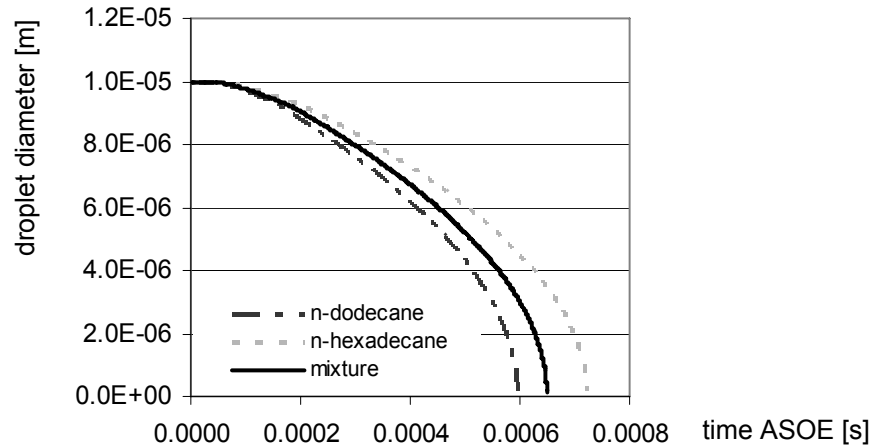


**Figure 10.13:** Droplet diameter vs. time

To have an idea of the droplet heating transient phase, Fig.10.14 reports the droplet surface temperature time traces. The n-dodecane curve shows an anticipated end time, indicating the beginning of the vaporization phase (and the end of heating); due to the lower boiling point (in respect to the n-hexadecane, it happens at lower temperature, as well). In the same figure, the temperature time evolution of n-hexadecane is traced. It is obtained by a second model; in such a case, the liquid thermal conductivity is considered to be infinite (infinite conductivity model).

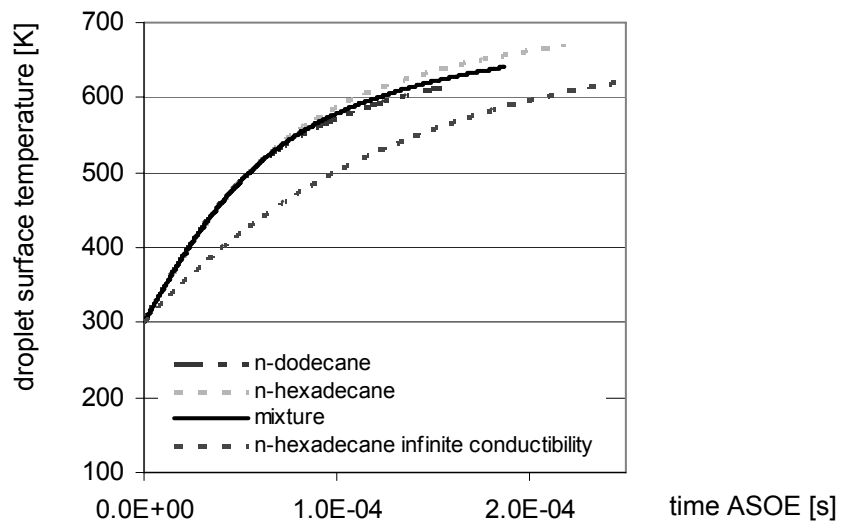


**Figure 10.14:** Droplet surface temperature - heating phase

As a consequence, the heating phase results wider in time, due to the different droplet internal heat transfer. Concerning the mixture behavior during the evaporation process, the time evolutions of liquid molar fractions are traced in Fig.10.15. As visible, the liquid droplet is progressively formed by the high boiling point component (n-hexadecane), influencing the composition of the vapor phases.

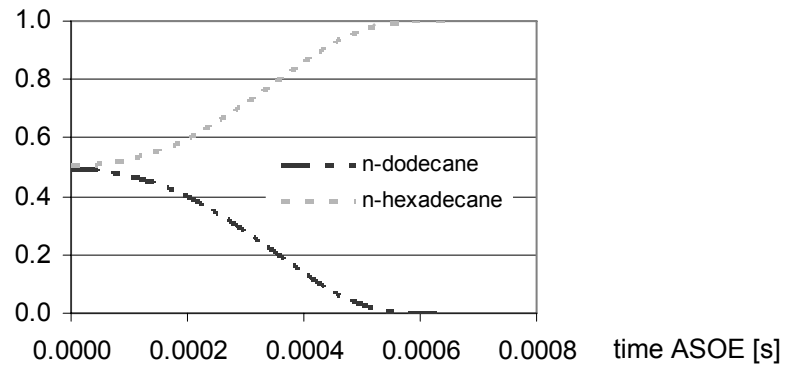


**Figure 10.15:** Liquid fuel volume fraction during evaporation

Looking at Fig.10.16, it is possible to quantify the residual fuel liquid masses during the vaporization. Due to the lower n-dodecane density, the initial fuel quantities differ from each other. It is evident that after the complete vaporization of the low boiling point component, the only vapor produced comes from the residual component; such a circumstance is well predicted by the model and it is useful to evaluate its impact on mixture formation and combustion properties. In addition, the residual n-hexadecane mass obtained from infinite conductivity model is traced on the same graph, showing different heating and evaporation rates.

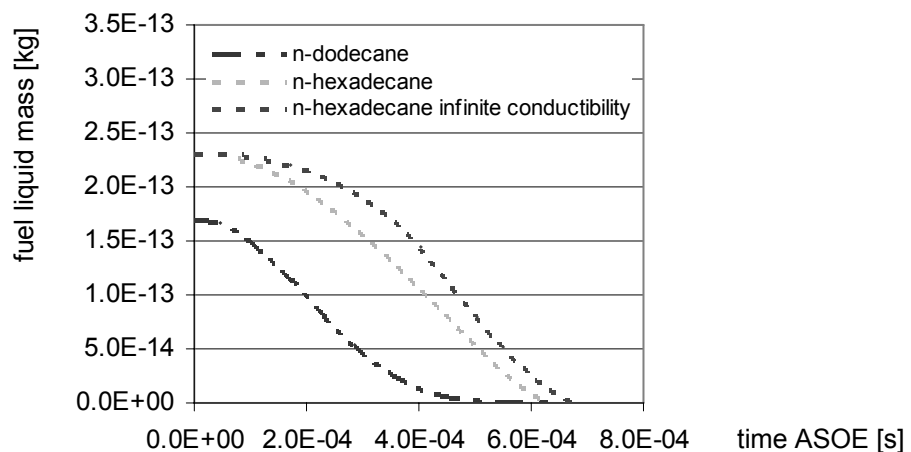


**Figure 10.16:** Liquid fuel residual mass



As shown in Fig.10.11, the atomization differences are evaluated for the considered fuels. The high boiling point fuel (n-hexadecane) is characterized by the highest SMD; it means that the lengthy evaporation process highlighted by the vaporization model has to be corrected to take into account the influence of the larger initial droplet diameter, too. From a complementary point of view, the use of n-dodecane tends to be balanced by a couple of factors; the former one is the faster evaporation rate (intrinsic), the latter one is the smaller SMD value, that shortens the process duration. Such a topic is deepened in the next subsection, simulating the combustion of the predicted flow rates (n-dodecane and n-hexadecane fuels).

**10.10 Fuel influence on engine performance.** Figure 10.17 shows two in-cylinder pressure trends, that are referred to n-dodecane and n-hexadecane. As visible, on the one hand, n-dodecane pressure rise is slightly delayed in respect to the other (due to the injection delay and to the ignition delay); on the other hand, the faster fuel vaporization enhances the heat release (and the pressure rise) and the n-dodecane pressure trace tends to come through the other for the earl (premixed) combustion process.

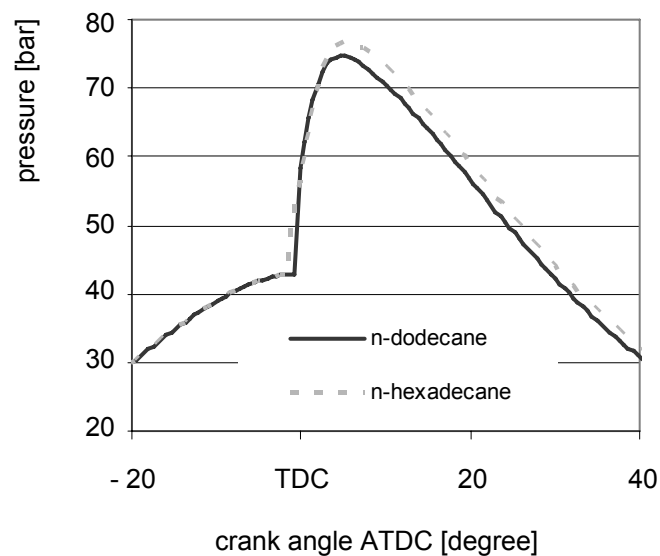


**Figure 10.17:** Simulated cylinder pressure traces

**10.11 Concluding remarks.** A comprehensive diesel injection system model is built, presented and used. Such a model shows a good aptitude for representing the influence and the interdependence of the single injection phenomena. The construction of the model is sub ordered to the realization of a detailed mechanical-hydraulic injection system model and to the accurate modeling of fuel features. Moving from the flow rate/injection velocity it is possible to obtain relevant indications concerning the injection

process characterization, essentially by means of relatively simple correlations. As shown, the model is certainly suitable for the evaluation of fuel feature influence on the process. More in detail, the integration of injection-vaporization model with a relatively simple single-zone combustion simulation enables to evaluate the influence of the whole injection process on the engine performance, with a comprehensive approach. It must be pointed out that the same model can be used to evaluate the influence of component layout, injection strategy, phasing and parametric studies in general at low computation cost.

#### 10.12 Nomenclature

A	component A; numerical constant
ASOI	After Start Of Injection
ASOE	After Start Of Evaporation process
B	component B
$B_M$	molecular diffusion coefficient
$B_T$	thermal diffusion coefficient
$C_D$	discharge coefficient
Fo	Fourier number
$L_a$	vaporization latent heat, component A
$L_{TBnA}$	vaporization latent heat, component A, normal condition
Nu	Nusselt number
P	Pressure
PM	molar weight
Pr	Prandtl number
R	Gas constant
Re	Reynolds number
S	penetration length
SMD	Sauter mean diameter
$T_{crA}$	critic temperature
$T_{bnB}$	boiling point, normal condition
We	Weber number
X	molar fraction, liquid phase
Y	molar fraction, gas phase
$c_p$	specific heat, P=const.
d	droplet diameter
$d_n$	nozzle hole diameter
$d_{32}$	Sauter mean diameter

h	thermal exchange coefficient
k	thermal conductivity
l	length
$\dot{m}$	time mass derivative
r	radius
t	time
u	droplet velocity

#### **Greek symbols**

$\Delta$	algebraic difference
$\zeta$	non-dimensional constant
$\theta$	spray angle; non-dimensional temperature
$\mu$	absolute viscosity
$\xi$	non-dimensional constant
$\rho$	density
$\sigma$	surface tension
$\psi$	non-dimensional constant

### **10.12 Appendix A. III COMPUTATION MODULE.**

Input data - Ambient condition, component/fuel characteristics (molar weight, density, boiling point, vaporization latent heat, critic temperature, viscosity and thermal conductivity), spray diameter distribution matrix (or a single reference diameter value), droplet initial temperature, ambient gas-droplet relative velocity and component molar concentration within the droplet (for a binary mixture) are given as input data. For each considered droplet diameter class, the time evolution of the vaporization process is computed; the results are arrayed in a matrix in which diameter and specie concentration are stored.

Thermal and physical properties computation - Thermal and physical properties of ambient gas and evaporating fuel are computed on the basis of the surface temperature of the droplet  $T_s$ ; in case of finite conductivity model, mean liquid temperature is considered, as well.

Vaporization latent heat - It is obtained from Watson formula

$$L_a = L_{TBnA} \left( \frac{T_{crA} - T_s}{T_{crA} - T_{bnB}} \right)^{-0.38} \quad (10)$$

Interface molar fraction - For a single component fuel, the Clausius-Clapeyron molar fraction formulation is used

$$X_{s,A}^* = \frac{P_{atm}}{P_g} \exp \left[ \frac{L_A}{R_A} \left( \frac{1}{T_{bnA}} - \frac{1}{T_s} \right) \right] \quad (11)$$

where the symbol (\*) indicates that its validity is limited to the single component; subscript (s) indicates that such values are computed at droplet surface (it means at gas-vapor interface). For binary mixtures, Rault's law is used in order to compute the molar fraction of each component (eq. 12 is referred to the component "A" of the mixture "A-B")

$$X_{s,A} = X_{s,A}^* \cdot X_A \quad (12)$$

During a mixture vaporization, molar concentrations within the droplet vary with different rates, due to the different values of latent heat. The mixture molecular weight is

$$PM_{MIX} = X_A PM_A + X_B PM_B \quad (13)$$

Fuel concentration at interface is given by eq. 14

$$Y_{s,F} = Y_{s,A} + Y_{s,B} \quad (14)$$

where

$$Y_{s,A} = \frac{X_{s,A} PM_A}{X_{s,A} PM_A + X_{s,B} PM_B + (1 - X_{s,A} - X_{s,B}) PM_{AIR}} \quad (15)$$

LIQUID PHASE ANALYSIS - Equation 16 is used to compute the mass concentration in the liquid phase

$$Y_A = \frac{X_A PM_A}{PM_{MIX}} \quad (16)$$

The following equations (17,18) give the representation of latent heat and thermal conductivity, respectively

$$L = L_A Y_A + L_B Y_B \quad (17)$$

$$k_l = k_A Y_A + k_B Y_B \quad (18)$$

Concerning the specific heat capacity  $c_{pl}$  used in the finite conductivity model, the values  $c_{plA}$  and  $c_{plB}$  are computed by means of polynomial expressions [50,51]; the polynomials depend on the surface temperature  $T_s(t)$ , as follows:  $c_{plA} = f(T_s)$ ,  $c_{plB} = f(T_s)$  and  $c_{pl} = c_{plA} Y_A + c_{plB} Y_B$ . When finite thermal conductivity is considered, such a computation is referred to the droplet mean temperature,  $c_{pl} = f(\bar{T})$ .

## GAS-VAPOR INTERFACE ANALYSIS

### Reference temperature

$$T_r = T_s + \frac{T_g - T_s}{3} \quad (19)$$

### Reference concentration

$$Y_r = \frac{2}{3} Y_{s,F} \quad (20)$$

Gas specific heat capacity - it is a function of the reference temperature, and it is computed on the basis of a polynomial law [51].

### Thermal conductivity of gas

$$k_{AIR} = f(T_r) \quad (21)$$

$$k_{vA} = f(T_r, T_{bnA}) \quad (22)$$

$$k_g = k_{AIR} Y_{AIR} + k_{vA} Y_{s,A} + k_{vB} Y_{s,B} \quad (23)$$

### Gas density

$$\rho_g = \left( \frac{Y_{AIR}}{\rho_{AIR}} + \frac{Y_r}{\rho_l} \right)^{-1} \quad (24)$$

### Gas viscosity

$$\mu_{AIR} = f(T_r) \quad (25)$$

$$\mu_v = \mu_{s,A}(T_r) Y_{s,A} + \mu_{s,B}(T_r) Y_{s,B} \quad (26)$$

$$\mu_g = \mu_{AIR}(T_r) Y_{AIR} + \mu_v(T_r) Y_r \quad (27)$$

Computation of molecular diffusion coefficient ( $B_M$ ) and thermal diffusion coefficient ( $B_T$ )

$$B_M = (Y_{s,F} - Y_{F\infty}) / (1 - Y_{s,F}) \quad (28)$$

$$B_T = c_{pg} (T_g - T_s) / L \quad (29)$$

#### INFINITE CONDUCTIBILITY MODEL - DROPLET HEATING PHASE

Computation of mass flow rate ( $\dot{m}$ ) and diameter discrete time decrement ( $\frac{\Delta d}{\Delta t}$ )

$$\dot{m}_F = 2\pi d \left( \frac{k_g}{c_{pg}} \right) \left( 1 + 0.3 Re_D^{1/2} Pr_g^{1/3} \right) \ln(B_M + 1) \quad (30)$$

$$\frac{\Delta d}{\Delta t} = - \frac{4k_g (1 + 0.3 Re_D^{1/2} Pr_g^{1/3}) \ln(B_M + 1)}{c_{pg} \rho_l d} \quad (31)$$

Diameter time variation ( $d(t + \Delta t)$ )

$$d(t + \Delta t) = d(t) - \frac{\Delta d}{\Delta t} \cdot \Delta t \quad (32)$$

Evaporated flow rates for each component during the time step ( $\Delta t$ )

$$\dot{m}_A = \frac{Y_{s,A}}{Y_{s,A} + Y_{s,B}} \cdot \dot{m}_F \quad (33)$$

Computation of the surface temperature time evolution ( $T_s(t + \Delta t)$ ): according to the approach proposed in [33], the energy balance at interface is resolved and the following solution is obtained:

$$T = T_s = T_{eff} + (T_{s0} - T_{eff}) \exp\left(-\frac{3ht}{c_l \rho_l r_d}\right) \quad (34)$$

FINITE CONDUCTIBILITY MODEL - DROPLET HEATING PHASE Finite conductivity model uses a solution procedure similar to that previously described (infinite conductivity model), but it differs in the droplet surface temperature computation  $T_s(t + \Delta t)$ . In the current approach, the non-uniform temperature distribution within the droplet is taken into account. The thermal conduction equation is computed according to:

$$\frac{\partial T}{\partial t} = \frac{\alpha}{r^2} \frac{\partial}{\partial r} \left( r^2 \frac{\partial T}{\partial r} \right) + P(r) \quad (35)$$

where  $P(r)$  is the term that models the thermal radiation, neglected in the present case. Equation (35) is solved by means of Dombrovsky-Sazhin parabolic solution [49].

**STEADY EVAPORATION PHASE** - A single approach is used to model the steady evaporation phase, once the heating transient is completed. Vaporization is modeled on the basis of a modified  $D^2$  law: the Ranz-Marshall correlation is used to represent the convection effect; the time dependence of thermal and physical properties on component concentration and the time dependence of  $Re$  on droplet diameter and concentration are modeled.

$$[d(t + \Delta t)]^2 = [d(t)]^2 - \lambda \cdot \Delta t \quad (36)$$

where

$$\lambda = \frac{-8k_g (1 + 0.3 Re_D^{1/2} Pr_g^{1/3}) \ln(B_M + 1)}{c_{pg} \rho_l} \quad (37)$$

Then,  $X_A$  and  $X_B$  are computed and the thermal properties are updated:

$$\rho_l = \rho_A Y_A + \rho_B Y_B = f(Y_A, Y_B) \quad (38)$$

$$\text{where } (Y_A, Y_B) = f(X_A, X_B) \quad (39)$$

#### CONDUCTION EQUATION - DOMBROVSKY-SAZHIN PARABOLIC SOLUTION

The conduction equation is solved accounting for the *a priori* assumption that the droplet temperature profile assumes a parabolic shape. The solution is given by

$$T(r, t) = T_c(t) + [T_s(t) - T_c(t)](r/r_d)^2 \quad (40)$$

where  $T_c(t)$  and  $T_s(t)$  are the temperature at droplet centre and at droplet surface, respectively. After manipulations, whose details are provided in [49], the expression of the surface temperature is obtained

$$T_s = (\bar{T} + 0.2\zeta T_g) / \psi + 0.2\zeta \rho_l r_d \frac{dr_d}{dt} L / (k_l \psi) \quad (41)$$

$$\text{where} \quad \zeta = 0.5 \text{Nu} \frac{k_g}{k_l} \quad (42)$$

$$\text{Nu} = 2h \frac{r_d}{k_g} \quad (43)$$

$$\psi = 1 + 0.2\zeta \quad (44)$$

$$\bar{T} = \frac{3}{r_d^3} \int_0^d r^2 T(r) dr \quad (45)$$

with  $h$  and  $\frac{dr_d}{dt}$  supposed constant. Introducing the non-dimensional variables as follows,

$\theta = (T - T_0) / (T_g - T_0)$  and  $\text{Fo} = k_l t / (\rho_l c r_d^2)$  (Fourier number), eq. 58 becomes

$$\theta_s = (\bar{\theta} + 0.2\zeta) \quad (46)$$

$$\text{where} \quad \bar{\theta} = 1 - \exp(-3\zeta \text{Fo} / \psi) \quad (47)$$

with the initial condition  $\bar{T} = T_0$ . For relatively low Fourier number, the parabolic model solution detaches noticeably from the analytical result of the conduction problem. Therefore, the correction proposed by Sazhin is adopted, as well [49].

#### 10.14 References

- [1] Chiatti, G., Chiavola, O., Palmieri, F., Inline Pump Internal Flow Characterization for Optimized Diesel Injection, presented at ASME ICEF conference, 1663, 2008.
- [2] AMESim Tutorial and User Guide, AMESim Technical Bulletins, LMS.
- [3] Tanaka, Y., Hosokawa, H., Kubota, H., Makita, T. (1991). Viscosity and Density of Binary Mixtures of Cyclohexane with n-Octane, n-Dodecane, and n-Hexadecane Under High Pressures. International Journal of Thermophysics, 12(2).
- [4] Khasanshin, T. S., Shchamialiou, A. P., Poddubskij, O. G. (2003). Thermodynamic Properties of Heavy n-Alkanes in the Liquid State: n-Dodecane. International Journal of Thermophysics, 24(5).
- [5] Ball, S. J., Trusler, J. P. M. (2001). Speed of Sound of n-Hexane and n-Hexadecane at Temperatures Between 298 and 373 K and Pressures up to 100 MPa. International Journal of Thermophysics, 22(2).
- [6] Hiroyasu, H., Arai, M. (1980). Fuel Spray Penetration and Spray Angle of Diesel Engines. JSAE, 21.
- [7] Jung, D., Assanis, D. N., Multi-zone DI diesel spray combustion model for cycle simulation studies of engine performance and emissions, presented at SAE World Congress, 2001-01-1246, 2001.



- [8] Hiroyasu, H., Kadota, T., Arai, M. (1983). Development and Use of a Spray Combustion Modeling to Predict Diesel Engine Efficiency and Pollutant Emissions (Part 1 Combustion Modeling), Bulletin of the JSME, 26(214).
- [9] Kyriakides, S. C., Dent, J. C., Mehta, P. S., Phenomenological Diesel Combustion Model Including Smoke and NO Emission, presented at SAE World Congress, 860330, 1983.
- [10] Bazari, Z., A DI Diesel Combustion and Emission Predictive Capability for Use in Cycle Simulation, presented at International Congress & Exposition, 920462, 1992.
- [11] Gao, Z., Schreiber, W., A Multizone Analysis of Soot and NO<sub>x</sub> Emission in a D.I. Diesel Engine as a Function of Engine Load, Wall Temperature, and Intake Air O<sub>2</sub> Content, presented at ASME ICE conference 2000-ICE-314, 2000.
- [12] Reitz, R. D., Bracco, F. B., On the Dependence of Spray Angle and Other Spray Parameters on Nozzle Design and Operating Conditions, presented at International Congress & Exposition, 790494, 1979.
- [13] Dan, T., The Turbulent Mechanism and Structure of Diesel Spray, Ph. D. Thesis, Toshiya University, 1996.
- [14] Hiroyasu, H., Arai, M., Tabata, M., Empirical Equations for the Sauter Mean Diameter of a Diesel Spray, presented at SAE International Congress & Exposition, 890464, 1989.
- [15] G. M. Faeth (1977). Current Status of Droplet and Liquid Combustion. Prog. Energy Combust. Sci., 3.
- [16] G. M. Faeth (1983). Evaporation and Combustion of Sprays. Prog. Energy Combust. Sci., 9.
- [17] G. M. Faeth (1987). Mixing, Transport and Combustion in Sprays. Prog. Energy Combust. Sci., 13.
- [18] C. K. Law (1975). A Theory for Monodisperse Spray Vaporization in Adiabatic and Isothermal Systems. International Journal of Heat and Mass Transfer, 18.
- [19] C. K. Law (1988). On the Controlling Parameter in the Gasification Behavior of Multicomponent. Combustion and Flame, 73.
- [20] W. A. Sirignano (1983). Fuel Droplet Vaporization and Spray Combustion Theory. Prog. Energy Combust. Sci., 9.
- [21] W. A. Sirignano, Molecular Mixing in a Turbulent Flow: Some Fundamental Considerations, presented at AIAA 22th Aerospace Sciences Meeting, 1984.
- [22] B. Abramzon, W. A. Sirignano (1989). Droplet vaporization model for spray combustion calculations. International Journal Heat and Mass Transfer, 32.
- [23] S. Prakash, W. A. Sirignano (1978) .Liquid Fuel Droplet Heating with Internal Circulation. International Journal of Heat and Mass Transfer, 21.
- [24] S. Prakash, W. A. Sirignano, Theory of Convective Droplet Vaporization with Unsteady Heat Transfer in the Circulating Liquid Phase, presented at 17th Aerospace Sciences Meeting, 1979.
- [25] A. Y. Tong, W. A. Sirignano (1986). Multi-component Transient Droplet Vaporization with Internal Circulation: Integral Equation Formulation and Approximate Solution. Numerical Heat Transfer, 10.
- [26] S. K. Aggarwal, A. Y. Tong, W. A. Sirignano (1983). A Comparison of Vaporization Models in Spray Calculations. AIAA Journal, 20(10).
- [27] S. K. Aggarwal, A. Y. Tong, W. A. Sirignano, A Study of Inter-Phase Exchange Laws in Spray Combustion Modeling, presented at AIAA 21th Aerospace Sciences Meeting, 83-0152, 1983.
- [28] J. S. Chin, A. H. Lefebvre, The Role of the Heat-Up Period in Fuel Drop Evaporation, presented at AIAA 21th Aerospace Sciences Meeting, 1983.
- [29] J. S. Chin, A. H. Lefebvre (1983). Effective Values of Evaporation Constant for Hydrocarbon Fuel Drop. AIAA Journal, 21(10).

- [30] J. S. Chin, A. H. Lefebvre (1983). Steady-State Characteristics of Hydrocarbon Fuel Drops, *AIAA Journal*, 21.
- [31] J. S. Chin, R. Durrett, A. H. Lefebvre (1984). The Interdependence of Spray Characteristics and Evaporation History of Fuel Sprays", *Journal of Engineering for Gas Turbines and Power*, 106.
- [32] S. Sazhin, T. Kristyadi, W. A. Abdelghaffar, M. R. Heikal (2006). Models For Droplet Heating and Evaporation: Comparative Analysis, *Journal of Fuel*, 85.
- [33] S. Sazhin, T. Kristyadi, A Conduction Model for Transient Heating of Fuel Droplets, presented at 3d International ISAAC Congress Berlin, 2001.
- [34] S. Sazhin (2006). Advanced Models of Fuel Droplet Heating and Evaporation. *Progress in Energy and Combustion Science*, 32.
- [35] S. S. Sazhin, W. A. Abdelghaffar, P. A. Krutitskii, E. M. Sazhina, M. R. Heikal (2008). Numerical Modelling of Droplet Transient Heating and Evaporation, *Heat Transfer Research*, 39(1.20).
- [36] S. S. Sazhin, W. A. Abdelghaffar, P. A. Krutitskii, E. M. Sazhina, S. V. Mikhlovsky, S. T. Meikle, M. R. Heikal (2004). Transient Heating of Diesel Fuel Droplets, *International Journal of Heat and Mass Transfer*, 47.
- [37] W. A. Abdelghaffar, S. S. Sazhin, M. R. Heikal, E. M. Sazhina, P. A. Krutitskii (2005). Advanced Gas-Droplets Heat Transfer Models and Their Applications, *Progress in Energy and Combustion Science*, 32.
- [38] S. S. Sazhin, Modeling of Heating, Evaporation and Ignition of Fuel Droplets: Combined Analytical, Asymptotic and Numerical Analysis, School of Engineering, Faculty of Science and Engineering, University of Brington (UK).
- [39] S. S. Sazhin , P. A. Krutitskii, S.B. Martynov, D. Mason, M. R. Heikal, E. M. Sazhina, Transient Heating of a Semitransparent Droplet, School of Engineering, Faculty of Science and Engineering, University of Brington (UK).
- [40] W. A. Abdelghaffar, S. S. Sazhin, M. R. Heikal, E. M. Sazhina, Models for Transient Droplet Heating: A Comparative Analysis, presented at International Conference on Heat Transfer, Fluid Mechanics and Thermodynamics, Cairo, Egypt, 2005.
- [41] B. Abramzon, S. S. Sazhin (2006). Convective Vaporization of Fuel Droplet with Thermal Radiation Absorption. *Progress in Energy and Combustion Science*, 32(2).
- [42] S. S. Sazhin, E. M. Sazhina, M. R. Heikal, P. A. Krutitskii, L. A. Dombrovsky, J. Pozorski, Modelling of Diesel Fuel sprays: Penetration, Heating, Autoignition. presented at the Second Mediterranean Combustion Symposium, 2002.
- [43] S. S. Sazhin, W. A. Abdelghaffar, P. A. Krutitskii, E. M. Sazhina, S. V. Mikhlovsky, S. T. Meikle (2004). Radiative Heating of Semitransparent Diesel Fuel Droplets. *ASME Journal of Heat Transfer*, 126(1).
- [44] L. A. Dombrovsky, S. S. Sazhin, E. M. Sazhina, G. Peng, M. E. A. Beadsley, S. V. Mikhlovsky, M. R. Heikal (2001). Heating and Evaporation of Semi-transparent Diesel Fuel Droplets in presence of thermal radiation. *Fuel*, 80.
- [45] L. A. Dombrovsky, S. S. Sazhin (2003). Absorption of Thermal Radiation in a Semitransparent Spherical Droplet: a Simplified Model. *International Journal Heat and Fluid Flow*, 24.
- [46] L. A. Dombrovsky, S.S. Sazhin (2004). Absorption of External Thermal Radiation in Asymmetrically Illuminated Droplets. *Journal of Quantitative Spectroscopy and Radiation Transfer*, 87(2).
- [47] K. K. Varanasi, H. L. Clack, R. S. Miller (2004). On Preferential Diffusion of Binary Component Liquid Droplets Evaporating in Two-Phase Mixing Layer, *International Journal of Multiphase Flow*, 30(10).
- [48] Atomization and Sprays, A. H. Lefebvre, Hemisphere Publishing Corporation, 1989, USA.

- [49] L. A. Dombrovsky, S. S. Sazhin (2003). A parabolic temperature profile model for heating of droplets. *Journal of Heat Transfer*, 125.
- [50] *An Introduction to Combustion*, S. R. Turns, McGraw-Hill, Inc, 1996.
- [51] *Handbook of Heat Transfer Applications*, W. M. Rohsenow, J. P. Hartnett, Y. I. Cho. McGraw-Hill, 1985.
- [52] D. J. Torres, P. J. O'Rourke, A. A. Amsden (2003). Efficient Multicomponent Fuel Algorithm, *Combustion Theory and Modelling*, 7.
- [53] H.O. Hardenberger et Al., An Empirical Formula for Computing Rise delay of a Fuel from its Cetane Number and From the Relevant Parameters of Direct Injection Diesel Engines, presented at SAE International Congress & Exposition, 790493, 1979.

## 11. References of Published Works

- [1] Chiavola, O. and Palmieri, F., "Coupling Codes for Nozzle Flow Modeling in Diesel Injection Systems", ICES2006 ASME Paper No. 1414.
- [2] Chiavola, O., Palmieri, F. and Chiatti, G., "Integrated Modeling of Fuel Influence on Common Rail Injection System Performance", ICEF2006 ASME Paper No. 1556.
- [3] Chiavola, O. and Palmieri, F., "Modeling Needle Motion Influence on Nozzle Flow in High Pressure Injection System", SAE Paper No. 2007-01-0250.
- [4] Chiatti, G., Chiavola, O. and Palmieri, F., "Diesel Injector Modeling for 3D in-Cylinder Flow Simulation", 2007 AST Conference, AVL List - Graz.
- [5] Chiatti, G., Chiavola, O. and Palmieri, F., "Injector Dynamic and Nozzle Flow Features in Multiple Injection Modeling", SAE Paper No. 2007-24-0238.
- [6] Chiatti, G., Chiavola, O. and Palmieri, F., "Flow Features in Reduced Dwell Time Diesel Injector ", SAE Paper No. 2008-01-0927.
- [7] Chiavola, O. and Palmieri, F., "Inline Pump Internal Flow Characterization for Optimized Diesel Injection", ICES2008 ASME Paper No. 1663.
- [8] Chiatti, G., Chiavola, O. and Palmieri, F., "Flow Features in Reduced Dwell Time Diesel Injector ", SAE Paper No. 2008-01-0927.
- [9] Chiatti, G., Chiavola, O. and Palmieri, F., " Spray Modeling for Diesel Engine Performance Analysis", SAE Paper No. 2009-01-0835.

## 12. Concluding Remarks

In the frame of direct injected diesel engines, a preliminary role is played by the strong link that exists between the combustion behavior and the strategies that are adopted to promote the mixing among reactants in combustion chamber. As it is pointed out through the present work, the research approaches take advantage of consideration that fuel introduction involves several interrelated phenomena; indeed, all the presented models have been based on the following consideration: besides the uncertainties typical of the simulations, modeling gives the possibility to describe the interactions and the interdependencies among the relevant processes. Therefore, the work has been aimed at developing a comprehensive modeling approach, having the capability of take the deep connection between fuel injection phenomena (e.g. injection strategy, fuel flows, jet atomization, evaporation and mixture formation) into account. In practice, such a unitary approach has been realized outlining three different simulation procedures.

A comprehensive computational tool in which two different codes are coupled has been built and presented, predicting the performance of the entire injection system, the spray characteristics, the interaction among spray-cones, chamber flows and geometry. The injection system simulation has been the first step of the modelling procedure: the obtained results, concerning needle lift injection and flow rate time evolution have been used to initialize the nozzle flow simulation. Summarizing:

- the first step of the modeling procedure highlights the complex pressure dynamics of the transient phenomena, and the obtained results, as the needle lift time evolution, are used to initialize the nozzle flow simulation;

- the dynamic CFD analysis on the nozzle shows its attitude to point out the behavior of the flow streams, the formation of the cavitating zones and the role of geometrical details like the inlet edge hole, nozzle layout and needle motion;

- finally, by means of the 'nozzle interface' activation, the spray modeling can take into account the nozzle exit flow data, allowing for a complete and unitary representation of the injection process.

In the second simulation procedure, with an upside-down order, 3D-CFD investigations have been regarded as the starting point to properly lump some critical parameters like the flow coefficients of the fuel metering components. Such a modeling approach is helpful, due to the fact that the fine modeling of fuel delivery process is directly tied to the description accuracy of combustion processes; therefore, it represents a key factor during the engine optimization in the matter of performance optimization and emission reduction.

In the third procedure, a comprehensive diesel injection system model is built, presented and used; the simulations are based on three lumped parameter computation modules, whose details have been extensively discussed. Moving from the flow rate/injection velocity it is possible to obtain relevant indications concerning the injection process characterization, essentially by means of relatively simple correlations. As shown, the model is certainly suitable for the evaluation of fuel feature influence on the process. More in detail, the integration of injection-vaporization model with a relatively simple single-zone combustion simulation enables to evaluate the influence of the whole injection process on the engine performance, with a comprehensive approach. The same model can be used to evaluate the influence of component layout, injection strategy, phasing and parametric studies in general at low computation cost, as well.

## **13. Next Outlooks**

It has to be highlighted that the performed activity represents a useful starting point for the next research programs in which the author is involved. It can be inferred that internal combustion engine will still keep its role for some decades; however, it must be continuously improved, and great efforts have to be made in order to increase efficiency and to fulfill future emission legislation. A systematic and precise control of mixture formation with modern high-pressure injection systems, including fully variable rate shaping, variable nozzle geometry, pressure-modulated injection etc., is crucial for realizing future combustion concepts. Due to the growing number of free parameters, the prediction of spray and mixture formation is becoming increasingly complex. For this reason, the optimization of the processes using numerical models is important. A continuous improvement of existing models as well as the development of models describing new effects, which can arise from the development of new injection systems and injection strategies, is necessary; thus, a detailed and accurate modeling of the relevant sub-processes has to be guaranteed, increasing the predictive quality of calculations. All the models and the proposed approaches in the work have been presented in such a frame of reference.